Inaugural dissertation

for
obtaining the doctoral degree
of the
Combined Faculty of Mathematics, Engineering and Natural Sciences
of the
Ruprecht-Karls University
Heidelberg

Presented by
M.Sc. Sandy Stephanie Burkart
Born in Heidelberg, Germany
Oral examination: 28.10.2022

Kinetic Characterization and Dynamic Mathematical Modeling of the RIG-I Signaling Pathway and the Antiviral Responses

Referees:

Prof. Dr. Ursula Klingmüller

Dr. Marco Binder

Für meine Familie

Acknowledgements

Ich möchte mich ganz herzlich bei allen bedanken, die mich während dieser Arbeit begleitet und unterstützt haben.

Zuallererst möchte ich mich bei meinem Betreuer Dr. Marco Binder bedanken. Vielen Dank Marco, dass du mich sowohl als HiWi als auch als Doktorandin aufgenommen hast. Vielen Dank für deine Betreuung, Unterstützung und deine zahlreichen Ratschläge. Danke auch für deine stets offene Tür und die tolle Arbeitsatmosphäre.

Ich möchte Prof. Dr. Ursula Klingmüller dafür danken, dass sie nicht nur Fakultätsgutachterin für diese Arbeit ist, sondern mich außerdem während meiner Promotion als Teil meines Thesis Advisory Committees unterstützt hat.

Vielen Dank an PD Dr. Carl Herrmann und Dr. Viet Loan Dao Thi, die sich bereit erklärt haben diese Arbeit zu lesen und Teil meiner Prüfungskommission zu sein.

Vielen Dank an Prof. Dr. Volker Lohmann, für die Unterstützung und hilfreichen Anregungen als Teil meines Thesis Advisory Committees.

Außerdem möchte ich der Helmholtz-Graduiertenschule für Krebsforschung und dem Deutschen Krebsforschungszentrum für das Stipendium zur Finanzierung meiner Promotion danken.

Danke an alle ehemaligen und aktuellen Mitglieder des Binder Labs für die vielen Diskussionen, die großartige Arbeitsatmosphäre, die frühzeitige Einstimmung auf die Weihnachtszeit, die gemeinsamen Kaffeepausen, und viele weitere schöne Momente. Danke Sandra, für deine Geduld, deine stetige Hilfsbereitschaft und die gemeinsame Zeit sowohl im als auch außerhalb des Labors. Danke Vladi, für deine Hilfe und deine Tipps im Labor. Danke, dass du dir immer Zeit für mich genommen hast und dafür dass du dein Brigadeiro Rezept mit mir geteilt hast.

Den aktuellen und ehemaligen Mitgliedern von F170 möchte ich für das tolle Arbeitsumfeld, die Hilfsbereitschaft, sowie die zahlreichen Zusammenkünfte und Veranstaltungen danken.

Vielen Dank an Darius Schweinoch und Prof. Dr. Lars Kaderali für die Kollaboration, die für dieses Projekt entscheidend war.

Ganz besonderer Dank geht an Hendrik, David, und Christopher. Danke, für die gemeinsame Zeit im Labor, die Kaffeepausen, und unsere morgendlichen Frühstückstreffen. Vor allem aber danke für die Zeit außerhalb des Labors, für die gemeinsamen Kochabende und eure Freundschaft.

Vielen Dank an Anna, die mich durch ihren Online Aufruf seit dem ersten Tag des Studiums begleitet und die es glücklicherweise nach dem Studium auch nach Heidelberg gezogen hat. Danke für die gemeinsame Zeit, ob Mädels Abende in München oder Poetry Slams und gemeinsame Mittagspausen in Heidelberg. Danke für dein offenes Ohr, dein Verständnis und deine Freundschaft.

Von ganzem Herzen möchte ich mich bei meiner Familie, besonders bei meinen Eltern Christine und Eduard, sowie bei meinem Bruder Marcel, bedanken. Danke, dass ihr immer für mich da seid, mir in jeder Lebenslage beisteht und mich ermuntert meinen eigenen Weg zu gehen.

Mein größter Dank geht an meinen Mann Moritz für die Liebe, die endlose Unterstützung, die aufbauenden Worte und dafür, dass du immer für mich da bist.

Summary

RIG-I-like receptors (RLR) are cytosolic pattern recognition receptors (PRR) which are pivotal for the detection of virus infection. RIG-I senses viral double-stranded RNAs (dsRNA) and initiates cellular antiviral defense responses, resulting in the expression of type I and III interferons (IFN). Secreted IFNs signal in an auto and paracrine manner and mediate the transcriptional induction of distinct IFN-stimulated genes (ISG), which collectively establish an antiviral state of the cell. Whereas the topology of this pathway has been described thoroughly, the dynamics, particularly of the RIG-I-mediated IFN induction, are much less understood. In this study, I employed electroporation-based transfection with virus-like 5'ppp-dsRNA to synchronously activate the RIG-I signaling pathway in human lung adenocarcinoma (A549) cells and thus characterize the dynamics of cell-intrinsic innate immune responses. For this purpose, I focused on time-resolved western blotting of key pathway components, live-cell imaging of transcription factor relocalization, and quantitative RT-PCR of various target genes. Although previous studies reported intriguing cell-intrinsic stochasticity in the activation of the RLR and IFN signaling pathways, simultaneous 5'ppp-dsRNA stimulation of A549 cells resulted in highly deterministic and synchronous RIG-I signaling. By employing an IFN-blind A549 cell line, harboring functional knockouts of the receptors required for type I, II, and III IFN signaling, I analyzed the differences between primary RIG-I-mediated signaling and the subsequent signaling phase downstream of the IFN receptors. Interestingly, IFN signaling through the JAK/STAT cascade was not required to induce the production of IFN. Utilizing the generated kinetic data of antiviral signaling as foundation and collaborating with computational scientists, we developed and calibrated a comprehensive mathematical model of the cell-intrinsic antiviral response system. This model is able to predict the kinetics of signaling events induced upon dsRNA recognition by RIG-I as well as feedback and signal amplification through IFN and JAK/STAT signaling. Furthermore, I examined the impact of viral antagonists on signaling dynamics by employing viral proteins interfering with the host antiviral response system at defined steps: the dengue virus (DENV) protein NS5 interferes with IFN signaling, whereas the NS3/4A protease of hepatitis C virus (HCV), the N^{pro} protease of classical swine fever virus (CSFV), as well as NS1 of influenza A virus (IAV) all target RLR signaling and thereby inhibit the induction of IFN. Additionally, the ORF6 protein of SARS-CoV-2 exhibits a multi-level strategy to impede defense responses by targeting both IFN induction and IFN signaling. Strikingly, the impact of these viral antagonists on antiviral signaling dynamics could be properly simulated by the established mathematical model. Consequently, our model permits *in silico* simulation of viral interference with the antiviral response system and provides a powerful tool to study the impact of yet unknown viral antagonists or other factors perturbing antiviral innate immune responses. Lastly, since previous work in our lab demonstrated an unexpectedly high overlap of RLR and IFN signaling-induced ISG expression, I used whole-transcriptome expression profiling to examine and compare the underlying

roles of the transcription factors IRF1 and IRF3 in IFN-independent RIG-I-mediated signaling. Interestingly, dsRNA-induced expression of certain genes was both IRF3 and IFN-independent. The dsRNA-induced expression of some of those genes was partially NF-κB-dependent, whereas others seemed to be dependent on IRF1 or other transcription factors. In conclusion, this study provides insights into RIG-I-mediated but IFN-independent signaling upon virus-like dsRNA stimulation and might, in conjunction with the established mathematical model, facilitate deciphering the complexity of the virus-host interface.

Zusammenfassung

RIG-I-ähnliche Rezeptoren (RLR) sind zytosolische Mustererkennungsrezeptoren (PRR), die für die Erkennung von Virusinfektionen von zentraler Bedeutung sind. RIG-I erkennt virale doppelsträngige RNAs (dsRNA) und initiiert zelluläre antivirale Abwehrreaktionen, die zur Expression von Interferonen (IFN) des Typs I und III führen. IFNs werden sekretiert, vermitteln Signale auf auto- und parakriner Weise und induzieren die Transkription einer Vielzahl von IFN-stimulierten Genen (ISG), die kollektiv einen antiviralen Zustand der Zelle etablieren. Während die Topologie dieses Signalpfades ausführlich beschrieben wurde, ist die Dynamik, insbesondere die durch RIG-I vermittelte IFN-Induktion, weit weniger bekannt. In dieser Studie habe ich eine auf Elektroporation basierende Transfektion mit virusähnlicher 5'ppp-dsRNA zur synchronen Aktivierung des RIG-I-Signalwegs in menschlichen Lungenadenokarzinomzellen (A549) eingesetzt und somit die Dynamik der zelleigenen angeborenen Immunantwort charakterisiert. Hierfür habe ich mich auf zeitaufgelöstes Western Blotting von Schlüsselkomponenten des Signalwegs, Live-Cell-Imaging der Translokation von Transkriptionsfaktoren und quantitative RT-PCR von verschiedenen Zielgenen fokussiert. Obwohl vorherige Studien über eine erstaunliche zelleigene Stochastizität bei der Aktivierung der RLR- und IFN-Signalwege berichteten, führte die synchrone 5'ppp-dsRNA-Stimulation von A549 Zellen zu einer hochgradig deterministischen und synchronen RIG-I-vermittelten Signalübertragung. Die Verwendung einer IFN-blinden A549 Zelllinie mit funktionellen Knockouts der für die IFN-Signalübertragung erforderlichen Rezeptoren vom Typ I, II und III ermöglichte es mir, die Unterschiede zwischen der primären RIG-I-vermittelten Signalübertragung und der sekundären, den IFN-Rezeptoren nachgeschalteten Signalkaskade zu analysieren. Interessanterweise war die IFN-Signalübertragung durch die JAK/STAT-Kaskade nicht erforderlich, um die IFN-Produktion in einer Art Auto-Feedback zu induzieren. In Kollaboration mit Bioinformatikern haben wir ein umfassendes mathematisches Modell des zelleigenen antiviralen Abwehrsystems entwickelt und kalibriert, wobei wir die kinetischen Daten der antiviralen Signalübertragung als Grundlage verwendeten. Das Modell ermöglicht eine genaue Vorhersage der Kinetik von Signalprozessen, die der dsRNA-Erkennung durch RIG-I nachgeschaltet sind, sowie der Rückkopplung und Signalverstärkung durch sekretiertes IFN und die JAK/STAT-Signalübertragung. Darüber hinaus untersuchte ich die Auswirkungen viraler Antagonisten auf die Signaldynamik, indem ich einige bekannte virale Proteine, die das antivirale Abwehrsystem des Wirts in definierten Prozessen beeinträchtigen, verwendete: während das Dengue Virus (DENV) Protein NS5 den IFN-Signalweg beeinträchtigt, greifen die NS3/4A Protease des Hepatitis C Virus (HCV), die N^{pro} Protease des klassischen Schweinepest Virus (CSFV), sowie NS1 des Influenza A Virus (IAV) alle in den RLR-Signalweg ein und hemmen somit die Induktion von IFN. Darüber hinaus zeigt das ORF6 Protein von SARS-CoV-2 eine mehrstufige Strategie zur Hemmung des antiviralen Systems, indem es sowohl auf die IFN-Induktion als auch auf die IFN-Signalübertragung

abzielt. Die Auswirkungen dieser viralen Antagonisten auf die antivirale Signaldynamik konnten mit dem etablierten mathematischen Modell korrekt simuliert werden. Folglich ermöglicht unser Modell eine *in silico* Simulation der viralen Interferenz auf das antivirale Abwehrsystem und bietet ein wertvolles Werkzeug zur Untersuchung der Wirkungsweise noch unbekannter viraler Antagonisten oder anderer Faktoren, die die RLR- und/oder IFN-Signalübertragung beeinträchtigen. Da frühere Arbeiten aus unserem Labor eine unerwartet hohe Überlappung von RLR- und IFN-induzierter ISG-Expression aufzeigten, untersuchte und verglich ich mittels Expressionsanalysen die zugrundeliegenden Rollen der Transkriptionsfaktoren IRF1 und IRF3 bei der IFN-unabhängigen RIG-I-vermittelten Signalübertragung. Interessanterweise war die dsRNA-induzierte Expression bestimmter Gene sowohl IRF3- als auch IFN-unabhängig. Die dsRNA-induzierte Expression einiger dieser Gene war teilweise NF-κB-abhängig, während andere von IRF1 oder anderen Transkriptionsfaktoren abhängig zu sein schienen. Die vorliegende Studie gibt Einblicke in die RIG-I-vermittelte aber IFN-unabhängige Signalübertragung bei der Erkennung virusähnlicher dsRNA und könnte in Verbindung mit dem etablierten mathematischen Modell die Entschlüsselung der Komplexität der Schnittstelle zwischen Virus und Wirt erleichtern.

Abbreviations

A	Adenosine
A1AT	Alpha-1-antitrypsin
A549	Human lung adenocarcinoma cells
ACT	α1-antichymotrypsin
ADAR	Adenosine deaminases acting on RNA
AGS	Aicardi–Goutières syndrome
AIM2	Absent in melanoma 2
ALR	AIM2-like receptor
AMP	Adenosine monophosphate
APC	Antigen-presenting cell
APS	Ammonium persulfate
ASC	Apoptosis-associated speck-like protein containing a CARD
ATF3	Activating transcription factor 3
ATP	Adenosin triphospate
au	Arbitrary unit
Bcl-10	B cell Lymphoma/Leukemia 10
BCR	B cell receptor
BSA	Bovine serum albumin
BST2	Bone marrow stromal cell antigen 2
CARD	Caspase activation and recruitment domain
CBP	CREB-binding protein
CCL	Chemokine (C-C motif) ligand
CD54	Cluster of differentiation 54
cDNA	Complementary DNA
cGAMP	Cyclic guanosine monophosphate–adenosine monophosphate
cGAS	Cyclic GMP-AMP synthase
CH25H	Cholesterol-25-hydroxylase
cIAP	Cellular inhibitor of apoptosis protein
CIP	Calf intestine phosphatase
CK2	Casein kinase II
CLR	C-type lectin receptor
COVID-19	Coronavirus disease 2019
CRE	Cyclic AMP response element
CRISPR	Clustered regularly interspaced short palindromic repeats
CSFV	Classical swine fever virus
CTD	C-terminal domain
CXCL10	C-X-C motif chemokine ligand 10
CYP1A1	Cytochrome P450 1A1
DAA	Direct-acting antiviral
DAI	DNA-dependent activator of interferon-regulatory factor
DAMP	Damage-associated molecular pattern
DAPK1	Death-associated protein kinase 1
Daxx	Death domain-associated protein 6
DC	Dendritic cell
ddH_2O	Double distilled H_2O
DDIT3	DNA damage inducible transcript 3
dNTP	Deoxyribose nucleoside triphosphate
DDX60	DExD/H-box helicase 60
Dectin	Dendritic cell-associated C-type lectin
DEG	Differentially expressed gene
DENV	Dengue virus
DHX15	DEAH-box helicase 15
DIP	Defective interfering particle
DMEM	Dulbecco's modified eagle medium
DMSO	Dimethyl sulfoxid
DNase	Desoxyribonuclease
dNTP	Desoxyribonucleotide triphosphate
dsRNA	Double-stranded RNA
DTT	Dithiothreitol
E. coli	*Escherichia coli*
EBV	Epstein-Barr virus
EDTA	Ethylenediaminetetraacetic acid
EF1α	Elongation factor 1α
EGR2	Early growth response protein 2
eIF2α	Eukaryotic translation initiation factor 2 subunit α
ELISA	Enzyme-linked immunosorbent assay
EMCV	Encephalomyocarditis virus
env	Viral envelope protein
ER	Endoplasmic reticulum
FCS	Fetal calf serum
FDR	False discovery rate
fwd	Forward
GAF	Interferon-γ activated factor
GAPDH	Glyceraldehyde-3-phosphate dehydrogenase
GAS	Interferon-γ activation site
GBP	Guanylate-binding protein
GFP	Green fluorescent protein
GMP	Guanosine monophosphate
GOBP	Gene Ontology terms of biological processes
HA	Human influenza hemagglutinin
HAT	Histone acetyltransferase
HBV	Hepatitis B virus
HCMV	Human cytomegalovirus

HCV	Hepatitis C virus
HDAC	Histone deacetylase
HERC5	HECT domain and RCC1-like domain-containing protein 5
HEV	Hepatitis E virus
HIV	Human immunodeficiency virus
HRP	Horseradish peroxidase
HSV	Herpes simplex virus
I	Inosine
IAV	Influenza A virus
IC50	Half maximal inhibitory concentration
ICAM-1	Intercellular adhesion molecule 1
IE62	Immediate-early protein 62
IFI	Interferon-α inducible protein
IFIT	Interferon-induced protein with tetratricopeptide repeat
IFITM	Interferon-induced transmembrane protein
IFN	Interferon
IFNAR	Interferon-α/β receptor
IFNGR	Interferon-γ receptor
IFNLR	Interferon-λ receptor
IFNR DKO	IFNAR1 IFNLR double KO
IFNR TKO	IFNAR1 IFNLR IFNGR1 triple KO
IKK	IκB kinase
IL	Interleukin
IL10R2	Interleukin-10 receptor 2
IL-8	Interleukin-8
INHBA	Inhibin beta A
IRAK	IL-1 receptor-associated kinase
IRF	Interferon regulatory factor
ISG	Interferon-stimulated gene
ISGF3	Interferon-stimulated gene factor 3
ISRE	Interferon-stimulated response element
IU	International unit
IκBα	Inhibitor of NF-κB
JAK	Janus protein kinase
K63	Lysine 63
KO	Knockout
LB	Lysogeny broth
LGP2	Laboratory of genetics and physiology 2
LMP2	Low molecular mass polypeptide 2
LPS	Lipopolysaccharide
LRR	Leucine-rich repeat
LUBAC	Linear ubiquitin chain assembly complex
MAM	Mitochondria-associated membranes of the ER
MAMP	Microbe-associated molecular pattern
MAPK	Mitogen-activated protein kinase
MAVS	Mitochondrial antiviral signaling protein
M-CSF	Macrophage colony-stimulating factor
MDA5	Melanoma differentiation antigen 5
MEF	Mouse embryonic fibroblast
MOI	Multiplicity of infection
MREG	Melanoregulin
MX	MX dynamin-like GTPase
MyD88	Myeloid differentiation primary response 88
NBD	Nucleotide-binding domain
NEMO	NF-κB essential modulator
NF-κB	Nuclear factor κ light chain enhancer of activated B cells
NK	Natural killer
NKLAM	Natural killer lytic-associated molecule
NLR	NOD-like receptor
NLRC	NLR family CARD domain-containing
NLRP	NLR family leucine rich repeat and pyrin domain-containing
NLRP3	NLR family pyrin domain-containing 3
NOD	Nucleotide-binding oligo-merization domain
N^{pro}	N-terminal protease
NR4A3	Nuclear receptor 4A3
NS	Nonstructural protein
OAS	Oligoadenylate synthetase
ODE	Ordinary differential equation
p300	E1A binding protein p300
PACT	Protein activator of the interferon-induced protein kinase
PAGE	Polyacrylamide gel electrophoresis
PAMP	Pathogen-associated molecular pattern
PARP14	Poly(ADP-ribosyl)ation
PBS	Phosphate buffered saline
PCR	Polymerase chain reaction
pDC	Plasmacytoid dendritic cell
PDL1	Programmed cell death 1 ligand 1
PGN	Peptidoglycan
PIAS1	Protein inhibitors of activated STAT1
PIK3AP1	Phosphoinositide-3-kinase adaptor protein 1
Pin1	Peptidyl-prolyl cis/trans iso-

	merase NIMA-interacting 1
PKC	Protein kinase C
PKR	Protein kinase R
poly(C)	Polycytidylic acid
poly(I:C)	Polyinosinic:polycytidylic acid
PP2A	Protein phosphatase 2A
PPM1B	Protein phosphatase 1B
PRD	Positive regulatory domain
PRD-LE	PRD-like element
PRR	Pattern-recognition receptor
PTM	Post-translational modification
PTP	Protein tyrosine phosphatase
qRT-PCR	Quantitative real-time PCR
RACK1	Receptor for activated C kinase 1
RD	Repressor domain
RdRp	RNA-dependent RNA polymerase
rev	Reverse
RIG-I	Retinoic acid-inducible gene-I
RIOK3	RIO kinase 3
RLR	RIG-I-like receptor
RNase	Ribonuclease
RNaseL	Ribonuclease latent
rNTP	Ribose nucleoside triphosphate
Riplet	Ring finger protein 135
ROS	Reactive oxygen species
RSV	Respiratory syncytial virus
RT	Reverse transcription
RVFV	Rift Valley fever virus
SARS-CoV	Severe acute respiratory syndrome coronavirus
sc	Single cell
SCF^{HOS}	Skp1-Cullin1-HOS-Roc1
SDS	Sodium dodecyl sulfate
SENP2	Sentrin/SUMO-specific protease 2
SERPINA	Serpin family A member
SeV	Sendai virus
SF1	Helicase superfamily 1
SHP	SH2 domain-containing phosphatase
SVR	Simeprevir
SLE	Systemic lupus erythematosus
SLIM	STAT-interacting LIM protein
SMS	Singleton-Merten syndrome
Smurf1	SMAD-specific E3 ubiquitin protein ligase 1
SOCS	Suppressor of cytokine signaling
ssRNA	Single-stranded RNA
STAT	Signal transducer and activator of transcription
STING	Stimulator of interferon response cGAMP interactor 1
SUMO	Small ubiquitin-like modifier
TAE	Tris acetate EDTA
TAK1	Transforming growth factor-activated kinase 1
TANK	TRAF family member-associated NF-κB activator
TBK1	TANK-binding kinase 1
TBS	Tris-buffered saline
TCR	T cell receptor
TEMED	N, N, N′, N′-tetramethylethyl-enediamine
TF	Transcription factor
TGS	Tris glycine sulfate
TIR	Toll/IL-1 receptor
TLR	Toll-like receptor
TNF	Tumor necrosis factor
TNFAIP3	TNF-α-induced protein 3
TRADD	TNFRSF1A-associated via death domain
TRAF	TNF receptor-associated factor
TRIF	TIR domain-containing adapter inducing interferon-β
TRIM	Tripartite motif-containing
TVR	Telaprevir
TYK2	Tyrosine-protein kinase 2
UBCH8	Ubiquitin carrier protein L6
UBE1L	Ubiquitin-like modifier-activating enzyme 7
USP	Ubiquitin specific peptidase
U-STAT	Unphosphorylated STAT
VSG	Virus-stimulated genes
VSV	Vesicular stomatitis virus
VZV	Varicella-Zoster virus
WNV	West Nile virus
wt	Wild type
ZAP	Zinc antiviral protein
ZC3HAV1	Zinc finger CCCH-type antiviral protein 1
ZCCHC3	Zinc finger CCHC domain-containing protein 3
ZNFX1	Zinc finger NFX1-type-containing 1

List of Figures

List of Tables

Contents

1. Introduction

Humans and other mammals are continuously exposed to a variety of pathogenic and non-pathogenic microbes, which can threaten normal homeostasis or cause disease. Hence, they have developed an intricate immune system to sense pathogens, mount a fast defense response, and remember the pathogen to protect themselves against future infections. The immune system in mammals contributes to maintaining the hosts integrity through its two major parts, the innate and the adaptive immune system, which are tightly interconnected. Adaptive immune responses are highly specific and induce the production of antibodies through T and B lymphocytes but take time to develop after the initial encounter with a pathogen (reviewed in [1, 2]). Receptors expressed on the surface of T and B lymphocytes, the T cell receptors (TCR) and B cell receptors (BCR), respectively, recognize distinct antigens and initiate immune responses. In order to identify a variety of antigens, diversity of TCRs and BCRs is generated through gene rearrangements during T cell and B cell development, as well as somatic hypermutation. In contrast to adaptive immune responses, the evolutionary ancient and highly conserved innate immune responses are not specific to a particular pathogen, but rather provide immediate host defenses against invading pathogens by broadly recognizing non-self structures (reviewed in [3–5]).
The evolutionary battle between pathogens and their hosts resulted in a continuous improvement and adaptation of the host immune system. In turn, pathogens, especially viruses, developed complex mechanisms to counteract and evade immune responses. Viruses are intracellular pathogens which can only replicate within a host cell. Depending on the viral evasion strategy, immune responses can either be delayed or overall dampened, providing an opportunity for efficient virus replication (reviewed in [6]). To determine the outcome of an infection, it is essential to investigate the dynamics of the immune response as well as the dynamic impact of viral antagonists. This will ultimately provide insights into the cellular antiviral signaling system, viral immune evasion, and virus-host interactions.
This work focusses on the investigation of the above-mentioned dynamics of cell-intrinsic innate antiviral signaling. Thus, the following introduction will cover the composition and function of innate immunity, mainly regarding the signaling network that is activated and modulated in response to viral infections.

1.1 Cellular Components of the Innate Immune System

The innate immune system not only comprises physical and chemical barriers but encompasses specialized cells originating from precursor cells in the bone marrow (Figure I). For instance, cells of the myeloid lineage are derived from a common myeloid progenitor cell and not only give rise to blood-building cells like megakaryocytes and erythrocytes, but to

different forms of granulocytes, mast cells, monocytes, and dendritic cells. Cells of the granulocyte lineage, i.e., neutrophils, eosinophils, and basophils, possess essential functions in innate immune responses. As an example, neutrophils are recruited to sites of infection by cytokines or chemokines and are able to phagocytize invading pathogens. They produce large amounts of reactive oxygen species (ROS), which are cytotoxic to bacterial pathogens [7]. Additionally, they have been described to produce considerable amounts of distinct cytokines and chemokines, such as tumor necrosis factor (TNF) [8, 9], and interleukin-8 (IL-8) [10, 11], emphasizing their pivotal role in innate immunity. Similarly, eosinophils secrete toxic substances as well as pro-inflammatory cytokines and are particularly active against helminths (reviewed in [12]). On the other side, although deriving from distinct lineages, basophils share many features with mast cells, both potently inducing inflammatory responses (reviewed in [13]). Maturing from monocytes cycling the blood upon macrophage colony-stimulating factor (M-CSF) stimulation, macrophages recognize and destruct foreign antigens and damaged cells by phagocytosis. Activated macrophages present antigens to helper T cells, produce large amounts of cytokines, e.g., TNF, IL-6, IL-12, or interferon (IFN)-γ, and thereby recruit specialized immune cells to the site of infection (reviewed in [14]).

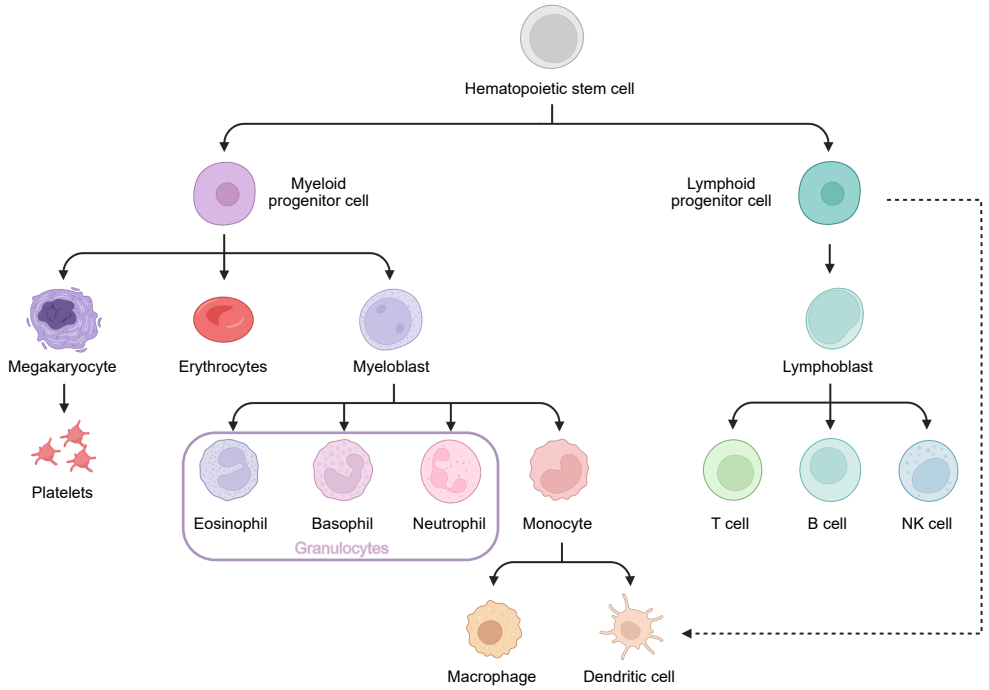

Figure I: Simplified scheme of hematopoiesis comprising the myeloid and lymphoid lineages.

Immune cells originate from a common precursor in the bone marrow, the hematopoietic stem cell. The major effectors of adaptive immunity, the T and B cells, arise from a common lymphoid progenitor cell, whereas most cells of the innate immune system originate from a common myeloid progenitor cell. As exception, natural killer (NK) cells classify as innate immune cells but develop from a lymphoid progenitor cell. Figure is created with BioRender.com.

Another type of professional antigen-presenting cells (APC) are dendritic cells (DC), originating from both, myeloid and lymphoid progenitor cells [15, 16]. Plasmacytoid DCs (pDC) present antigens to T cells (reviewed in [17]), are characterized by the secretion of high levels of type I IFNs [18–21], and are described to be essential in viral infections [22–24] (reviewed in [25]). Lastly, originating from the lymphoid lineage, natural killer (NK) cells detect and induce apoptosis in abnormal cells, i.e., cancer or virus-infected cells, upon recognition by distinct mechanisms (reviewed in [26–29]). Interestingly, NK cells are also able to produce and secrete cytokines, such as TNF, IFN-γ, and IL-1, which are crucial for defense responses against distinct pathogens [30].

1.2 Pattern Recognition Receptors

An essential element of the cellular response of innate immunity is the discrimination of self and non-self. Non-self recognition is based on conserved molecular motifs, i.e., pathogen-associated molecular patterns (PAMP), recently often referred to as microbe-associated molecular patterns (MAMP[1]), or damage-associated molecular patterns (DAMP), by pattern recognition receptors (PRR). PAMPs are conserved structures usually found within invading microbes, whereas DAMPs are endogenous molecules released or activated during tissue stress and cell damage. Commonly, PAMPs include, for instance, bacterial lipopolysaccharides (LPS) or flagellin, fungal β-Glucan, or viral DNA and RNA molecules. In contrast, DAMPs are classified into intracellular and extracellular DAMPs and comprise, e.g., extracellular ATP and extracellular matrix fragments, respectively (reviewed in [31–33]). Naturally, given the broad spectrum of molecular patterns of both, invading microbes or endogenous stress, PRRs are numerous and can either be membrane-associated or cytoplasmic. Upon activation, PRRs induce anti-microbial and pro-inflammatory responses to eliminate or contain the (infectious) elicitors (Figure II).

Generally, PRRs are subdivided into five major families: the nucleotide-binding oligomerization domain (NOD)-like receptors (NLR), the C-type lectin receptors (CLR), the AIM2-like receptors (ALR), the toll-like receptors (TLR), and the retinoic acid-inducible gene-I (RIG-I)-like receptors (RLR) (reviewed in [34–36]). Since NLRs, CLRs, and ALRs are of minor relevance within this thesis, they are only briefly introduced, whereas TLRs and RLRs are described in separate sections.

NLRs are cytosolic receptors which are comprised of several C-terminal leucine-rich repeats (LRR) required for ligand binding, a central nucleotide binding domain (NBD, also NACHT) that facilitates oligomerization, and a variable N-terminal region. Depending on the N-terminal region, NLRs can be subdivided into two main groups: NLRs harboring an N-terminal caspase activation and recruitment domain (CARD) are classified as the NLR family CARD domain containing (NLRC) subfamily, whereas a pyrin domain in the N-terminal region characterizes the NLR family of proteins (NLRP) [37]. The most prominent members

[1] PAMPs are not exclusive to pathogens, but generally described for microbes, thus, the term MAMP may be more accurate. However, throughout this thesis, the conventional term PAMP is employed.

of the NLRC subfamily, NOD1 (NLRC1) and NOD2 (NLRC2), are crucial for detection of bacterial peptidoglycan (PGN) and, thus, essential for host defense against bacterial pathogens (reviewed in [38]). NLR pyrin domain-containing 3 (NLRP3) belongs to the NLRP subfamily and is part of the most-studied canonical inflammasome comprised of NLRP3, apoptosis-associated speck-like protein containing a CARD (ASC), and caspase-1. Interestingly, NLRP3 can be activated by a wide range of stimuli, including bacterial and fungal components or toxins [39–43], as well as pathogen-associated RNA [44–46]. However, a direct binding between NLRP3 and the biochemically dissimilar ligands could not be observed. Moreover, inflammasome activation upon PAMP or DAMP recognition leads to the processing and, thus, activation of pro-inflammatory cytokines, such as IL-1β and IL-18, ultimately resulting in inflammation and pyroptotic cell death (reviewed in [47, 48]).

Membrane-bound C-type lectin receptors (CLR) are mainly expressed on APCs and recognize carbohydrate structures present on the surface of distinct pathogens, e.g., β-glucans on fungal cell walls. Some CLRs, such as dendritic cell-associated C-type lectin (Dectin)-1 and Dectin-2, can induce signaling pathways that directly activate nuclear factor-κB (NF-κB), thus, mediating innate inflammatory responses (reviewed in [49, 50]).

Cytoplasmic proteins, such as cyclic GMP-AMP synthase (cGAS), absent in melanoma 2 (AIM2), and DNA-dependent activator of interferon-regulatory factors (DAI), sense cytoplasmic DNA which could be released upon damage to the nucleus or mitochondria and during bacterial or viral (e.g., herpes simplex virus-1, HSV-1) infections [51, 52]. Similarly to NLRP3, AIM2 induces inflammasome-dependent IL-1β maturation and pyroptosis [53–55]. In contrast, cGAS produces a cyclic dinucleotide second messenger (cGAMP) that activates stimulator of interferon genes (STING) upon DNA recognition and subsequently triggers an IFN-mediated defense response [56, 57].

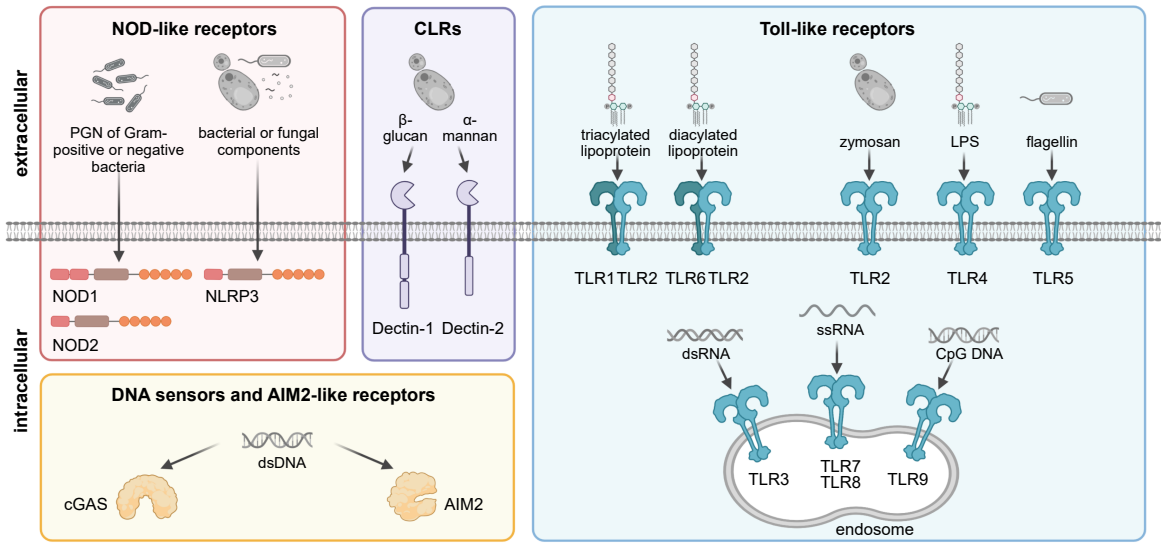

Figure II: Schematic depiction of PRR families and exemplary ligands.
NOD-like receptors (NLR), AIM2-like receptors (ALR), and the DNA sensor cGAS are cytosolic sensors of PAMPs and DAMPs, whereas C-type lectin receptors (CLR) and toll-like receptors (TLR) belong to the membrane-bound sensors. Most TLRs reside within the plasma membrane but TLR3, -7, -8, and -9 are located within the endosomal membrane, detecting foreign nucleic acids of different types. Figure is created with BioRender.com.

1.2.1 Toll-Like Receptors

Toll-like receptors (TLR) likely represent the most multifaceted class of PRRs. In humans, all of the ten functional TLRs are membrane-bound signal receptors, but are expressed in membranes of different subcellular structures, thus, able to detect distinct ligand types found in various microbes. For instance, homodimers or heterodimers of TLR1, -2, -4, -5, -6, and -10 are expressed on the cell surface of numerous immune and non-immune cells and specifically recognize a variety of PAMPs, including lipoproteins, LPS, and flagellin. Notably, distinct ligands are described for most TLRs but the specific ligand of TLR10 is still unknown. Furthermore, homodimers of TLR3, -7, -8, and -9 are expressed in endosomal membranes and recognize nucleic acids. Specifically, TLR3 senses double-stranded RNA (dsRNA), TLR7 and TLR8 both bind single-stranded RNA (ssRNA), and TLR9 recognizes DNA with non-methylated CpG.
Generally, TLRs elicit inflammatory responses upon pathogen recognition. However, TLR10 is the only TLR reported to exhibit anti-inflammatory properties (reviewed in [58]). TLRs are composed of a cytoplasmic toll/IL-1 receptor (TIR) domain, a transmembrane domain, and an extracellular domain harboring LRRs. The TIR domain mediates signal transduction by binding different adapter proteins and the extracellular domain is responsible for PAMP recognition. Upon PAMP detection, TLRs trigger intracellular signaling pathways resulting in the induction of pro-inflammatory cytokines, chemokines, and IFNs. Depending on the specific adapter proteins recruited to the cytoplasmic TIR domain upon ligand detection, TLR signaling can be divided into the myeloid differentiation primary response 88 (MyD88)-

dependent and/or TIR domain-containing adapter inducing IFN-β (TRIF)-dependent pathway. The association of all TLRs (except TLR3) with MyD88 in the MyD88-dependent pathway recruits members of the IL-1 receptor-associated kinase (IRAK) family, which in turn interact with TNF receptor-associated factor (TRAF) 6. This ultimately results in the activation of mitogen-activated protein kinases (MAPK) and NF-κB signaling. Within the TRIF-dependent pathway, TRIF is either directly recruited by TLR3 or indirectly recruited to TLR4 by the bridging adapter protein TRAM. Hence, TLR4 exemplifies the TRIF and MyD88-dependent pathway. Interestingly, in addition to activating NF-κB and MAPK signaling for the expression of inflammatory cytokines, TRIF is mediating the recruitment of the IKK-ε/TBK1 kinases leading to IRF3 phosphorylation and eventually the expression of IFN-β (reviewed in [59–61]).

1.2.2 RIG-I-Like Receptors

Retinoic acid-inducible gene I-like receptors (RLR) are cytosolic sensors specifically detecting viral RNAs upon infection and subsequently initiating antiviral defense responses. The RLR family encompasses the three members retinoic acid-inducible gene-I (RIG-I), melanoma differentiation antigen 5 (MDA5), and laboratory of genetics and physiology 2 (LGP2). RLRs are expressed in most tissues and cell types, share a number of structural similarities, and are comprised of up to three distinct domains (Figure III). Specifically, shared between all RLR family members are a C-terminal domain (CTD) and a central DExD/H box RNA helicase domain. The central helicase domain is described to hydrolyze ATP and bind RNA. It is subdivided into two tandem helicase domains, Hel-1 and Hel-2, an interspaced helicase insertion domain, Hel-2i, and a pincer domain (reviewed in [62–64]). Furthermore, a repressor domain (RD) within the CTD is a common feature of RIG-I and LGP2 and is described to be involved in the autoregulation of RIG-I [65]. RIG-I and MDA5 both additionally possess two N-terminal CARD domains, which mediate downstream signal transduction. Although LGP2 is still able to bind viral RNA, it lacks the N-terminal CARDs, rendering it unable to transduce signaling upon RNA detection [66]. Nonetheless, LGP2 is suggested to act as a regulator of RIG-I and MDA5 signaling. Whereas LGP2 inhibits RIG-I signaling by competitively binding the RIG-I agonist [67], it facilitates the binding of MDA5 to its ligand and, thus, enhances MDA5 signaling [68, 69].

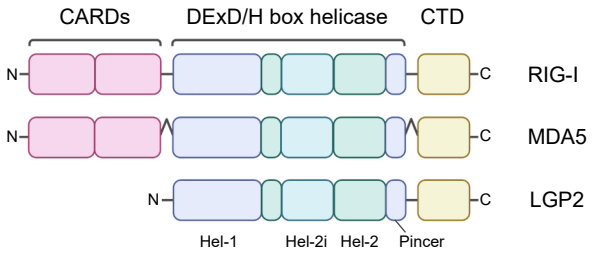

Figure III: Domain structure of RIG-I-like receptors.

All RLRs comprise a C-terminal domain (CTD) and a central DExD/H box RNA helicase domain. The latter is subdivided into two tandem helicase domains, Hel-1 and Hel-2, an interspaced helicase insertion domain, Hel-2i, and a pincer domain. Unlike RIG-I and MDA5, LGP2 does not possess the N-terminal caspase activation and recruitment domains (CARD). Figure is created with BioRender.com.

Although similarly organized, RIG-I and MDA5 seem to prefer distinct ligand properties. RIG-I is described to be involved in the recognition of sendai virus (SeV), respiratory syncytial virus (RSV), vesicular stomatitis virus (VSV), influenza A virus (IAV), and hepatitis C virus (HCV), whereas MDA5 rather recognizes encephalomyocarditis virus (EMCV) or coronaviruses. Interestingly, both RIG-I and MDA5 are involved in the detection of dengue virus (DENV), West Nile virus (WNV), and rotaviruses (reviewed in [70, 71]).

Intensive studies on the mechanisms of viral recognition by RIG-I and MDA5 specified the distinct characteristics of the respective ligands. In essence, RIG-I monitors the 5'-end of RNA molecules for distinct biochemical properties and specifically recognizes foreign structures. For instance, viral RNAs typically harbor diphosphate or triphosphate moieties at the 5'-end (5'-(p)pp). Host mRNAs, however, are capped at their 5'-ends and mature tRNAs as well as rRNAs usually only have a single phosphate or lack the phosphorylation completely and, thus, are not recognized by RIG-I [72, 73]. The double-stranded nature of viral RNAs, preferentially forming a blunt end [74,75], and an unmethylated 5'-terminal nucleotide at its 2'-O position [76] are additional RNA properties essential to induce RIG-I activation. These RNA characteristics substantially improve foreign RNA detection by RIG-I, however, recent studies demonstrated that at least 5'-phosphorylation becomes dispensable with increasing length of dsRNA [77,78]. Naturally, many viral RNAs match the required characteristics of RIG-I agonists. For instance, the genome of several negative-sense, single-stranded RNA viruses, such as IAV, contains partially self-complementary segments, which can form double-stranded RNA structures and, thus, be recognized by RIG-I upon viral infection [74, 79].

Specific ligand properties for MDA5 are much less understood. Whereas RIG-I depends on distinct RNA 5'-end properties and engages in terminal RNA binding, MDA5 senses longer dsRNAs with no end specificity, binds internally, and assembles into ATP-dependent, oligomeric filaments on the RNA [78, 80–82]. MDA5 was also shown to be crucial for the recognition of defective interfering particles (DIP), also known as defective interfering viruses, generated during, e.g., paramyxovirus replication [83]. DIPs have lost important functions required for proper viral replication and hence require the concurrent infection of a cell by a helper virus [84].

Crystal structure investigations of RLRs in ligand-free or ligand-bound conditions provided further insights into the mechanism of receptor activation. In the absence of any ligand, RIG-I remains in an inactive, auto-repressed conformation state mediated by the interaction of the two CARDs and the Hel-2i domain within the DExD/H box. Consequently, in this form the CARDs are sterically unable to interact with other binding partners, such as the mitochondrial antiviral-signaling protein (MAVS), and are, hence, unable to induce downstream defense responses. However, upon recognition of viral dsRNA, RIG-I undergoes conformational rearrangements. The CTD of RIG-I binds the 5'-ppp while the helicase domain wraps around the RNA in a C-clamp-like fashion, thereby triggering an RNA binding-dependent conformational change and exposing the sequestered CARDs for signaling. Subsequently, multiple RIG-I proteins cooperatively oligomerize along the dsRNA molecule [77] and the exposed CARDs are now accessible for homotypic binding with the CARD-containing adapter protein MAVS [85, 86]. Notably, RIG-I oligomers are stabilized by covalent lysine 63 (K63)-linked ubiquitination of the CTD and CARDs, whereas non-covalently bound K63-linked polyubiquitination has been shown to activate RIG-I [87, 88]. Although the distinct E3 ubiquitin ligases tripartite motif containing (TRIM) 25 and ring finger protein 135 (RNF135), also known as Riplet, have been proposed to be involved in RIG-I K63-polyubiquitination, recent studies demonstrated that only Riplet directly catalyzed RIG-I ubiquitination, whereas TRIM25 was dispensable for RIG-I-mediated antiviral immune responses [89–92].
Despite structural similarities, MDA5 recognizes its ligand in a different manner than RIG-I. In contrast to RIG-I, the CARDs of MDA5 are not sequestered in the absence of a ligand, thus, MDA5 remains in a more open and flexible conformation [80]. Upon ligand detection, the helicase domain of MDA5 wraps around dsRNA molecules and the CTD interacts with the Hel-1 domain, forming a closed ring around the dsRNA [82]. Similar to RIG-I, MDA5 assembles in oligomeric filaments along the dsRNA, enabling the interaction of MDA5 CARDs with the CARD of MAVS [82, 93]. Furthermore, the E3 ubiquitin ligase TRIM65 catalyzes a K63-linked ubiquitination of MDA5, thus enhancing MDA5 activation and oligomerization on the dsRNA molecule [94].

1.3 RLR Signaling

Upon ligand binding, CARD exposure of RIG-I and MDA5 enables oligomerization on the RNA molecule and the subsequent interaction with other (regulatory) proteins, such as the adapter protein MAVS. MAVS is comprised of a C-terminal transmembrane domain and an N-terminal CARD domain involved in the interaction with CARDs of RIG-I and MDA5. MAVS predominantly localizes to the outer mitochondrial membrane but was additionally identified in mitochondria-associated membranes of the ER (MAM) and peroxisomal membranes [95–99]. However, a recent study demonstrated that the subcellular localization of MAVS had no effect on the activation of antiviral responses in hepatocytes [95]. Interaction of RIG-I and MDA5 with MAVS results in the initiation of MAVS aggregation on MAVS-associated

membranes, forming highly ordered helical structures, which serve as a signaling platform for the recruitment of additional interaction partners [97,100–103]. Interestingly, the formation of these prion-like aggregates of MAVS upon viral infection is further promoted by the E3 ubiquitin ligase TRIM31, which interacts with MAVS and catalyzes the K63-linked polyubiquitination of distinct lysine residues on MAVS [104].

Antiviral responses upon RLR and MAVS activation commence two distinct signaling pathways (Figure V, left panel). First, activated MAVS recruits TRAF proteins, in particular, TRAF2, -3, and -6, the TNF receptor 1-associated protein (TRADD), and other regulatory proteins to the MAVS signalosome. K63-linked autoubiquitination of the E3 ubiquitin ligase TRAF3 subsequently recruits and activates the TANK-binding kinase 1 (TBK1) and IKK-ε, which in turn phosphorylate and, thus, activate the transcription factors interferon regulatory factor (IRF) 3 and/or IRF7 [105–109]. IRF3 is basally expressed in most human cells, whereas basal expression of IRF7 is restricted to distinct immune cells, predominantly pDCs, and is otherwise induced upon IFN stimulation (reviewed in [110]). Intriguingly, the presence of both IRF3 and IRF7 was described to be crucial for IFN-α expression upon viral infections [111]. Phosphorylated IRF3 and IRF7 homo or heterodimerize, translocate to the nucleus, and induce the expression of IFNs, pro-inflammatory cytokines, and some interferon-stimulated genes (ISG) [105–109]. Second, recruitment of TRAF6 to the MAVS signalosome induces its autoubiquitination to further recruit transforming growth factor-activated kinase 1 (TAK1) and the canonical IKKs (IKK-α, IKK-β, IKK-γ/NEMO) [112–115]. Notably, activation of TAK1 not only activates canonical NF-κB signaling but induces the MAPK pathway [116, 117]. Upon subsequent phosphorylation of the inhibitor of NF-κB (IκBα) by the IKK complex, NF-κB translocates to the nucleus and culminates in the expression of a large array of genes, predominantly encoding pro-inflammatory cytokines [112, 118]. These NF-κB-mediated responses are characterized by the expression of NF-κB target genes, such as the TNF-α-induced protein 3 (TNFAIP3) and the C-C motif chemokine ligand 5 (CCL5) [119–121].

1.4 Regulation of RLR Signaling

Precise ligand recognition and signal transduction are crucial for accurate innate immune responses and cellular homeostasis upon RLR activation. In fact, dysregulation of the RLR pathway has been described to facilitate immune disorders. For instance, gain-of-function mutations in the RLRs result in constitutive activation of the antiviral signaling response and are known as the Singleton-Merten syndrome (SMS) [122]. Consequently, RLR signaling is regulated by distinct mechanisms, including post-translational modifications (PTM) by regulatory proteins, such as phosphorylation or ubiquitination, and general regulation by interacting proteins. These mechanisms enable both positive and negative regulation of RLR signaling (Figure IV, reviewed in [62–64]).

1.4.1 RLR Regulation by Post-Translational Modifications

Protein ubiquitination is among the most extensively studied PTMs, and, as briefly mentioned in Section 1.3, ubiquitination of the RLRs is essential for signal induction upon dsRNA recognition. In general, ubiquitination refers to the covalent attachment of one (monoubiquitination) or more (polyubiquitination) ubiquitin molecules to the ε-amino group of a lysine residue. Based on numerous studies, each type of polyubiquitination seems to have the ability to act as a distinct intracellular signal, facilitating diverse outcomes of ubiquitination, e.g., changing the stability, localization, or activity of a target protein. Specifically, whereas K48-polyubiquitination regulates protein stability and marks proteins for degradation, monoubiquitination is rather involved in the regulation of signal transduction and, in the case of histone ubiquitination, transcriptional regulation [123]. Ubiquitination of target proteins comprises a three-step process: ATP-dependent activation of ubiquitin by a ubiquitin-activating enzyme (E1) enables its transfer to a ubiquitin-conjugating enzyme (E2) resulting in the ubiquitin attachment to a target protein mediated by a ubiquitin-ligating enzyme (E3). Strikingly, more than 600 distinct E3 ubiquitin ligases have been identified in humans, emphasizing the importance of ubiquitination in the regulation of cellular homeostasis (reviewed in [124–126]).

Commonly, K63-linked and K48-linked polyubiquitination comprise the canonical protein ubiquitination and are both essential in the regulation of RLR-mediated innate immunity. In contrast to K48-linked ubiquitination, mostly targeting proteins for degradation [127, 128], K63-linked ubiquitination results in protein activation [104, 129]. For instance, K63-linked ubiquitination of the RIG-I CARDs by the E3 ubiquitin ligases TRIM25 and, more importantly, Riplet, are crucial for oligomerization, MAVS interaction, and hence signal transduction [87–91]. Further, USP4 proteolytically cleaves K48-linked ubiquitination from RIG-I and thereby enhances RIG-I stability [130]. In contrast, RNF125-mediated K48-linked ubiquitination targets RIG-I for proteasomal degradation [131], removal of K63-linked polyubiquitin by ubiquitin-specific peptidase (USP)-21 inhibits RIG-I [132], and linear ubiquitin chain assembly complex (LUBAC) negatively affects TRIM25 stability and, thus, its interaction with RIG-I [133]. Similarly, RNF125-mediated ubiquitination targets MDA5 for degradation [131] and USP3-mediated deubiquitination additionally inhibits MDA5 [134]. Recently, the E3 ubiquitin ligase TRIM65 was described to promote K63-linked ubiquitination of MDA5, which is required for MDA5 activation and oligomerization [94].

Naturally, the adapter protein MAVS as well as downstream signaling components are also highly regulated by ubiquitination. For instance, whereas TRIM31-mediated K63-linked polyubiquitination of MAVS promotes its activation and oligomerization [104], K48-linked ubiquitination by TRIM25 was reported to target MAVS for proteasomal degradation [135]. TRAF3 and TRAF6 are involved in the activation of TBK1 and IKKs through K63-linked ubiquitination and are also regulated themselves [112]. Specifically, cellular inhibitor of apoptosis protein (cIAP)-1, cIAP2, and RNF166 mediate K63-linked ubiquitination and, thus, positive regulation of TRAF3 and TRAF6. OTUB1 and OTUB2, however, deubiquitinate both

TRAFs resulting in the inhibition of antiviral responses [136–139]. Lastly, IRF3 is targeted for proteasomal degradation by TRIM26-mediated K48-linked polyubiquitination [140]. Upon nuclear translocation, IRF3 binds to peptidyl-prolyl cis/trans isomerase NIMA-interacting 1 (Pin1), which promotes its degradation through polyubiquitination [141]. Intriguingly, the E3 ubiquitin ligase TRIM21 exerts contrary regulatory mechanisms. In addition to negatively regulating the stability of IRF3 by mediating polyubiquitination and proteasomal degradation, TRIM21 further sustains IRF3 activation by interfering with the Pin1-IRF3 interaction, thus preventing IRF3 ubiquitination and proteasomal degradation [142, 143].

In addition to ubiquitination, protein phosphorylation is a common PTM, regulating protein activation and signal transduction. In essence, phosphorylation is the ATP-dependent transfer of a phosphoryl (PO_3) group to target proteins by kinases. Although phosphorylation can occur on multiple amino acid residues, the most common phosphorylation sites are on serine, threonine, and tyrosine residues. In contrast, phosphatases remove phosphate groups from target proteins and are, thus, the counterpart to kinases. Both phosphorylation and dephosphorylation are crucial for proper RLR-mediated antiviral signaling. For instance, whereas phosphorylation of the CARDs keeps RIG-I in an inactive state, dephosphorylation of both RIG-I and MDA5 is required for their activation and further signal transduction. Previous studies established that the conventional protein kinase C-α (PKC-α) and PKC-β are responsible for the phosphorylation of RIG-I at distinct sites [144]. However, upon ligand detection, the CARDs of RIG-I and MDA5 are dephosphorylated by the phosphatases PP1α and PP1γ, resulting in their activation [145]. In addition to CARD (de)phosphorylation, the CTDs of both RIG-I and MDA5 were demonstrated to be phosphorylated by the casein kinase II (CK2) and RIO kinase 3 (RIOK3), respectively [146, 147]. Remarkably, upon viral infection RIG-I activity is additionally inhibited in a negative feedback loop through phosphorylation by the death-associated protein kinase 1 (DAPK1) [148].

Although TBK1 and IKK-ε are kinases themselves, both are activated by auto and transphosphorylation at serine (S) 172. In fact, a recent study suggested the involvement of other kinases since inhibition of TBK1 and IKK-ε still resulted in S172 phosphorylation upon distinct stimulation approaches [149–151]. Conversely, S172 dephosphorylation by the protein phosphatase 1B (PPM1B) negatively regulated TBK1 activation, resulting in decreased antiviral signaling upon viral infection [152]. Likely the most extensively studied phosphorylation event within the RLR signaling pathway comprises TBK1/IKK-ε-mediated IRF3 phosphorylation. In homeostatic conditions, IRF3 shuttles between the nucleus and the cytoplasm, but nuclear export and thus cytoplasmic localization of IRF3 is dominant [153]. Upon RLR pathway activation, cytosolic IRF3 is phosphorylated at distinct residues within its C-terminal region, resulting in nuclear translocation and the subsequent association with the transcriptional coactivators CREB-binding protein (CBP) and E1A binding protein p300 (p300) [153–155]. This association remains stable until the protein phosphatase 2A (PP2A) and its adapter protein receptor for activated C kinase 1 (RACK1) mediate IRF3 dephosphorylation, and thus, relocalization to the cytoplasm [156]. Recently, protein SUMOylation, i.e., the covalent attachment or detachment of small ubiquitin-like modifier (SUMO) proteins,

has emerged as crucial regulatory mechanism of RIG-I and MDA5 activity. For instance, TRIM38-mediated CARD and CTD SUMOylation prevents K48-linked polyubiquitin-induced degradation of RIG-I and MDA5 in uninfected cells. However, at late phases of viral infections, RIG-I and MDA5 are deSUMOylated by sentrin/SUMO-specific protease 2 (SENP2), which thus results in their proteasomal degradation [157]. Lastly, the attachment or removal of an acetyl functional group mediated by (de)acetylases is able to modulate RLR signal transduction. Acetylation of RIG-I within the CTD impairs its capability to bind viral RNA and hence prevents RIG-I activation and oligomerization. Correspondingly, histone deacetylase (HDAC) 6-mediated deacetylation of RIG-I reverses the impairment of RIG-I in RNA binding [158, 159]. Notably, whereas the regulatory mechanisms of PTMs on RIG-I and MDA5 have been characterized extensively, PTMs regulating LGP2 are yet to be identified.

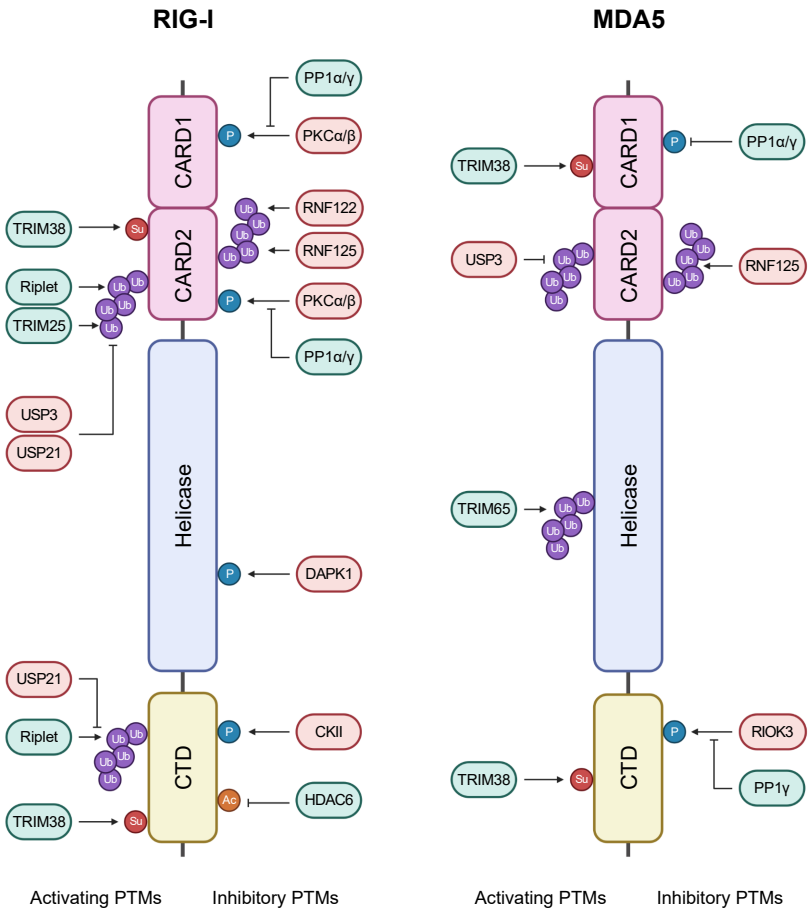

Figure IV: Major post-translational modifications of RIG-I and MDA5.

RIG-I and MDA5 both comprise distinct post-translational modifications (PTM) regulating their activity and signal transduction. Major PTMs include polyubiquitination (Ub), specifically K63 and K48-linked ubiquitination, phosphorylation (P), SUMOylation (Su), and acetylation (Ac). PTMs can either have activating or inhibiting regulatory functions, indicated on the left or right site, respectively. Proteins which ultimately lead to RLR activation are shown in green, proteins leading to RLR inhibition are illustrated in red. Figure is adapted from [64] and created with BioRender.com.

1.4.2 RLR Regulation by Interacting Proteins

Apart from the regulatory mechanisms by PTMs, RLR activity is also modulated by numerous host or even pathogen-derived proteins (Section 1.7). A remarkable example of host-derived proteins regulating RLR signaling is the third RLR, LGP2. As described in Section 1.2.2, LGP2 is able to bind viral RNA but lacks the CARD domains required for MAVS interaction and activation. Nevertheless, positive and negative regulation of the RLR signaling pathway through multiple mechanisms are described for LGP2. For instance, LGP2 recognizes RIG-I ligands in a competitive manner, thus diminishing RIG-I-induced antiviral signaling [67, 160]. In contrast, LGP2 facilitates RNA recognition by MDA5, MDA5-RNA binding, and MDA5 oligomerization, ultimately enhancing MDA5-mediated antiviral signaling [69, 160–162]. However, how the contradictory roles of LGP2 in RLR signaling are concisely regulated remains to be investigated.
A crucial feature of RLR signaling is the discrimination of self and non-self, which is ensured through distinct mechanisms. For instance, adenosine deaminases acting on RNA (ADAR) 1 catalyzes the conversion of adenosine (A) to inosine (I) in dsRNA molecules, which was recently reported to be a key process for marking dsRNA as self. This RNA-editing process by ADAR1 thus limits cytosolic RNA sensing by RIG-I and MDA5, further preventing adverse innate immune activation which could ultimately lead to immune-mediated diseases [163–166]. Another dsRNA-binding protein reported to be involved in modulating RLR signaling is the protein activator of the interferon-induced protein kinase (PACT). Besides interacting with the CTD of RIG-I in order to stimulate its ATPase activity [167,168], PACT was recently shown to promote MDA5 activity by facilitating its oligomerization [169]. Furthermore, numerous other DExD/H-box helicases have been implicated in regulating RLR signaling. For instance, DEAH-box helicase 15 (DHX15) acts as a co-receptor of RIG-I, facilitating ATP hydrolysis and binding of viral RNA [170], whereas DExD/H-box helicase 60 (DDX60) promotes RIG-I-dependent signaling as well as IFN and ISG induction [171–173]. The zinc finger CCHC domain-containing protein 3 (ZCCHC3), another protein acting as co-receptor of RIG-I and MDA5, was reported to modulate RLR signaling. Besides binding to RLR-activating RNAs with its C-terminal zinc finger domain, ZCCHC3 also interacts with the helicase and CTD domain of both RIG-I and MDA5, ultimately enhancing RNA binding by the RLRs [174]. Interestingly, a recent study identified a novel mechanism of interplay between the NLR and RLR pathways. Here, upon virus infection or 5'ppp-dsRNA stimulation, NLRP12 diminished RIG-I-mediated antiviral signaling responses, supposedly by interacting with TRIM25, and thus hindering its ability to ubiquitinate and activate RIG-I. Additionally, NLRP12 destabilized RIG-I by enhancing RNF125-mediated K48-linked ubiquitination [175]. Lastly, 14-3-3ε, a member of the 14-3-3 protein family, forms a complex with RIG-I and TRIM25, thereby stabilizing their interaction and facilitating their association with MAVS [176]. Likewise, 14-3-3η was reported to mediate the relocalization of MDA5 to mitochondrial-associated membranes, thus enhancing MDA5-dependent antiviral signaling [177].

1.5 The Interferon System

Viral infections induce intricate multi-layered immune responses in the host, ultimately preventing viral spread and clearing the infection. An essential component of innate defense responses are secreted cytokines, in particular IFNs. IFNs, termed after their ability to interfere with viral replication, function as signaling molecules and enable cell-to-cell communication crucial for many biological processes, specifically immune and inflammatory responses (reviewed in [178–180]). Based on the respective receptor complex, IFNs are subdivided into three classes: type I, type II, and type III IFNs.

1.5.1 Type I Interferons

Commonly, viral infections and recognition of dsRNA by PRRs result in the production of type I IFNs. Type I IFNs comprise the largest IFN family, encoding 13 partially homologous IFN-α subtypes, a single IFN-β, and several less-characterized IFNs (IFN-ε, IFN-τ, IFN-κ, IFN-ω, IFN-δ, and IFN-ζ). The best-studied and most broadly expressed type I IFNs are IFN-α and IFN-β, which induce potent antiviral signaling responses in both virus-infected and uninfected cells. Previous studies identified at least four positive regulatory domains (PRD) in the promoter of the IFN-β gene, whereas promoters of IFN-α genes contain similar PRD-like elements (PRD-LE) [181, 182]. Interestingly, PRD I and III within the IFN-β promoter are activated by members of the IRF family, whereas PRD II and IV are activated by NF-κB and the heterodimer AP-1, respectively. Besides IRF3 and IRF7, other members of the IRF family, specifically IRF1 and IRF5, have also been implicated in binding PRDs in type I IFN promoter regions [183–189].

Expressed and secreted type I IFNs are detected by a heterodimeric receptor complex comprised of the interferon α and β receptor subunit (IFNAR) 1 and IFNAR2, which are both ubiquitously expressed on cell surfaces. Intriguingly, although all type I IFNs are able to bind the IFNAR receptor complex, differential responses mediated by distinct type I IFNs have been described. This was mainly attributed to protein turnover rates, complex stability, and distinct ligand affinities towards the receptor subunits, which ultimately determines extent and dynamics of signaling complex formation (reviewed in [190, 191]). For instance, previous studies demonstrated a higher binding affinity of IFN-β to the IFNAR receptors as compared to the remaining type I IFNs [192–194]. The interaction of type I IFNs with the heterodimeric IFNAR receptor elicits an intracellular signaling cascade encompassing members of the janus protein kinase (JAK) family, specifically JAK1 and the non-receptor tyrosine-protein kinase 2 (TYK2), which are associated with the cytoplasmic domains of IFNAR2 and IFNAR1, respectively. First, JAK1 and TYK2 phosphorylate cytoplasmic residues of the IFNAR receptors, thereby recruiting signal transducer and activator of transcription (STAT) 1 and STAT2. Notably, besides canonical STAT1-STAT2 heterodimerization, type I IFN-mediated signaling also induces STAT1 homodimers, which are commonly associated with type II IFN-mediated signaling [195]. Subsequently, the kinases phosphorylate both

STAT1 and STAT2, which heterodimerize and then associate with IRF9, forming the trimeric IFN-stimulated gene factor 3 (ISGF3) complex [196]. Lastly, the ISGF3 complex translocates to the nucleus, binds to IFN-stimulated response elements (ISRE) within gene promoter regions [197], and induces the expression of a large number of ISGs. ISGs exert a variety of biological functions (Section 1.6), e.g., impacting viral replication and amplifying RLR and IFN signaling, to ultimately establish an antiviral state (Figure V, reviewed in [198–203]).

1.5.2 Type II Interferons

The only type II IFN, IFN-γ, is very distinctive from other IFNs. Although IFN-γ is predominantly produced in specialized immune cells, such as activated T and NK cells, it can stimulate many different cell types if the IFN-γ receptor (IFNGR) complex is expressed on their cell surface [204]. The heterodimeric IFNGR complex is composed of the IFNGR1 and IFNGR2 subunits. Ligand detection by the IFNGR1 subunit results in receptor complex formation, induction of JAK2 autophosphorylation and activation, and subsequently transphosphorylation of JAK1 by activated JAK2 [205–207]. Activated JAK1 then phosphorylates IFNGR1, recruiting STAT1 to the complex and further enabling STAT1 activation through phosphorylation [208, 209]. Phosphorylated STAT1 forms a homodimer, also known as IFN-γ activated factor (GAF), translocates to the nucleus, and binds IFN-γ activation site (GAS) elements within the promoter regions of, e.g., ISGs (Figure V, [210, 211]). Strikingly, IFNGR phosphorylation was reported to emerge within one minute of IFN-γ treatment [207, 212].
IFN-γ signaling is able to induce the expression of some ISGs, which contribute to a direct antiviral defense. However, the establishment of an antiviral state is still mainly attributed to type I and III IFN signaling [213, 214]. Instead, IFN-γ was reported to rather promote antiviral immunity through regulatory effects on innate immunity and to further link innate and adaptive immune responses. For instance, IFN-γ initializes the release of ROS by, e.g., macrophages, through the upregulation of required cellular components [215–217], promotes macrophage polarization, and subsequently primes these cells to produce proinflammatory cytokines [218, 219]. Lastly, IFN-γ affects and enhances the antigen presentation process on APCs which ultimately increases stimulation of the adaptive antiviral response [220, 221] (reviewed in [222]).

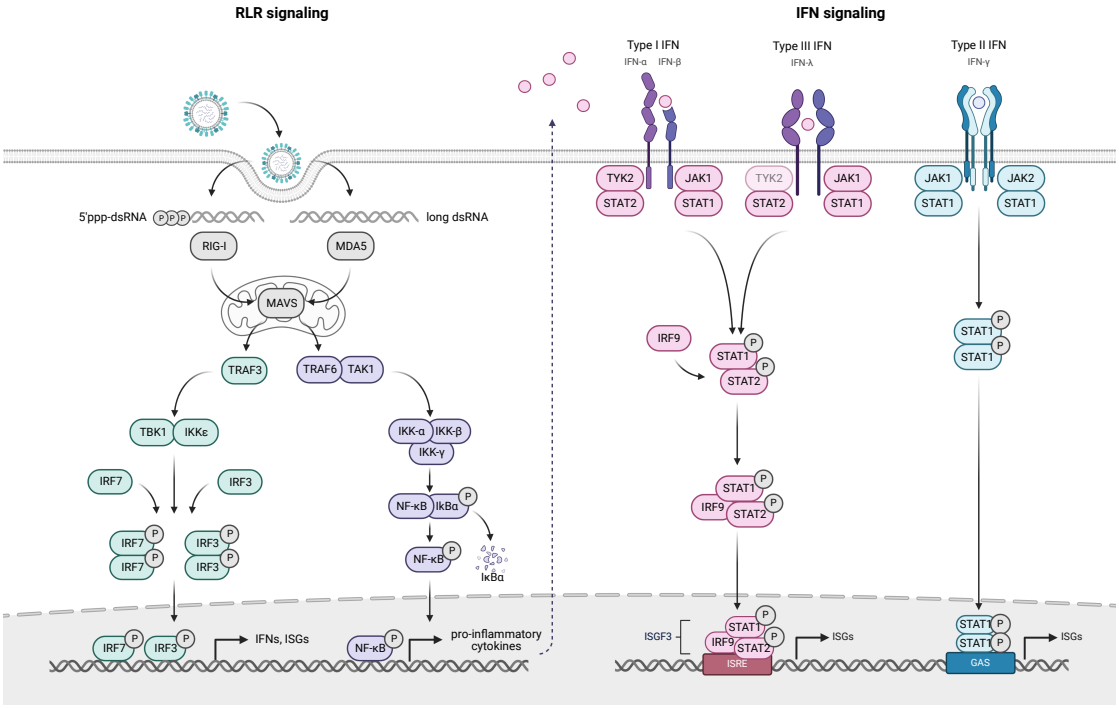

Figure V: Schematic illustration of the RLR and IFN signaling pathway.
The cytosolic RLRs RIG-I and MDA5 are activated by immunostimulatory RNAs, for instance, viral RNAs. Upon ligand binding, both undergo conformational changes, exposing and oligomerizing their CARDs, which enables homotypic CARD-CARD interactions with MAVS. MAVS predominantly localizes to the outer mitochondrial membrane and upon activation and oligomerization, triggers signal transduction via two distinct signaling pathways. First, activation of the kinases TBK1 and IKK-ε results in the phosphorylation and nuclear translocation of IRF3 and/or IRF7. Second, IKK-α/IKK-β/IKK-γ complex-induced degradation of the NF-κB inhibitor, IκBα, enables NF-κB to translocate to the nucleus. Consequently, the translocated transcription factors induce the expression of IFNs, pro-inflammatory cytokines, and some ISGs. Secreted IFNs further act in an autocrine and paracrine manner and induce IFN signaling via their cognate IFN receptors. Type I and III IFN signaling results in the formation of the ISGF3 complex, comprised of STAT1, STAT2, and IRF9, binding to ISRE elements within the genome. Type II IFN signaling leads to STAT1 homodimerization, which, upon translocation into the nucleus, binds GAS elements within the genome. Both ISGF3 and STAT1 homodimer binding induces the expression of a large variety of ISGs, ultimately establishing the antiviral state of the cell. Figure is created with BioRender.com.

1.5.3 Type III Interferons

Type I and III IFNs exhibit similar functions and were originally considered to be redundant. However, type III IFNs differ structurally and were hence designated a new class of IFNs. Four distinct type III IFNs, specifically IFN-λ1 (IL-29), IFN-λ2 (IL-28A), and IFN-λ3 (IL-28B), as well as the most recently detected IFN-λ4 were identified so far [223–225]. Interestingly, although all type III IFNs share a high degree of sequence homology, different receptor binding affinities were reported. Specifically, IFN-λ1 exhibited the highest binding affinity to IFNLR1, whereas IFN-λ3 had the lowest [226]. The function of IFN-λ1, IFN-λ2, and IFN-λ3 in antiviral defense responses has been characterized extensively and is broadly accepted. However, the precise function of IFN-λ4 remains disputed. Although exogenously produced IFN-λ4 showed antiviral activity, it is still debated whether cells can produce IFN-λ4 themselves [227–229] (reviewed in [230]).

Type III IFNs are produced and secreted by most cell types but the required receptor complex is only expressed on the surface of some cells, resulting in cell type-specific responses [231–233]. Type III IFNs bind to a heterodimeric receptor complex composed of the type III IFN receptor (IFNLR1), also known as IL28R1, and the interleukin 10 receptor 2 (IL10R2). Interestingly, the latter is not only used by type III IFNs but shared with other IL-10 family members [223, 225]. The IL10R2 receptor is ubiquitously expressed in almost all cell types, whereas IFNLR1 represents the limiting factor in type III IFN signaling. IFNLR1 is expressed on cell surfaces of epithelial cells, e.g., lung, intestine, and liver cells [231–233], as well as some immune cells, e.g., DCs, NK cells, and neutrophils [234–237]. Although type I and III IFNs employ distinct receptor complexes, they both signal through the JAK/STAT pathway, utilizing the ISGF3 complex to ultimately induce the expression of ISGs [238, 239]. Nevertheless, kinetic differences in gene expression upon type I and III IFN stimulation were described recently [240, 241]. For instance, IFN-λ stimulation resulted in a long-lasting ISG induction, whereas IFN-α stimulation led to early-peaking gene expression, which quickly declined again due to negative feedback regulation [242, 243]. Importantly, the delayed IFN-λ-induced expression of ISGs was not a consequence of lower receptor levels, since overexpressing IFNLR1 did not lead to a faster ISG induction, indicating that type I and III IFNs possess unique mechanisms to regulate downstream signaling cascades [241]. In fact, a recent study demonstrated that although JAK1 is critical for the activation of both type I and III IFNs, TYK2 seems to be dispensable for the latter [244, 245]. In humans several mutations within the TYK2 locus have been identified, however, their susceptibility to viral infections was unimpaired. This further emphasizes a TYK2-independent type III IFN signaling which might ultimately serve as a first line barrier to control viral infections [246, 247]. Still, how signaling downstream of the type III IFN receptor culminates in further differences between type I and III IFNs remains to be investigated.

1.5.4 Regulation of Interferon Signaling

Dysregulation of both the RLR and IFN pathway have been linked to autoinflammatory diseases, which in the case of IFN are termed interferonopathies. Generally, they are characterized by a constant overproduction of IFNs, either by constitutive upregulation of activating processes or constraints in negative regulatory systems (reviewed in [248, 249]). Classic examples of diseases with enhanced type I interferon signaling include the Aicardi–Goutières syndrome (AGS) and systemic lupus erythematosus (SLE) [250, 251]. Thus, tight regulation mechanisms of this pathway are crucial for cellular homeostasis.

As demonstrated previously for RLR signaling, PTMs such as phosphorylation, ubiquitination, and acetylation are crucial for IFN-mediated positive and negative regulation of innate immune responses. Activating phosphorylation events of JAK1, TYK2, STAT1, and STAT2 are commonly known to be induced by type I IFN signaling. Notably, STAT1 was reported to be additionally phosphorylated on a distinct serine residue through the MAPK pathway [252]. Consistently, negative regulation through dephosphorylation is mediated

by distinct phosphatases, for instance members of the suppressor of cytokine signaling (SOCS) and protein tyrosine phosphatases (PTP) families. SOCS1 is able to bind IFNAR1 and to diminish the kinase activity of JAKs by directly binding them, thus abrogating STAT1 phosphorylation [253]. Similarly, the SH2 domain containing phosphatase (SHP1) and SHP2 of the PTP family specifically dephosphorylate JAK1 and STAT1, respectively [254–256].
Regulation through ubiquitination-mediated protein degradation was reported for various IFN pathway components. For example, the ubiquitin ligase Skp1-Cullin1-HOS-Roc1 (SCF^{HOS}) induces the ubiquitination and degradation of the IFNAR1 receptor [257]. The STAT interacting LIM protein (SLIM) interacts with both STAT1 and STAT4 to catalyze their ubiquitin-mediated degradation, thus negatively regulating STAT signaling upon IFN stimulation [258]. Furthermore, the SMAD specific E3 ubiquitin protein ligase 1 (Smurf1) targets STAT1 for K48-linked polyubiquitination and, hence, proteasomal degradation upon IFN-γ signaling [259]. In contrast to this, deubiquitinating enzymes enhance IFN-mediated antiviral activity. For instance, the deubiquitinase USP2a sustains IFN signaling by associating with activated STAT1, thereby blocking its K48-linked ubiquitination and degradation [260]. Upon IFN-γ stimulation, K63-linked polyubiquitination of STAT1 is mediated by the natural killer lytic-associated molecule (NKLAM), promoting STAT1 phosphorylation and thus positively regulating its transcriptional activity [261]. Further, the conjugation of SUMO moieties on STAT1 by the protein inhibitors of activated STAT 1 (PIAS1) negatively regulates STAT1-mediated transcription and thus diminishes IFN signaling and ISG expression [262].
Although lysine acetylation is predominantly known as modification of histones, serving as a marker associated with transcriptional activation, acetylated non-histone proteins were also identified. Upon type I IFN stimulation, dimerized IFNAR receptors recruit the cytoplasmic histone acetyltransferase (HAT) CBP, which in turn acetylates IFNAR2 [263]. Likewise, CBP catalyzes the IFN-mediated acetylation of STAT2 and IRF9 which is crucial for IRF9 or STAT1 binding, respectively, and is consequently essential for the formation of the ISGF3 complex [263]. Remarkably, STAT1 is regulated by a dynamic phosphorylation and acetylation-dependent cross-regulation: a CBP/HAT complex catalyzes STAT1 acetylation, which recruits a phosphatase resulting in STAT1 dephosphorylation and hence inactivation. In turn, HDAC3 deacetylases STAT1 upon IFN stimulation, thus promoting STAT1 phosphorylation and signal transduction [264].
Recently, the PTM termed ISGylation gained importance in the regulation of IFN signaling. The IFN-induced protein ISG15 represents the first identified ubiquitin-like protein, containing two ubiquitin-like domains [265]. Similar to ubiquitination, ISG15 can be covalently attached to target proteins in a three-step process resulting in their ISGylation [266]. ISGylation is performed by the three E1-E3 proteins ubiquitin-like modifier-activating enzyme 7 (UbE1L, E1), ubiquitin carrier protein L6 (UBCH8, E2), and HECT domain and RCC1-like domain-containing protein 5 (HERC5, E3). However, only one ISG15 deconjugating protein, the ubiquitin-specific peptidase 18 (USP18), was implicated in this process [267–272]. Components of the IFN-mediated antiviral signaling are engaged in both, ISGylation and deconjugation of ISG15. For instance, JAK1 and STAT1 are heavily ISGylated in

USP18 knockout cells, resulting in sustained phosphorylation and thus DNA association of STAT1 [273, 274]. Consequently, USP18 knockout mice were reported to be resistant to viral infections [275], whereas the lack of UbE1L resulted in an increased susceptibility to influenza B virus infection [276].

1.6 Interferon-Stimulated Genes

Viral infections trigger distinct signaling cascades, leading to the production and secretion of IFNs, which ultimately induce the expression of a wide array of interferon-stimulated genes (ISG). ISG-encoded proteins collectively establish an antiviral state of a cell and promote distinct processes, including direct antiviral defenses, antiproliferative effects, and the stimulation of adaptive immune responses. Counterintuitively, many ISGs are also direct targets of primary RLR signaling, thus can even be induced in the absence of IFN signaling and are sometimes referred to as virus-stimulated genes (VSG). In fact, several studies demonstrated an IRF3 or NF-κB-mediated induction of VSG expression during the early phase of infection [106, 277] (reviewed in [278–280]). Whereas most ISGs are strictly expressed upon IFN stimulation, some are basally expressed in addition to being IFN-inducible [281]. For instance, basal expression of the PRRs RIG-I and MDA5 is crucial for viral sensing and the activation of IRFs. However, IFN-induced expression of both additionally primes cells for further pathogen detection in a positive feedback manner [160, 173, 282–284]. Notably, some members of the IRF family, in particular IRF1, IRF7, and IRF9, are IFN-inducible and thus considered ISGs, whereas IRF3 expression seems to be IFN-independent [173, 185, 285–288]. Another remarkable ISG example is interferon-induced protein with tetratricopeptide repeats (IFIT) 1, whose expression is induced by both, primary RLR and IFN-mediated signaling [106].

Since ISGs are usually induced as part of a broad cooperating transcriptional program, identifying specific effects of individual ISGs can be challenging. However, recent studies determined distinct molecular mechanisms behind the antiviral properties of some classical ISGs, mediating antiviral effects through, e.g., blocking of viral entry, viral RNA degradation, or inhibition of viral translation and replication (Figure VI). For instance, although it was known for a while that interferon-induced transmembrane protein (IFITM) 3 inhibits viral entry, only recently studies determined the mechanism by which IFITM3 blocks membrane fusion of viruses entering cells through an endocytic route [289–291]. According to Spence *et al.*, IFITM proteins reside in endocytic vesicles which fuse with invading viruses and thus facilitate trafficking of virus-containing vesicles to lysosomes [292]. The MX dynamin-like GTPase (MX) 1 targets another post-entry process and specifically blocks trafficking of the viral machinery through the nuclear pore complex. Additionally, early gene expression of some single-stranded RNA viruses, such as IAV, can be inhibited by MX1 [293–296] (reviewed in [297, 298]).

A critical step in the viral replication cycle targeted by many ISGs is translation. The protein kinase R (PKR), another classical ISG, is a dsRNA-dependent kinase which phosphorylates the eukaryotic translation initiation factor 2 α (eIF2α) to modulate multiple cellular processes including (viral) translation (reviewed in [299–301]). In contrast, members of the IFIT family target viral protein synthesis and replication via distinct mechanisms. For instance, IFIT1 acts on a wide range of viruses by recognizing viral RNA molecules, either harboring 5'ppp moieties or lacking a 5'-O-methylation at their cap structure [302]. Binding of IFIT1 to 5'ppp-RNAs sequesters viral RNAs out of replication complexes and thus limits viral replication, whereas binding of RNAs with non-methylated caps impedes viral protein translation through the competition with the translation initiation factors eIF4E and eIF4F [303–307].

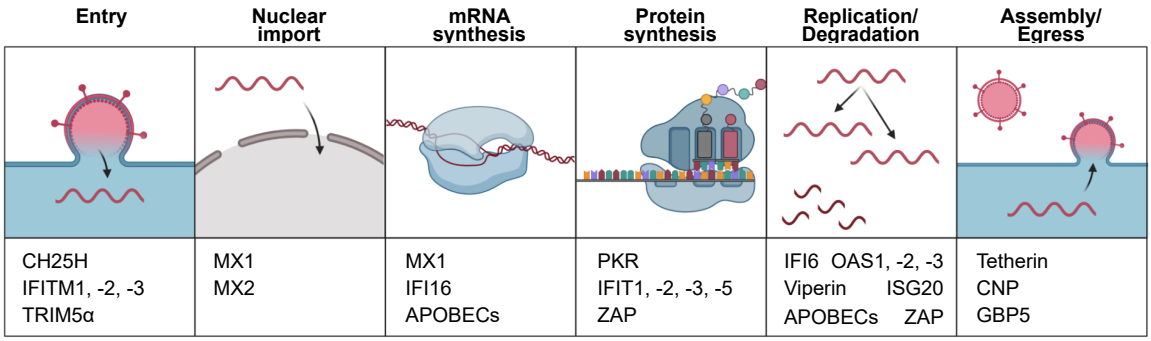

Figure VI: Different ISGs targeting distinct steps in the viral replication cycle.
The viral replication cycle can be subdivided into six major steps: (1) viral entry, (2) viral genome nuclear import, (3) mRNA synthesis, (4) viral protein synthesis, (5) viral genome replication and degradation of viral RNAs, and (6) virion assembly and egress. Examples of ISG effectors targeting each step are indicated. Figure is adapted from [202] and created with BioRender.com.

A recently characterized example of an ISG effector suppressing viral, specifically flavivirus, replication is the endoplasmic reticulum (ER)-localized interferon α inducible protein (IFI) 6. Mechanistically, the formation of replication organelles, which are characterized by single-membrane invaginations at the ER and harbor the viral replication machinery, is inhibited by IFI6, likely by interfering with the membrane-perturbing function of flaviviruses [173,308–310]. A more direct mechanism to impair viral replication is the immediate degradation of viral RNAs upon infection. Members of the oligoadenylate synthetases (OAS) family, the zinc antiviral protein (ZAP), and ISG20 are among the best-studied examples. Upon viral RNA binding, OAS proteins synthesize 2'-5'-linked oligoadenylates to activate ribonuclease latent (RNaseL), which efficiently degrades viral genomes (reviewed in [311, 312]). ZAP targets viral mRNAs for exosome-mediated degradation and thus also acts as an inhibitor of viral translation [313]. Lastly, ISG20 suppresses replication of multiple viruses by degrading their genomes with its 3' to 5' exonuclease function [314]. Late stages of viral replication are characterized by virion assembly and egress from the infected cell. Although many ISGs target earlier phases of the viral replication cycle, only few ISGs targeting these late steps have been identified. Among those few are the transmembrane

protein tetherin (encoded by BST2) and the guanylate binding protein (GBP) 5. Interestingly, GBP5 impairs incorporation of the viral envelope protein (env) into virions [315], whereas tetherin anchors budding virions to the cell surface and thus prevents them from being released [316]. In summary, ISGs cooperatively act on cellular processes as well as distinct phases of the viral life cycle to ultimately inhibit viral replication and establish viral defenses.

1.7 Viral Evasion Strategies

While the full induction of host-cellular antiviral responses potently inhibits viral replication, most viruses evolved intricate strategies capable of evading innate immunity to efficiently replicate and spread. The distinct antagonistic mechanisms against RLR-mediated immune responses are extensive and can occur at every level of signaling. For instance, some viral antagonists directly interact with host proteins, whereas others degrade or cleave them to avert activation of antiviral signaling. The viral nonstructural protein (NS) 1 of IAV prevents induction of IFN signaling by binding dsRNA, thus sequestering the mediator of RIG-I activation [317–319]. In addition to sequestering dsRNA, NS1 was reported to directly bind RIG-I, thereby inhibiting the transcriptional induction of IFN-β [320]. In contrast, the N-terminal protease (N^{pro}) of classical swine fever virus (CSFV) specifically targets IRF3 for proteasomal degradation [321–323]. In fact, the inhibition of phosphorylation and thus activation of IRF3 as a key transcription factor seems to be a commonly used mechanism of distinct viruses. For instance, the immediate-early protein 62 (IE62) of Varicella-Zoster virus (VZV) blocks the sequential phosphorylation of IRF3 by TBK1 [324], whereas the NS3/4A protease of HCV directly cleaves MAVS from mitochondrial or peroxisomal membranes and thus prevents downstream activation and signaling [325, 326]. Interestingly, the suppression of IFN response has been proposed to be one of the causes for HCV persistence upon infection [327–331].

In contrast to the above-described virus-encoded proteins targeting the RLR-mediated signaling cascade, some viruses rather focus on interfering with the IFN-mediated signaling. Accordingly, the nonstructural protein 5 (NS5) of DENV antagonizes type I IFN signaling by interacting with the host protein UBR4 to mediate proteasome-dependent STAT2 degradation [332–334]. Notably, DENV encodes several antagonist of both IFN production and signaling, but the NS5 protein seems to be the most potent inhibitor of antiviral signaling [332, 335–337]. Interestingly, NS5 proteins of distinct flaviviruses were reported to target different steps of the antiviral signaling pathway. For instance, whereas DENV NS5 promotes STAT2 degradation, the NS5 protein of WNV potently prevents STAT1 phosphorylation [338]. The severe acute respiratory syndrome coronavirus (SARS-CoV) 2 represents another remarkable example of multi-level antagonism of antiviral signaling, involving almost all its encoding viral proteins (reviewed in [339]). The accessory protein ORF6 was consistently identified as the most potent inhibitor of the antiviral response [340–342]. ORF6 binds to nuclear complexes, blocking nuclear translocation of IRF3, STAT1, and STAT2, and conse-

quently causes a compromised induction of ISGs [340, 343, 344]. ORF6-mediated blocking of the nuclear pore can further cause nuclear retention of host mRNAs, leading to an even stronger reduction in host gene expression [343].

1.8 Mathematical Modeling of Biological Systems

Evidently, the antiviral signaling response is complex and, hence, dissecting individual mechanisms of regulation and viral antagonism proved to be non-trivial. Advanced technologies generating large amounts of, e.g., single cell data might provide insights into this intricate system, however, require clever and innovative ways to be interpreted. A powerful tool to dissect complex biological processes are mathematical models, which often use a system of biochemical reactions converted into ordinary differential equations (ODE). ODEs are based on the law of mass action, which states that reactants must collide for a reaction to occur. It further states that the rate of a reaction is proportional to the product of the molar concentrations of the reactants as well as the reaction rate constant (also known as reaction rate coefficient, k). Hence, the reaction rate constant quantifies the rate and direction of a chemical reaction and thereby serves as a proportionality factor. Mass action kinetics state that a reaction rate is the product of a rate constant (k) and the mass (i.e., the concentration of a substrate) and thus mass action kinetics describe the dynamics of systems of chemical reactions. In addition to kinetic rate constants of biological processes, the initial conditions, i.e., concentrations, of model species are another essential parameter of mathematical models. In experimental settings, initial conditions are often based on, e.g., steady state protein and mRNA concentrations (reviewed in [345–347]).
Mathematical models can contribute to explain and to predict experimental outcomes and thus promote the interpretation and comprehension of biological systems. In fact, they have provided crucial insights for many biological systems, including the type I IFN responses. For instance, Qiao *et al.* developed a computational model of the innate immune responses in IFN-pretreated DCs. Experimentally, pretreated cells were infected with IAV and intracellular dynamics of IRF7, IFN-α, IFN-β, and SOCS1 mRNA expression was examined. The arising model provided critical insights into the kinetics of type I IFN induction upon virus infection and further predicted saturation threshold values for IFN treatment, which could be confirmed with experimental data [348]. Another recent study established a comprehensive mechanistic model of the type I IFN responses in human hepatoma cells (Huh7.5), comprising IRF9 and STAT1/2-mediated positive feedback loops, as well as negative feedback regulation through USP18 and SOCS [349]. Here, kinetic measurements of distinct signaling components in IFN-α-primed and treated Huh7.5 cells were used for model calibration. Remarkably, model analysis revealed a STAT2 and IRF9-mediated hypersensitization of the IFN pathway upon low dose IFN-α prestimulation. Contrarily, prestimulation with a high dose of IFN-α led to USP18 and SOCS1-mediated desensitization [349]. Similarly, during the current global pandemic of coronavirus disease 2019 (COVID-19) caused by

SARS-CoV-2, mathematical model simulations have been applied to improve clinical outcomes of infected patients. Specifically, some models determined cost-effective strategies for distinct drug therapy combinations, whereas others were established to serve as a basis for personalized treatments [350–352]. In conclusion, mathematical modeling provides critical insights in complex biological systems, which might be difficult to obtain solely experimentally. The combination of experimental data and *in silico* modeling facilitates the identification of key mechanisms in innate immune signaling as well as the intricate viral-host interaction and thus promotes the development of effective vaccines and antiviral therapies.

2. Materials

2.1 Consumables

Table 1: Consumables.

Product	Company
AD1 4D-Nucleofector Y Kit	Lonza
Cell culture plate 6 well, 12 well, 24 well, 96 well	Greiner Bio-One GmbH
Cell scraper	Sarstedt AG & Co.
Cellstar cell culture dish 6 cm, 10 cm, 15 cm	Greiner Bio-One GmbH
Costar 50 ml reagent reservoir	Corning GmbH
Costar stripette 5 ml, 10 ml, 25 ml, 50 ml,	Corning GmbH
Cover slip	Glaswarenfabrik Karl Hecht GmbH
Cryo vials	Greiner Bio-One GmbH
Electroporation cuvettes, 0.4 cm gap	Bio-Rad Laboratories
Falcon petri dish 10 cm	Corning GmbH
Falcon tubes 15 ml, 50 ml	Corning GmbH
Filter 0.2 µm	GE Healthcare
Hard-Shell PCR plates 96 well	Bio-Rad Laboratories
Immun-Blot PVDF membrane for protein blotting	Bio-Rad Laboratories
Kimtech Science prevision wipes	Kimberly-Clark Worldwide
Micro tube 1.5 ml, 2 ml	Sarstedt AG & Co.
Microscope slides	Thermo Fisher Scientific
Microseal 'B' PCR plate sealing film	Bio-Rad Laboratories
Millipore Stericup 150 ml Durapore 0.22 µm filter unit	Merck KGaA
Neubauer counting chamber	Neolab
PCR SingleCap 8er-SoftStrips	Biozym Scientific GmbH
Pipet tips 10 µl, 100 µl, 1000 µl, filtered	STARLAB GmbH
Pipet tips 10 µl, 20 µl, 200 µl, 1000 µl	STARLAB GmbH
Pipet tips 5 ml	Eppendorf AG
SafeSeal micro tube 1.5 ml, 2 ml	Sarstedt AG & Co.
Scalpel	B. Braun Melsungen AG
Syringe 5 ml , 10 ml , 20 ml	BD Biosciences
Whatman filter paper	GE Healthcare Life Sciences
XCEED nitrile gloves	Barrier Safe Solutions International, Inc.

2.2 Chemicals, Reagents, and Kits

Table 2: Chemicals, Reagents, and Kits.

Product	Company	Identifier
β-mercaptoethanol	Sigma-Aldrich	M6250
Acrylamide:Bisacrylamide (BAA; 29:1)	Roth	A515.1
Adenosine 5'-triphosphate (ATP)	Sigma-Aldrich	A2383
Agar	Sigma-Aldrich	A1296
Agarose	Roth	3810.3
Alkaline phosphatase, calf intestinal (CIP)	NEB	M0290
Ammonium persulfate (APS)	Roth	9592.1
Benzonase nuclease	Merck Millipore	70746-4
Blasticidin S hydrochloride	MP Biomedicals	15047750
Bromphenol blue	AppliChem GmbH	A2331
Calcium chloride	AppliChem GmbH	A4689
CalPhos Mammalian Transfection Kit	Takara Bio Europe	631312
Carbenicillin disodium salt	Sigma-Aldrich	C1389
Clarity Western ECL Substrate	Bio-Rad Laboratories	170-5061
Coelenterazine	PJK Biotech	102171
Cytotox Green Dye	Sartorius	4633
Deoxyribose nucleoside triphosphate (dNTP)	VWR	733-1270
Dimethyl sulfoxide (DMSO)	VWR	23.500.297
DIY Human IFN-λ1/2/3 ELISA (TCM)	PBL Assay Science	61840-1
D-Luciferin	PJK GmbH	N/A
DMEM, high glucose	Thermo Fisher Scientific	41965062
Double-stranded RNA (dsRNA; 400 bp)	*in vitro*-generated	N/A
DTT	Sigma-Aldrich	10197777001
EGTA	AppliChem GmbH	A0878
Ethanol	VWR	20.821.330
Ethylenediaminetetraacetic acid (EDTA)	AppliChem GmbH	A3553
Fetal calf serum (FCS)	Thermo Fisher Scientific	10270106
Gateway BP Clonase II Enzyme mix	Thermo Fisher Scientific	11789-100
Gateway LR Clonase II Enzyme mix	Thermo Fisher Scientific	1946833
Gel electrophoresis DNA loading dye	Thermo Fisher Scientific	R0611
Gel electrophoresis RNA loading dye	Thermo Fisher Scientific	R0641
Gene Ruler 1 kb	Thermo Fisher Scientific	SM0311
Gene Ruler 100 bp	Thermo Fisher Scientific	SM0241
Geneticin (G418) Sulfate	Santa Cruz Biotechnology	SC-29065B
Gentamicin (50 mg/mL)	Thermo Fisher Scientific	15750037
Glycerol	Sigma-Aldrich	15523-1L-M
Glycine	Sigma-Aldrich	3326
Glycyl Glycin	Sigma-Aldrich	G3915-500G
Hepes	Roth	9105.2
High-Capacity cDNA Reverse Transcription Kit	Thermo Fisher Scientific	43-688-14
IFN-α	BIOZOL GmbH	11100-1
IFN-β	R & D Systems	8499-IF-010/CF
IFN-γ	R & D Systems	285-IF-100

Product	Company	Identifier
IFN-λ1	PeproTech	300-02L
Isopropanol	VWR	89370-086
iTaq Universal SYBR Green Supermix	Bio-Rad Laboratories	17251525
Kanamycin sulphate	Thermo Fisher Scientific	15470594
L-Glutathion	Sigma-Aldrich	G-4251
Lipofectamine 2000 Transfection Reagent	Thermo Fisher Scientific	11668030
LumiKine Xpress hIFN-beta 2.0 ELISA	InvivoGen	luex-hifnbv2
Magnesium chloride	Merck Millipore	7791-18-6
MEM Non-Essential Amino Acids Solution (NEAA; 100x)	Thermo Fisher Scientific	11140050
Methanol	Sigma-Aldrich	322415
Midori Green Advance	Biozym	617004
Milk powder	Roth	T145.1
Monarch DNA Gel Extraction Kit	NEB	T1020
Monarch Plasmid Miniprep Kit	NEB	T1010
Monarch Total RNA Miniprep Kit	NEB	T2010
NucLight Rapid Red Reagent	Sartorius	4717
NucleoBond PC 500	Macherey-Nagel	740574.50
NucleoSpin RNA Plus	Macherey-Nagel	740984250
OptiMEM	Thermo Fisher Scientific	31985047
PBS (10x Dulbecco's) powder	AppliChem GmbH	A0965,9050
PEI (Polyethylemine) 25 kDa linear	Polysciences, Inc.	23966-2
Penicillin-Streptomycin (10 000 U/mL)	Thermo Fisher Scientific	15140122
Poly(C)	Sigma-Aldrich	P4903
Poly(I:C)	Sigma-Aldrich	P9582
Polyethylenglycol 8000 (PEG)	Roth	0263.2
Potassium chloride	Roth	6781.1
Potassium hydroxide (10 N)	LabChem	LC193701
Precision plus dual color prestained protein marker	Bio-Rad Laboratories	1610374
Puromycin dihydrochloride	Sigma-Aldrich	P7255
Q5 High-Fidelity PCR Kit	NEB	E0555
Restriction enzymes and buffers	NEB	N/A
Ribose nucleoside triphosphate (rNTP)	Thermo Fisher Scientific	R0481
RNasin (40 U/µl)	Promega	N2511
Simeprevir	Hölzel Diagnostika	HY-10241
Sodium acetate	Roth	6773.1
Sodium dodecyl sulfate (SDS)	Roth	CN30.3
Spermidin	Sigma-Aldrich	S0266
ssRNA ladder	NEB	N0362S
T4 DNA ligase	NEB	M0202S
T4 DNA ligase reaction buffer	NEB	B0202S
T4 polynucleotide kinase	NEB	M0201S
T7 RNA polymerase	NEB	M0251S
Telaprevir	Hölzel Diagnostika	S1538-5
Tetramethylenediamine (TEMED)	Roth	8142.1
Tris Base	Roth	4855.2
Tris-HCl	Roth	9090.3
Triton X-100	AppliChem GmbH	A497
Trypsin-EDTA (0.05 %), phenol red-20	Thermo Fisher Scientific	25300-096

Product	Company	Identifier
U-PLEX Interferon Combo Human Kit	Meso Scale Diagnostics	K15094K
V-PLEX Chemokine Panel 1 Human Kit	Meso Scale Diagnostics	K15047D
V-PLEX Pro-inflammatory Panel 1 Human Kit	Meso Scale Diagnostics	K15049D
V-PLEX Viral Panel 2 Human Kit	Meso Scale Diagnostics	K15346D
Western Lightning Plus ECL	PerkinElmer	NEL104001EA
Yeast Extract BioChemica	AppliChem GmbH	A1552

2.3 Media, Buffers, and Solutions

Table 3: Media, Buffers, and Solutions.
If not stated otherwise, buffers and solutions were prepared in ddH_2O.

Solution	Composition
Annealing buffer	50 mM NaCl, 10 mM Tris (pH 8.0)
Cell freezing cryo medium	90 % FCS, 10 % DMSO
Cytomix	120 mM KCl, 0.15 mM $CaCl_2$, 10 mM KPO_4 buffer, 25 mM Hepes, 2 mM EGTA, 5 mM $MgCl_2$
DMEM (complete)	DMEM with 10 % fetal calf serum, 1x MEM NEAA, 1x Penicillin-Streptomycin
DMEM (P/S-free)	DMEM with 10 % fetal calf serum, 1x MEM NEAA
Firefly luciferase assay buffer	25 mM Glycyl Glycin, 15 mM KPO_4 buffer, 15 mM $MgSO_4$, 4 mM EGTA, 2 mM ATP, 1 mM DTT, 80 µM D-Luciferin
KPO_4 buffer	90.8 mM K_2HPO_4, 9.2 mM KH_2PO_4
LB agar	LB medium with 0.5 % Agar
LB medium	1 % Bacto-Trypton, 0.5 % Yeast extract, 0.5 % NaCl
Luciferase lysis buffer	10 % Glycerol, 1 % Triton X-100, 25 mM Glycyl Glycin, 15 mM $MgSO_4$, 4 mM EGTA, 1 mM DTT
PBS-Tween (PBS-T)	PBS with 0.1 % Tween-20
Phosphate-buffered saline (PBS)	0.01 % PBS powder
Protein sample buffer	5 % glycerol, 16.25 mM Tris (pH 6.8), 0.5 % SDS, 1.25 % β-mercaptoethanol, bromophenol blue
Renilla luciferase assay buffer	25 mM Glycyl Glycin, 15 mM KPO_4 buffer, 15 mM $MgSO_4$, 4 mM EGTA, 2 mM ATP, 1 mM DTT, 3.36 µM Coelenterazine
Reverse transcription mix	20 % RT Buffer (10x), 20 % RT Random Primers (10x), 8 % dNTP Mix (25x), 10 % RNase Inhibitor, 10 % MultiScribe Reverse Transcriptase
RRL buffer	80 mM Hepes, 12 mM magnesium chloride, 2 mM Spermidin, 40 mM DTT, 10 mM sodium acetate
SDS-PAGE resolving gel	25 % resolving gel buffer, 8-12 % BAA, 0.1 % TEMED, 0.1 % saturated ammonium persulfate solution
SDS-PAGE resolving gel buffer	1.5 M Tris Base, 0.4 % SDS, pH 8.8
SDS-PAGE stacking gel	13 % stacking gel buffer, 10 % BAA, 0.1 % TEMED, 0.15 % saturated ammonium persulfate solution
SDS-PAGE stacking gel buffer	1 M Tris Base, 0.8 % SDS, pH 6.8
Semi-dry transfer buffer	2.5 mM Tris Base (pH 8.3), 15 mM Glycine, 10 % Methanol
T4 dimerization mix	10 % T4 10x ligation buffer, 10 % T4 PNK, 10 µM forward oligo, 10 µM reverse oligo
T4 DNA ligation mix (10 µl)	1 µl ligation buffer (10x), 1 µl T4 DNA ligase, 1 µl DNA oligo dimers (pre-diluted 1:200), 100 ng linearized vector backbone
TBS-Tween	TBS with 0.1 % Tween-20
TE buffer	10 mM Tris, 1 mM EDTA, pH 8.0
Tris-acetate-EDTA (TAE) buffer	40 mM Tris, 20 mM acetic acid, 1 mM EDTA
Tris-buffered saline (TBS)	2 nM Tris-HCl (pH 7.5), 15 nM NaCl
Tris-glycine-sulfate (TGS) buffer	192 mM Glycine, 25 mM Tris Base, 0.1 % SDS, pH 8.3
Western blot blocking buffer	PBS with 0.5 % Tween-20, 5 % protease free milk powder
Wet blot transfer buffer	2.5 mM Tris Base (pH 8.3), 15 mM Glycine, 20 % Methanol

2.4 Bacteria and Viruses

For all cloning experiments and re-transformations, the following bacteria strain was used: *E. coli* DH5α: F'/endA1 hsdR17A (rk-mk+) supE44 thi-1 recA1 gyrA (Nalr) relA1Δ(lacZYA-argF)U169 deoR (ϕ80dlacΔ(lacZ)M15).

Sendai virus (SeV) was provided by Prof. Dr. Rainer Zawatzky (DKFZ, Heidelberg).

2.5 Cell Lines

Table 4: Cell Lines.

Cell line	Source
A549	Heidelberg University Hospital
A549 EF-1α-ORF6 SARS-CoV-2	[353]
A549 EF-1α-N^{pro} CSFV	[353]
A549 EF-1α-NS1 IAV	This study
A549 EF-1α-NS3/4A HCV	[353]
A549 EF-1α-NS5 DENV	[353]
A549 IFNAR1 KO IFNLR1 KO (IFNR DKO)	[353]
A549 IFNAR1 KO IFNLR1 KO IFNGR1 KO (IFNR TKO)	[287]
A549 IFNR TKO IRF1 KO	This study
A549 IFNR TKO IRF3 KO	This study
A549 IFNR TKO MAVS KO	This study
A549 IRF3-eGFP H2B-mCherry	[353]
A549 IRF3 KO	[354]
A549 IRF3 KO ROSA26-IRF3	[353]
A549 IRF9 KO	[287]
A549 IRF9 KO ROSA26-IRF9	[353]
A549 STAT1 KO	[355]
A549 STAT2 KO	[353]
HEK293T	DKFZ, Heidelberg
HepG2	DKFZ, Heidelberg
HepG2 EF-1α-ORF6 SARS-CoV-2	[353]
Huh7 LucUbiNeo-Con1	DKFZ, Heidelberg
Huh7 LucUbiNeo-JFH	DKFZ, Heidelberg

2.6 DNA Oligonucleotides

Table 5: DNA Oligonucleotides.
5′ to 3′: forward (fwd); 3′ to 5′: reverse (rev).

Oligo	Purpose	Sequence
attB CSFV N^{pro} fwd	Cloning	GGGGACAAGTTTGTACAAAAAAGCAGGCTTC atggagttgaatcattttga
attB CSFV N^{pro} rev	Cloning	GGGGACCACTTTGTACAAGAAAGCTGGGTC gcaactggtaacccacaatg
attB H2B-mCherry fwd	Cloning	GGGGACAAGTTTGTACAAAAAAGCAGGCTTC atgccagagccagcgaagtc
attB H2B-mCherry rev	Cloning	GGGGACCACTTTGTACAAGAAAGCTGGGTC ttacttgtacagctcgtccatg
attB IAV NS1 fwd	Cloning	GGGGACAAGTTTGTACAAAAAAGCAGGCTTC atggatccaaacactgtgtc
attB IAV NS1 rev	Cloning	GGGGACCACTTTGTACAAGAAAGCTGGGTC tcaaacttctgacctaattg
CCL5 fwd	qPCR primer	GCTGTCATCCTCATTGCTACTG
CCL5 rev	qPCR primer	TGGTGTAGAAATACTCCTTGATGTG
cppt fwd	Sequencing	TAATAGCAACAGACATAC
GAPDH fwd	qPCR primer	TCGGAGTCAACGGATTTGGT
GAPDH rev	qPCR primer	TTCCCGTTCTCAGCCTTGAC
hU6-promoter	Sequencing	ACGATACAAGGCTGTTAGAGAGA
IFIT1 fwd	qPCR primer	GAATAGCCAGATCTCAGAGGAGC
IFIT1 rev	qPCR primer	CCATTTGTACTCATGGTTGCTGT
IFNA1 fwd	qPCR primer	AGCCATCTCTGTCCTCCATGAG
IFNA1 rev	qPCR primer	GATCTCATGATTTCTGCTCTGA
IFNB1 fwd	qPCR primer	CATTCGGAAATGTCAGGAGC
IFNB1 rev	qPCR primer	TGGAGCATCTCTTGGATGG
IFNL1 fwd	qPCR primer	GGTGACTTTGGTGCTAGGCT
IFNL1 rev	qPCR primer	TGAGTGACTCTTCCAAGGCG
IFNL2/3 fwd	qPCR primer	CTGCCACATAGCCCAGTTCA
IFNL2/3 rev	qPCR primer	AGCGACTCTTCTAAGGCATCT
IRF9 fwd	qPCR primer	TCCTCCAGAGCCAGACTACT
IRF9 rev	qPCR primer	CAATCCAGGCTTTGCACCTG
MX1 fwd	qPCR primer	ACCATTCCAAGGAGGTGCAG
MX1 rev	qPCR primer	TGCGATGTCCACTTCGGAAA
N^{pro} fwd	qPCR primer	CGGTCTACCATAGAGCCCCT
N^{pro} rev	qPCR primer	GCCTTCCGTCACTACCTGTC
NS1 fwd	qPCR primer	TCTTTGGCATGTCCGCAAAC
NS1 rev	qPCR primer	GTGCTGCCCCTTCCTCTTAG
NS5 fwd	qPCR primer	GACACCGCAGGATGGGATAC
NS5 rev	qPCR primer	GGCCTCGGCTAGTTTCTTGT
ORF6 fwd	qPCR primer	ATGTTTCATCTCGTTGACTTTCAGG
ORF6 rev	qPCR primer	TTAATCAATCTCCATTGGTTGCTCTT
RIG-I fwd	qPCR primer	CCCTGGTTTAGGGAGGAAGA
RIG-I rev	qPCR primer	TCCCAACTTTCAATGGCTTC
TNFAIP3 fwd	qPCR primer	TCCTCAGGCTTTGTATTTGAGC
TNFAIP3 rev	qPCR primer	TGTGTATCGGTGCATGGTTTTA

2.7 Plasmids

Table 6: Plasmids.
Antibiotic resistance for selection in eukaryotic cells: Blr, blasticidin; Neo, neomycin/G418; Puro, puromycin.

Plasmid	Source
LentiCRISPRv2 puro	Feng Zhang, Addgene # 52961
LentiCRISPRv2 IFNGR1 gRNA	[287]
LentiCRISPRv2 IRF1 gRNA	[287]
LentiCRISPRv2 IRF3 gRNA	[287]
LentiCRISPRv2 IRF5 gRNA	[287]
LentiCRISPRv2 MAVS gRNA	[95]
LentiCRISPRv2 STAT1 gRNA	[355]
pcDNA EF-1α TLR3-Flag	[77]
pCMV-dr8.91	Didier Trono, EPFL, Lausanne, Switzerland
pDONR207	Invitrogen/Thermo Fisher Scientific
pGL3 IFIT1 Firefly luciferase	AG Binder, DKFZ, Heidelberg
pGL3 p125 IFN-β Firefly luciferase	AG Bartenschlager, DKFZ, Heidelberg
pMD2.G	Didier Trono, EPFL, Lausanne, Switzerland
pRL SV40 Renilla luciferase	AG Binder, DKFZ, Heidelberg
pWPI EF-1α blr rfB	[356]
pWPI EF-1α blr rfB HA	AG Binder, DKFZ, Heidelberg
pWPI EF-1α H2B-mCherry	[354]
pWPI EF-1α IRF3-eGFP	[355]
pWPI EF-1α IRF9-HA	Sandra Wüst, DKFZ, Heidelberg
pWPI EF-1α N^{pro} (CSFV)-HA	[353], pDONR kindly gifted by Andreas Pichlmair
pWPI EF-1α NS1 (IAV)-HA	This study, pDONR kindly gifted by Andreas Pichlmair
pWPI EF-1α NS3/4A (HCV)	Volker Lohmann, Heidelberg University Hospital
pWPI EF-1α NS3/4A S139A (HCV)	Volker Lohmann, Heidelberg University Hospital
pWPI EF-1α NS5 (DENV)-HA	[353], pDONR kindly gifted by Mirko Cortese
pWPI EF-1α ORF6 (SARS-CoV-2)-HA	[353], pDONR kindly gifted by Christopher Neufeldt
pWPI ROSA26 blr HA	AG Binder, DKFZ, Heidelberg
pWPI ROSA26-IRF3-HA	Sandra Wüst, DKFZ, Heidelberg
pWPI ROSA26-IRF9-HA	Sandra Wüst, DKFZ, Heidelberg
pWPI ROSA26-STAT2-HA	[353]

2.8 Antibodies

Table 7: Antibodies.
If not stated otherwise, antibodies were used in a dilution of 1:1000.

Antibody	Host	Clonality	Source
anti-beta-actin	mouse	mono	Santa Cruz Biotechnology (SC-47778)
anti-calnexin	rabbit	poly	Enzo Life Sciences (ADI-SPA-865-F)
anti-Flag	mouse	mono	Sigma-Aldrich (F3165)
anti-HA	mouse	mono	Sigma-Aldrich (H3663)
anti-IκBα	rabbit	poly	Cell Signaling (9242)
anti-IFIT1	rabbit	poly	Abnova, Taiwan (H00003434-DO1)
anti-IRF1	rabbit	mono	Cell Signaling (8478S)
anti-IRF3	mouse	mono	Santa Cruz Biotechnology (SC-33641)
anti-IRF5	rabbit	mono	Abcam (ab181553)
anti-IRF9	rabbit	poly	Abcam (ab126940)
anti-MAVS	rabbit	poly	Cell Signaling (3993S)
anti-mouse-HRP	goat	poly	Sigma Aldrich (A4416), used 1:10 000
anti-MX1	mouse	mono	Kind gitf of Georg Kochs
anti-NS3	rabbit	poly	Kind gift of Darius Moradpour
anti-phospho-IRF3	rabbit	mono	Cell Signaling (4947S)
anti-phospho-NF-κB	rabbit	mono	Cell Signaling (3033)
anti-phospho-STAT2	rabbit	mono	Cell Signaling (D3P2P)
anti-phospho-TBK1	rabbit	mono	Cell Signaling (5483S)
anti-rabbit-HRP	goat	poly	Sigma Aldrich (A6154), used 1:20 000
anti-RIG-I	mouse	mono	Adipogen (AG-20B-0009)
anti-STAT1	mouse	mono	BD (610115)
anti-STAT2	mouse	mono	Santa Cruz Biotechnology (SC-514193)

2.9 Equipment

Table 8: Equipment.

Device	Company
4D-Nucleofector® Core Unit	Lonza
4D-Nucleofector® Y Unit	Lonza
Bio-Rad SDS-PAGE gel casting system	Bio-Rad Laboratories
CellDropTM BF brightfield cell counter	DeNovix
Centrifuge, Rotina 380 R	Hettich GmbH & Co. KG
Centrifuge, Sorvall RC 5C	Thermo Fisher Scientific
Centrifuge, tabletop (5424, 5424R)	Eppendorf
CFX96 Real-Time PCR Detection System	Bio-Rad Laboratories
ECL ChemoCam Imager 3.2	Intas Science Imaging Instruments GmbH
Gene Pulser Xcell™ Electroporation Systems	Bio-Rad Laboratories
HI2211 Basic pH/ORP Meter	Hanna Instruments Deutschland GmbH
Incucyte S3 Live-Cell Analysis System	Sartorius AG
MESO QuickPlex SQ 120	Meso Scale Diagnostics
MilliQ Barnstead GenPure Pro	Thermo Fisher Scientific
Mini-PROTEAN Tetra Vertical Electrophoresis Cell	Bio-Rad Laboratories
Mithras LB 943	Berthold Technologies GmbH & Co. KG
NanoDrop	Thermo Fisher Scientific
Nikon Eclipse Ti	Nikon Corporation, Japan
Trans-Blot Turbo Transfer System	Bio-Rad Laboratories

2.10 Software

Table 9: Software.

Software	Source
Affinity Designer	Serif Ltd.
BioRender	Biorender.com
CFX Manager (V3.1)	Bio-Rad Laboratories
ChemoStar	Intas Science Imaging Instruments
e-crisp.org	Boutros Lab, DKFZ
ilastik	Ilastik.org, cite Ilastik paper
ImageJ	Imagej.nih.gov
ImageLab	Bio-Rad Laboratories
IncuCyte Software (2019B Rev2)	Sartorius AG
MSD Discovery Workbench	Meso Scale Diagnostics
PANTHER GO Enrichment Analysis	Pantherdb.org
Prism (V9)	GraphPad Software
RStudio	Rstudio.com
SnapGene	GSL Biotech LLC

3. Methods

If not stated otherwise, kits and assays were used following the protocol provided by the manufacturer (Table 2). Media, buffers, and solutions are listed in Table 2 and Table 3.

3.1 Basic Molecular Biology Techniques

3.1.1 Plasmid Amplification and Purificiation

Plasmid DNA was amplified in *E. coli* DH5α. Single colonies were transferred into either 2 ml (small-scale plasmid purification) or 300 ml (large-scale plasmid purification) LB medium containing the required selection antibiotic and incubated for 16 h at 37 °C. Plasmid DNA was isolated using the Monarch Plasmid Miniprep Kit for small-scale plasmid preparation or the NucleoBond PC 500 kit for large-scale plasmid preparation. DNA pellets were re-suspended in ddH_2O and DNA concentrations were determined using the Nanodrop photo spectrometer.

3.1.2 Polymerase Chain Reaction

Polymerase chain reactions (PCR) were performed using the NEB Q5 High-Fidelity Polymerase. A 50 µl reaction mix contained 22.5 µl ddH_2O, 10 µl 5x Q5 Reaction Buffer, 10 µl Q5 High GC Enhancer, 2.5 µl each of forward primer and reverse primer (10 µM), 1 µl dNTPs (10 mM), 1 µl template DNA, and 0.5 µl Q5 High-Fidelity DNA Polymerase. The PCR reaction was performed on a PCR cycler using the manufacturer's program: initial denaturation for 30 s at 98 °C; 35 cycles of 10 s at 98 °C, 20 s at 50-72 °C*, 30 s/kb at 72 °C; then final extension for 2 min at 72 °C. The annealing temperature (*) was dependent on the primer sequence and was calculated with SnapGene for each primer pair.

3.1.3 Agarose Gel Electrophoresis

For 1 % agarose gels, 0.5 g agarose was dissolved in 50 ml 1x TAE buffer upon heating in a microwave. After cooling to 60 °C, 2 µl Midori Green were added and the solution was poured into a gel chamber. Nucleic acids in H_2O were supplemented with Gel Loading Dye (6x) to a final concentration of 1x. 6 µl of molecular weight standard Gene Ruler 1 kb and nucleic acids were loaded on the agarose gel, gel electrophoresis was performed at 120 V, and bands were analyzed under UV light.

3.1.4 PCR Purification and Agarose Gel Extraction

For PCR purification and agarose gel clean-up, the NucleoSpin Extract II kit was used following the manufacturer's protocol. DNA was either purified directly after PCR or desired DNA fragments were cut out from agarose gels. DNA was eluted in 30 µl ddH_2O.

3.1.5 Restriction Digest

Restriction endonucleases from NEB were used for restriction digestion of DNA. 1 µg DNA was digested with 1 U restriction enzyme in a 20 µl reaction mixture containing 1x of the required NEBuffer. Digestion was performed for up to 1 h at 25 °C or 37 °C.

3.1.6 DNA Ligation

Upon DNA restriction digest, vectors were treated with calf intestine phosphatase (CIP) for 30 min at 37 °C to prevent religation. Purified insert DNA was mixed with phosphatase-treated vector in a 3:1 ratio, and 1 µl 10x ligase buffer as well as 1 µl T4 ligase were added in a total volume of 10 µl. Ligation reactions were incubated at 16 °C for up to 16 h and subsequently transformed into competent bacteria (Section 3.1.7).

3.1.7 Transformation of Competent Bacteria with Plasmid DNA

100 µl of chemo-competent *E. coli* DH5α solution was thawed on ice and incubated with either 100 ng plasmid DNA for retransformations or the total volume of BP, LR, or ligation mixture on ice for 5 min. The mixture was heat-treated at 42 °C for 40 s, incubated on ice for 20 min, and 200 µl LB medium was added. Bacteria were incubated on a shaker for 30 min at 37 °C, plated onto LB agar plates containing the required selection antibiotic, and subsequently incubated for 16 h at 37 °C.

3.1.8 Sequencing of Plasmid DNA

100 ng isolated plasmid DNA was mixed with 5 µl sequencing primer (5 µM) in a total reaction volume of 10 µl. Sequencing was performed by Eurofins Genomics Germany.

3.1.9 Gateway Cloning

Gateway cloning uses site-specific recombination to first shuttle a PCR product in an entry vector (BP reaction) and then shuttle the insert into distinct destination (expression) vectors (LR reaction). In the BP reaction, 150 ng pDONR or pENTR vector harboring attP recombination sites and 150 ng PCR product harboring attB sites were mixed with 1 µl BP clonase

in TE buffer in a total reaction volume of 8 µl and incubated at 25 °C for 1 h. 1 µl proteinase K was added and the reaction mixture was incubated at 37 °C for 10 min. Plasmids were transformed into competent bacteria (Section 3.1.7), isolated (Section 3.1.4), and subsequently used for the LR reaction. 150 ng pDONR/pENTR containing the PCR product and 150 ng destination vector were mixed with 1 µl LR clonase in TE buffer in a total reaction volume of 8 µl and incubated at 25 °C for 1 h. 1 µl proteinase K was added and the reaction mixture was incubated at 37 °C for 10 min. Plasmids were transformed into competent bacteria, isolated, and subjected to DNA sequencing (Section 3.1.8).

3.2 Cell Culture

3.2.1 Cultivation and Passaging of Cells

A549, HepG2, and HEK 293T cell lines were cultured in complete DMEM at 37 °C, 85 % humidity, and 5 % CO_2. Cells were passaged twice per week when they reached about 80 % confluency. For passaging, medium was aspirated, cells were washed with PBS, and subsequently treated with 0.05 % Trypsin-EDTA for 5 min for detachment. Detachted cells were resuspended in complete DMEM and passaged in a 1:10 ratio.

3.2.2 Cryopreservation

For cryopreservation, detachted cells of a confluent 15 cm dish were centrifuged (5 min, 700 x g, 4 °C), supernatant was aspirated, and cell pellet was resolved in ice-cold cell freezing cryomedium. The cell suspension was transferred to cryopreservation tubes and frozen at -80 °C. For thawing, cells were quickly thawed in a water bath at 37 °C, mixed with pre-warmed complete DMEM, and cultured on a 10 cm dish. Upon attachment, medium was replaced with fresh complete DMEM to remove remaining DMSO.

3.2.3 Liposome-Based Transfection of 5'ppp-dsRNA

A549 cells stably expressing histone H2B-mCherry and IRF3-eGFP were seeded at a density of 7.5×10^4 cells per 24 well. The next day, cells were stimulated with *in vitro* transcribed and chromatographically purified 400 bp 5'ppp-dsRNA (Section 3.9) or poly(C) using Lipofectamine 2000 following the manufacturer's protocol. Briefly, 30 min prior transfection, complete DMEM medium was replaced with pre-warmed P/S-free DMEM. 1 µl Lipofectamine 2000 reagent was diluted in 49 µl OptiMEM and incubated at room temperature for 5 min. 5'ppp-dsRNA was diluted in OptiMEM to a final volume of 50 µl, mixed with the Lipofectamine reaction, and incubated at room temperature for 20 min. 100 µl transfection mixture was added to each well. Non-stimulatory poly(C) served as negative control and was used to fill up small amounts of 5'ppp-dsRNA to the highest concentration used in one

experiment. IRF3-GFP nuclear translocation and H2B-mCherry colocalization was analyzed using a confocal microscope equipped with an incubation chamber (Olympus FluoView FV1000) or monitored in short time periods using the Incucyte S3 live-cell analysis system (Section 3.10.2).

3.2.4 In-Well Electroporation-Based Transfection of 5'ppp-dsRNA

A549 cells stably expressing histone H2B-mCherry and IRF3-eGFP were seeded at a density of 7.5×10^4 cells per 24 well. The next day, cells were stimulated with *in vitro* transcribed and chromatographically purified 400 bp 5'ppp-dsRNA (Section 3.9) or poly(C) using an in-well electroporation approach. Here, the 4D Nucleofector Y Unit, the AD2 4D Nucleofector Y Kit, as well as a homemade cytomix were utilized. To decrease the intensity of electroporation in order to maximize cell survival and transfection efficiency, a mock transfection with the provided Dipping Electrode Array was crucial. For in-well electroporation of seeded A549 cells, DMEM was replaced with 350 µl cytomix and the electrode was inserted into the 24 well plate, strictly avoiding the formation of air bubbles. In-well electroporation was performed using the FB-166 program and cytomix was replaced with warm DMEM subsequently. Nuclear translocation of IRF3-eGFP and colocalization with H2B-mCherry was analyzed using confocal microcopy equipped with an incubation chamber (Olympus FluoView FV1000) or monitored in short time periods using the Incucyte S3 live-cell analysis system (Section 3.10.2).

3.2.5 Electroporation-Based Transfection of 5'ppp-dsRNA

Synchronous stimulation of the RIG-I pathway in A549 or HepG2 cells was performed using the Gene Pulser Xcell modular electroporation system and a ShockPod cuvette chamber. Cell suspensions containing 4×10^6 cells were centrifuged (700 x g, 5 min), resuspended in 400 µl cytomix, and transferred to a 0.4 cm cuvette containing 220 ng 5'ppp-dsRNA (Section 3.9). Electroporation was performed at 150 V with exponential decaying pulse for 10 ms. Electroporated cells were directly transferred to P/S-free DMEM (37 °C), washed twice in complete DMEM, and resuspended in 9.6 ml complete DMEM. Cells were seeded on 6 well plates using 1.2 ml cell suspension per well and time point, resulting in 5×10^5 cells per well, and were subsequently subjected to qRT-PCR (Section 3.4) or immunoblotting (Section 3.5).

3.2.6 Protease Inhibitor Treatment

Confluent 10 cm dishes of A549 NS3/4A (S139A) cells were treated with 1 µM, 200 nM, 100 nM, and 10 nM Simeprevir. After 16 h, cells were used for synchronous 5'ppp-dsRNA stimulation (Section 3.2.5) and subsequent qRT-PCR (Section 3.4) or immunoblotting (Section 3.5).

3.3 Cell Line Generation

Both overexpression and knockout cell lines were generated by transduction with lentiviral vectors.

3.3.1 Lentiviral Vector Particle Production

1×10^6 human embryonic kidney (HEK293T) cells were seeded in a 6 cm dish the day before transfection. DMEM was replaced with 4 ml pre-warmed medium 30 min prior transfection. Calcium phosphate transfection using the Takara CalPhos Mammalian Transfection Kit required a total of 15 µg DNA (pCMV-dr8.91, pMD2.G, and retroviral vector in a 3:1:3 ratio) mixed with 62 µl 2 M $CaCl_2$ and ddH_2O to a final volume of 500 µl. 500 µl 2 x HBS was added drop-wise while air was constantly introduced to the solution using a glass pipette and a Pipetboy. Subsequently, the solution was added drop-wise to the cells. Medium was exchanged 8 h after transfection. Supernatant was harvested 48 h and 72 h after transfection, sterile-filtered through a 0.2 µM filter, and stored at -80 °C.

3.3.2 Generation of Overexpression Cell Lines

8×10^4 cells per well were seeded on 6 well plates. The next day, medium was replaced by 2 ml filtered supernatant containing desired lentiviral particles, incubated for 24 h, and repeated once. Overexpression cell lines were continuously cultured in the presence of the required selection antibiotic to ensure stable transgene expression (blasticidin: 5 µg/ml; neomycin resistance: 1 mg/ml geneticin (G418); puromycin: 1 µg/ml). Overexpression was validated by immunoblotting (Section 3.5).

3.3.3 Generation of Knockout Cell Lines

The Clustered Regularly Interspaced Short Palindromic Repeats (CRISPR)/Cas9 technology was used for stable KO generation in A549 cells. DNA oligonucleotides coding for guideRNAs against the respective genes were designed with e-crisp.org [357] and cloned into the expression vector LentiCRISPRv2. For this, oligos were dimerized in a T4 dimerization mix (Table 3) for 30 min at 37 °C, 5 min at 95 °C, followed by a temperature reduction to 25 °C with -5 °C/min. Dimerized oligos were diluted 1:200 in ddH_2O. 3 µg lentiCRISPRv2 plasmid were digested with BsmBI, incubated with calf intestinal phosphatase for 90 min at 37 °C, and digested fragments were separated on an agarose gel (Section 3.1.3). The vector backbone was cut out of the agarose gel, purified (Section 3.1.4), and vector backbone and annealed oligos were ligated (Section 3.1.6). The ligation reaction was transformed into competent bacteria (Section 3.1.7), purified (Section 3.1.4), and sequenced (Section 3.1.8). The lentiCRISPRv2 plasmid containing the required guideRNA was used for

large-scale purification and subsequent lentiviral particle production as described in Section 3.3.1. Single cell clones of successfully transduced cells were isolated, and KO was validated by immunoblotting (Section 3.5) and, if appropriate, functional tests.

3.4 RNA Quantification by Quantitative Real-Time PCR

RNA isolation, reverse transcription (RT), and quantitative real-time PCR (qRT-PCR) were performed according to the manufacturer's protocols on a CFX96 real time system. Briefly, cells were lysed in Monarch RNA lysis buffer, RNA was purified using the Monarch Total RNA Miniprep Kit, and eluted in 50 µl RNase-free ddH_2O. 3 µl isolated RNA was mixed with 3 µl RT Mix, cDNA synthesis was performed on a PCR cycler (25 °C for 10 min, 37 °C for 2 h, 85 °C for 5 min), and the cDNA was subsequently diluted 1:20 in ddH_2O. 6 µl cDNA were mixed with 9 µl iTaq Universal SYBR Green Supermix containing the forward and reverse primers for target genes at a final concentration of 0.25 µM. Sequences of specific exon spanning PCR primers are listed in Table 5. qRT-PCR was performed using a standard protocol (3 min at 95 °C, then 44 cycles of 10 s at 95 °C, 30 s at 60 °C, fluorescence emission measurement). Data was evaluated using the Bio-Rad CFX Manager software. Values were normalized to the housekeeping gene GAPDH using the $2^{-\Delta Ct}$ method or fold changes were calculated relative to the 0 h time point using the $2^{-\Delta\Delta Ct}$ method [358].

3.5 Protein Quantification by Immunoblotting

Synchronously stimulated cells were washed with PBS, lysed with 100 µl Laemmli buffer, treated with Benzonase Nuclease for 10 min at room temperature, and incubated at 95 °C for 5 min. Protein extracts were separated on 8 – 12 % polyacrylamide gels by SDS polyacrylamide gel electrophoresis (SDS-PAGE) at 80 V for 15 min and 120 V for 2 h. Separated proteins were transferred to PVDF membranes in a wet transfer approach using the Mini Trans Blot cell at 350 mA for 2 h at 4 °C. Membranes were blocked in PBS-T or TBS-T (for phospho-antibodies) complemented with 5 % (w/v) bovine serum albumin (BSA) for up to 3 h at room temperature. Subsequently, membranes were incubated with PBS-T or TBS-T complemented with 5 % BSA and primary antibodies (Table 7) for 16 h at 4 °C. Membranes were washed 3 x in PBS-T or TBS-T for 5 min and subsequently incubated with anti-rabbit-horseradish-peroxidase (HRP) (1:20 000) or anti-mouse-HRP (1:10 000) for 1 h at room temperature. For detection, Amersham ECL Prime Western Blotting Detection Reagent was applied for 1 min and luminescence was detected using the INTAS ECL ChemoCam Imager 3.2. Western blot bands were analyzed and quantified using Image J.

3.6 Luciferase Reporter Assay

1.5×10^5 cells were seeded per well of a 24 well plate. The next day, medium was aspirated and replaced with P/S-free DMEM. 75 ng Firefly luciferase reporter and 25 ng Renilla luciferase reporter were transfected using Lipofectamine 2000 (Section 3.2.3). After 8 h, medium was exchanged and cells were stimulated with SeV (Section 3.8) or RLR agonists using transfection (Section 3.2.3) for 16 h. Cells were washed with 500 µl PBS, lysed with 100 µl luciferase lysis buffer, and stored for at least 15 min at -80 °C. Lysates were thawed and Firefly and Renilla luciferase signals directly measured in a Mithras plate reader using 400 µl Firefly and Renilla luciferase assay buffer per well. For multiple well measurements, 100 µl 10 % SDS were used to quench the light reaction in between well measurements. Renilla luciferase is constitutively expressed and thus serves as control. Samples were measured in technical replicates and Firefly luciferase values were divided by Renilla luciferase values.

3.7 LucUbiNeo Luciferase Reporter Assay

Huh7 LucUbiNeo-JFH and LucUbiNeo-Con1 cells were seeded at 5×10^4 cells per well on a 24 well plate in complete DMEM. The next day, cells were treated with medium containing 1 µM, 100 nM, or 10 nM Telaprevir or Simeprevir for 8 h, 24 h, and 48 h. Cells were washed with 500 µl PBS, lysed with 100 µl luciferase lysis buffer, and stored for at least 15 min at -80 °C. Lysates were thawed and Firefly luciferase directly measured in a Mithras plate reader using 400 µl Firefly luciferase assay buffer per well.

3.8 Sendai Virus Infection

1×10^5 cells per well in a 24 well plate were infected with Sendai virus at MOI = 0.004 and subjected to luciferase measurement (Section 3.6) 16 h after infection.

3.9 *In Vitro* Transcription

In vitro transcription and chromatographical purification of 400 bp 5'ppp-dsRNA was performed as described previously [77]. Briefly, a 400 bp fragment of the TLR3 gene was amplified by PCR (Section 3.1.2), subjected to agarose gel electrophoresis on a 2 % gel (Section 3.1.3), and subsequently purified from the gel (Section 3.1.4). For *in vitro* transcription, 20 µl RRL buffer (5x), 12 µl rNTPs (25 mM), 2.5 µl RNAsin (40 U/µl), 4 µl T7 RNA polymerase, and 1 µg dsDNA sample were mixed and incubated at 37 °C for 16 h. The next day, 2 µl DNase were added to the solution, incubated at 37 °C for 2 h, centrifuged (14 000 rpm, 5 min), and transferred to a new tube. 60 µl of ssRNA-fwd and 60 µl of ssRNA-rev were added to 120 µl

annealing buffer, incubated at 98 °C for 2 min, and slowly let cool down to room temperature. Successful *in vitro* transcription and annealing was examined using agarose gel electrophoresis (Section 3.1.3) and generated dsRNA was subjected to size exclusion chromatography.

3.10 Cell Imaging

3.10.1 Fluorescence Microscopy

Subcellular localization of IRF3-eGFP and H2B-mCherry was analyzed with a Nikon Eclipse Ti microscope equipped with an X-Cite 120 LED, a SD-Qi2 camera and the NIS-Elements AR 4.40.00 software. 1×10^5 A549 cells expressing IRF3-eGFP and H2B-mCherry were seeded in a 24 well plate and imaged in PBS or DMEM. Images were taken at 100 % LED intensity for 1 s using a 10x lens.

3.10.2 Live-Cell Imaging

Cell proliferation, IRF3-GFP nuclear translocation, and H2B-mCherry colocalization upon 5'ppp-dsRNA stimulation was monitored over time by live-cell imaging in an Incucyte S3 live-cell analysis system. 7.5×10^4 cells per 24 well or 2×10^3 cells per 96 well were seeded and either stimulated with 5'ppp-dsRNA (Section 3.2.3, Section 3.2.4) or treated with the NucLight Rapid Red Reagent to label nuclei. 16 images per well were taken with a 10x objective and 400 ms acquisition time in phase, red, and green channels every 10 - 20 min and analyzed with the Incucyte S3 software and ilastik (Section 3.10.3). For cell proliferation, number of cells were determined by counting red events per image equaling the number of nuclei containing H2B-mCherry or NucLight Rapid Red Reagent.

3.10.3 Quantification with Ilastik

Image analysis was performed using ilastik [359]. Pixel and object classifications were set to distinguish between background and cellular nuclei and to determine IRF3-eGFP and H2B-mCherry colocalization, respectively. For object classification, a size range of 60 to 500 and a threshold of 0.85 were applied. At least 500 and up to 2500 individual cells were analyzed for each time point in each condition.

3.11 Mass Spectrometry

Protein copy number estimations of A549 wt, A549 IFNR DKO, and HepG2 wt cells were performed by total proteome analysis using mass spectrometry. A confluent 10 cm dish was washed with PBS and cells were detachted with a cell scraper using 5 ml ice-cold PBS. Cells were centrifuged (3 min, 700 x g, 4 °C), PBS was aspirated, and cells were frozen in liquid nitrogen. Further sample preparation, mass spectrometry, and data analysis were performed by Christian Urban, Antonio Piras, and Andreas Pichlmair as described in detail in [353].

3.12 Enzyme-Linked Immunosorbent Assay (ELISA)

To determine IFN-β and IFN-λ contents in the supernatants of stimulated A549 and HepG2 cells, the LumiKine Xpress IFN-β 2.0 and the DYI human IFN-λ1/2/3 ELISA were used. Cells were synchronously stimulated with 5'ppp-dsRNA (Section 3.2.5) and supernatants of 5×10^5 cells in a 6 well plate were harvested for each measured time point. Supernatants were centrifuged (700 x g, 5 min), transferred into new tubes, and IFN concentrations were determined according to the manufacturer's protocol.

3.13 Multiplex Electrochemiluminescence Assay

Quantitative measurement of secreted cytokines within supernatants was performed using the Meso Scale Diagnostics' (MSD) electrochemiluminescence technology in a multiplex approach. Supernatants of synchronously stimulated A549 wt, A549 IFNR DKO, and HepG2 wt cells (Section 3.2.5) were harvested, centrifuged (3 min, 700 x g, 4 °C), and assays were conducted according to the manufacturer's instructions. Concentrations of IFN-α, IFN-β, and IFN-λ1 were measured using the human U-PLEX Interferon Combo. Pro-inflammatory cytokines IL-1β, IL-4, IL-6, IL-8, IL-10, and TNF were analyzed with the MSD V-PLEX Viral Panel 2 Human Kit. Chemokines CCL4/MIP-1β, CCL17/TARC, CCL3/MIP-1α, CCL2/MCP-1, CCL22/MDC, CCL13/MCP-4, CXCL10/IP-10, as well as IL-6 and TNF were analyzed with the MSD V-PLEX Pro-inflammatory and Chemokine Panel Kit. All assays were perfomed with undiluted supernatants following the manufacturer's protocol. Measurements were conducted with the MESO QuickPlex SQ 120 instrument and evaluated using the MSD Discovery Workbench software.

3.14 RNA Expression Profiling

A549 cells were synchronously stimulated as described in Section 3.2.5. RNA was harvested at 0 h and 8 h after stimulation, isolated using the Monarch Total RNA Miniprep Kit, eluted in 50 µl RNase-free ddH_2O, and RNA integrity was confirmed by agarose gel electrophoresis (10 µl RNA on a 2 % agarose gel). The Microarray Unit of the Genomics and Proteomics Core Facility at the DKFZ measured gene-level expression from > 20 000 genes on a Clariom S human microarray and provided analysis data (normalized mean expression values and mean fold changes between 0 h and 8 h) and statistics (two-sample t-test p-values corrected for multiple testing with Benjamini-Hochberg). Further data analysis, cleanup, identification of DEGs, and visualization was performed with R in RStudio with support of Ana Luísa Simões Costa and PD Dr. Carl Herrmann from the BioQuant Heidelberg. Genes were determined to be significantly regulated it they were at least 2-fold up or downregulated and the Benjamini-Hochberg-corrected p-value was below 0.05. Gene Ontology (GO) enrichment analysis was performed using PANTHER [360, 361] and pathways were classified as enriched with a false discovery rate (FDR) of < 0.05.

4. Results

The cell-intrinsic innate immune response is a major contributing factor in control and clearance of viral infections. The combined expression of IFNs and ISGs ultimately establishes an antiviral state of a cell. To counteract the rapid viral replication within an infected cell, an even faster detection of the viral pathogen and the ensuing antiviral responses is decisive. In doing so, this cell-intrinsic process functions as a first line of defense against viral invasion. Naturally, most viruses have developed sophisticated strategies to evade or interrupt innate immune recognition and defense [362, 363], either by delaying signal transduction or leading to a lower amplitude of the response.
In this work, using a cell culture system and stimulation with virus-like 5'ppp-dsRNA, I aimed at characterizing the dynamics and putative stochastic nature of the RLR and the IFN response. For this purpose, I focused on time-resolved western blotting of key pathway components, live-cell imaging of transcription factor relocalization, and quantitative RT-PCR of a variety of target genes. Examining the dynamic impact of distinctive viral antagonists on the antiviral response system to further decipher and gain insights in the underlying mechanisms of viral immune evasion was another objective of this thesis. Collaborating with computational scientists and employing the generated kinetic data of antiviral signaling as foundation, we aimed at developing a comprehensive mathematical model of the cell-intrinsic antiviral response system, able to simulate and analyze critical virus-host interactions during the early infection phase. Lastly, as the strong overlap and linkage between RLR and IFN signaling precluded experimental distinction of the pathways previously, I intended to dissect the differences between primary RLR and secondary IFN-mediated antiviral responses using "IFN-blind" cells.

4.1 Simultaneous dsRNA Stimulation Results in Highly Deterministic and Synchronous RIG-I Signaling in Human Lung Adenocarcinoma Cells

Numerous studies suggested that intracellular activities, i.e., signaling events, display a high degree of stochasticity and thus cell-to-cell variability. However, most studies rely on actual virus infection or liposome-based transfection of virus-like RNA, which are based on endocytic processes and hence introduce a large variability of intracellular PAMP accessibility themselves [364, 365]. By synchronizing dsRNA delivery, a potential stochasticity of cell-intrinsic RIG-I-mediated signal transduction could be analyzed in more detail. For this, I employed human lung adenocarcinoma (A549) cells, which are known for their RLR and IFN signaling competence. In a first approach, I generated A549 cells stably co-expressing cytosolic IRF3-eGFP as a marker for early pathway activation, and the nuclear marker H2B-mCherry to analyze nuclear translocation of IRF3 upon RIG-I stimulation. According

to the protocol used in Binder *et al.* [77], I generated a 400 bp long, 5' triphosphorylated dsRNA (5'ppp-dsRNA), which serves as highly specific ligand for RIG-I.
Using two distinct ligand delivery approaches, namely liposome-based transfection and in-well electroporation of adherent cells, I analyzed the differences of RIG-I signaling dynamics upon 5'ppp-dsRNA stimulation (Figure 1A). Transfection efficiency and cytotoxicity of predefined in-well electroporation settings are depicted in Supplementary Figure S1A and S1B. For an initial insight, I stimulated A549 IRF3-eGFP H2B-mCherry cells with 5'ppp-dsRNA by transfection or electroporation and analyzed IRF3-eGFP nuclear translocation by employing confocal microscopy (Figure 1B). As expected, IRF3-eGFP remained cytosolic in mock-stimulated A549 cells, whereas both liposome and electroporation-based transfections of 5'ppp-dsRNA resulted in nuclear IRF3 translocation. However, IRF3-eGFP translocation in electroporated cells appeared more rapid and synchronous compared to liposome-based transfection of 5'ppp-dsRNA. For a more quantitative assessment of IRF3 translocation in both stimulation approaches, I analyzed the colocalization of IRF3-eGFP and H2B-mCherry using the live-cell imaging system Incucyte and employed the ilastik software for an automated and unbiased quantification. Here, colocalization was analyzed for at least 500 individual cells for each time point in each condition and I calculated nuclear IRF3-eGFP as percentage over all imaged cells. An exemplary image excerpt of the ilastik quantification depicting the object classification for IRF3-eGFP is illustrated in Supplementary Figure S1C. Indeed, whereas electroporation of 5'ppp-dsRNA induced a synchronous and rapid increase already starting 30 minutes upon stimulation, liposome-based transfection resulted in a constant but slower increase of nuclear IRF3-eGFP (Figure 1C). This indicates that the previously described stochasticity was a result of staggered uptake of the stimulatory RNA during infection as seen for liposome-based transfection. Following this, I titrated the amount of 5'ppp-dsRNA used for stimulation of A549 IRF3-eGFP H2B-mCherry cells to examine whether the observed effects are a result of possible differences in dsRNA level successfully entering the cytosol. Decreasing 5'ppp-dsRNA concentrations only slightly affected the activation kinetics but had a considerable effect on the maximum fraction of activated cells. The qualitative characteristics, however, remained fully consistent. Independent of the 5'ppp-dsRNA amount used for stimulation, electroporation led to steeper activation kinetics (Figure 1D) as compared to liposome-based transfection (Figure 1E). Consequently, these experiments demonstrate that RIG-I signaling is highly deterministic and synchronous after simultaneous 5'ppp-dsRNA stimulation, whereas liposome-based transfection (i.e., virus infection) seems to lead to a staggered 5'ppp-dsRNA uptake and might thereby be interpreted as cell-to-cell heterogeneity and stochasticity.

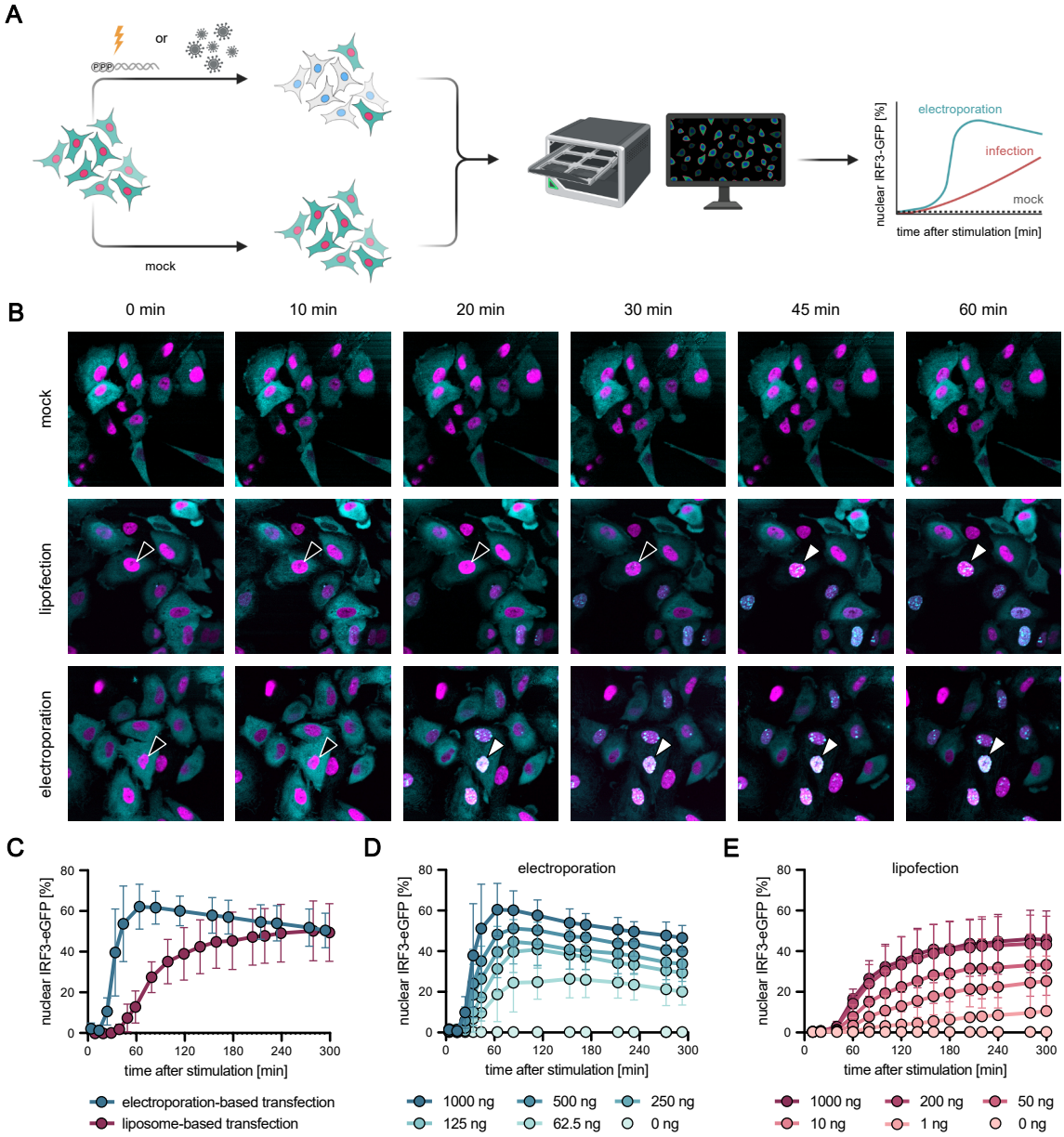

Figure 1: RIG-I signaling upon 5'ppp-dsRNA electroporation is highly deterministic and synchronous in A549 cells.

(A) Schematic representation of the experimental setup. A549 cells stably expressing IRF3-eGFP and H2B-mCherry were either mock-treated or stimulated with 5'ppp-dsRNA using liposome-based transfection or in-well electroporation. IRF3-eGFP nuclear translocation upon stimulation was imaged for up to 3 hours using the Incucyte live-cell imaging system and automatically quantified with the ilastik software. **(B)** Confocal microscopy time course of A549 IRF3-eGFP (cyan) H2B-mCherry (magenta) cells upon different stimulation approaches. Cells were mock-treated or stimulated with 1 µg 5'ppp-dsRNA using liposome-based transfection or in-well electroporation. IRF3-eGFP nuclear translocation was monitored for 1 h. Black arrowheads indicate cytoplasmic IRF3-eGFP, white arrowheads indicate nuclear IRF3-eGFP. **(C)** Quantification of nuclear IRF3-eGFP translocation upon liposome-based transfection or in-well electroporation of 1 µg 5'ppp-dsRNA. Nuclear translocation of IRF3-eGFP and colocalization with H2B-mCherry was analyzed using the Incucyte live-cell imaging system and quantified using ilastik. **(D)** Quantification of IRF3-eGFP nuclear translocation upon in-well electroporation of varying 5'ppp-dsRNA concentrations. **(E)** Quantification of IRF3-eGFP nuclear translocation upon liposome-based transfection of varying 5'ppp-dsRNA concentrations. Graphs depict (B) representative images, or (C) mean ± SD of 4 or (D-E) 3 biologically independent experiments, respectively. Subfigures (B-E) were originally published in Burkart *et al.* [353].

4.2 Synchronous RIG-I Stimulation Results in a Fast Onset of RLR Pathway Signaling in A549 Cells

Synchronous stimulation and activation of the RLR pathway in A549 cells by electroporation allowed for a more detailed characterization of RIG-I signaling dynamics. For this reason, I mock-treated or synchronously stimulated, i.e., electroporated, A549 wild type (wt) cells with 5'ppp-dsRNA. Then, I examined the activation status and protein abundance of some key RLR signaling pathway components within the IRF3 (Figure 2A, left panel) and NF-κB-axis (Figure 2A, right panel) in short time intervals using western blot analysis[2].

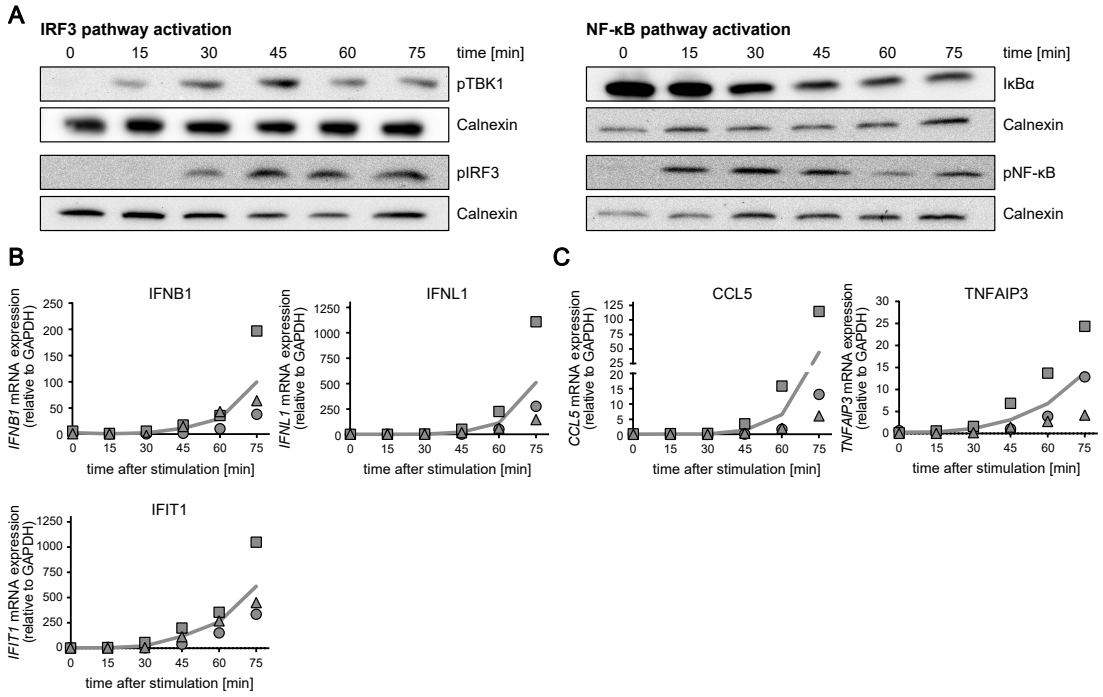

Figure 2: Synchronous RIG-I stimulation results in a fast onset of RLR pathway signaling in A549 cells.

A549 wt cells were either mock-treated or electroporated with 220 ng 5'ppp-dsRNA to kinetically characterize the dynamics of the RIG-I signaling pathway. **(A)** Protein abundance and phosphorylation status of RLR signaling pathway components were determined in 15 min intervals using western blot analysis. Early mRNA expression onset of **(B)** IFNB1, IFNL1, IFIT1, **(C)** CCL5, and TNFAIP3 after 5'ppp-dsRNA electroporation was measured using qRT-PCR. Values were normalized to the housekeeping gene GAPDH using the $2^{-\Delta Ct}$ method [358]. Graphs depict (A) representative blots or (B, C) mean and individual, biological replicate values of 3 biologically independent experiments. Subfigures (B-C) were originally published in Burkart *et al.* [353]. The respective mock electroporation controls are depicted in Supplementary Figure S2.

Remarkably, phosphorylation of the kinase TBK1 as well as the transcription factors IRF3 and NF-κB appeared in the earliest sample obtained 15 minutes after 5'ppp-dsRNA stimulation. Similarly, the onset of decay of the NF-κB inhibitor, IκBα, was detectable in the earliest sample harvested. In accordance with the established sequential RLR signal transmission, IRF3 phosphorylation occurred slightly after TBK1 phosphorylation. Surprisingly,

[2] A more detailed characterization of the activation status of RLR signaling pathway components upon synchronous dsRNA stimulation can be found in our recent publication, Burkart *et al.* [353].

NF-κB phosphorylation seemed to decrease over time, whereas IRF3 phosphorylation was stable within the experimental timeframe, despite the decline of TBK1 phosphorylation (Figure 2A). Consistent with the rapid onset of RIG-I signaling, I detected early transcripts of the target genes IFNB1, IFNL1, and IFIT1 (Figure 2B), as well as CCL5 and TNFAIP3 (Figure 2C) by qRT-PCR already 45 to 60 minutes after synchronous 5'ppp-dsRNA stimulation. In summary, the obtained results demonstrate that signal transduction from detection of 5'ppp-dsRNA by RIG-I to the expression of target mRNAs is very fast and only requires several minutes.

4.3 Establishment of a Dynamic RIG-I Signaling Model Which Accurately Reproduces the Activation Kinetics of Key Pathway Components

Combining the previously described kinetic data of the RIG-I signaling pathway with an additional data set (see joint publication, [353]) generated by a former PhD student, Dr. Jamie Frankish, resulted in an unprecedented, high resolution description of the RIG-I signaling dynamics in this specific experimental system. In the interest of investigating kinetic characteristics, such as rate-limiting steps, in the RIG-I signaling pathway in a universally applicable system, we collaborated with Darius Schweinoch, PhD student in Lars Kaderali's lab in Greifswald, in order to establish a mathematical model. He developed a set of ODEs representing essential steps within the RIG-I signaling pathway which are based on regular mass action kinetics [353].

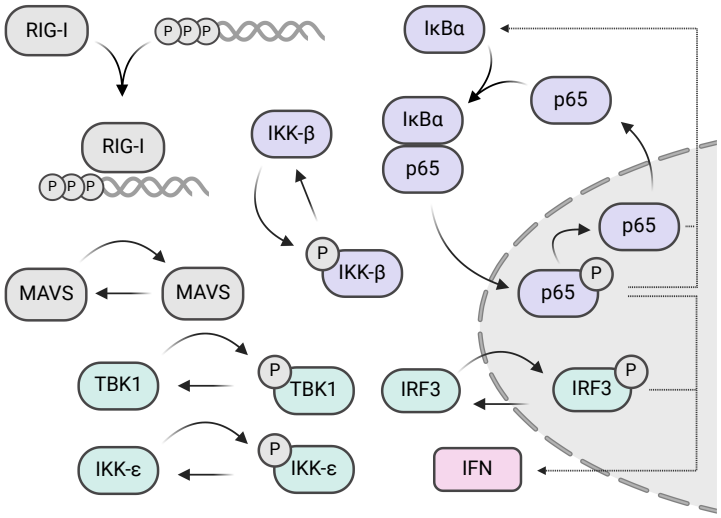

Figure 3: Mathematical model of the core RIG-I signaling pathway.

Schematic depiction of key RIG-I signaling pathway components required for the establishment of a mathematical model. RIG-I binds cytoplasmic dsRNA and interacts with MAVS, thus recruiting the kinases TBK1, IKK-ε, and IKK-β. The kinases are phosphorylated and induce the phosphorylation of IRF3 and NF-κB, which in turn translocate to the nucleus and induce IFN expression. Arrows correspond to reactions included in the mathematical model.

This mathematical model comprises 19 pathway components distributed into two distinct compartments, the cytoplasm and the nucleus. We implemented 20 rate constants representing canonical steps of the RIG-I signaling cascade, as well as additional parameters (i.e., normalization factors) to account for experimental conditions (Figure 3). Subsequently, in order to determine absolute protein concentrations necessary for the mathematical model, I acquired quantitative full proteome data of naïve A549 cells using label-free mass spectrometry with support of Christian Urban of the Pichlmair lab in Munich [353]. Of all kinetic rate constants, 9 were used from previous publications and 11 were left open for parameter and model fitting. For the purpose of model calibration, we utilized relative protein levels, phosphorylation intensities, and mRNA levels of the combined, previously established data on the activation kinetics of RIG-I signaling (Figure 2, [353]).
In fact, we could identify a parameter combination, for which our model was able to accurately capture the experimentally measured signaling dynamics (Figure 4A, B). In order to examine and validate the model with conditions not used for its establishment, I additionally characterized RIG-I signaling dynamics in A549 cells with artificially lowered IRF3 concentrations. For this purpose, I employed an A549 IRF3 KO cell line [287]. Using lentiviral transduction and the very weak murine promoter ROSA26, I restored IRF3 to a substantially lower-than-wild-type level (Supplementary Figure S3A). Experimentally, I synchronously stimulated A549 wt, A549 IRF3 KO, and A549 IRF3 KO ROSA26-IRF3 cells with 5'ppp-dsRNA and monitored IFNB1 mRNA expression over time. As anticipated, the knockout of IRF3 diminished IFNB1 induction by more than 1000-fold, whereas cells expressing a low level of IRF3 displayed an intermediate phenotype (Figure 4C). Specifically, A549 IRF3 KO ROSA26-IRF3 cells showed a slower induction kinetics and more than 10-fold reduced transcript levels at 4 hours post stimulation compared to A549 wt. Remarkably, simulating IFNB1 mRNA expression after only adjusting initial IRF3 concentrations adequately matched the actual measurements, capturing the qualitative changes as well as the dampened induction kinetics (Figure 4D). This validation not only suggests a usability of the mathematical model to meaningfully fit measured data, but also to comprehensively predict the outcome of RIG-I signaling under perturbed conditions.

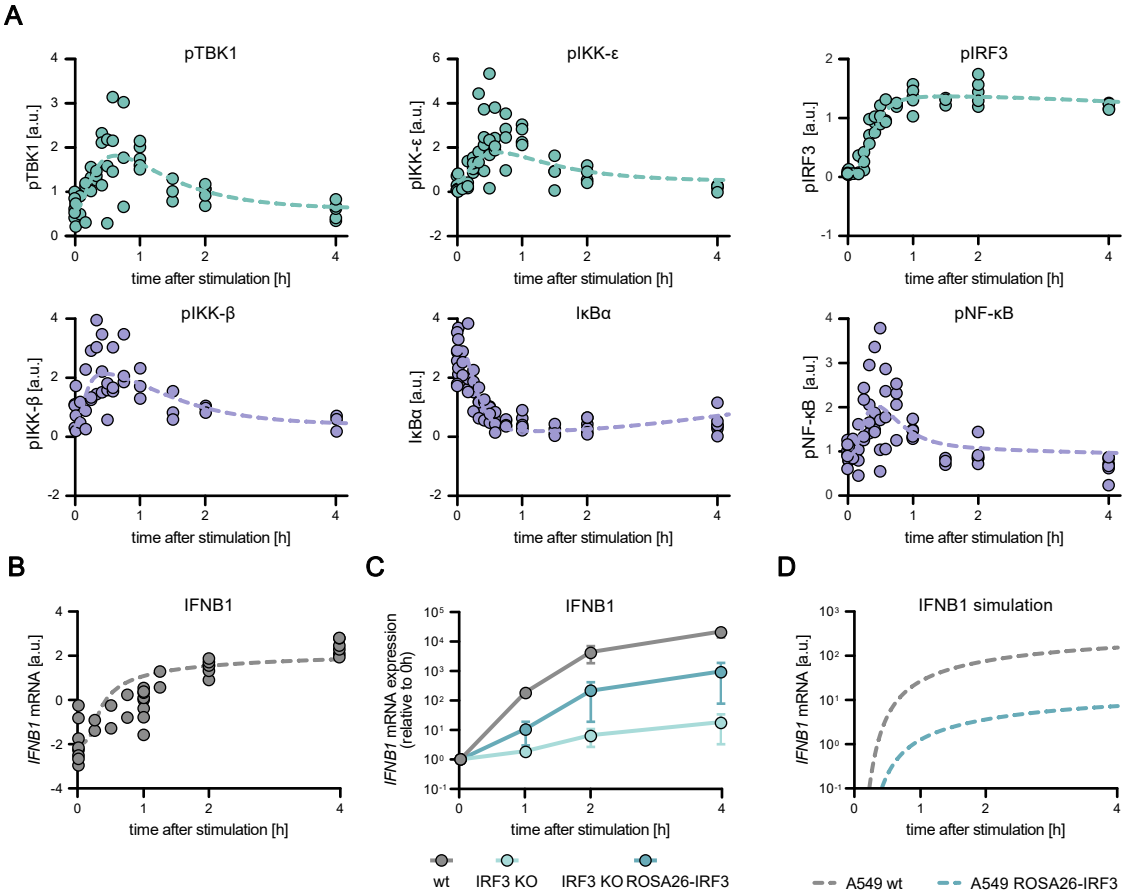

Figure 4: Establishment of a mathematical model of the core RIG-I pathway based on quantitative data.

Time-resolved data was used to establish and calibrate a mathematical model able to reproduce the kinetics of essential signaling events within the core RIG-I pathway. **(A)** Quantitative protein abundance, protein phosphorylation, and **(B)** mRNA data of A549 wt cells electroporated with 220 ng 5'ppp-dsRNA were used to set-up and calibrate the mathematical model. Experimental data were obtained in conjunction with Jamie Frankish, mathematical modeling was conducted by Darius Schweinoch. Dots represent quantitative data of (A-C) 4 biologically independent experiments, lines represent average model fit. **(C)** IFNB1 mRNA expression kinetics upon synchronous 5'ppp-dsRNA stimulation was analyzed in A549 wt, A549 IRF3 KO, and A549 IRF3 KO ROSA26-IRF3-expressing cells and used for model validation. Values were normalized to the housekeeping gene GAPDH, and the 0 hour time point using the $2^{-\Delta\Delta Ct}$ method [358]. Graphs depict mean ± SD of 3 biologically independent experiments. **(D)** Core model simulation of IFNB1 mRNA expression in reduced IRF3 protein level conditions. Subfigures (A-D) were previously published in Burkart *et al.* [353].

4.4 IFN Feedback upon RLR Stimulation is Essential for High and Sustained ISG Expression but Not for IFN Production

Becoming increasingly appreciated recently, IFN recognition by its cognate receptor and downstream signaling through JAK/STAT does not induce the production of IFN in an autofeedback manner (Supplementary Figure S4). However, in addition to inducing the expression of a large variety of ISGs, IFN signaling indeed upregulates many components of PRR signaling. For instance, IFN-mediated expression of RIG-I might result in further IFN production and thus indirect positive feedback, if potentially remaining and/or replicating viral RNA was still detected (Section 1.6).

To expand our model of the core RIG-I signaling pathway to the full antiviral system and to additionally characterize RLR signaling dynamics in the presence or absence of IFN, I conducted synchronous 5'ppp-dsRNA stimulations of a previously established A549 KO cell line, termed IFN receptor double KO (IFNR DKO). In this cell line both IFNAR1 and IFNLR are knocked out, rendering it unable to detect produced IFN and hence unable to pursue further signaling upon IFN stimulation (Supplementary Figure S5). Upon synchronous 5'ppp-dsRNA stimulation of A549 wt and IFNR DKO cells using electroporation, I monitored mRNA expression of type I and III IFNs (Figure 5A) as well as ISGs (Figure 5B) over time using qRT-PCR. In accordance with the RLR-dependent but IFN-independent IFN production discussed above, type I and III IFN expression was not affected by the KO of both IFN receptors and hence displayed identical kinetic patterns as A549 wt cells (Figure 5A). Both cell lines exhibited a fast onset of IFN induction, reached peak levels between 4 and 8 h, and declined again afterwards. Whereas CCL5 mRNA expression, similarly to IFN expression, was not affected by the KO of IFN receptors and showed similar kinetics in both A549 wt and IFNR DKO cell lines, mRNA expression kinetics of the ISGs IFIT1 and MX1 clearly differed (Figure 5B). Although the initial, RLR-induced expression of IFIT1 up to 6 hours was still unaffected, the lack of IFN feedback and subsequent secondary upregulation of IFIT1 was clearly visible in the IFNR DKO cell line (Figure 5B, middle panel). Similarly, MX1 induction kinetics did not differ between A549 wt and IFNR DKO cells up to 2 hours but lead to a significantly lower overall induction in cells lacking IFN signaling (Figure 5B, right panel).
Since mRNA expression does not necessarily correlate with protein production, I further measured IFN-β and IFN-λ1 protein secretion in A549 wt and IFNR DKO cells upon synchronous 5'ppp-dsRNA stimulation using a multiplex electrochemiluminescent immunoassay. Matching the previously observed mRNA kinetics (Figure 5A), IFN secretion was not affected in the IFNR DKO cell line, and initial IFN-β as well as IFN-λ1 protein was detected 4 hours after stimulation, increasing continuously over the next hours and eventually reaching a plateau at 24 hours (Figure 5C). These results further support the notion of an IFN-independent IFN production. Nevertheless, apart from IFNs, many other cytokines and chemokines are reported to be IFN-dependent. Utilizing the A549 IFNR DKO cell line and a distinct multiplex electrochemiluminescent immunoassay, I was interested in analyzing RLR and IFN-mediated cytokine secretion upon synchronous 5'ppp-dsRNA stimulation. Interestingly, and in contrast to IFN production, all examined cytokines, i.e., TNF, IL-1β, IL-4, IL-6, and IL-10, exhibited diminished protein levels in IFNR DKO cells compared to wt cells, indicating that the induction of those cytokines is indeed IFN-dependent. The only exception was IL-8, which exhibited a higher protein concentration in IFNR DKO cells 24 hours after stimulation (Supplementary Figure S7).

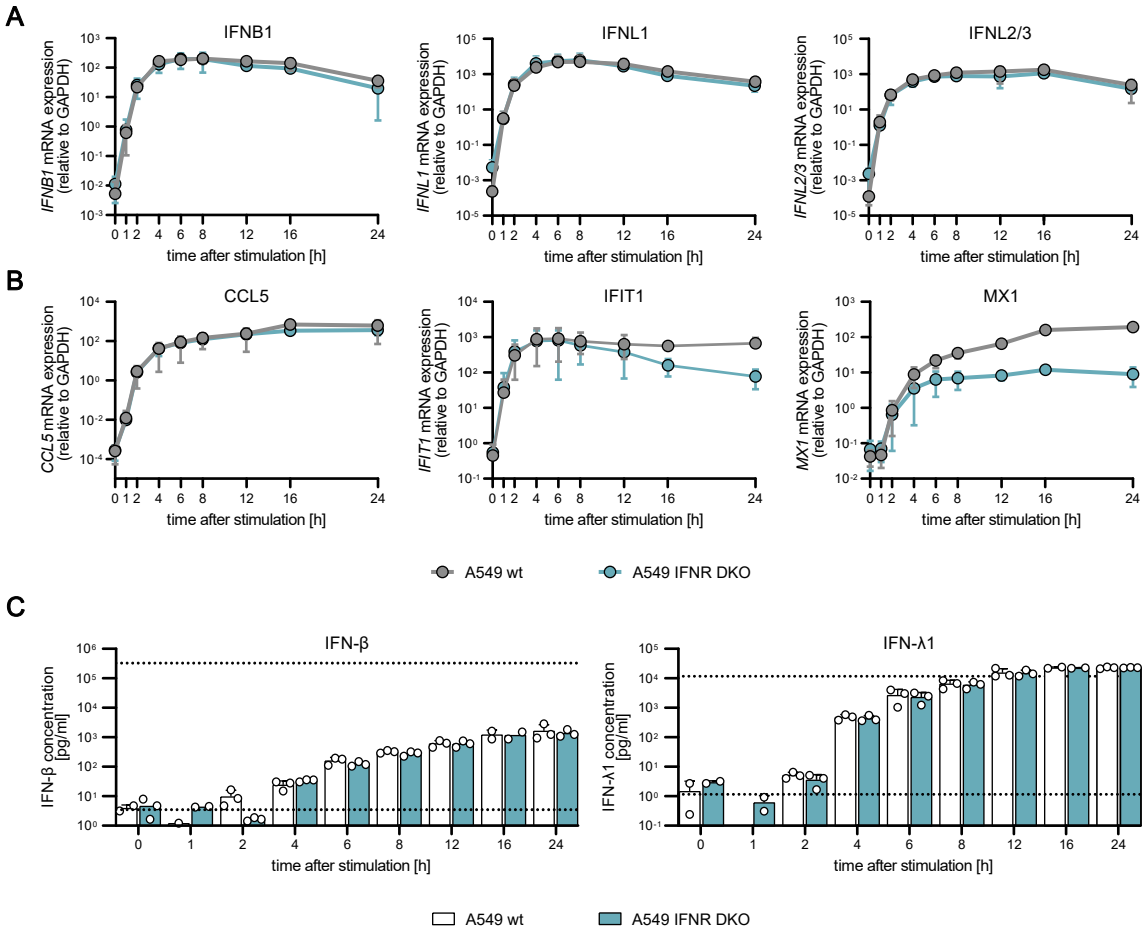

Figure 5: Kinetic characterization of mRNA expression and IFN secretion upon RIG-I stimulation in a type I and III IFN signaling-independent system.

A549 wt cells and an A549 IFNAR1 IFNLR double knockout cell line (IFNR DKO) were electroporated with 220 ng 5'ppp-dsRNA. **(A)** IFNB1, IFNL1, and IFNL2/3 or **(B)** CCL5, IFIT1, and MX1 mRNA expression kinetics were analyzed using qRT-PCR. Values were normalized to the housekeeping gene GAPDH by applying the $2^{-\Delta Ct}$ method [358]. **(C)** Secreted IFN-β and IFN-λ1 protein concentrations in pg/ml were determined using a multiplex immunoassay (U-PLEX IFN Combo, Meso Scale Diagnostics) in supernatants of 5'ppp-dsRNA-stimulated A549 wt and A549 IFNR DKO cells. Dashed lines indicate upper and lower limit of quantification, respectively. Graphs depict (A-B) mean ± SD or (C) individual values ± SD of 3 biologically independent experiments. Subfigures (A-C) were previously published in Burkart *et al.* [353]. Respective RIG-I signaling kinetics upon mock electroporation in A549 wt and IFNR DKO cells are depicted in Supplementary Figure S6A and S6B.

Moreover, using western blot analysis, I further characterized protein activation and expression kinetics in A549 wt (Figure 6A, left panel) and IFNR DKO (Figure 6A, right panel) cells upon synchronous 5'ppp-dsRNA stimulation. Strikingly, although IFNR DKO cells still produced measurable amounts of MX1 mRNA, MX1 protein could not be detected (Figure 6A, right panel), whereas A549 wt cells showed increasing expression from 12 hours onwards (Figure 6A, left panel). Similarly, phosphorylated STAT2, commonly considered as marker for active IFN signaling and ISGF3 formation, was completely absent in IFNR DKO cells, further highlighting the missing ability to respond to IFN in those cells. Apart from that, key components of RLR signaling, such as IRF3 phosphorylation, IkBα degradation, as well as RIG-I protein expression, showed similar kinetic patterns in both A549 wt and IFNR DKO cells.

Whereas analyzing the activation state or general expression kinetics of selected proteins using western blot analysis is easily achieved, I aimed at a broader and unbiased approach to identify kinetic differences in A549 wt and IFN-blind cells. For this, I again synchronously stimulated A549 wt and IFNR DKO cells with 5'ppp-dsRNA, harvested protein samples at 0, 12, and 24 hours after stimulation, and, in collaboration with Christian Urban of the Pichlmair group in Munich, subjected those samples to label-free mass spectrometry. This enabled the identification of differences in basal expression levels of critical proteins in the antiviral signaling pathway as well as differences in antiviral signaling upon 5'ppp-dsRNA stimulation in the presence or absence of IFN feedback. Interestingly, although MDA5 protein expression was completely unaffected by the knockout of both IFN receptors, RIG-I protein expression was significantly reduced in the A549 IFNR DKO cell line 24 hours upon stimulation (Figure 6B). Conversely, MAVS protein expression was diminished in A549 IFNR DKO cells at basal expression level, which persisted over the course of the experimental time frame (Figure 6B). Furthermore, a slight decrease of basal protein expression was detectable for the IKK-β kinase and the transcription factor p65, whereas TBK1 and IRF3 protein expressions were unaffected (Figure 6C). Coherently, as STAT2 phosphorylation was completely absent in A549 IFNR DKO cells (Figure 6A), protein expression 24 hours after 5'ppp-dsRNA stimulation was also clearly impaired in those cells (Figure 6D). Similarly, JAK1 and TYK2 expression kinetics were undistinguishable in both cell lines but the missing IFN feedback led to a significant reduction of STAT1 protein expression 24 hours after 5'ppp-dsRNA stimulation (Figure 6D). In contrast to IFN expression kinetics being similar in both A549 wt and IFNR DKO cells, ISG protein expression was highly affected by the lack of IFN feedback, as seen for CCL5, IFIT1, and MX1 (Figure 6E).

In conclusion, basal protein expression of most antiviral signaling components seemed to be IFN-independent, and although IFN signaling again had no impact on IFN production itself, it considerably affected feedback-induced protein expression of the detected ISGs. Remarkably, since RIG-I protein expression appeared to be slightly affected by the KO of IFN receptors but was clearly upregulated over time (Figure 6B), this indicates that the RIG-I signaling pathway itself might exhibit an IFN-independent feedback regulation through which the pathway reinforces itself.

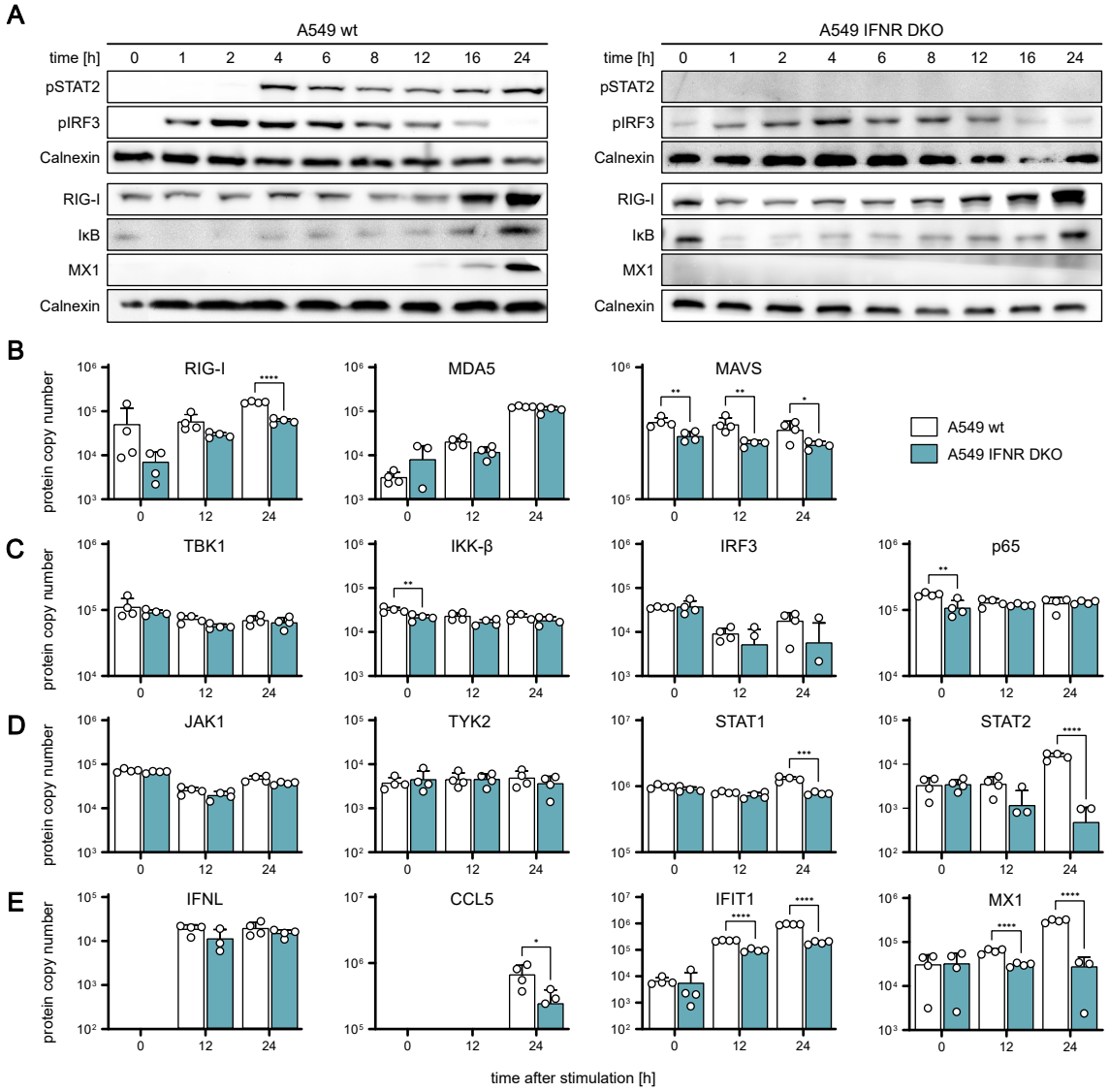

Figure 6: Kinetic characterization of protein abundance and phosphorylation upon RIG-I stimulation in a type I and III IFN signaling-independent system.

A549 wt and A549 IFNR DKO cells were synchronously stimulated with 220 ng 5'ppp-dsRNA using electroporation. **(A)** Protein abundance and phosphorylation status of key signaling components were kinetically characterized in A549 wt and A549 IFNR DKO cells using western blot analysis. (B-E) Protein abundance of key RIG-I signaling components in A549 wt and A549 IFNR DKO cells upon synchronous 5'ppp-dsRNA stimulation for 0, 12, and 24 hours using mass spectrometry. Protein copy numbers of **(B)** sensors, **(C)** the adapter protein MAVS, **(D)** kinases, and **(E)** transcription factors of RIG-I signaling. Protein copy numbers of **(F)** kinases, and **(G)** transcription factors of IFN signaling. **(H)** Protein copy numbers of common ISGs. Graphs depict (A) representative blots of 2 biologically independent experiments or (B-E) individual values ± SD of 4 biologically independent experiments. Statistical significance was determined with Student's t-test (****: $p < 0.0001$, ***: $p < 0.001$, **: $p < 0.01$, *: $p < 0.05$). Subfigure (A) and original data (B-H) was originally published in Burkart *et al.* [353]. Complete lists of detected proteins in both A549 wt and IFNR DKO cells were published previously [353].

4.5 Establishment of an Expanded RIG-I Pathway Model Comprising IFN Feedback

Our established model of the primary, RLR-mediated signaling pathway is capable of accurately predicting the pathway outcome from recognition of viral RNA by RIG-I to transcription of IFN-β by IRF3. However, it does not comprise translation and secretion of IFNs and thus effects of IFN-mediated signaling, which considerably contribute to antiviral signaling responses. Consequently, we combined our core RIG-I signaling model with an ODE-based model of type I IFN-triggered signaling, which was previously established by Maiwald and colleagues [288]. The latter is a detailed model of JAK/STAT signaling upon stimulation with IFN-α. To combine both models, IFN secretion of 5'ppp-dsRNA-stimulated A549 cells (as seen in Figure 5C) was quantified by a former master student, Carola Sparn. This allowed us to link IFN production to the IFN-β mRNA levels and thus establish an input dose for the IFN signaling model.

The combined model encompasses the full cell-intrinsic antiviral defense response, comprising all signaling events from viral dsRNA recognition to the expression of antiviral effector proteins (i.e., ISGs) downstream of IFN signaling. The IFN signaling model introduced 66 additional components, which are engaged in 41 individual reactions (Figure 7A), including the production of antiviral proteins and ISGs downstream of RLR or IFN signaling (Figure 7B). Strikingly, fixing all rate constants to the values determined previously for the RIG-I model or as determined by Maiwald *et al.* for the IFN signaling model [288] and only fitting the newly introduced rate constant, which links the amount of produced IFN to the effective concentration triggering IFNAR signaling, was sufficient to combine both models. Notably, the type I IFN model was established on data from human hepatocarcinoma (Huh7.5) cells, deviating from the RIG-I model, which is based on A549 data. Thus, we updated protein concentrations of JAK/STAT pathway components obtained in A549 wt cells to account for cell type-specific variations in protein expression (Figure 6). In fact, without adjusting any further parameters, the model was able to accurately describe all measured signaling events upon synchronous dsRNA stimulation over the course of the experimental time frame (Figure 7C). For instance, similarly as seen in our core RIG-I model, the combined model accurately predicted phosphorylation of TBK1, IKK-β, and IRF3 as well as the subsequent mRNA and protein expression of IFN-λ and IFIT1. Correspondingly, phosphorylation of STAT2 and expression of antiviral effector proteins, such as MX1, could be reproducibly quantified experimentally and precisely predicted by the model (Figure 7C).

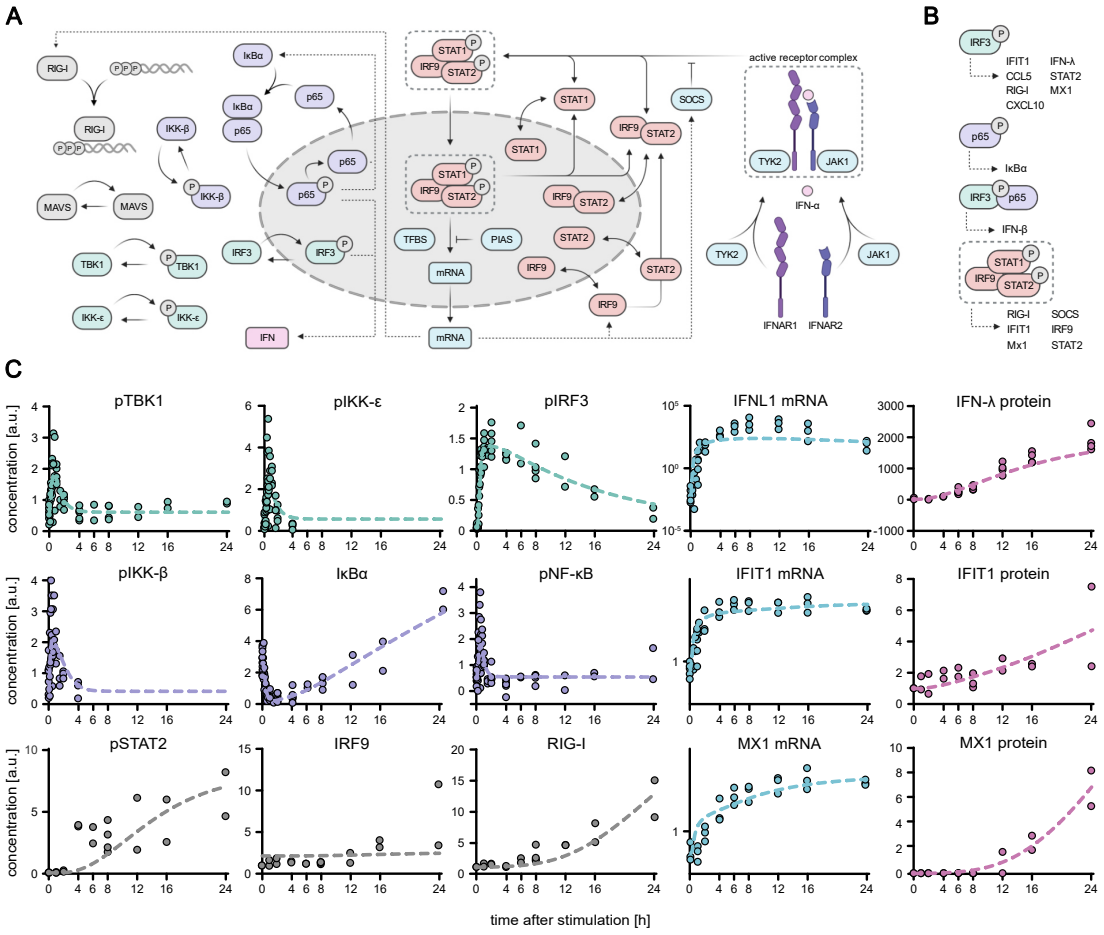

Figure 7: Establishment of a dynamic pathway model of the antiviral response system by coupling core RIG-I model to model of IFN signaling.

Previously obtained data comprising quantitative mRNA expression, protein phosphorylation, and protein abundance of synchronously stimulated A549 cells was utilized to extend the core RIG-I model and include IFN signaling. **(A)** Schematic depiction of the established RIG-I signaling model coupled to a previously published mathematical model of IFN and JAK/STAT signaling [288]. **(B)** Gene expression outcome for different transcription factors used in the extended mathematical model. **(C)** Quantitative protein abundance, protein phosphorylation, and mRNA data were used to combine and calibrate the extended model of the full cell-intrinsic antiviral response system. Dots represent quantitative data of 2 biologically independent experiments and lines represent average model fit. Experimental data were obtained in conjunction with Carola Sparn and mathematical modeling was conducted by Darius Schweinoch. Subfigures (A-C) were originally published in Burkart *et al.* [353].

Interestingly, Maiwald *et al.* demonstrated IRF9 to be a rate-limiting component of IFN signaling [288]. Thus, to challenge and validate our combined mathematical model, I experimentally modulated IRF9 protein levels in A549 cells and analyzed the outcome of antiviral signaling upon 5'ppp-dsRNA stimulation. Surprisingly, IRF9 appeared not to be limiting in our A549 IRF9 overexpression cell line, since no major kinetic differences in IFNB1 or IFIT1 mRNA expression compared to A549 wt cells were apparent upon synchronous 5'ppp-dsRNA stimulation (Supplementary Figure S8).
Consequently, I utilized an A549 IRF9 KO cell line [287] and reintroduced IRF9 expression from the weak murine promoter ROSA26 (ROSA26-IRF9) by lentiviral transduction (Supplementary Figure S3B). I electroporated A549 wt, A549 IRF9 KO, and A549 IRF9 KO ROSA26-IRF9 cells with 5'ppp-dsRNA and measured mRNA expression (Figure 8A) as well as protein phosphorylation and expression (Figure 8B) over time. Similarly as seen in the A549 IFNR DKO cell line previously (Figure 5A), IFNB1 mRNA expression was not affected by IRF9 modulation and thus exclusively induced by RLR-mediated signaling. IFIT1 mRNA expression, however, was slightly impaired at later time points (Figure 8A). In contrast, MX1 was considerably impacted by diminished IRF9 levels (Figure 8A). In fact, this was also resembled in western blot analysis, where MX1 protein could not be detected in A549 IRF9 KO cells. The late, IFN-dependent expression of IFIT1 and RIG-I as well as phosphorylation of STAT2, were also affected by the knockout of IRF9 (Figure 8B). Strikingly, the combined model of the full antiviral system was able to correctly predict the measured outcome of this experimental perturbation of the IFN signaling system (Figure 8C).

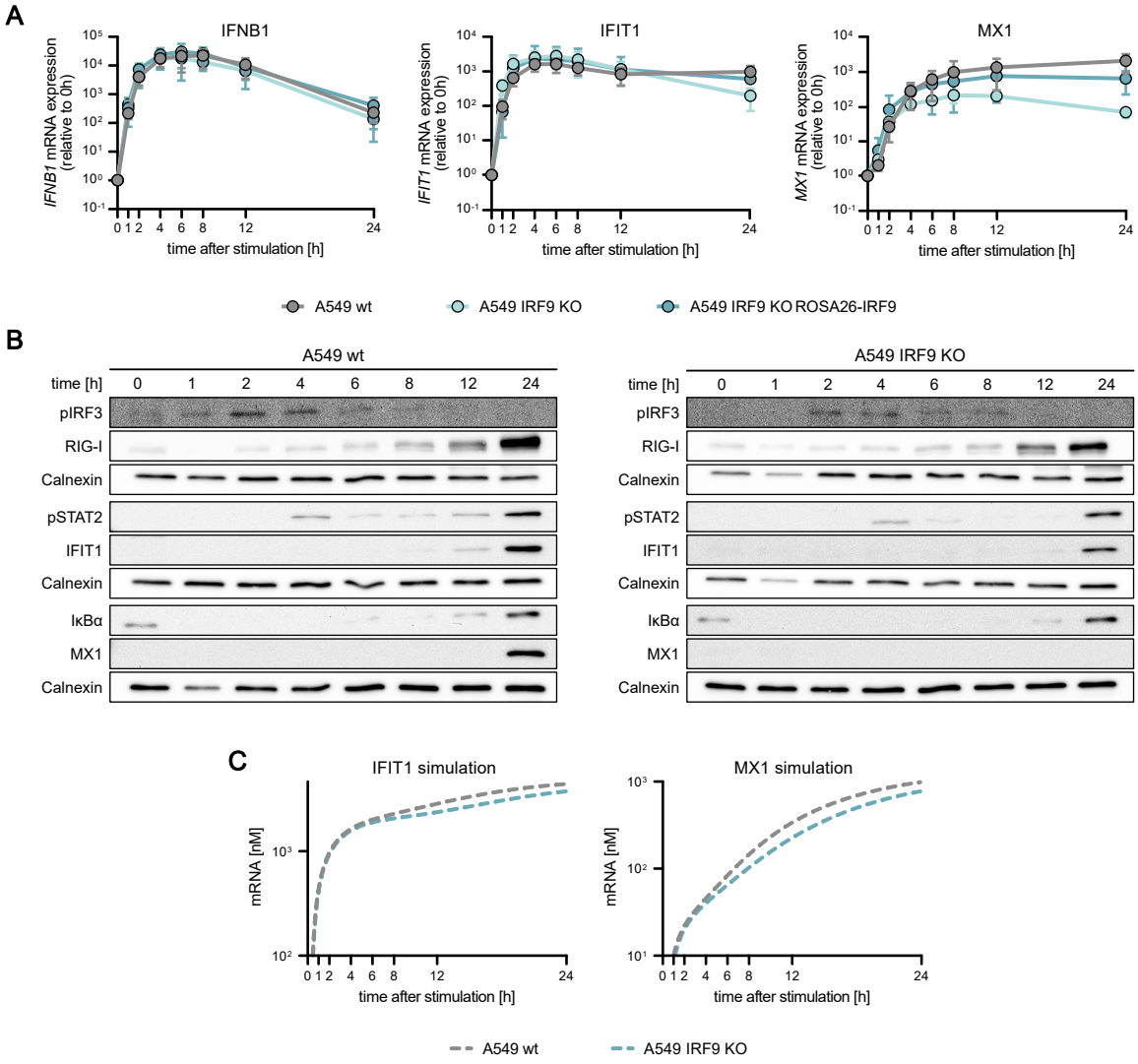

Figure 8: Validating the combined model of antiviral signaling by experimentally modifying IRF9 protein level.

(A) IFNB1, IFIT1, and MX1 mRNA expression kinetics upon 5'ppp-dsRNA electroporation was analyzed in A549 wt, A549 IRF9 KO, and A549 ROSA26-IRF9 (A549 IRF9 KO ROSA26-IRF9)-expressing cells. Values were normalized to the housekeeping gene GAPDH, and the 0 hour time point using $2^{-\Delta\Delta Ct}$ [358]. **(B)** Protein abundance and phosphorylation status of relevant pathway components of RIG-I and IFN signaling were analyzed upon 5'ppp-dsRNA electroporation of A549 wt and A549 IRF9 KO cells using western blot analysis. **(C)** Model simulation of IFIT1 and MX1 mRNA upon varying IRF9 protein levels. Graphs depict (A) mean ± SD of 3 biologically independent experiments or (B-C) representative blots. Subfigures (A, C) were originally published in Burkart *et al.* [353].

4.6 Antiviral Signaling Dynamics Can Be Accurately Modelled in Different Cell Lines

Innate immune signaling pathways are described as being evolutionarily conserved across different animals and cell types [5]. Since model establishment was exclusively based on A549 cells, I further aimed at testing the model's potential to be adapted to cell types it was not trained for. For this purpose, I employed the hepatocellular carcinoma cell line HepG2, performed synchronous 5'ppp-dsRNA stimulations of both A549 and HepG2 cells, and examined mRNA as well as protein expression dynamics (Figure 9A, B). Interestingly, IFIT1 and CCL5 mRNA expression kinetics were identical in both cell lines. The expression of IFNB1, IFNL1, RIG-I, and MX1 mRNA, however, was considerably diminished in HepG2 directly upon 5'ppp-dsRNA stimulation (Figure 9A, B). Correspondingly, IFN-dependent signaling, i.e., STAT2 phosphorylation as well as subsequent RIG-I and MX1 protein expression were clearly affected and reduced in HepG2 cells (Figure 9C). Surprisingly, although IFIT1 mRNA expression kinetics (Figure 9A) was similar in both cell lines, protein expression was decreased in HepG2 (Figure 9C). Notably, I could not detect phosphorylation of IRF3 in HepG2 cells, however, the reason for this remains to be investigated. In line with this, IFN-β and IFN-λ1 protein concentrations measured in supernatants of 5'ppp-dsRNA-stimulated A549 and HepG2 cells using a multiplex electrochemiluminescent immunoassay, which appeared by far more sensitive than standard ELISA measurements (Supplementary Figure S9), also demonstrated a reduction in HepG2 (Figure 9D).

Furthermore, apart from IFNs, I examined the production and secretion dynamics of additional cytokines in A549 and HepG2 supernatants upon synchronous 5'ppp-dsRNA stimulation. In accordance with the reduced IFN production in HepG2, measured cytokines in those cells were strongly reduced compared to A549 cells (IL-1β, IL-4, IL-8, and IL-10) or even absent (IL-6), although surprisingly, HepG2 produced a comparable level of TNF (Supplementary Figure S10).

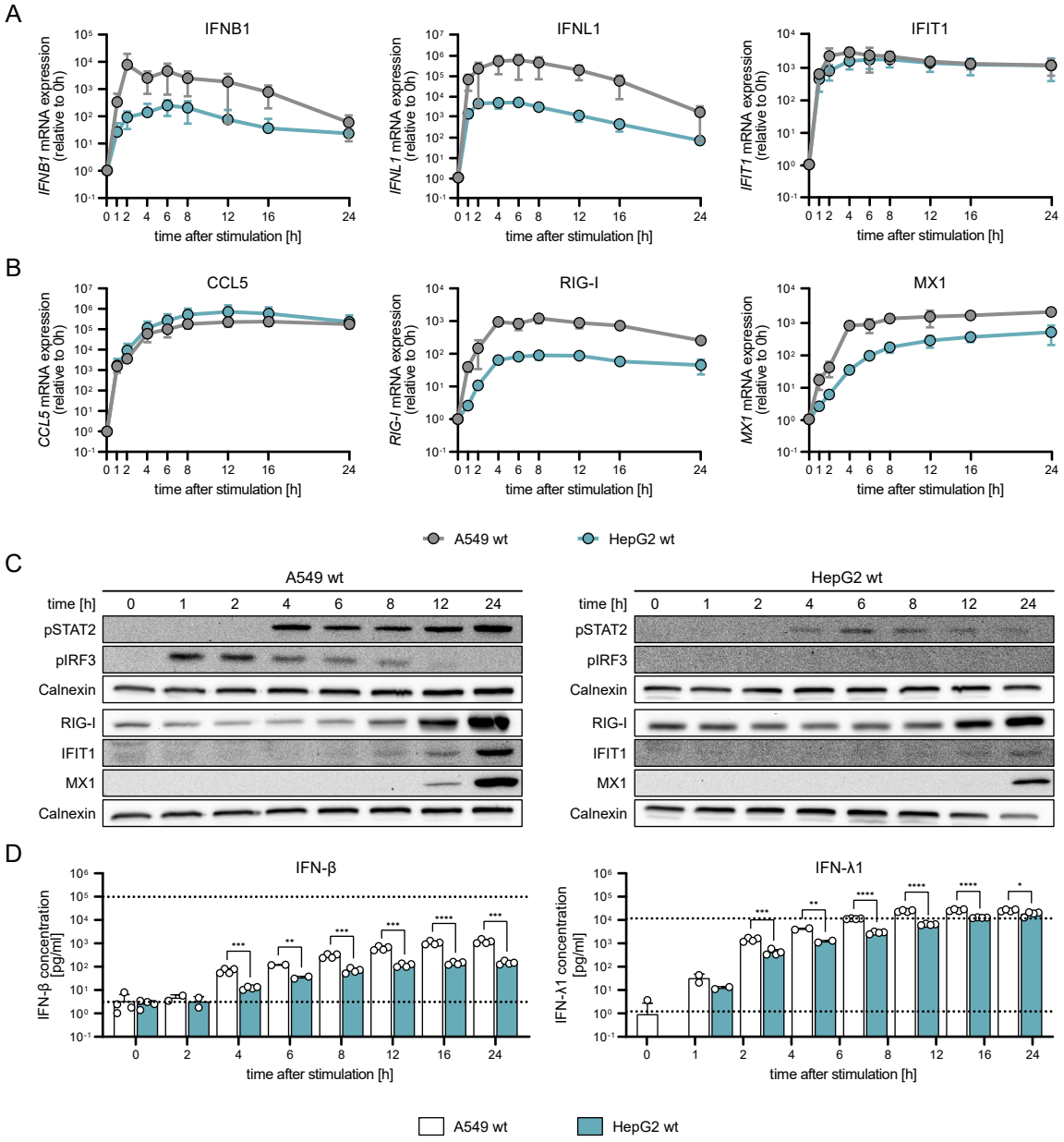

Figure 9: Kinetic characterization of RIG-I signaling upon synchronous 5'ppp-dsRNA stimulation in A549 and HepG2 cells.

A549 and HepG2 wt cells were electroporated with 220 ng 5'ppp-dsRNA. **(A)** IFNB1, IFNL1, IFIT1, and **(B)** CCL5, RIG-I, MX1 mRNA expression kinetics in A549 wt and HepG2 wt cells was analyzed using qRT-PCR. Values were normalized to the housekeeping gene GAPDH, and the 0 hour time point using $2^{-\Delta\Delta Ct}$ [358]. **(C)** Quantitative protein abundance and protein phosphorylation upon 5'ppp-dsRNA electroporation in A549 wt and HepG2 wt cells was examined using western blot analysis. **(D)** Secreted IFN-β and IFN-λ1 concentrations were determined using a multiplex immunoassay (U-PLEX IFN Combo, Meso Scale Diagnostics) in supernatants of 5'ppp-dsRNA-stimulated A549 wt and HepG2 wt cells. Dashed lines indicate upper and lower limit of quantification, respectively. Graphs depict (A, B) mean ± SD of 3, (C) representative blots, or (D) individual values ± SD of 4 biologically independent experiments. Statistical significance was determined with Student's t-test (****: $p < 0.0001$, ***: $p < 0.001$, **: $p < 0.01$, *: $p < 0.05$). Subfigures (A-D) were originally published in Burkart *et al.* [353].

To adapt the combined model of antiviral signaling to the new cell line I acquired quantitative full proteome data of naïve HepG2 cells using label-free mass spectrometry [353]. Examining basal protein concentrations of key signaling components revealed lower levels of MAVS protein, the kinases TBK1 and IKK-β, as well as the transcription factors p65 and IRF3 in HepG2 compared to A549 (Figure 10A). Surprisingly, IFN signaling components, such as JAK1 and STAT1, were reduced in HepG2 as well, whereas basal STAT2 protein levels seemed to be increased compared to A549 cells. Furthermore, basal protein levels of the RNA sensors RIG-I and MDA5 were identical in both cell lines (Figure 10A). Strikingly, adjusting solely the obtained initial protein concentrations in the combined model without changing any kinetic rate constants sufficed to accurately simulate mRNA kinetics of IFNB1, IFIT1, and MX1 (Figure 10B) in HepG2 cells. Taken together, these results emphasize the potential of this combined mathematical model to be adapted to different cell lines by only adjusting steady state protein levels of essential signaling components, further corroborating the notion that cell-intrinsic antiviral innate immune responses are highly conserved systems.

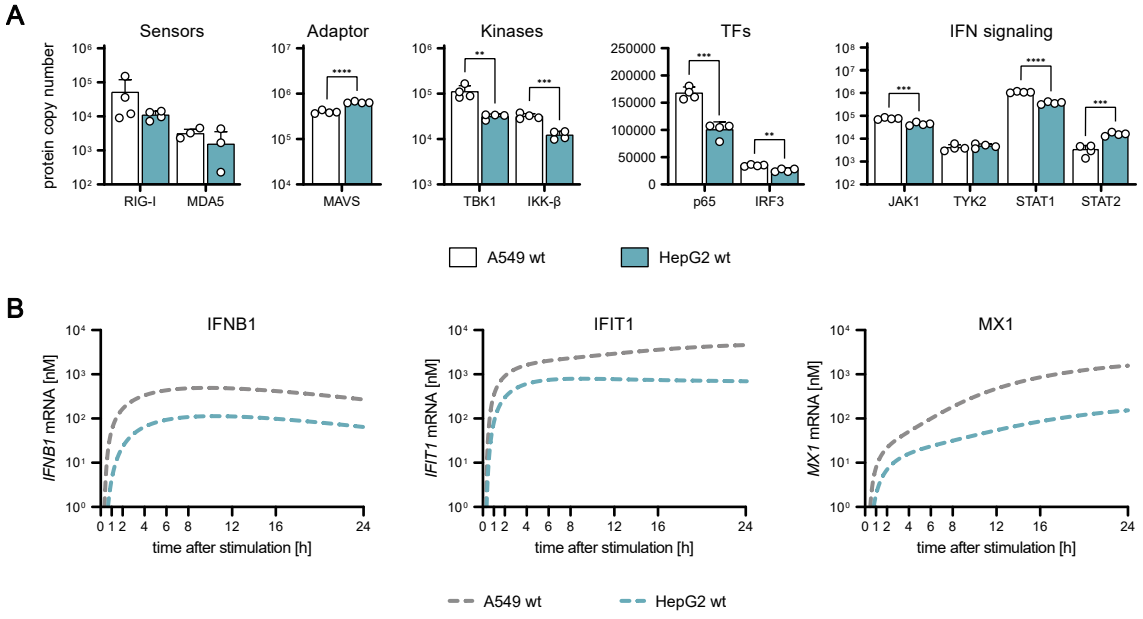

Figure 10: Determination of basal protein abundance in A549 and HepG2 cells using label-free mass spectrometry to utilize as input for model simulations.

(A) Basal protein abundance of key RIG-I signaling components in A549 and HepG2 wt cells using label-free mass spectrometry. Depicted are protein copy numbers of sensors, the adapter protein MAVS, kinases, transcription factors of RIG-I signaling, and IFN signaling components. **(B)** Model simulation for IFNB1, IFIT1, and MX1 mRNA expression upon synchronous dsRNA stimulation of A549 and HepG2 wt cells. Graph (A) depicts individual values ± SD of 4 biologically independent experiments. Statistical significance was determined with Student's t-test (****: $p < 0.0001$, ***: $p < 0.001$, **: $p < 0.01$, *: $p < 0.05$). Subfigure (B) and original data of (A) were originally published in Burkart *et al.* [353].

4.7 The Impact of Viral Antagonists on Antiviral Signaling Dynamics Can Be Accurately Simulated by the Established Mathematical Model

Most viruses have evolved sophisticated strategies to evade or interrupt innate immune recognition and defense. Upon viral infections, kinetics and magnitude of the antiviral response define the outcome of an infection. However, viruses developed powerful antagonists capable of perturbing host cellular antiviral responses (Section 1.7). Surprisingly, many studies examining viral antagonists disregard the gradual increase of viral protein concentrations in natural infections and mostly focus on the degree of inhibition at fixed time points. Depending on the exact target in the antiviral system, viral perturbance may lead to a delay of the IFN response rather than an overall reduction of its amplitude. To better understand these virus-host interactions it is therefore important to examine viral immune antagonism at a dynamic level.

The previously described mathematical model of the antiviral signaling pathway might provide a powerful tool for studying the kinetic impact of viral antagonists on, e.g., ISG induction. Therefore, I selected several well-described viral proteins with different strategies to impede antiviral signaling: NS3/4A of HCV proteolytically cleaves and thus inactivates MAVS [326], N^{pro} of CSFV induces the proteolytic degradation of IRF3 [321, 366], NS5 of DENV is described to target STAT2 for degradation [332, 333], and NS1 of IAV binds dsRNA with its N-terminal RNA-binding domain [367, 368]. Additionally, ORF6 of the recently emerged SARS-CoV-2 was described to affect both IFN induction and IFN signaling [369] by blocking nuclear translocation of IRF3 [341, 342], STAT1, and STAT2 [344]. Hence, whereas NS3/4A, N^{pro}, and NS1 target RLR signaling and thus IFN induction, NS5 blocks JAK/STAT signaling downstream of the IFN receptors. In contrast, ORF6 targets both RLR and IFN-mediated antiviral signaling responses.

Using lentiviral transduction, I generated A549 cells stably expressing each of the above-mentioned viral antagonists and examined the effect of their expression on regular cell proliferation using live-cell imaging. Except for the A549 ORF6 cell line, exhibiting a slightly diminished cell proliferation rate (Supplementary Figure S11B), all cell lines expressing the distinct viral proteins displayed a comparable proliferation behavior as compared to wt cells (Supplementary Figure S11A, S11C). To obtain a negative control for the NS3/4A-expressing A549 cell line, I additionally generated A549 cells stably expressing a catalytically inactive version of the HCV protease, NS3/4A S139A, harboring a serine to alanine mutation at position 139. In order to modulate the amount of active kinase and thereby mimic the effect of decreasing NS3/4A abundance, I further titrated a pharmacological compound (Simeprevir) described to specifically inhibit NS3/4A protease activity [370, 371]. In contrast to traditionally used inhibitors, such as Telaprevir or Boceprevir, Simeprevir showed an at least 10-fold lower half maximal inhibitory concentration (IC50, Supplementary Figure S12, [372]). I synchronously stimulated A549 NS3/4A wt (± Simeprevir) and A549 NS3/4A S139A cells with 5'ppp-dsRNA and assessed mRNA as well as protein

expression kinetics (Figure 11A). Analyzing IFIT1 mRNA kinetics over the course of 24 hours revealed a substantial mRNA reduction in A549 NS3/4A cells not receiving any inhibitor treatment (Figure 11B), which might be attributed to the very efficient cleavage of MAVS by NS3/4A (Figure 11C). Notably, albeit hardly detectable in western blot, a certain level of MAVS seemed to resist NS3/4A cleavage (Figure 11C) resulting in remaining induction of IFIT1 expression (Figure 11B). Nonetheless, increasing protease inhibitor concentrations dose-dependently decreased NS3/4A activity and thus lead to increasing amounts of intact MAVS protein (Figure 11C). Likewise, increasing concentrations of Simeprevir restored IFIT1 expression to the level observed in the catalytically inactive NS3/4A S139A control (Figure 11B). The strong effect of increasing NS3/4A activity dampening IFIT1 mRNA expression was less pronounced at later time points (12 and 24 hours), however, the overall kinetics of induction was not affected. Strikingly, our mathematical model was able to simulate the observed IFIT1 induction kinetics when MAVS level were systematically reduced (Figure 11D), emphasizing the usability of the modeling approach to investigate viral immune evasion.

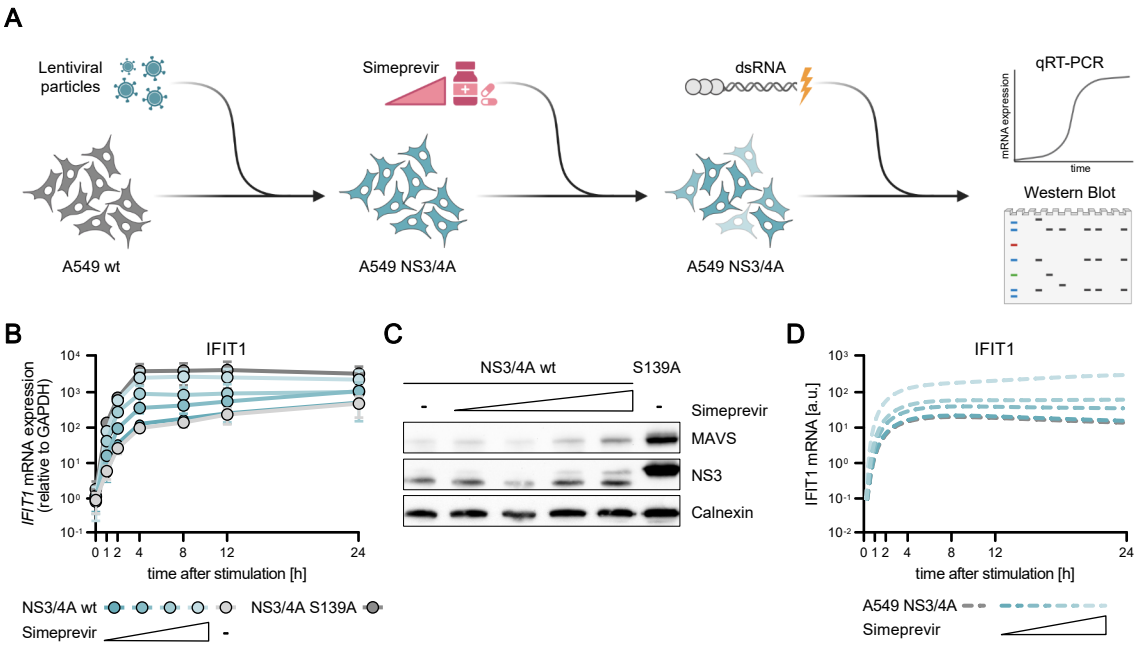

Figure 11: Influence of the HCV protease NS3/4A on RIG-I signaling dynamics in A549 cells.

(A) Schematic depiction of the experimental setup. A549 cells stably expressing the viral protein NS3/4A of HCV or a catalytically inactive version (NS3/4A S139A) were generated using lentiviral transduction. The protease inhibitor Simeprevir was used in increasing concentrations to gradually restore NS3/4A protease activity. Cells were then stimulated with 220 ng 5'ppp-dsRNA by electroporation and mRNA expression as well as protein abundance was examined. **(B)** IFIT1 mRNA expression kinetics as well as **(C)** NS3 and MAVS protein levels were analyzed in A549 NS3/4A wt and A549 NS3/4A S139A overexpression cell lines in the presence of varying levels of Simeprevir. **(D)** Model simulation of IFIT1 mRNA kinetics for varying MAVS protein levels. Graphs depict mean ± SD (B) or representative blot (C) of 3 biologically independent experiments. qRT-PCR values were normalized to the housekeeping gene GAPDH using the $2^{-\Delta Ct}$ method [358]. Subfigures (B-D) were originally published in Burkart *et al.* [353].

In a next step, using lentiviral transduction, I generated A549 cells stably expressing varying levels of the CSFV protein N^{pro}, which targets IRF3 for degradation [321, 366]. I synchronously stimulated A549 wt, A549 IRF3 KO, and A549 N^{pro}-expressing cells with 5'ppp-dsRNA and assessed mRNA and protein expression kinetics (Figure 12A). Analyzing N^{pro} mRNA and protein expression in unstimulated conditions demonstrated a gradual increase of N^{pro} level (Figure 12B, C) in addition to a very effective IRF3 degradation capacity (Figure 12B). Here, IRF3 protein was no longer detectable in the second lowest N^{pro}-expressing cell line. Consequently, upon synchronous 5'ppp-dsRNA stimulation I observed a near complete inhibition of IFIT1 induction for the cell line expressing the highest N^{pro} level, almost reaching the level of the A549 IRF3 KO cell line. However, decreasing level of the viral protein resulted in a dose-dependent recovery of IFIT1 induction (Figure 12D). Surprisingly, in contrast to NS3/4A, N^{pro} strongly inhibited particularly the early expression of IFIT1 up to 8 hours post stimulation, although N^{pro} similarly to the HCV protease targets the RLR cascade upstream of IFN expression (Figure 12D). Notably, although not detectable in western blot, again a small portion of IRF3 seemed to withstand N^{pro} expression leading to remaining signaling and induction of IFIT1 expression as compared to A549 IRF3 KO cells (Figure 12D). Gradually reducing IRF3 abundance in our mathematical model simulated the effect of the viral protein N^{pro} and the predicted kinetics of the antiviral response matched our experimental data decently (Figure 12E).

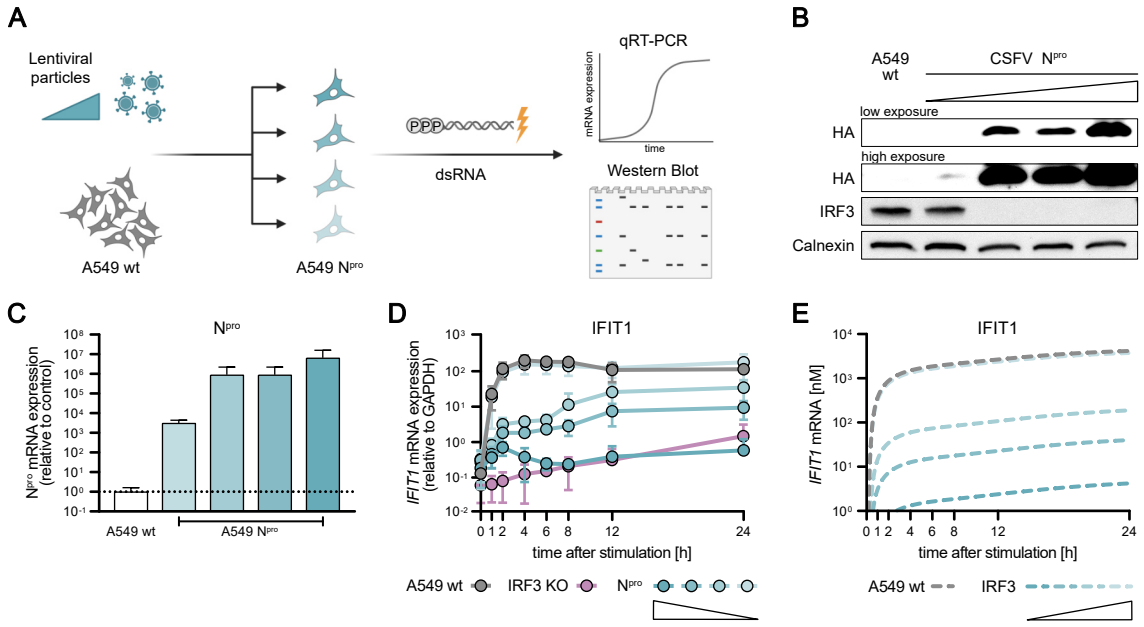

Figure 12: Influence of the CSFV protein N^{pro} on RIG-I signaling dynamics in A549 cells.
(A) Schematic depiction of the experimental setup. A549 cells stably expressing the viral protein N^{pro} of CSFV were generated using lentiviral transduction. Varying protein expression levels of the viral protein were obtained by gradually decreasing lentiviral concentrations. N^{pro}-expressing cells were synchronously stimulated with 5'ppp-dsRNA using electroporation. mRNA kinetics as well as protein abundance were examined using qRT-PCR and western blotting, respectively. **(B)** N^{pro}-HA and IRF3 protein levels were analyzed in unstimulated A549 wt or N^{pro}-expressing cell lines using western blotting. **(C)** N^{pro} mRNA expression in A549 cells stably expressing varying level of CSFV N^{pro} was analyzed using qRT-PCR. **(D)** IFIT1 mRNA expression kinetics in A549 wt, IRF3 KO cells, and cells expressing different levels of HA-tagged N^{pro} upon synchronous stimulation with 220 ng 5'ppp-dsRNA was analyzed using qRT-PCR. **(E)** Model simulation of IFIT1 mRNA kinetics upon decreasing IRF3 protein levels. qRT-PCR values were normalized to the housekeeping gene GAPDH using the $2^{-\Delta Ct}$ method [358] (D) or additionally normalized to the control cell line A549 wt (C). Graphs depict mean ± SD (C, D) or representative blot (B) of 3 biologically independent experiments. Subfigures (B-E) were originally published in Burkart *et al.* [353].

NS5 of DENV affects signaling downstream of the IFN receptors by targeting STAT2 for degradation [332, 333]. Using lentiviral transduction, I generated A549 cells stably expressing varying levels of the DENV protein NS5, synchronously stimulated those cells with 5'ppp-dsRNA, and assessed mRNA and protein expression kinetics (Figure 13A). Analyzing NS5 mRNA and protein expression in unstimulated conditions demonstrated a gradual increase of NS5 level (Figure 13B, D) in addition to a modest STAT2 degradation ability (Figure 13D). Specifically, even the highest concentration of NS5 was incapable of completely degrading STAT2. STAT1 and IRF3 protein expression, however, were unaffected by NS5 expression (Figure 13D). Aiming at analyzing the competence of NS5-expressing cells to still signal via the JAK/STAT pathway, I stimulated A549 wt as well as A549 NS5-expressing cells with IFN and measured IFIT1 mRNA expression over time (Figure 13C). A549 wt cells produced substantial amounts of IFIT1 upon IFN stimulation, whereas A549 NS5-expressing cell lines were essentially IFN signaling incompetent. Only the cell line expressing the lowest NS5 level was able to produce a small amount of IFIT1 at the earliest measured time point (Figure 13C). Intriguingly, examining IFIT1 mRNA expression upon synchronous 5'ppp-dsRNA stimulation revealed an impaired IFIT1 expression not only at late time points when its expression is driven by IFN-induced signaling, but already at the earliest measured time point (Figure 13E). In addition, I analyzed the impact of STAT1 and STAT2 KO on IFIT1 mRNA kinetics upon synchronous 5'ppp-dsRNA stimulation and, surprisingly, observed a different dynamic pattern as compared to NS5-expressing cells (Figure 13F). Here, IFIT1 mRNA expression was unaffected in the RLR-driven phase up to 6 hours after stimulation, but clearly impaired at later time points. In fact, our model was able to simulate a similar kinetic pattern of IFIT1 induction under conditions of reduced STAT2 availability (Figure 13G). In conclusion, these results indicate that DENV NS5 might additionally impede the early stages of the antiviral response which has not been widely appreciated before.

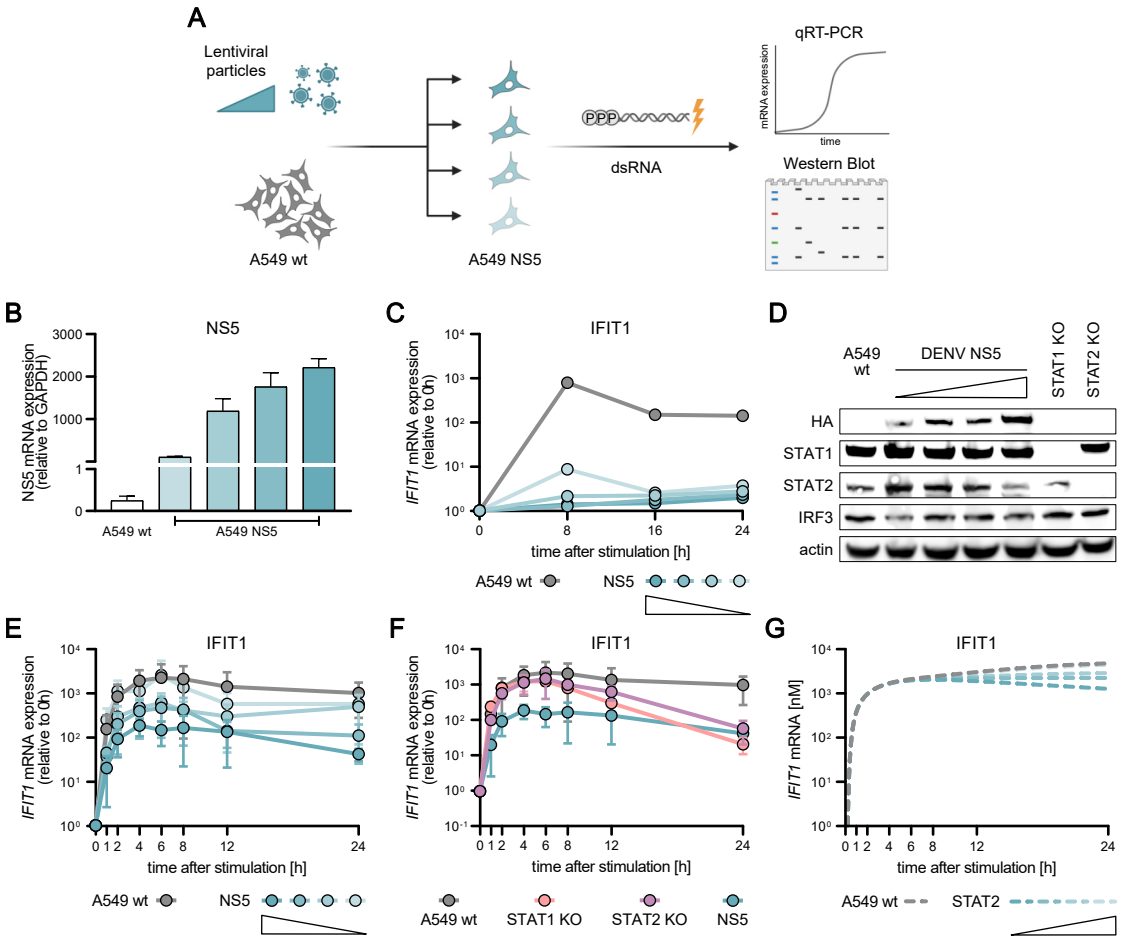

Figure 13: Influence of the DENV protein NS5 on RIG-I signaling dynamics in A549 cells.
(A) Schematic depiction of the experimental setup. A549 cells stably expressing the viral protein NS5 of DENV were generated using lentiviral transduction. Varying protein expression levels of the viral protein were obtained by gradually decreasing lentiviral concentrations. NS5 expressing cells were synchronously stimulated with 5'ppp-dsRNA using electroporation and mRNA kinetics as well as protein abundance were examined using qRT-PCR and western blotting, respectively. **(B)** NS5 mRNA expression in A549 cells stably expressing varying level of DENV NS5 was analyzed using qRT-PCR. **(C)** Using qRT-PCR, IFIT1 mRNA expression in A549 wt cells and cells stably expressing NS5 upon stimulation with 200 IU IFN-β for 16 hours was analyzed. **(D)** NS5-HA, STAT1, STAT2, and IRF3 protein levels were examined in A549 wt, STAT1 KO, STAT2 KO, and NS5-expressing cell lines using western blot analysis. **(E)** IFIT1 mRNA expression kinetics in A549 wt cells and cells expressing different levels of HA-tagged DENV NS5 upon synchronous stimulation with 220 ng 5'ppp-dsRNA was analyzed using qRT-PCR. **(F)** IFIT1 mRNA expression kinetics in A549 wt, A549 NS5-HA, A549 STAT1 KO, and A549 STAT2 KO cells upon synchronous stimulation with 220 ng 5'ppp-dsRNA was examined using qRT-PCR. **(G)** Model simulation of IFIT1 mRNA kinetics upon decreasing STAT2 protein levels. qRT-PCR values were normalized (C, E-F) to the housekeeping gene GAPDH and the 0 hour time point, or (B) to the housekeeping gene GAPDH and the control cell line A549 wt using $2^{-\Delta\Delta Ct}$ [358]. Graphs depict mean ± SD (C, E-F) or representative blot (D) of 3 biologically independent experiments. Subfigures (D-G) were originally published in Burkart *et al.* [353].

In contrast to the previously described viral proteins, the NS1 protein of IAV pursues a different antagonistic strategy. Whereas many viral antagonists directly bind and mark their target for proteasomal degradation, NS1 was reported to sequester dsRNA, thus preventing access of host dsRNA sensors during viral replication [318, 367, 368]. Using lentiviral transduction, I generated A549 cells stably expressing IAV NS1, confirmed its expression by qRT-PCR and western blot analysis (Figure 14A), and, subsequently synchronously stimulated A549 wt and NS1-expressing cells with 5'ppp-dsRNA. Surprisingly, examining IFIT1 mRNA expression revealed an unaffected kinetic pattern in A549 cells expressing the viral antagonist, despite the high NS1 protein expression in those cells (Figure 14B). Ensuring that this effect was not due to a 5'ppp-dsRNA overload during synchronous electroporation, I gradually reduced the amount of dsRNA used during synchronous stimulation and reassessed IFIT1 mRNA kinetics (Figure 14C-F). Nonetheless, even with a very low amount of 5'ppp-dsRNA, IFIT1 mRNA kinetics was still unaffected by the expression of NS1 (Figure 14F). Aiming at assessing the impact of NS1 expression on RLR signaling in A549 cells upon different stimulation approaches including viral infection, I performed an IFN-β promoter luciferase assay (Figure 14G). Again, 5'ppp-dsRNA stimulation resulted in an unimpaired IFN-β luciferase response as compared to A549 wt cells, whereas poly(I:C), a synthetic RLR agonist, as well as SeV infection yielded reduced IFN-β luciferase signals (Figure 14G). This suggested that the expressed NS1 protein was functional in our A549 cell line, to a small extent interfering with RLR signaling upon, e.g., viral infection, however, not affecting IFIT1 mRNA expression upon synchronous 5'ppp-dsRNA stimulation. Strikingly, reducing dsRNA abundance in our mathematical model and thus simulating the described effect of the viral protein NS1 resulted in IFIT1 mRNA kinetics matching our experimental data (Figure 14H).

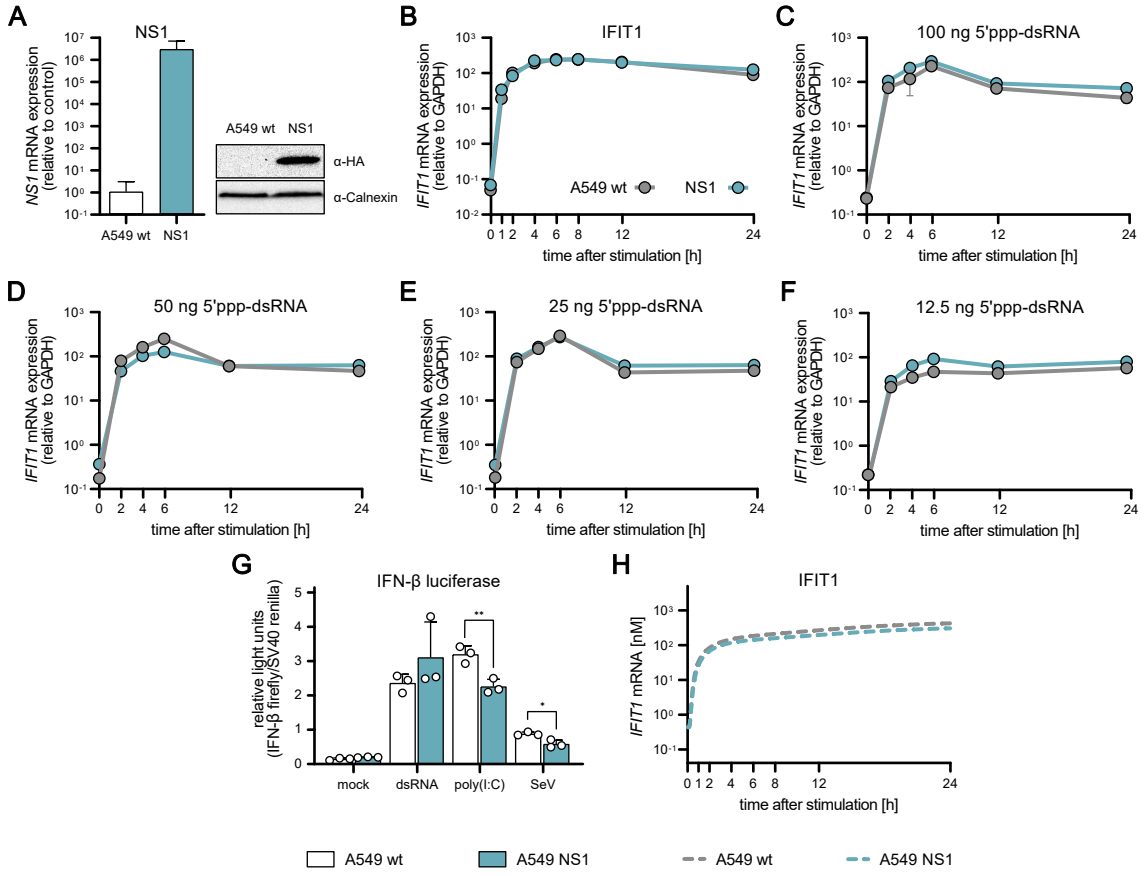

Figure 14: Influence of the IAV protein NS1 on RIG-I signaling dynamics in A549 cells.
(A) IAV NS1 mRNA and protein expression in A549 cells stably expressing the viral antagonist was analyzed using qRT-PCR and western blot analysis, respectively. **(B)** IFIT1 mRNA expression kinetics in A549 wt cells and cells expressing HA-tagged IAV NS1 upon synchronous stimulation with 220 ng 5'ppp-dsRNA was analyzed using qRT-PCR. **(C-F)** IFIT1 mRNA expression kinetics in A549 wt cells and cells expressing HA-tagged IAV NS1 upon synchronous stimulation with (C) 110 ng, (D) 55 ng, (E) 25 ng, and (F) 12.5 ng 5'ppp-dsRNA was analyzed using qRT-PCR. **(G)** IFN-β promoter luciferase signal in A549 wt and A549 NS1-HA cells upon mock stimulation, dsRNA transfection (100 ng), poly(I:C) transfection (100 ng), and SeV infection (MOI = 0.004). **(H)** Model simulation of IFIT1 mRNA kinetics upon varying levels of signaling-competent dsRNA. qRT-PCR values were normalized (B-F) to the housekeeping gene GAPDH or (A) to the housekeeping gene GAPDH and the control cell line A549 wt. IFN-β Firefly luciferase values were normalized to SV40 Renilla luciferase for each measurement. Graphs depict mean ± SD (B-F) of 3 biologically independent experiments. Statistical significance was determined with Student's t-test (**: $p < 0.01$, *: $p < 0.05$).

Lastly, I investigated the impact of the SARS-CoV-2 protein ORF6, which was demonstrated to affect both IFN induction and IFN signaling [369] by blocking nuclear translocation of IRF3 [341,342], STAT1, and STAT2 [344]. I generated A549 cells stably expressing ORF6 and confirmed its expression by qRT-PCR (Figure 15A). Subsequently, I either infected A549 wt and ORF6-expressing cells with SeV and assessed IFIT1 and IFN-β luciferase signals (Figure 15B, D), or synchronously stimulated them with 5'ppp-dsRNA and examined IFIT1 and IFNB1 mRNA expression kinetics (Figure 15C, E). Surprisingly, even though the production of IFIT1 and IFN-β luciferase upon SeV infection was significantly affected in ORF6-expressing cells (Figure 15B, D), ORF6 expression had no impact on IFIT1 and IFNB1 mRNA expression upon 5'ppp-dsRNA electroporation (Figure 15C, E). Although the underlying reason remains elusive, I could observe a different outcome in HepG2 cells. Here, albeit similarly expressed in HepG2 as in A549 cells (Figure 15F, compare to 15A), ORF6 not only significantly reduced IFIT1 and IFN-β luciferase production upon SeV infection (Figure 15G, I) but also affected IFIT1 and IFNB1 mRNA induction upon 5'ppp-dsRNA stimulation with a slight decrease at early time points but a clear reduction between 8 and 24 hours after stimulation (Figure 15H, J). These results are consistent with model predictions of IFIT1 and IFNB1 mRNA kinetics under conditions of concurrently reduced IRF3 and STAT2 levels (Figure 15K, L).
In conclusion, the established model of the full antiviral system, comprising RLR signaling, IFN induction, and JAK/STAT signaling downstream of the IFN receptors, is able to accurately simulate the activation of individual signaling components, the induction of ISGs, as well as the production of antiviral effector proteins. Consequently, enabling predictions of viral interference with the cell-intrinsic innate response system provides a valuable tool to study the impact of yet unknown viral proteins perturbing host antiviral signaling.

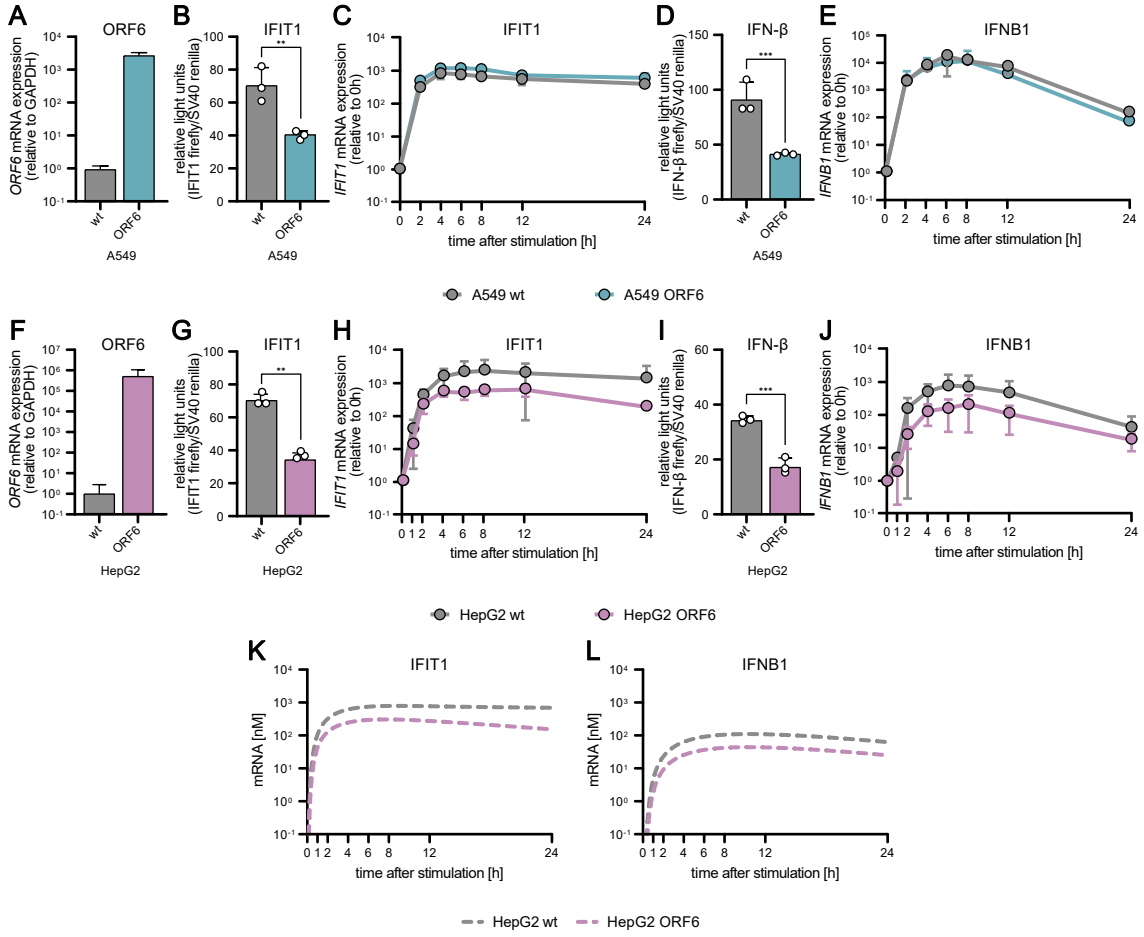

Figure 15: Influence of the SARS-CoV-2 protein ORF6 on RIG-I signaling dynamics in A549 and HepG2 cells.

(A, F) ORF6 mRNA expression in A549/HepG2 wt cells and cells stably expressing SARS-CoV-2 ORF6 was analyzed using qRT-PCR. **(B, G)** A549/HepG2 wt and ORF6-expressing cells were co-transfected with IFIT1 Firefly luciferase and SV40 Renilla luciferase, stimulated with SeV (MOI = 0.004) for 16 hours, and luciferase signals were measured. **(C, H)** IFIT1 mRNA expression kinetics in A549/HepG2 wt cells and cells expressing SARS-CoV-2 ORF6 upon electroporation with 220 ng 5'ppp-dsRNA was analyzed using qRT-PCR. **(D, I)** A549/HepG2 wt and ORF6-expressing cells were co-transfected with IFN-β Firefly luciferase and SV40 Renilla luciferase, stimulated with SeV (MOI = 0.004) for 16 hours, and luciferase signal was measured. **(E, J)** IFNB1 mRNA expression kinetics in A549/HepG2 wt cells and cells expressing SARS-CoV-2 ORF6 upon electroporation with 220 ng 5'ppp-dsRNA was analyzed using qRT-PCR. **(K, L)** Model simulation of (K) IFIT1 (L) and IFNB1 mRNA kinetics upon decreased IRF3 and STAT2 protein levels. qRT-PCR values were normalized to GAPDH and the 0 hour time point (C, E, H, I) or to the housekeeping gene GAPDH and the control cell line (A, F) using $2^{-\Delta\Delta Ct}$ [358]. IFIT1 and IFN-β Firefly luciferase values were normalized to SV40 Renilla luciferase for each measurement and additionally normalized to mock conditions. Graphs depict mean ± SD (C, E, H, J) or individual values ± SD (B, D, G, I) of 3 biologically independent experiments. Statistical significance was determined with Student's t-test (****: $p < 0.0001$, ***: $p < 0.001$, **: $p < 0.01$, *: $p < 0.05$). Subfigures (A, C, E-F, H, I-L) were originally published in Burkart *et al.* 2022 [353].

4.8 The Additional Knockout of IFNGR1 in A549 IFNR DKO Cells Does Not Affect Antiviral Signaling Dynamics Upon Synchronous 5'ppp-dsRNA Stimulation

Although A549 cells express the IFN gamma receptor complex on their cell surface, there is limited evidence for IFN-γ production upon RLR stimulation in those cells. However, they still exhibit the genetic basis for IFN-γ expression and are known to produce the type II IFN upon, e.g., *M. tuberculosis* infection [373]. Consequently, the characterization of an actual IFN-independent RLR signaling response required not only the knockout of the type I and III IFN receptors, but also needed to include a knockout of the type II receptor. Thus, using the CRISPR/Cas9 technique and the previously described A549 IFNR DKO cell line (A549 IFNAR1 IFNLR double KO), I additionally knocked out the receptor for type II IFN (IFNGR1), generating an A549 IFN receptor triple KO (IFNR TKO) cell line (Supplementary Figure S13A, [287]).

Similarly, as done previously with the A549 IFNR DKO cell line (Figure 5, Figure 6A), I synchronously stimulated A549 wt and IFNR TKO cells with 5'ppp-dsRNA and assessed mRNA and protein expression kinetics (Figure 16). Both cell lines displayed similar kinetics of IFNB1, IFNL1, as well as IFNL2/3 mRNA expression, exhibiting a fast onset of IFN induction, reaching peak levels between 4 and 8 hours, and declining again afterwards (Figure 16A). Whereas CCL5 mRNA expression was not affected by the KO of IFN receptors and showed similar kinetics in A549 wt, IFNR DKO (Figure 5), as well as IFNR TKO cell lines, mRNA expression kinetics of the ISGs IFIT1 and MX1 clearly differed between wt and IFNR TKO cells (Figure 16B). Although the initial RLR-induced expression of IFIT1 was still unaffected, the lack of IFN feedback and subsequent secondary upregulation of IFIT1 was clearly visible in the IFNR TKO cell line at 24 hours (Figure 16B, middle panel). Similarly, MX1 induction kinetics did not differ between A549 wt and IFNR TKO cells up to 4 hours but lead to a lower overall induction in cells lacking IFN signaling (Figure 16B, right panel). In addition to characterizing mRNA expression kinetics, I further measured IFN-β and IFN-λ1 protein secretion in A549 wt and IFNR TKO cells upon synchronous 5'ppp-dsRNA stimulation using a multiplex electrochemiluminescent immunoassay. Matching mRNA kinetics (Figure 16A), IFN secretion was not affected in the IFNR TKO cell line and initial IFN-β as well as IFN-λ1 protein was detected between 2 and 4 hours after stimulation, increasing continuously over the next hours (Figure 16C).

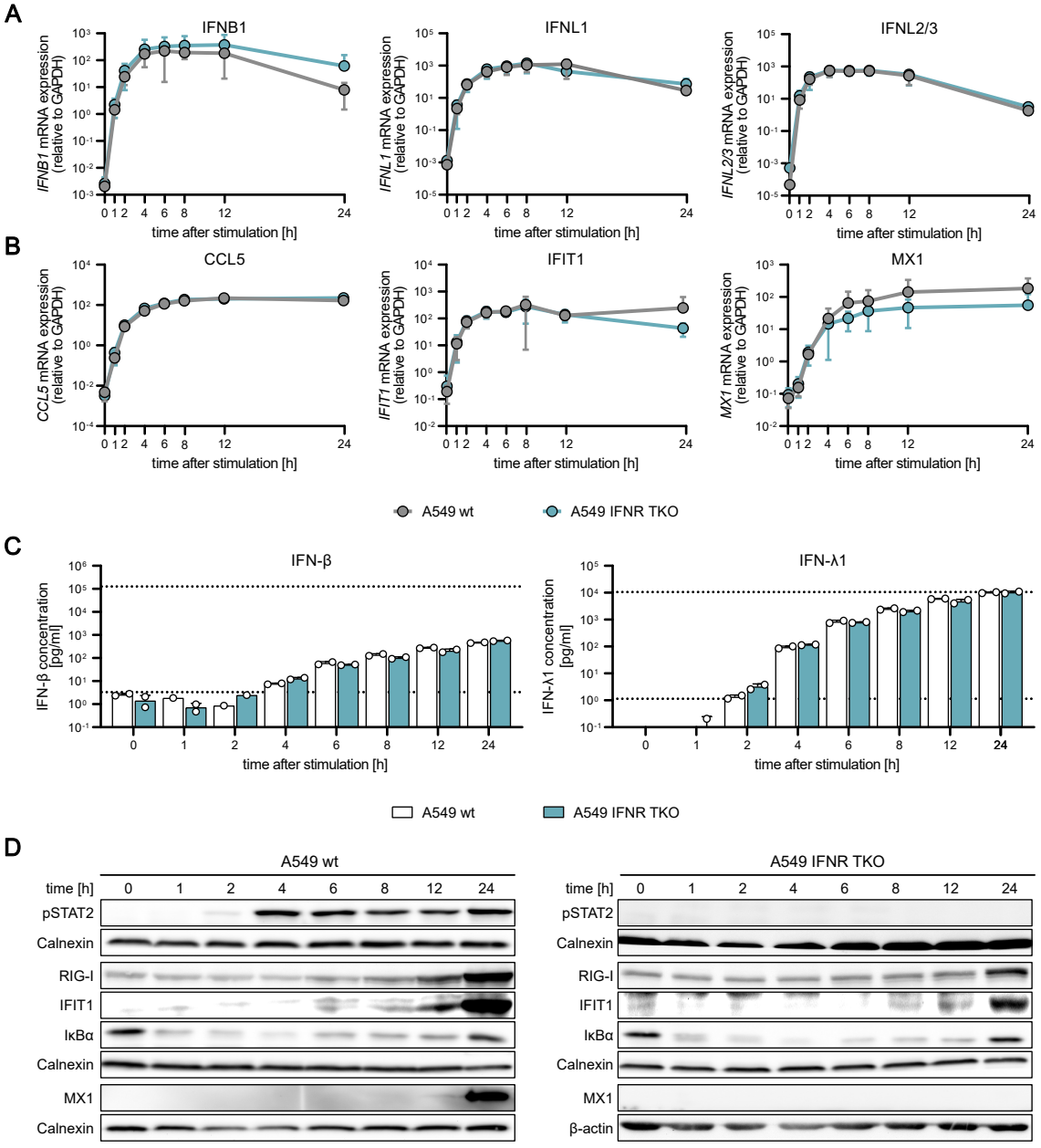

Figure 16: Kinetic characterization of the RIG-I signaling pathway upon synchronous 5'ppp-dsRNA stimulation in a type I, II, and III IFN signaling-independent system.

A549 wt cells and an A549 IFNAR1 IFNLR IFNGR1 triple knockout cell line (IFNR TKO) were electroporated with 220 ng 5'ppp-dsRNA. **(A)** IFNB1, IFNL1, and IFNL2/3 as well as **(B)** CCL5, IFIT1, and MX1 mRNA expression kinetics were examined using qRT-PCR. **(C)** Secreted IFN-β and IFN-λ1 protein concentrations in pg/ml were determined using a multiplex electrochemiluminescent immunoassay (U-PLEX IFN Combo, Meso Scale Diagnostics) in the supernatants of 5'ppp-dsRNA-stimulated A549 wt and A549 IFNR TKO cells. Dashed lines indicate upper and lower limit of quantification, respectively. **(D)** Kinetics of protein abundance and phosphorylation status of key signaling components in A549 wt and A549 IFNR TKO cells using western blot analysis. qRT-PCR values were normalized to the housekeeping gene GAPDH by applying the $2^{-\Delta Ct}$ method [358]. Graphs depict (A-B) mean ± SD, (C) individual values ± SD, or (D) representative blot of 2 biologically independent experiments.

Moreover, using western blot analysis, I further characterized protein activation and expression kinetics in A549 wt (Figure 16D, left panel) and IFNR TKO (Figure 16D, right panel) cells upon synchronous 5'ppp-dsRNA stimulation. Strikingly, despite the non-negligible MX1 mRNA expression, MX1 protein could not be detected in IFNR TKO cells (Figure 16D, right panel), whereas A549 wt cells showed increasing expression from 12 hours onwards (Figure 16D, left panel). Similarly, phosphorylated STAT2 was completely absent in IFNR TKO cells, again highlighting the missing ability to respond to IFN in those cells. Apart from that, key components of RLR signaling, such as IkBα degradation, as well as IFIT1 and RIG-I protein expression, showed similar kinetic patterns in both A549 wt and IFNR TKO cells.

In conclusion, the characterization of antiviral signaling dynamics in both the A549 IFNR DKO (Figure 5, Figure 6A) and the A549 IFNR TKO cell line (Figure 16), indicated, that with the experimental conditions I applied, i.e., synchronous stimulation using 5'ppp-dsRNA, intrinsic production of IFN-γ did either not occur in biologically relevant levels or did not affect the examined signaling kinetics. Nevertheless, the additional KO of the type II IFN receptor remains a precautionary measure for the effective interruption of IFN signaling in those cells and was thus used for further investigations.

Evidently, the A549 IFNR TKO cell line is optimally suited to decipher the inherent differences of the primary RLR-driven as well as the secondary IFN-driven signaling pathway upon 5'ppp-dsRNA stimulation. Hence, I aimed at further disentangling those differences and, in addition to assessing mRNA and protein expression of canonical antiviral response components (Figure 5, Figure 6, Figure 16), I also measured chemokine production in A549 wt and IFNR TKO cells upon synchronous 5'ppp-dsRNA stimulation using a multiplex electrochemiluminescent immunoassay (Figure 17). Interestingly, although a substantial IFN-dependency was apparent especially for IP-10 (Figure 17A), MCP-1 (Figure 17B), MIP-1α (Figure 17C), MIP-1β (Figure 17D), as well as the pro-inflammatory cytokine TNF (Figure 17E), A549 IFNR TKO cells were still able to produce considerable amounts themselves. In contrast, the chemokines MDC (Figure 17F) and TARC (Figure 17G), as well as the pro-inflammatory cytokine IL-6 (Figure 17H) only exhibited minor IFN-dependencies, whereas MCP-4 was not produced at all in both A549 cell lines (Figure 17I). These results indicate, that in addition to IFNs being produced upon RIG-I stimulation, also various cytokines and chemokines are secreted in an IFN-independent manner, likely to control infection at an early state. However, the production of most of them was significantly increased in the presence of IFN.

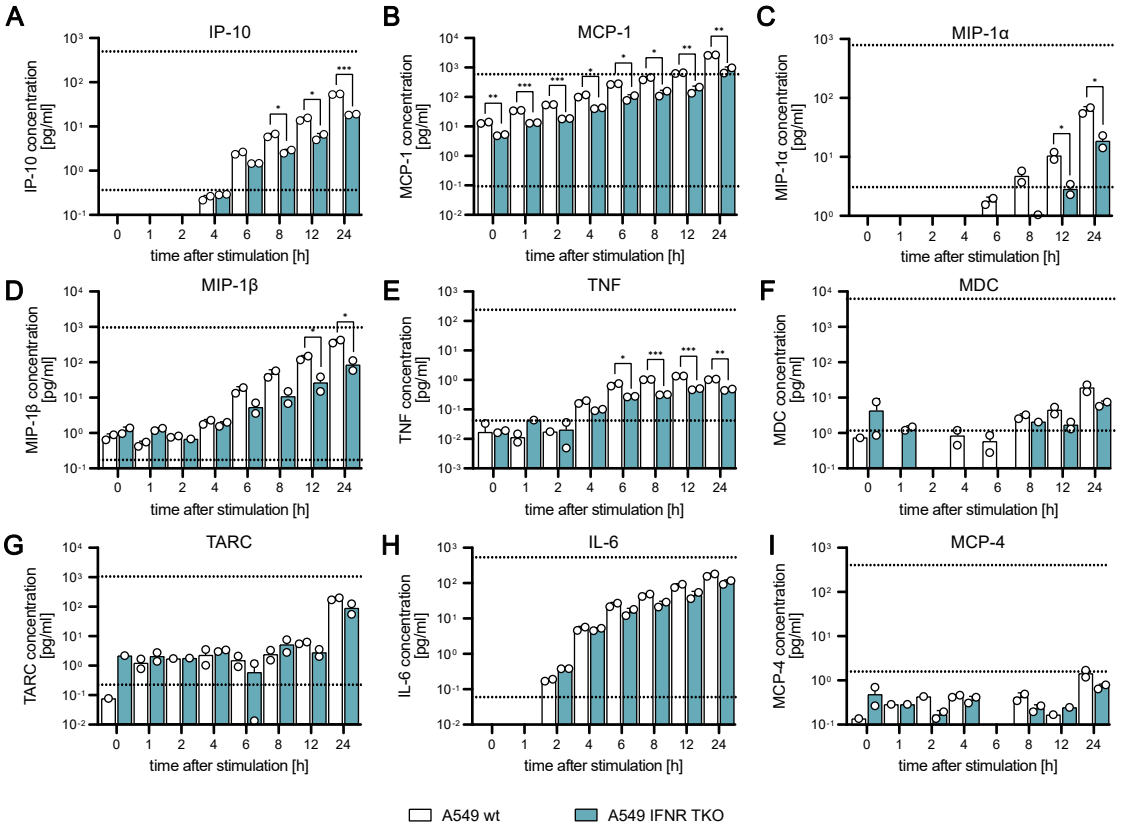

Figure 17: IFN-dependent and -independent cytokine and chemokine secretion upon synchronous 5'ppp-dsRNA stimulation in A549 cells.

A549 wt and A549 IFNR TKO cells were electroporated with 220 ng 5'ppp-dsRNA, supernatants were harvested, and cytokine production for **(A)** IP-10, **(B)** MCP-1, **(C)** MIP-1α, **(D)** MIP-1β, **(E)** TNF, **(F)** MDC, **(G)** TARC, **(H)** IL-6, and **(I)** MCP-4 was determined using a multiplex immunoassay (U-PLEX Chemokine & Inflammatory Panel, Meso Scale Diagnostics). Dashed lines indicate upper and lower limit of quantification, respectively. Graphs depict individual values ± SD of 2 biologically independent experiments. Statistical significance was determined with Student's t-test (***: $p < 0.001$, **: $p < 0.01$, *: $p < 0.05$).

4.9 Characterization of IFN-Independent RLR Signaling and the Underlying Influence of Distinct Transcription Factors

Based on the previous findings, I further aimed at examining the IFN-independent effect of cytokines and chemokines produced in A549 wt cells upon 5'ppp-dsRNA stimulation using A549 IFNR TKO cells. In order to assess this in an unbiased approach, I utilized a generic transcriptomic analysis. For this purpose, I mock-treated or synchronously stimulated A549 wt cells with 5'ppp-dsRNA using electroporation, collected supernatants after 16 hours, and stimulated A549 IFNR TKO cells with the respective supernatant. 8 hours upon supernatant stimulation, I retrieved RNA samples and subjected those to whole-transcriptome expression profiling (Figure 18A). Surprisingly, although considerable amounts of cytokines and chemokines are produced upon 5'ppp-dsRNA stimulation in A549 cells (Figure 16C, Figure 17, Supplementary Figure S7), comparing A549 IFNR TKO cells treated with mock supernatant or supernatant of electroporated cells revealed no difference between both stimulation approaches (Figure 18B). This finding suggests that, apart from IFNs, other cytokines and chemokines being produced and secreted upon RLR stimulation do not induce further gene expression in A549 IFNR TKO cells.

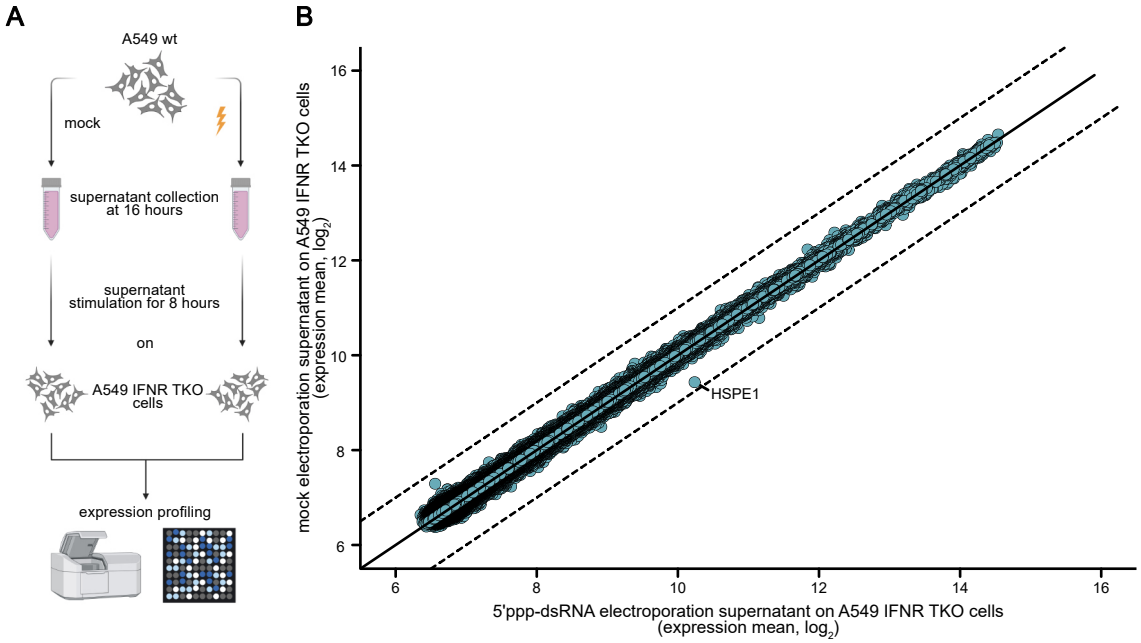

Figure 18: Whole-transcriptome expression profiling of IFN-independent signaling upon synchronous 5'ppp-dsRNA stimulation in A549 cells.

(A) Schematic depiction of the experimental setup. A549 wt cells were either mock-treated or synchronously stimulated with 220 ng 5'ppp-dsRNA. Supernatants were harvested after 16 hours and A549 IFNR TKO cells were subsequently stimulated with those supernatants. After 8 hours, RNA was harvested and subjected to whole-transcriptome expression profiling using the Illumina HumanHT-12 Expression BeadChip. **(B)** Scatter plot of transcriptomic analysis comparing expression means (log_2) of IFNR TKO cells stimulated with mock or 5'ppp-dsRNA-electroporated supernatants of A549 wt cells. Shown are expression means of 3 biologically independent experiments. Dots represent measured, individual gene mRNA expressions.

Hence, I anticipated to characterize the IFN-independent outcome of primary RLR signaling upon 5'ppp-dsRNA stimulation and the influence of individual signaling components. Whereas IRF3 is known to be essential for RLR signaling, previous findings in our lab using transcriptomic profiling of 5'ppp-dsRNA-stimulated A549 cells additionally suggested a prominent role of the transcription factor IRF1 in antiviral signaling, its expression being induced particularly fast. Thus, I generated additional KOs in the A549 IFNR TKO cell line, specifically MAVS (IFNR TKO MAVS KO), IRF3 (IFNR TKO IRF3 KO), and the abovementioned IRF1 (IFNR TKO IRF1, Supplementary Figure S13B-D). I synchronously stimulated those cell lines with 5'ppp-dsRNA, harvested RNA samples at 0 and 8 hours post stimulation, and analyzed changes in transcriptional levels using a whole-transcriptome expression profiling approach (Figure 19A). Along a commonly appreciated consensus, genes were classified as significantly up or downregulated if they exhibited at least a 2-fold change in transcript levels compared to the start of stimulation (0 hour time point), and if the p-value after correction for multiple testing (Benjamini-Hochberg) was additionally below 0.05. Remarkably, of the almost 20 000 genes analyzed, only few were found to be significantly regulated and were hence depicted in blue (Figure 19B-E).

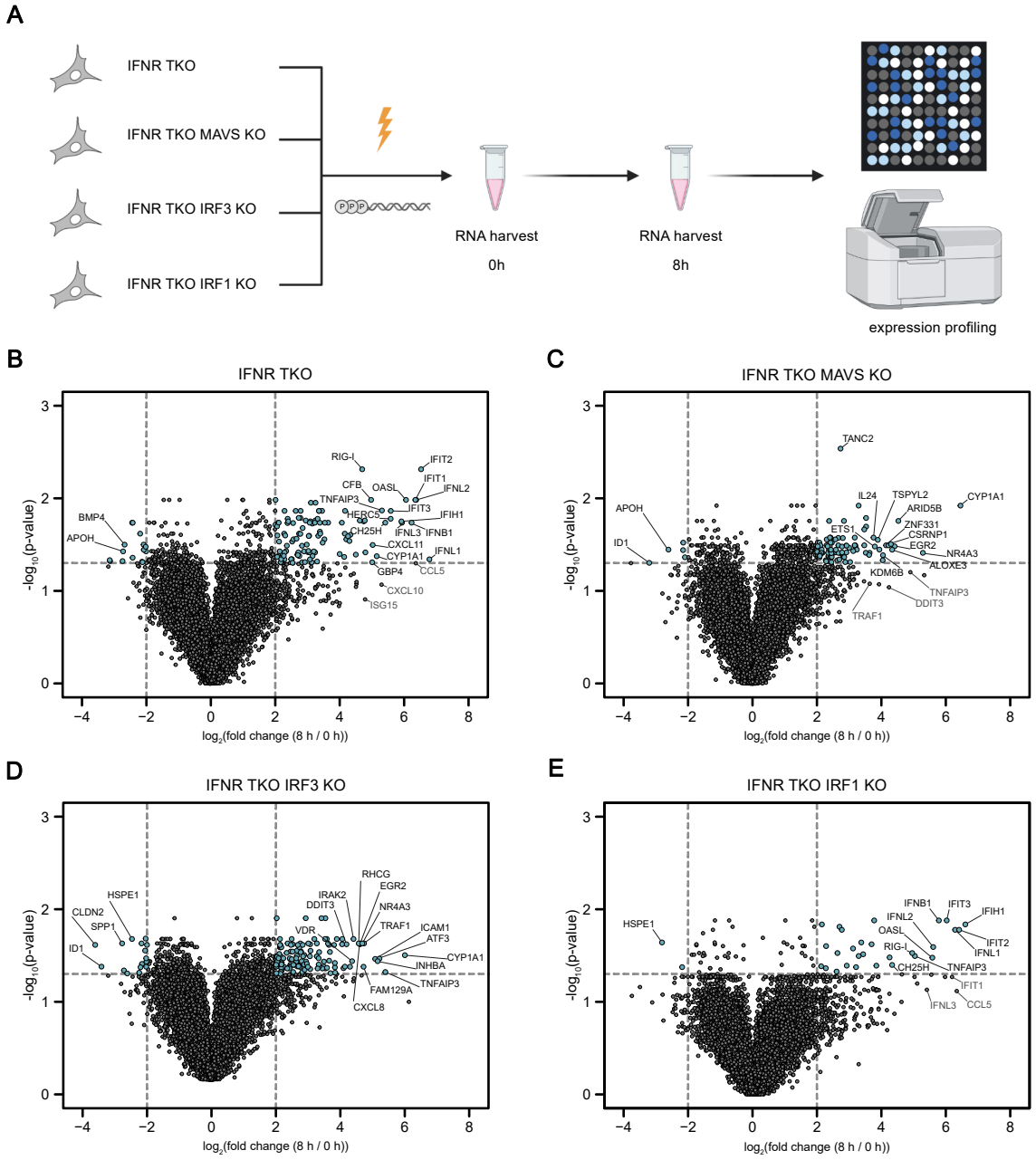

Figure 19: Whole-transcriptome expression profiling of 5'ppp-dsRNA-stimulated A549 IFNR TKO cells.

(A) A549 IFNR TKO, IFNR TKO IRF3 KO, IFNR TKO MAVS KO, and IFNR TKO IRF1 KO cells were synchronously stimulated with 220 ng 5'ppp-dsRNA. RNA samples were harvested at 0 and 8 hours post stimulation and subjected to whole-transcriptome expression profiling using the Clariom S microarray (Affymetrix). (B-E) Volcano plots displaying mRNA expression fold changes (8 hour over 0 hour time point) and the respective p-value of **(B)** IFNR TKO, **(C)** IFNR TKO IRF3 KO, **(D)** IFNR TKO MAVS KO, and **(E)** IFNR TKO IRF1 KO cells stimulated with 5'ppp-dsRNA. Shown are data of 3 biologically independent experiments. Significantly, differentially regulated genes (DEG, at least 2-fold up or downregulation and p-value below 0.05 after Benjamini-Hochberg correction for multiple testing) are highlighted in blue.

Interestingly, all cell lines showed significantly regulated transcripts upon synchronous 5'ppp-dsRNA stimulation. In line with previous results (Figure 16), the A549 IFNR TKO cell line induced the expression of classical ISGs (IFIT1, -2, -3, CCL5, OASL), as well as IFNs (IFNB1, IFNL1, -2, -3) upon 5'ppp-dsRNA stimulation (Figure 19B), the latter further highlighting the notion of an IFN-independent IFN production (Supplementary Figure S4). Surprisingly, in addition to inducing the expression and production of IFNs and few previously reported ISGs, such as IFIT1, 5'ppp-dsRNA stimulation and thus IFN-independent RLR signaling in A549 IFNR TKO cells induced the expression of many other genes (Figure 19B). Strikingly, although known to be ISGs themselves [70,374], RIG-I and MDA5 (IFIH1) were upregulated upon synchronous 5'ppp-dsRNA stimulation in an IFN-independent manner. In total, 243 genes were identified as being significantly up or downregulated in A549 INFR TKO cells upon synchronous 5'ppp-dsRNA stimulation (Figure 19B).

The additional knockout of the adapter protein MAVS or the transcription factor IRF3 mostly inhibited the induction of IFN and classical ISG expression (Figure 19C, D). Interestingly, in contrast to the IFNR TKO MAVS KO cell line, IFNR TKO IRF3 KO cells displayed an NF-κB pathway signature by inducing the expression of NF-κB target genes, e.g., the chemokine (C-X-C motif) ligand 8 (CXCL8, also IL-8) or negative regulators of NF-κB signaling, such as TNFAIP3 and the activating transcription factor 3 (ATF3, Figure 19D). However, whereas classical ISGs, IFNs, and (as seen in the IFNR TKO IRF3 KO cell line) NF-κB-dependent genes were absent, several genes were still considerably upregulated in the IFNR TKO MAVS KO cell line upon 5'ppp-dsRNA stimulation (Figure 19C). Here, among others, mRNA expression levels of the transcription factors nuclear receptor 4A3 (NR4A3), early growth response protein 2 (EGR2), as well as the cytokine interleukin-24 (IL-24) were induced. Intriguingly, cytochrome P450 1A1 (CYP1A1) mRNA expression was upregulated in the IFNR TKO, IFNR TKO MAVS KO, as well as the IFNR TKO IRF3 KO cell line, but was absent in IFNR TKO IRF1 KO cells (Figure 19E). Unexpectedly, the additional KO of IRF1 had a major impact on the amount of significantly regulated genes upon 5'ppp-dsRNA stimulation. Here, predominantly IFNs (i.e., IFNB1, IFNL1, -2, -3), classical ISGs (e.g., IFIT1, -2, -3, OASL), as well as RIG-I and MDA5 (IFIH1) mRNA levels were upregulated upon 5'ppp-dsRNA stimulation, similar as seen in IFNR TKO cells. Significantly regulated genes upon 5'ppp-dsRNA for each individual cell line are listed in Supplementary Tables S1, S2, S3, S4.

To gain insights into the biological relevance of the described gene expression alterations upon synchronous 5'ppp-dsRNA stimulation, I further performed a Gene Ontology terms of biological processes (GOBP) enrichment analysis of all significantly regulated genes in the respective cell lines. With regard to the wide range of significantly regulated genes identified in each cell line, expectedly, these were also enriched in many distinct GOBPs, all of which are illustrated in Supplementary Figure S14 and listed in Supplementary Tables S5, S6, S7, S8. The number of annotated genes, the respective p-value ($-\log_{10}$), and the false discovery rate (FDR, $-\log_{10}$) for a subset of enriched terms, harboring most of the annotated genes, are depicted in Figure 20.

Differentially expressed genes in the IFNR TKO cell line mostly mapped to the terms “regulation of transcription by RNA polymerase II”, “regulation of signal transduction”, and the “response to stimulus” (Figure 20A), whereas regulated genes in IFNR TKO MAVS KO were annotated to general terms, such as “organism development”, “regulation of metabolic processes”, as well as the “cellular response to chemical stimulus” (Figure 20B). This coincides with the fact that A549 IFNR TKO cells are still able to respond to 5’ppp-dsRNA stimulation via RLR signaling, inducing the expression of genes involved in antiviral signaling, whereas the additional KO of MAVS rendered the cell line unable to pursue further signaling upon 5’ppp-dsRNA stimulation. Similarly, significantly regulated genes in the IFNR TKO IRF3 KO cell line mapped to “organ development” or “regulation of cell differentiation”, however, with NF-κB signaling being still intact, “immune response” was among the enriched terms as well (Figure 20C). Although the IFNR TKO IRF1 KO cell line exhibited the least amount of significantly regulated genes upon 5’ppp-dsRNA stimulation (Figure 19E), identified genes were almost exclusively enriched in terms of antiviral signaling, such as “response to stimulus”, “innate immune response”, and “defense response to virus” (Figure 20D).

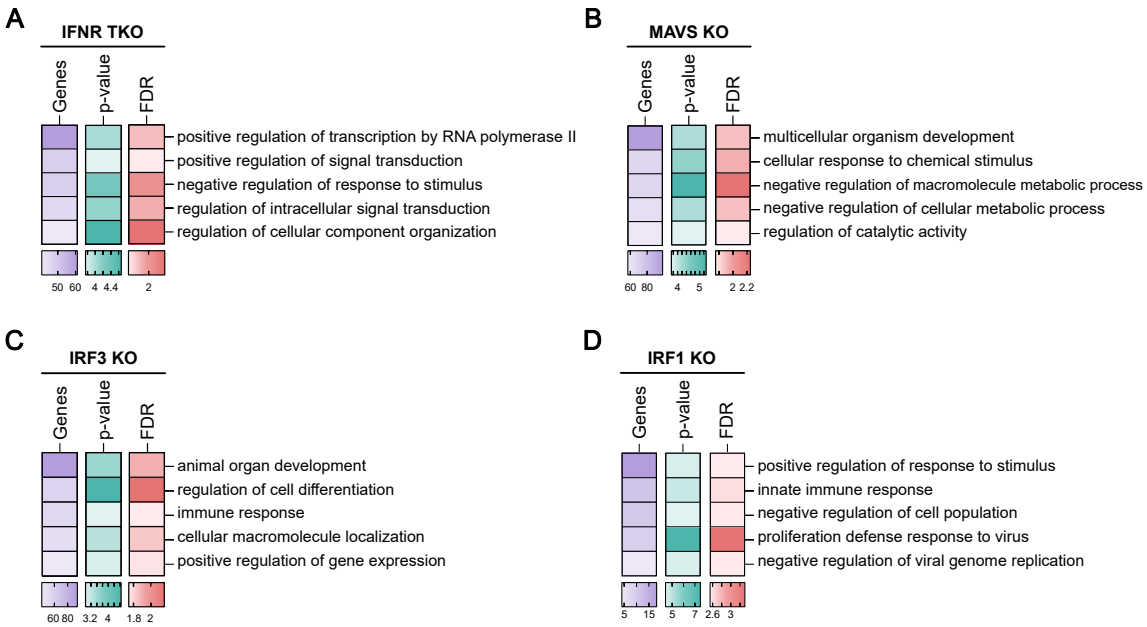

Figure 20: GOBP term enrichment analysis of 5’ppp-dsRNA-stimulated A549 IFNR TKO cells.

Heat maps displaying number of genes, the p-value ($-\log_{10}$), as well as the false discovery rate (FDR, $-\log_{10}$) of Gene Ontology terms for biological processes (GOBP) enriched in **(A)** A549 IFNR TKO, **(B)** IFNR TKO MAVS KO, **(C)** IFNR TKO IRF3 KO, and **(D)** IFNR TKO IRF1 KO cells upon synchronous stimulation with 220 ng 5’ppp-dsRNA. Genes were classified as significantly regulated if they were at least 2-fold up or down-regulated and the p-value after correction for multiple testing was below 0.05. Values were normalized to the 0 hour time point of the corresponding cell line and the FDR was set to be below 0.05. Graph depicts top five GOBP term hits for each cell line, remaining enriched terms are listed in the Supplementary Tables S5, S6, S7, S8.

In a next step, I aimed at dissecting mRNA level changes upon synchronous 5'ppp-dsRNA stimulation in A549 INFR TKO cells compared to the IFNR TKO cell lines harboring the additional MAVS, IRF3, or IRF1 KO. Thus, I calculated fold changes (f.c., 8 hour over 0 hour time point) of significantly regulated gene expression means in the individual cell lines and examined differences in A549 IFNR TKO compared to either IFNR TKO MAVS KO (Figure 21A), IFNR TKO IFR3 KO (Figure 21B), or IFNR TKO IRF1 KO (Figure 21C). At least 2-fold changes in mRNA levels between both cell lines are indicated in blue (Figure 21A-C). Expectedly, comparing mRNA fold changes of synchronously stimulated IFNR TKO cells and the IFNR TKO MAVS KO cell line clearly demonstrated the absence of antiviral signaling upon 5'ppp-dsRNA stimulation in the latter (Figure 21A). Specifically, while in the IFNR TKO cell line the IFNs IFNB1, IFNL1, -2, and -3, as well as the ISGs IFIT1, -2, and -3, were amongst the highest upregulated genes, none of these were induced upon 5'ppp-dsRNA stimulation in IFNR TKO MAVS KO cells. The induction of mRNAs such as RIG-I, IFIH1, OASL, and CXCL11 in the A549 IFNR TKO cell line upon 5'ppp-dsRNA stimulation suggests, that primary RLR signaling does not only result in the expression of IFNs, but rather induces the expression of a wide range of other antiviral and pro-inflammatory genes. Interestingly, the most prominently induced mRNA in the IFNR TKO MAVS KO cell line compared to IFNR TKO was the cytokine IL-24 (Figure 21A). IL-24 is reported to be released predominantly by activated monocytes, macrophages, as well as T helper cells and might control cell survival and proliferation by activating the transcription factors STAT1 and STAT3 [375–377].

Likewise, comparing mRNA fold changes of A549 IFNR TKO and IFNR TKO IRF3 KO cells upon synchronous 5'ppp-dsRNA stimulation revealed a clear antiviral signaling signature in IFNR TKO cells, which was absent in IFNR TKO IRF3 KO cells (Figure 21B). As seen before, IFNR TKO cells induced the expression of IFNs (IFNL1, -2, -3, IFNB1) and ISGs (IFIT1, -2, -3, RIG-I, IFIH1) among others. However, in contrast to the IFNR TKO MAVS KO cell line (Figure 21A), a few mRNAs were differentially regulated in the IFNR TKO IRF3 KO cell line upon 5'ppp-dsRNA stimulation compared to IFNR TKO cells. Here, identified mRNAs induced in the IFNR TKO IRF3 KO cell line were, for instance, the mRNAs of intercellular adhesion molecule 1 (ICAM-1) also known as cluster of differentiation 54 (CD54), inhibin beta A (INHBA), and CCL2 (Figure 21B).

Surprisingly, comparing mRNA fold changes in IFNR TKO and IFNR TKO IRF1 KO cells upon 5'ppp-dsRNA stimulation revealed only minor differences between both cell lines (Figure 21C). In fact, both cell lines upregulated antiviral signaling components, such as IFIT1, -2, and -3, as well as IFNB1, IFNL1, -2, and -3, although to a lesser extent in the IFNR TKO IRF1 KO cell line. Among the differently regulated genes in the IFNR TKO cell line were melanoregulin (MREG), programmed cell death 1 ligand 1 (PDL1/CD274), and phosphoinositide-3-kinase adaptor protein 1 (PIK3AP1), all of which varied between 2 and 3.5-fold change difference.

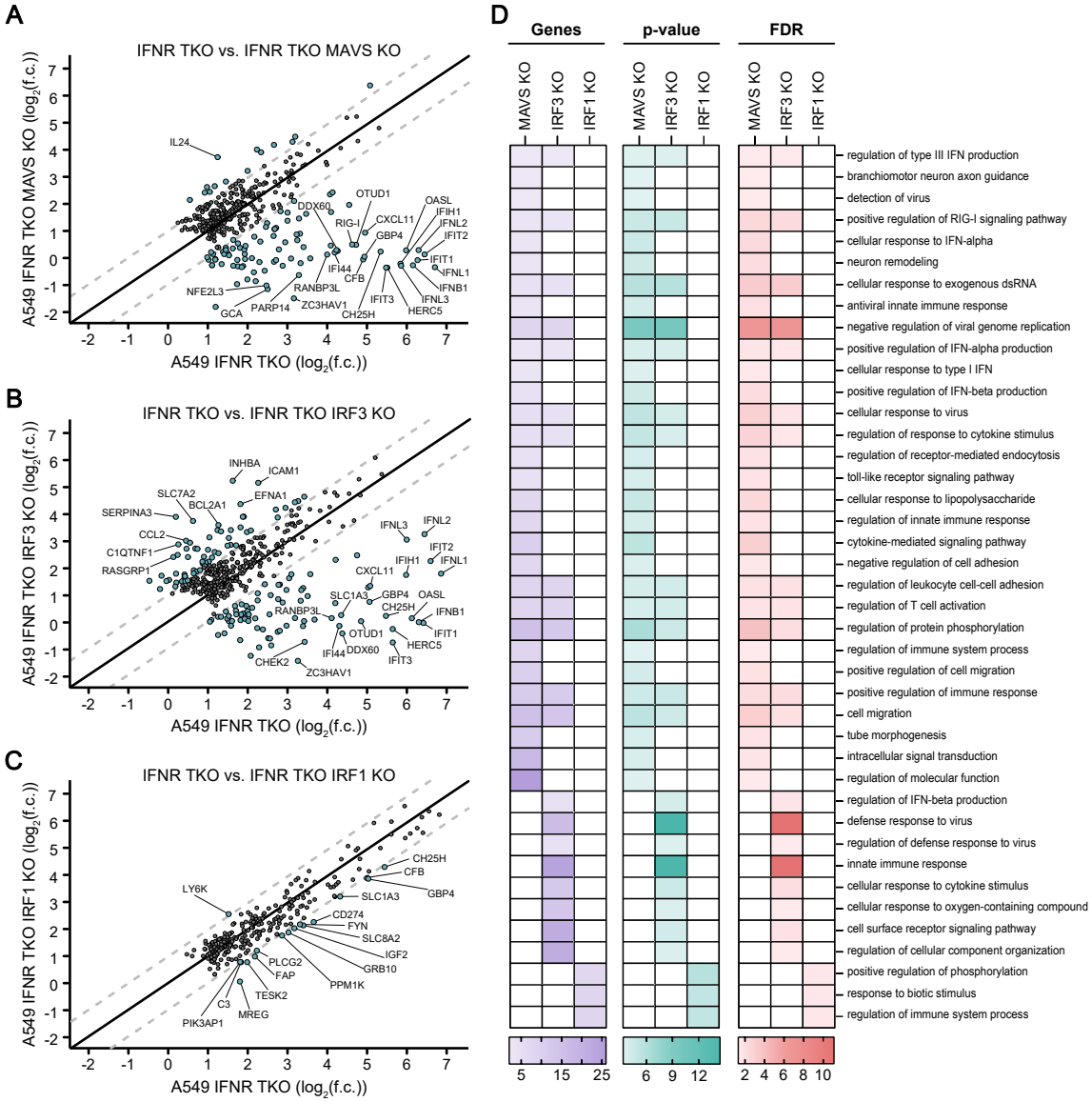

Figure 21: Effect of additional KO in A549 IFNR TKO cells on RNA expression profile upon synchronous 5'ppp-dsRNA stimulation.

A549 IFNR TKO, IFNR TKO MAVS KO, IFNR TKO IRF3 KO, and IFNR TKO IRF1 KO cells were synchronously stimulated with 220 ng 5'ppp-dsRNA. RNA samples were harvested at 0 and 8 hours post stimulation and subjected to whole-transcriptome expression profiling using the Clariom S microarray (Affymetrix). (A-C) Scatter plots displaying log_2 mRNA fold changes (f.c.) of differentially expressed genes in **(A)** A549 IFNR TKO and IFNR TKO MAVS KO cells, **(B)** A549 IFNR TKO and IFNR TKO IRF3 KO cells, as well as **(C)** A549 IFNR TKO and IFNR TKO IRF1 KO cells. Fold changes (8 hour over 0 hour time point) are calculated from 3 biologically independent experiments. Genes were classified as significantly regulated if they were at least 2-fold up or down-regulated and the p-value was below 0.05 after Benjamini-Hochberg correction for multiple testing and were thus marked in blue. **(D)** Heat maps displaying number of genes, the p-value ($-log_{10}$), as well as the false discovery rate (FDR, $-log_{10}$) of Gene Ontology terms for biological processes (GOBP) enriched in the IFNR TKO cell line normalized to the respective IFNR TKO MAVS, IRF3, or IRF1 KO. Enriched GOBP terms are listed in the Supplementary Tables S9, S10, S11.

To gain further insight on the impact of the additional knockouts in the IFNR TKO cell line on gene expression upon 5'ppp-dsRNA stimulation, I again performed a GOBP enrichment analysis. Here, I used the mRNAs which were differentially expressed in the IFNR TKO cell line as compared to the respective IFNR TKO MAVS, IRF3, or IRF1 KO cell line, effectively annotating mRNAs to GOBP terms which were at least 2-fold upregulated in the IFNR TKO cell line (IFNR TKO relative to other KO). The number of annotated genes, the respective p-value ($-\log_{10}$), and the false discovery rate (FDR, $-\log_{10}$) for enriched terms are depicted in Figure 21D.

As expected, DEGs in IFNR TKO cells as compared to the IFNR TKO MAVS KO cell line mostly mapped to terms of antiviral signaling, such as "regulation of type III interferon production", "detection of virus", and "positive regulation of immune response", in addition to more generic terms, such as "regulation of molecular function". Similarly, most DEGs in the IFNR TKO cell line compared to the IFNR TKO IRF3 KO cell line were enriched in the terms "innate immune response" and "cell surface receptor signaling pathway", whereas IFIH1 and RIG-I, which exhibited the highest fold enrichment, were clustered in "regulation of type III interferon production". Unsurprisingly, only terms regarding generic regulation processes, e.g., "positive regulation of phosphorylation" and "response to biotic stimulus" were identified for DEGs in IFNR TKO as compared to the IFNR TKO IRF1 KO cell line (Figure 21D). In comparison, a GOBP enrichment analysis of DEGs in the specific IFNR TKO MAVS, IRF3, or IRF1 KO cell lines compared to the IFNR TKO cell line (KO relative to IFNR TKO) is illustrated in Supplementary Figure S15A.

Whereas the previous analysis mostly examined the influence of MAVS, IRF3, and IRF1 on mRNA expression upon 5'ppp-dsRNA stimulation in an IFN-independent system, I further aimed at dissecting the differences between IRF3 and IRF1 in antiviral signaling. Therefore, I examined mRNA level changes upon synchronous 5'ppp-dsRNA stimulation in IFNR TKO IRF3 KO cells compared to the IFNR TKO MAVS KO or IFNR TKO IRF1 KO cell line. Accordingly, I calculated fold changes (f.c., 8 hour over 0 hour time point) of significantly regulated gene expression means in the individual cell lines and examined differences in A549 IFNR TKO IRF3 KO compared to either IFNR TKO MAVS KO (Figure 22A) or IFNR TKO IRF1 KO cell lines (Figure 22B). At least 2-fold changes in mRNA levels between both cell lines are indicated in blue. Expectedly, comparing mRNA fold changes of synchronously stimulated IFNR TKO IRF3 KO cells and the IFNR TKO MAVS KO cell line again clearly demonstrated the absence of antiviral signaling upon 5'ppp-dsRNA stimulation in the latter (Figure 22A).

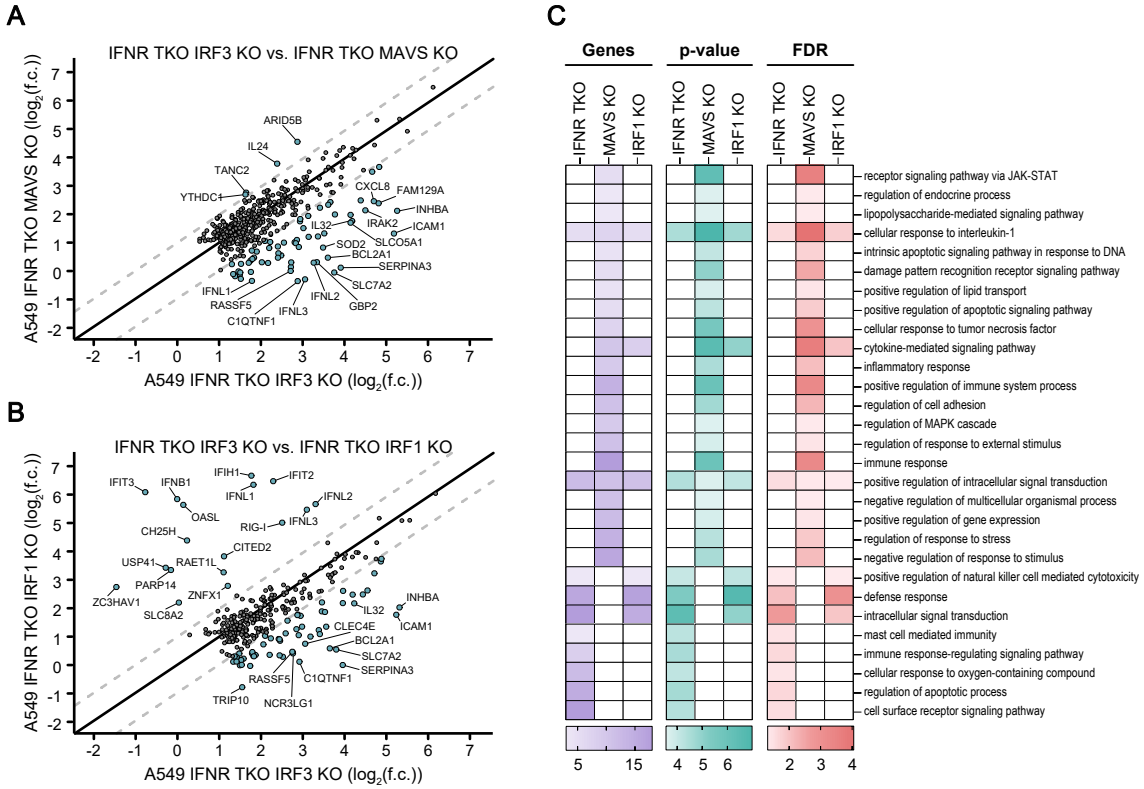

Figure 22: Whole-transcriptome expression profiling and GOBP term enrichment analysis upon synchronous 5'ppp-dsRNA stimulation compared to A549 IFNR TKO IRF3 KO cells.

A549 IFNR TKO, IFNR TKO MAVS KO, IFNR TKO IRF3 KO, and IFNR TKO IRF1 KO cells were synchronously stimulated with 220 ng 5'ppp-dsRNA. RNA samples were harvested at 0 and 8 hours post stimulation and subjected to whole-transcriptome expression profiling using the Clariom S microarray (Affymetrix). (A-C) Scatter plots displaying $\log_2$ mRNA fold changes (f.c.) of differentially expressed genes in **(A)** A549 IFNR TKO IRF3 KO and IFNR TKO MAVS KO cells, and **(B)** A549 IFNR TKO IRF3 KO and IFNR TKO IRF1 KO cells. Fold changes (8 hour over 0 hour time point) are calculated from 3 biologically independent experiments. Genes were classified as significantly regulated if they were at least 2-fold up or downregulated and the p-value was below 0.05 after Benjamini-Hochberg correction for multiple testing and were thus marked in blue. **(C)** Heat maps displaying number of genes, the p-value ($-\log_{10}$), as well as the false discovery rate (FDR, $-\log_{10}$) of Gene Ontology terms for biological processes (GOBP) enriched in the IFNR TKO IRF3 KO cell line normalized to the respective IFNR TKO MAVS KO or IFNR TKO IRF1 KO cell line.

Stimulation of the IFNR TKO IRF3 KO cell line with 5'ppp-dsRNA resulted in several DEGs involved in antiviral signaling, such as IFNL1, -2, -3, or the chemokine CXCL8. This might be attributed to active NF-κB signaling in the IFNR TKO IRF3 KO cell line, which, being downstream of MAVS, could not be activated in the IFNR TKO MAVS KO cell line (Figure 22A). In contrast to this, comparing fold changes in the IFNR TKO IRF3 KO and IFNR TKO IRF1 KO cell lines revealed several DEGs on both sides (Figure 22B). IFNL1, -2, and -3 are still expressed in the IFNR TKO IRF3 KO cell line (Figure 22A), however, fold changes in the IFNR TKO IRF1 KO cell line were considerably increased (Figure 22B). This further suggests that the type III IFN mRNA expression seen in IFNR TKO IRF3 KO cells might be induced by another signaling component, e.g., IRF7, although IFNL mRNA expression still seems to be predominantly induced by IRF3. Moreover, comparing fold changes of induced mRNAs in IFNR TKO IRF3 KO cells and the IFNR TKO MAVS KO (Figure 22A) or

IFNR TKO IRF1 KO (Figure 22B) cell line revealed distinct DEGs in IFNR TKO IRF3 KO cells, such as serpin family A member 3 (SERPINA3), ICAM-1, and the cytokine IL-32. In addition to IFNs and ISGs, IFNR TKO IRF1 KO cells further strongly induced the expression of zinc finger CCCH-type antiviral protein 1 (ZC3HAV1), which was reported to prevent viral infections [378, 379], as well as poly(ADP-ribosyl)ation (PARP14), which, among other functions, was described to negatively regulate STAT1 phosphorylation [380] (Figure 22B).

Finally, I subjected the identified DEGs of the IFNR TKO IRF3 KO cell line compared to IFNR TKO MAVS KO or IFNR TKO IRF1 KO cells to a GOBP enrichment analysis, annotating mRNAs to GOBP terms which were at least 2-fold upregulated in the IFNR TKO IRF3 KO cell line (IFNR TKO IRF3 KO relative to IFNR TKO MAVS KO or IFNR TKO IRF1 KO). Likewise, the number of annotated genes, the respective p-value ($-\log_{10}$), and the false discovery rate (FDR, $-\log_{10}$) for enriched terms are depicted in Figure 22C. As expected, DEGs in IFNR TKO IRF3 KO cells as compared to the IFNR TKO MAVS KO cell line mostly mapped to terms such as “immune response“, “negative regulation of response to stimulus”, and “regulation of response to stress”, with a high degree of overlaps between annotated genes (Figure 22C, Supplementary Table S12). DEGs in IFNR TKO IRF3 KO cells, as compared to the IFNR TKO IRF1 KO cell line, were assigned to more generic terms, such as “defense response” and “intracellular signal transduction”, but also to “cytokine-mediated signaling pathway” (Figure 22C, Supplementary Table S13). This indicates that the IFNR TKO IRF3 KO cell line is still able to signal upon 5’ppp-dsRNA stimulation, although classical antiviral signaling molecules could not be detected. The opposing analysis, examining GOBP terms of DEGs in the IFNR TKO IRF1 KO and IFNR TKO MAVS KO cell lines compared to IRF3 (IRF1 or MAVS KO relative to IFNR TKO IRF3 KO), is illustrated in Supplementary Figure S15B. Here, DEGs in IFNR TKO IRF1 KO compared to IFNR TKO IRF3 KO were assigned to various terms associated with the antiviral response system, such as “innate immune response” and the “positive and negative regulation of immune responses” (Supplementary Figure S15B).

In summary, these results indicate that 5’ppp-dsRNA stimulation of IFNR TKO cells, i.e., primary RLR signaling, does not only induce the expression of IFNs and a few individual ISGs, but rather upregulates a plethora of various mRNAs resulting in signal transduction, regulation, and the production of effector proteins. Furthermore, as expected, antiviral signaling is strongly dependent on MAVS, and to a large extent on IRF3, whereas IRF1 seems to only have a minor effect on the canonical antiviral signaling response. Comparing the impact of IRF1 and IRF3 in A549 IFNR TKO cells on mRNA expression upon 5’ppp-dsRNA stimulation indicated, that IRF3 is mostly involved in antiviral signaling and affects its regulation, whereas IRF1 might be involved in a more generic defense response and adjacent cytokine-mediated signaling pathways (Figure 22, Supplementary Figure S15B).

5. Discussion

The possession of reliable defense systems for the protection against invading microbes, such as viruses, is crucial for cellular homeostasis. Whereas most cells developed innate defense responses very early in evolution (reviewed in [3, 4]), higher organisms are characterized by the concomitance of both adaptive and innate immune systems. At early stages of infection, produced and secreted cytokines activate and coordinate innate and adaptive immune responses, such as the action of professional immune cells. However, immediate cell-intrinsic defense responses of infected cells potently suppress microbial or viral replication, which in many cases is required for successful control and clearance of the pathogen (reviewed in [3–5]). In this study, I employed synchronous stimulation with virus-like 5'ppp-dsRNA to kinetically characterize cell-intrinsic innate immune signaling and thus use these data to establish a comprehensive mathematical model of the cell-intrinsic antiviral response system, which is able to simulate and analyze critical virus-host interactions during the early infection phase.

5.1 Kinetic Characterization of RIG-I-Mediated Antiviral Signaling Dynamics

The antiviral innate immune response system is largely comprised of cytoplasmic sensors such as the RIG-I-like receptors. Synchronous activation of cell surface receptors, such as the TNF receptor [381], IL-1 receptor [382], and some toll-like receptors [383], can be realized by direct ligand application to the cell culture media. However, due to the cytoplasmic localization, simultaneous stimulation of a signaling pathway is particularly challenging for intracellular receptors such as RIG-I.

Upon viral infection, intracellular activities, i.e., signaling events, have been suggested to display a high degree of stochasticity and thus cell-to-cell variability. However, cellular uptake of a PAMP, e.g., viral RNA, depends on endocytic processes. Most kinetic studies are based on viral infections or liposome-based transfection of virus-like RNA and thereby introduce a large variability in intracellular PAMP recognition [364, 365]. Recently, Eyndhoven and colleagues summarized critical issues in deciphering the dynamics of IFN responses upon virus infection. New technologies such as single cell (sc) quantitative PCR and scRNA sequencing of infected cells highlighted the high degree of cellular heterogeneity during IFN responses [384]. This stochasticity was suggested to give rise to deterministic cellular events, resulting in fractions of responding (i.e., cells inducing IFN signaling upon nucleic acid detection) and nonresponding (i.e., cells which do not induce IFN signaling upon nucleic acid detection) cells. For instance, SeV-infected mouse embryonic fibroblasts (MEF) could be separated in fractions of IFN-β-expressing and non-expressing cells. Analysis of the distinct cell fractions suggested the stochastic IFN-β expression to be a consequence

of cellular heterogeneity in levels and/or activities of critical pathway components [152]. In fact, cellular heterogeneity of the antiviral response system has been proposed to be the result of multiple different stochastic events within distinct layers resulting in a multilayered stochasticity [365,385]. Each layer of stochasticity emerges in the course of a viral infection starting with the stochastic factors introduced by the virus itself, including for instance the distribution of viral particles prior to infection. Other layers comprise stochastic elements of the host cell as well as spatiotemporal diffusion gradients of both released viral particles and IFNs [384,386]. Consequently, this multilayered stochasticity can result in a wide range of distinct cellular outcomes in terms of infection onset, IFN expression, and ultimately the antiviral response.

5.1.1 Synchronous RIG-I Pathway Activation with Virus-Like 5'ppp-dsRNA

This heterogenous pathway activation pattern was not only observed for IFN signaling, but for RLR signaling as well. For instance, Rand *et al*. reported a cell-intrinsic stochasticity in the activation of IRF7 and NF-κB upon virus infection of murine cells and thus concluded that the observed heterogeneity in IFN production is of cellular rather than viral origin [365]. However, as mentioned previously, virus infections as well as liposome-based transfections of RLR agonists, such as dsRNA, and thereby cytosolic delivery of such stimulants, can be very heterogenous itself. By synchronizing virus-like dsRNA delivery, the stochastic elements introduced by viral infection can be eliminated, allowing for the investigation of cell-intrinsic stochasticity within the RIG-I-mediated signaling pathway. For this, I generated A549 cells stably co-expressing the nuclear marker H2B-mCherry and cytosolic IRF3-eGFP as a marker for early pathway activation and employed electroporation for synchronous dsRNA stimulation. Electroporation, also called electropermeabilization, is a highly efficient technique to deliver genetic material such as DNA and RNA into a variety of cells including mammalian, plant, and bacterial cells [387–389]. In essence, it comprises a precisely pulsed electrical current to induce temporary pore formation in cell membranes through which charged molecules can pass [390, 391]. Since the electrical field is typically applied for less than one milli second, introduction of stimulatory RNA into cells occurs simultaneously.

In fact, comparing classical liposome-based transfection and electroporation of A549 IRF3-eGFP expressing cells with 5'ppp-dsRNA demonstrated a clear difference in pathway activation kinetics (Figure 1B-E). Analyzing IRF3-eGFP nuclear translocation on a single cell level in liposome transfected cells displayed a slow and asynchronous kinetic pattern, which could be attributed to the staggered uptake of stimulatory RNA during endocytosis (Figure 1C). In contrast, electroporated cells exhibited a rapid and very synchronous nuclear translocation of IRF3 and thus pathway activation (Figure 1C). Here, the maximal amount of activated cells was reached within 60 minutes, whereas transfection led to a continuous increase within the experimental time frame. Notably, these effects were essentially preserved even with decreasing 5'ppp-dsRNA concentrations, indicating that electroporation-

mediated synchronicity does not emerge from RNA overload within the cells. Interestingly, although visible on a single cell level, cytoplasmic translocation upon IRF3 inactivation could not be observed within the population-averaged measurement of transfected cells. In contrast, the synchronous activation further seemed to lead to a synchronous inactivation and thus cytoplasmic translocation of IRF3, since electroporated cells displayed a continuous decrease of nuclear IRF3 from 60 minutes onwards (Figure 1C). The synchronous stimulation of RIG-I and the resulting pathway activation kinetics indicate, that previously observed cellular stochasticity was mainly introduced by viral infection and the process of nucleic acid release into the cellular cytoplasm, rather than resulting from host cellular components. Instead of the reported stochasticity of antiviral signaling, these results suggest RLR signaling to be highly deterministic upon synchronous stimulation. Thus, the established approach permitted the synchronous stimulation of A549 cells with virus-like dsRNA and hence the high resolution kinetic characterization of the RLR signaling pathway. Using live-cell imaging, quantitative western blotting, and qRT-PCR, I could examine phosphorylation and expression of critical proteins within the RIG-I signaling cascade in a fine-grained time course upon synchronous stimulation.

Strikingly, the obtained results demonstrate that signal transduction from detection of 5'ppp-dsRNA by RIG-I to the expression of target mRNAs is extremely fast and only requires several minutes. Phosphorylation of the kinase TBK1 as well as onset of degradation of the NF-κB inhibitor, IκBα, was detectable 15 minutes after 5'ppp-dsRNA stimulation (Figure 2A) and, in accordance with the established sequential RLR signal transmission, phosphorylation of the transcription factors NF-κB and IRF3 appeared 15 or 30 minutes upon stimulation, respectively (Figure 2A). The first transcripts of type I and III IFNs could be detected after 45 to 60 minutes (Figure 2B, C), with measurable amounts of secreted IFNs in the culture supernatants after 4 to 6 hours (Figure 5C). This strongly contrasts kinetic data of other studies, reporting an activation of the RLR signaling pathway 4 to 6 hours upon, e.g., virus infection [392,393]. However, comparably fast kinetic patterns of NF-κB activation and IκBα degradation upon TNF stimulation have been reported [394, 395]. Being expressed on the plasma membrane, signaling through the TNF receptor via TNF application can be considered to be synchronous and comparable to electroporation, hence, supporting the obtained kinetic data of RIG-I-mediated pathway activation.

Surprisingly, whereas NF-κB phosphorylation seemed to decrease over time, IRF3 phosphorylation was stable within the experimental timeframe, despite the decline of TBK1 phosphorylation (Figure 2A). This indicates that, although both are activated by 5'ppp-dsRNA resulting in nuclear translocation, inactivation of IRF3 and NF-κB seems to be differentially regulated, leading to distinct dephosphorylation kinetics. In fact, Wang *et al.* reported a requirement of IKK-β and NF-κB for the early induction of IFN-β upon viral infection in DCs and MEFs. However, they suggested NF-κB to be dispensable for virus-induced type I IFN expression, thus, highlighting differential roles of RLR-induced IRF3 and NF-κB-mediated IFN expression presumably through distinct kinetic patterns [396, 397].

Although kinetic characterization of the pathway downstream of, e.g., the TBK1/IKK-ε ki-

nases could be resolved by western blotting, I have not been able to show pathway activation of, e.g., RIG-I and MAVS upstream of the kinases. As mentioned in Section 1.4.1, RIG-I activation is characterized by distinct features such as ubiquitination, dephosphorylation, and oligomerization. These features have all been characterized in various studies using distinct stimulation methods, however, they have not been shown upon synchronous stimulation using electroporation. Since the first attempts to determine RIG-I activation kinetics upon dsRNA electroporation by measuring ubiquitination were unsuccessful, I tested different approaches to illustrate RIG-I oligomerization. Unfortunately, semi-denaturing agarose gels, non-reducing SDS-PAGE, and Native PAGE all exhibited ambiguous results which were additionally hard to reproduce. Moreover, Weber *et al.* presented a limited trypsin digest upon Rift Valley fever virus (RVFV) infection of A549 cells to be an alternative method to analyze alterations in protease sensitivity, indicating conformational changes of PRRs such as RIG-I [398]. Following this protocol, I had a look on trypsin resistant RIG-I fragments in A549 cells upon dsRNA electroporation, however, I was still unable to detect activated RIG-I in our short-term electroporation settings. Collectively, these attempts demonstrate that detection of activated RIG-I and MAVS upon synchronous dsRNA stimulation is non-trivial and might fail due to too low amounts of activated protein in the very early time points after electroporation. Developing a sensitive method to detect early RLR activation could contribute to the kinetic understanding of antiviral signaling.

5.2 Mathematical Model of the Antiviral Innate Immune Response

Given the underlying importance of the above-mentioned kinetic regulation of dsRNA-induced RLR signaling, we utilized mathematical modeling to gain further kinetic understanding of the pathway. Combined with experimental data, mathematical models can serve as powerful tools to dissect and predict the outcome of cellular signaling pathways [399, 400] (reviewed in [401, 402]). In fact, mathematical models have provided crucial insights into both the origins of cellular heterogeneity as well as the complexity of antiviral responses (reviewed in [384]). For instance, Bertolusso and colleagues developed a data-driven model of the innate immune response to investigate the dynamic cross-talk of RIG-I and TLR3-mediated signaling upon dsRNA electroporation [403]. In another study, our collaboration partners modelled dsRNA recognition by RIG-I and its downstream signaling, however, focused on the quantitative output rather than signaling kinetics [404].
Mechanistic models pursue the establishment of causal relationships between inputs, e.g., dsRNA and IFN stimulation, and outputs, e.g., downstream signaling. They can be calibrated on small data sets and can be used as predictive tools rather than inferring correlations (reviewed in [405]). In this study, literature knowledge of the topology of the primary RLR-mediated antiviral response served as basis for the establishment of a set of ODEs mechanistically representing key signaling events (Figure 3, Figure 4). However, despite be-

ing a crucial component of the antiviral system, positive feedback through IFN was not yet considered in the core model of RIG-I signaling. Although RLR signaling itself is known to directly induce the expression of certain ISGs, such as IFIT1 [406–408], the entirety of the transcriptional program that mediates the antiviral state of a cell is only established upon IFN signaling. As stated previously (Section 1.6), the RLRs themselves as well as some members of the IRF family, in particular IRF1, IRF7, and IRF9, are ISGs substantially induced upon IFN signaling [173, 185, 285–288] and, hence, autocrine IFN signaling reinforces sensing of viral RNAs and IFN production. Although crucial in actual viral infections, the increased RNA sensing and IFN production is negligible in our experimental system, since the electroporated (i.e., pulse-transfected) dsRNA is not replicated for prolonged periods of time.

Using "IFN-blind" cells, harboring a functional double knockout of the type I and III IFN receptors (IFNR DKO), for synchronous dsRNA stimulation, I analyzed RIG-I-mediated but IFN-independent mRNA expression kinetics (Figure 5, Figure 6). In fact, induction dynamics of the examined IFNs was not affected in IFNR DKO cells, emphasizing the requirement of RLR signaling for IFN production. Furthermore, being induced by both IRF3 and IFN signaling [406–408], IFIT1 expression was only impacted at later time points, whereas MX1, canonically strictly dependent on IFN signaling [173, 297, 409, 410], was considerably affected throughout the experimental time frame. Nevertheless, even in the absence of IFN signaling MX1 expression was still considerably induced, which has not been widely appreciated previously but has been demonstrated upon HCMV infection in human fibroblasts [277]. Interestingly, although the STAT proteins are not classified as ISGs by definition, STAT2 still contains a weak ISRE element in its promoter region, triggering upregulation of STAT2 upon type I IFN signaling [411]. Analyzing protein expression upon synchronous dsRNA stimulation in A549 wt and IFNR DKO cells strongly corroborated the IFN-induced expression of STAT1 and STAT2 (Figure 6D). The specific function of positive feedback regulation of STAT2 during antiviral signaling has not been determined yet. However, STAT1 upregulation was reported to be crucial for prolonging the induction of ISG expression [412], which could be conceivable for STAT2 as well.

Interestingly, recent studies assigned important tasks to unphosphorylated STATs (U-STAT) in IFN-dependent as well as IFN-independent conditions. Although U-STATs are able to shuttle between nucleus and cytoplasm, the nuclear export rate usually localizes most U-STATs to the cytoplasm at steady state [413]. However, some studies identified nuclear-localized U-STATs, which was proposed to be due to U-STAT association with DNA or chromatin, U-STAT association with non-STAT TFs such as IRF1, or direct contact with the nuclear pore complex [414–416]. For instance, in unstimulated conditions, the direct association of U-STAT1 with IRF1 was demonstrated to support the transcription and thus constitutive expression of the ISG low molecular mass polypeptide 2 (LMP2) in fibrosarcoma cells [416]. Furthermore, exogenously increased concentration of U-STAT1 in IFN-independent conditions increased the expression of a distinct subset of ISGs including IFI27, IFI44, OAS, bone marrow stromal cell antigen 2 (BST2), and even STAT1 itself [412]. It was hypothesized that increased U-STAT1 concentrations might occur through the accumulation of newly syn-

thesized STAT1 as a result of a positive feedback loop upon type I IFN signaling. Accordingly, prolonged IFN-β exposure was proposed to induce the expression of U-STAT2 and IRF9, which, together with U-STAT1, resulted in the formation of an unphosphorylated ISGF3 complex (U-ISGF3). Upon nuclear translocation, U-ISGF3 maintained the expression of a subset of ISGs, resulting in prolonged resistance to viruses and DNA damage [417].

Remarkably, since RIG-I protein expression appeared to only be slightly affected by the KO of IFN receptors but was clearly upregulated over time (Figure 6B), this suggests that the RLR pathway itself might exhibit an IFN-independent feedback regulation through which the pathway reinforces itself, e.g., by upregulation of the sensor RIG-I. This was even more pronounced for MDA5, whose protein expression was completely unaffected by the KO of IFN receptors and was still clearly upregulated upon dsRNA stimulation (Figure 6B). Since protein expression of both RIG-I and MDA5 appears to mostly be IFN-independent, it is conceivable that in IFN-independent conditions, U-ISGF3 or U-STAT1/2 mediate the expression of the RLR sensors.

For a holistic view of the cell-intrinsic antiviral response, feedback regulation of the RLR system through IFN has to be considered, especially over a period of more than 4 hours after which secreted IFN can be detected (Figure 5C). Consequently, we coupled our core RIG-I model to a previously published model of type I IFN signaling [288]. For this purpose, produced IFN was employed as the major output of the RIG-I model and used as input dose for the model of type I IFN-triggered signaling. Similar to our model of the core RIG-I signaling pathway, the IFN model is based on ODEs and was established with quantitative immunoblot data. Experimentally, Maiwald and colleagues used IFN-α for stimulation, which, however, is not produced downstream of RLRs in our cell system (Supplementary Figure S16) and further employed the human hepatoma cell line Huh7.5. Unlike A549, Huh7.5 cells harbor a mutation in the first CARD domain of RIG-I, thereby uncoupled signal transduction from viral RNA binding and hence lack functional RLR signaling upon viral RNA detection [418].

Remarkably, all kinetic rate constants of the IFN pathway model could be applied to our combined model of the full antiviral innate immune response, despite the two models being fitted to data from two distinct cell lines. The combined model of RIG-I and IFN signaling accurately reproduced the measured kinetic data after only adjusting the initial protein concentrations to the ones measured in A549 (Figure 7). Although previously demonstrated for two distinct hepatoma cell lines and primary human hepatocytes [349], the obtained findings decisively emphasize the high degree of conservation of the antiviral pathway across different cell types.

Nevertheless, to further corroborate the potential of the combined model of antiviral signaling to be adapted to cell types it was not trained for, I validated it using synchronous stimulation and kinetic measurements of the unrelated HepG2 cell line. Likewise, the sole adjustment of the cell line-specific initial protein concentrations sufficed for the combined model to accurately predict RLR and IFN signaling dynamics in HepG2 cells upon synchronous dsRNA stimulation (Figure 9, Figure 10). As a result, this indicates that, by only

adjusting the initial concentrations of the proteins involved in this signaling pathway, the combined model is generalizable to a range of distinct cell lines. Consequently, it serves as a valuable tool to examine antiviral signaling kinetics even with small experimental data sets. However, additional regulatory systems which are not represented in the model might need further consideration for some other cell types, e.g., cells of the professional immune system. Additionally, transcription factors with overlapping function, which require modifications of the model topology might exist in certain cell types. For instance, although highly similar to IRF3, the transcription factor IRF7 is not expressed in A549 cells [287]. It is, however, highly expressed in, e.g., pDCs, rendering them able to produce large amounts of IFN, including INF-α, even prior to the positive feedback loop through the IFN signaling pathway [285, 286, 419].

5.3 Impact of Viral Antagonists on RLR and IFN Signaling

The evolutionary battle between pathogens and their hosts resulted in a continuous improvement and adaptation of the host immune system. In turn, given the crucial impact of the IFN response on the outcome of viral infections, viruses evolved intricate mechanisms to counteract and evade cell-intrinsic innate immune responses. Depending on the viral evasion strategy, immune responses can either be delayed or overall dampened, providing an opportunity for efficient virus replication (reviewed in [6, 362, 363]). Stealth viruses, such as the hepatitis B virus (HBV), omit the initial recognition by PRRs and are thus able to establish themselves within a cell without inducing innate immune responses [420, 421]. In contrast, cunning viruses strongly induce innate immune responses, however, they developed several evasion strategies which include viral antagonists of host cellular antiviral responses [421, 422]. These virus-encoded factors display a wide range of points of attack or target proteins, and distinct virus families might target different cellular processes [423]. In fact, HCV is a prominent example for cunning viruses with multiple strategies. Besides evading RIG-I detection of its replicating RNA through HCV-induced membrane rearrangements [424], it cleaves MAVS, TRIF, and RIPLET to prevent downstream signaling [326, 425–429]. Additionally, HCV inhibits STAT1 to prevent ISG expression and further induces mitophagy to restrict IFN production [430, 431].

Although many viral antagonists have been characterized in detail, most studies are limited to strong overexpression of the viral protein and end-point determination of the degree of inhibition. However, the gradual increase of viral protein concentrations upon viral replication and gene expression in actual infections still needs to be considered. Thus, investigating the dynamics of the immune response as well as the dynamic impact of viral antagonists is crucial to determine the outcome of an infection. Moreover, the abundant and multi-level evasion strategies, interfering at every step of the antiviral signaling cascade, require a systematic approach to identify and characterize these distinct mechanisms and further promote, e.g., the development of therapeutics. Ultimately, this will provide insights into the

cellular antiviral signaling system, viral immune evasion, and virus-host interactions.
The previously described dynamic pathway model may offer a valuable tool for studying these virus-host interactions. To corroborate this, I have selected a couple of well-known viral proteins interfering with the host antiviral defense system at defined steps: the NS3/4A protease of HCV, the N^{pro} protease of CSFV, as well as NS1 of IAV all target RLR signaling and thereby inhibit IFN production, whereas DENV NS5 interferes with IFN signaling. Lastly, exhibiting a multi-level strategy to impede the antiviral system, the ORF6 protein of SARS-CoV-2 targets both IFN induction and IFN signaling.

5.3.1 NS3/4A protease of HCV

NS3/4A is a pivotal protease involved in polyprotein processing, maturation of the HCV nonstructural proteins, and thus HCV replication [432]. In fact, many studies focus on the development of direct-acting antiviral (DAA) agents, which interfere with the function of vital HCV proteins. Several DAAs inhibiting the NS3/4A protease, e.g., telaprevir and simeprevir, are commercially available and used for treatment of HCV infections (reviewed in [433, 434]). However, in addition to being pivotal for HCV replication, NS3/4A also suppresses the host innate antiviral response by efficiently cleaving and thereby inactivating the central adaptor protein MAVS [326]. Analyzing the impact of NS3/4A on RLR-mediated antiviral signaling demonstrated an overall dampening effect on IFIT1 mRNA expression (Figure 11). Coherent with NS3/4A targeting the primary induction phase upon viral dsRNA recognition, the inhibitory effect was most prominent for the very early time points.

5.3.2 N^{pro} protein of CSFV

On the other hand, N^{pro} of CSFV triggers the degradation of IRF3 [321, 366] and thus also targets early RLR-mediated IFN induction. Interestingly, pDCs have been described to respond to CSFV with IFN-α and IFN-β production. Although N^{pro} is still able to interact with the cognate transcription factor IRF7, which is constitutively expressed in pDCs, IRF7-mediated type I IFN production seems to be reduced but less affected by N^{pro} [435, 436]. N^{pro} additionally interacts with the NF-κB inhibitor, IκBα, but this interaction was reported to have no impact on NF-κB nuclear translocation [437]. Thus, in contrast to NS3/4A, NF-κB signaling remains unaffected and should allow for the production of some pro-inflammatory cytokines, such as IL-1β [438–440]. Intriguingly, the impact of N^{pro} on early IFIT1 induction was substantially stronger than the effect of NS3/4A (Figure 12), suggesting a more efficient target protein inactivation. Simulating the effects of these two viral antagonists with the mathematical model very closely resembled the experimentally observed kinetic impact of both NS3/4A and N^{pro} on RLR signaling (Figure 11D, Figure 12E).

5.3.3 NS5 protein of DENV

NS5 of DENV is comprised of distinct domains involved in various functions promoting viral replication and immune evasion. Whereas the methyltransferase domain is important for RNA capping during polyprotein translation [441], the RNA-dependent RNA polymerase (RdRp) is required for viral replication [442]. In contrast to NS3/4A and N^{pro}, NS5 of DENV impairs signaling downstream of the IFN receptors by targeting STAT2 for proteasomal degradation [332,333]. Consequently, I observed a strong NS5-mediated impact on IFIT1 induction at later time points, where its expression is mostly mediated by the IFN-dependent transcription factor ISGF3 (Figure 13E). However, NS5 surprisingly also exhibited a clear effect at earlier time points, which was distinct from a pure STAT2-mediated effect as demonstrated experimentally or by model simulations (Figure 13F, G). This argues for the existence of additional targets of NS5, which might potentially reside within the induction phase of the antiviral response system. In fact, a previous study proposed an interaction of NS5 and the death domain associated protein (Daxx) protein, in which NS5 competes with the NF-κB/Daxx interaction and thus leads to NF-κB release and the subsequent expression of RANTES [443, 444]. Only recently, high-throughput studies and bioinformatic analyses additionally suggested that NS5 interacts with diverse host proteins, many of which are involved in the spliceosome machinery (reviewed in [445]). One study demonstrated, that DENV NS5 binds to spliceosome complexes thereby reducing the efficiency of pre-mRNA processing and might, thus, indirectly impair antiviral signaling [446]. Following up on this in future studies could provide mechanistic insights into how NS5 further impairs antiviral innate immune signaling.

5.3.4 ORF6 protein of SARS-CoV-2

Lastly, ORF6 of the recently emerged SARS-CoV-2 impedes both IFN induction and IFN signaling [369], mostly by concurrently blocking nuclear translocation of IRF3 [341,342], STAT1, and STAT2 [344]. Thus, in contrast to the previous viral proteins, ORF6 targets both, RLR and IFN-mediated antiviral signaling responses. In addition to blocking TF nuclear translocation, ORF6-mediated blocking of the nuclear pore can further cause nuclear retention of host mRNAs, which might lead to an even stronger reduction in host gene expression [343]. Surprisingly, although ORF6 was reported to be amongst the strongest SARS-CoV-2 antagonists in 293T cells [369], and even though the production of IFIT1 and IFN-β luciferase upon SeV infection was significantly affected in ORF6-expressing A549 cells, ORF6 expression had no impact on IFIT1 and IFNB1 mRNA expression upon 5'ppp-dsRNA electroporation (Figure 15). Whether these inconsistent outcomes are a result of the different stimulation approaches or are associated with the nuclear retention of host mRNAs remains to be investigated. Hence, I examined the kinetic impact of ORF6 on antiviral signaling in HepG2 cells. In contrast to A549 cells, ORF6 affected both SeV-induced luciferase expression and dsRNA-induced mRNA expression in HepG2. Here, ORF6 had a modest impact

at the early phase upon dsRNA stimulation, but considerably reduced the level of IFIT1 and IFNB1 mRNA expression beginning at 2 to 4 hours after synchronous stimulation (Figure 15). This confirms ORF6-mediated inhibition of both RLR and IFN-induced antiviral signaling but further indicates that ORF6 exhibits a stronger antagonistic effect on signaling events downstream of the IFN receptor(s). Remarkably, this was corroborated by simulating IFIT1 and IFNB1 mRNA expression upon simultaneously reduced IRF3 and STAT2 levels in our mathematical model (Figure 15), approximating the experimental data much closer than only limiting IRF3 or STAT2 activity (Figure 12, Figure 13). Although the underlying reason for the observed differences of ORF6 antagonism in A549 and HepG2 cells remains elusive, unappreciated cell type specific-effects might contribute to this.

5.4 IFN-Independent RLR Signaling upon Synchronous dsRNA Stimulation

IFN-γ, the only type II IFN, is known to be predominantly produced by lymphoid cells [204, 447, 448], and although A549 cells express the required IFN gamma receptor (IFNGR) and are thereby able to transduce IFN-γ-induced signaling, there is limited evidence for A549 cells producing IFN-γ themselves. However, as demonstrated in a previous study, specific circumstances, specifically *M. tuberculosis* infection, might in fact induce IFN-γ expression in A549 cells [373]. Consequently, the characterization of an actual IFN-independent RLR signaling response required an additional knockout of the type II IFN receptor, generating a true "IFN-blind" cell line in which the receptors for all three IFN types are knocked out.
Reassuringly, mRNA and protein expression kinetics upon synchronous dsRNA stimulation was comparable between A549 IFNR DKO and IFNR TKO cells (Figure 5, Figure 16). Induction dynamics of the examined IFNs was not affected in both cell lines and initial IFN secretion was detected 4 hours upon stimulation. Similarly, IFIT1 expression was only impacted at later time points at which its expression is dependent on IFN feedback, whereas MX1 expression was affected throughout the experimental time frame (Figure 16).

5.4.1 IFN-Independent Cytokine and Chemokine Production

Apart from IFNs, several other cytokines and chemokines have been described to be induced by virus infection, predominantly through NF-κB signaling, and to be crucial for antiviral defenses (reviewed in [449–451]). Interestingly, a recent study suggested that virus-induced RLR signaling mediates a pro-inflammatory response using two distinct pathways [452]. Whereas the first pathway required RIG-I-mediated activation of NF-κB through the formation of a trimeric complex comprising MAVS, CARD9, and B-cell lymphoma/leukemia 10 (Bcl-10), in the second pathway RIG-I additionally bound the adapter protein ASC to trigger caspase-1-dependent inflammasome activation. However, this mechanism was independent of MAVS, CARD9, as well as NLRP3. Thus, this study suggests the CARD9/Bcl-10

module to be an essential component of the RIG-I-mediated pro-inflammatory response and further indicates that RIG-I is able to activate the inflammasome in response to some RNA viruses. Although a large number of studies demonstrate the ability of IFN signaling to trigger and regulate inflammatory responses, the vast majority of examined cytokine and chemokine promoters harbor regions to respond to signals from classical inflammatory pathways (reviewed in [453]).

Thus, to examine the effect of IFN signaling on inflammatory responses upon dsRNA stimulation, I used A549 wt and IFNR TKO cells and measured secreted cytokines and chemokines. Similar to the production of IFNs, upon dsRNA stimulation the production and secretion of certain examined cytokines and chemokines was IFN-independent (Figure 17). However, a considerable IFN-dependency was still apparent, especially for IP-10, MCP-1, MIP-1α, MIP-1β, as well as the pro-inflammatory cytokine TNF. In contrast, the chemokines MDC and TARC, as well as the pro-inflammatory cytokine IL-6 only exhibited minor IFN-dependencies, whereas MCP-4 was not produced at all in both A549 wt and IFNR TKO cells. Interestingly, MIP-1α (also known as CCL3) and MIP-1β (also known as CCL4) were reported to be upregulated upon IFN stimulation in various mouse cell lines [454, 455], whereas the contrary effect was demonstrated for human pDCs and T cells [456, 457]. This contradicts the obtained results of an impaired MIP-1α and MIP-1β expression in IFN signaling incompetent cells, indicating that individual IFN stimulations might not be sufficient to characterize the regulatory mechanisms of inflammatory responses.

5.4.2 IFN-Independent Feedback Regulation of RIG-I

Interestingly, analyzing protein expression dynamics in A549 wt and IFNR TKO cells, RIG-I expression again appeared to only be slightly affected by the KO of IFN receptors but was clearly upregulated over time, further emphasizing a type I, II, and III IFN-independent feedback regulation of RIG-I. Although some RLR-induced genes have been described, given the difficulty in dissecting RLR and IFN-mediated responses, this has not been widely appreciated previously. However, recently Szabo *et al.* demonstrated a type I IFN-independent upregulation of RIG-I expression in pDCs upon stimulation of TLR7 or TLR9 with TLR ligands [458]. Intriguingly, a canonical IRF1-binding site was identified in the RIG-I promoter [459], which could induce RIG-I expression in an IFN-independent manner. In fact, the related transcription factor IRF2 was reported to enhance RIG-I expression *in vitro* [460]. Recently, an interesting study identified a novel mechanism through which RIG-I IFN-independently limits hepatitis E virus (HEV) infection [283]. Activation of RIG-I resulted in an IRF3, IRF7, and IFN-independent induction of antiviral responses, which, however, were partially regulated by the activation of JAK/STAT signaling. Based on these studies, the classical paradigm of initial RLR-mediated production of IFNs and subsequent IFN-induced expression of antiviral effectors might disregard other existing regulatory mechanisms of antiviral signaling. Thus, in a next step, I utilized IFN-blind A549 cells to dissect primary RLR-mediated and secondary

IFN-mediated signaling responses and further characterized kinetic differences upon synchronous dsRNA stimulation.

5.5 IFN-Independent RLR Signaling and the Underlying Influence of Distinct Transcription Factors

Previous studies from our lab focused on examining transcriptional responses in A549 wt and IFNR DKO cells upon RIG-I stimulation. Surprisingly, a time-resolved, full-genomic transcriptomic analysis revealed an unexpectedly high overlap of ISG expression in both cell lines, indicating that RLR-induced activation of antiviral defense responses might already be sufficient for the cellular antiviral state. In fact, in collaboration with the Dittmann lab in New York, we observed a virus-specific response in A549 cells lacking the IFN receptors (i.e., A549 IFNR TKO cells), indicating that already these directly induced genes are able to affect viral replication. Moreover, the identified ISGs could be clustered in different kinetic classes: early induced but transient genes, late induced but sustained genes, as well as generally up or downregulated genes. Intriguingly, an extremely rapid response was observed for certain transcription factors including IRF1, which was activated upon both dsRNA and type I IFN stimulation.

5.5.1 DEGs in IFN and MAVS, IRF3, or IRF1-Independent Conditions

In view of this, I generated additional single KOs in the A549 IFNR TKO cell line, specifically MAVS (IFNR TKO MAVS KO), IRF3 (IFNR TKO IRF3 KO), and the above-mentioned IRF1 (IFNR TKO IRF1 KO) and aimed at analyzing and comparing the impact of those proteins in IFN-independent primary RIG-I signaling. Thus, I performed whole-genome transcriptomic profiling upon synchronous dsRNA stimulation and identified significantly up or downregulated genes (Figure 19). In essence, dsRNA-induced expression of certain genes was both IRF3 and IFN-independent. The dsRNA-induced expression of some of those genes was partially NF-κB-dependent, whereas others seemed to be dependent on IRF1 or other transcription factors.

All cell lines showed significantly regulated transcripts upon synchronous 5'ppp-dsRNA stimulation, even if MAVS and IFN-mediated signaling, and thus key mediators of the antiviral response, were impaired. In line with previous results, the A549 IFNR TKO cell line induced the expression of classical ISGs (IFIT1, -2, -3, CCL5, OASL), as well as IFNs (IFNB1, IFNL1, -2, -3) upon 5'ppp-dsRNA stimulation, which further corroborates the IFN-independent production of IFN upon RLR stimulation. Strikingly, mRNA expression of both RIG-I and MDA5 (IFIH1) was induced upon synchronous 5'ppp-dsRNA stimulation in an IFN-independent manner. However, although previous reports identified an IRF1-binding site in the RIG-I promoter [459], assumed to induce RIG-I expression in an IFN-independent manner, the additional KO of IRF1 indicated otherwise. Here, RIG-I expression was up-

regulated upon IRF1 KO, increasing from a 26-fold induction in IFNR TKO cells to a 31-fold induced expression in the IFNR TKO IRF1 KO cell line. This rather suggests a negative regulatory mechanism of IRF1 on RIG-I expression. Notably, whereas RIG-I expression was completely diminished in IFNR TKO MAVS KO cells, it was slightly upregulated in the IFNR TKO IRF3 KO cell line (5-fold), indicating that RIG-I might also be regulated through an IRF3-independent but MAVS-dependent pathway. However, the major IFN-independent induction of RIG-I expression seems to be directly or indirectly mediated by IRF3. Expectedly, the additional knockout of the adapter protein MAVS or the transcription factor IRF3 mostly inhibited the induction of IFN and classical ISG expression. However, in contrast to the IFNR TKO MAVS KO cell line, IFNR TKO IRF3 KO cells exhibited an NF-κB pathway signature by inducing the expression of NF-κB target genes, e.g., the chemokine CXCL8 (also known as IL-8) or negative regulators of NF-κB signaling, such as TNFAIP3 or the activating transcription factor (ATF) 3.

5.5.1.1 ATF3 and DDIT3

Although upregulated in the IFNR TKO cell line upon dsRNA stimulation (26-fold), the additional KO of IRF3 considerably induced ATF3 expression (38-fold). ATF3 is a member of the CREB family and constitutes a stress-induced transcription factor, which binds to cyclic AMP response elements (CRE) in various promoters. ATF3 expression was reported to be induced by numerous signals, such as ER stress, cytokines, chemokines, and LPS, and it is thus involved in a wide range of cellular systems, including immunity or oncogenesis (reviewed in [461]). Upon sustained cellular stress, the expression of the ATF3 downstream target DNA damage inducible transcript 3 (DDIT3, also known as CHOP) is induced, resulting in the expression of pro-apoptotic proteins and eventually apoptosis [462–465]. Both ATF3 and DDIT3 are significantly upregulated in A549 IFNR TKO IRF3 KO cells upon dsRNA stimulation. Notably, we previously observed a dsRNA-induced expression of DDIT3 and ATF3 in A549 wt and IFNR DKO cells which, however, was absent in mock electroporation (Master's Thesis, Carola Sparn). Interestingly, in another project from our lab, DDIT3 was identified as an essential component of IRF1-mediated cell death in A549 cells upon doxorubicin treatment (MD thesis, David Zander). However, although ATF3 has been reported to be a negative regulator of cellular antiviral signaling [466], a regulatory effect of IRF3 on ATF3/DDIT3 upon RLR signaling has not yet been identified. A mechanism through which IRF1 interacts with IRF3 and thereby regulates ATF3/DDIT3 expression upon viral infections might be assumed but requires further investigation.

5.5.1.2 CH25H

In numerous studies, the cholesterol 25-hydroxylase (CH25H) was reported to exert broad antiviral activities. For instance, CH25H efficiently inhibits HCV infection in hepatocytes by modulating host lipid biosynthesis [467]. Furthermore, CH25H was demonstrated to

inhibit SARS-CoV-2 replication by restricting spike protein-mediated membrane fusion [468]. Although initially characterized as being an ISG, the IFN-dependency of CH25H expression is still highly disputed. Whereas one report demonstrated CH25H expression in primary human hepatocytes to be significantly induced by type I IFN [469], another study stated that IFN-α and IFN-γ stimulation did not induce CH25H expression in those cells [467]. In A549 cells, CH25H expression was IFN-independent and strongly induced upon dsRNA stimulation. Intriguingly, whereas the expression of CH25H was induced 42-fold in IFNR TKO cells, the additional KO of IRF1 reduced CH25H expression, resulting in a 20-fold induction. The KO of IRF3 and MAVS, however, completely diminished CH25H expression upon dsRNA stimulation, indicating that CH25H expression is directly induced by the canonical RLR signaling pathway. Interestingly, in primary macrophages IRF1 was required for optimal CH25H expression and thus the restriction of gammaherpesvirus replication [470]. However, the mechanism through which IRF1 contributes to CH25H expression upon dsRNA stimulation is still elusive.

5.5.1.3 IRF1, IFIT1, and IFN

Surprisingly, whereas IRF1 expression itself was 8-fold upregulated in IFNR TKO cells, which was reduced to 4-fold in the IFNR TKO MAVS KO cell line, the KO of IRF3 increased IRF1 mRNA induction to 15-fold. Whereas IRF1 was demonstrated to enhance IRF3-mediated antiviral responses [471], the upregulation of IRF1 in IFNR TKO IRF3 KO cells might suggest an additional negative regulatory function of IRF3 on IRF1 expression upon dsRNA stimulation. The positive regulatory function of IRF1 on IRF3-mediated antiviral signaling, however, could be corroborated by examining IFN and classical ISG expression in the distinct KO cell lines. For instance, upon dsRNA stimulation IFN-β expression was predominantly induced in IFNR TKO cells (75-fold), less expressed in IFNR TKO IRF1 KO cells (55-fold), and not induced in the IFNR TKO IRF3 KO cell line. Another example, although less pronounced, constitutes IFIT1 expression, which was 81-fold induced in IFNR TKO, 73-fold in IFNR TKO IRF1 KO, and not expressed in IFNR TKO IRF3 KO cells. Similarly, IFN-λ1 expression was induced to 110-fold, 78-fold, and 3-fold in the IFNR TKO, IFNR TKO IRF1 KO, and IFNR TKO IRF3 KO cell line, respectively. Interestingly, the additional KO of MAVS further reduced IFN-λ1 mRNA expression, indicating a small portion of IRF3-independent and probably MAVS/NF-κB-mediated expression.

5.5.2 IFN and IRF1 or IRF3-Independent RIG-I-Mediated Signaling

To further decipher the specific impact of IRF3 and IRF1 on mRNA expression, I compared differentially expressed genes upon dsRNA stimulation in the IFNR TKO IRF3 KO and IFNR TKO IRF1 KO cell line (Figure 22). Apart from IFNs and certain ISGs, which are still upregulated in IFNR TKO IRF1 KO cells but absent in the IFNR TKO IRF3 KO cell line, also the expression of zinc finger NFX1-type containing 1 (ZNFX1) protein was significantly induced

in the IFNR TKO IRF1 KO cell line. ZNFX1 is reported to be an IFN-induced, mitochondria-localized helicase belonging to the helicase superfamily 1 (SF1). Similar to RIG-I and MDA5, ZNFX1 acts as a dsRNA sensor which can interact with MAVS and thus promote IFN and ISG expression [472]. ZNFX1 further enhances the expression of RLRs and thus primes the subsequent antiviral defense. Consequently, loss of ZNFX1 results in an impairment of IFN production and thus in an increased susceptibility to viral infection [472, 473]. Although ZFNX1 is able to induce IFN and ISG expression, this seems to be RLR, TRIF, MyD88, and STING-independent [472]. However, the lack of ZFNX1 expression in the IFNR TKO IRF3 KO cell line (Figure 22) hints towards an IRF3-dependent positive feedback regulation.
Conversely, the expression of serpin family A member 3 (SERPINA3, also known as α1 antichymotrypsin (ACT)) is strongly induced in IFNR TKO IRF3 KO cells, suggesting a negative feedback regulation mechanism which seems to be IRF1 but also MAVS-independent. SERPINA3 belongs to the most broadly distributed superfamily of protease inhibitors and its dysregulation has been associated with various diseases, such as Alzheimer's and prion disease (reviewed in [474]). Its close relative, SERPINA1 (also known as alpha-1-antitrypsin (A1AT)), has been described to have anti-inflammatory as well as antiviral properties, in particular against HIV and SARS-CoV-2 [475–477]. Although SERPINA3 has not yet been specifically described to be involved in antiviral signaling, its promoter still harbors binding sites for NF-κB, AP-1, and STAT1/3 [478–481]. Moreover, SERPINA3 has a unique function to bind to DNA, although the physiological significance of this binding is still unclear [482]. However, unveiling the mechanism through which SERPINA3 is regulated by IRF3 upon dsRNA stimulation might provide further insights into this.

5.6 Conclusion

In this study, having established an approach permitting the synchronous stimulation of A549 cells with virus like dsRNA, I characterized the dynamics of cell-intrinsic innate immune signaling to virus infection. Using IFN-blind A549 cells, I was able to dissect the induction phase downstream of RLRs and the secondary effector phase downstream of the IFN receptors, which are usually tightly interconnected and overlapping. The generated quantitative time-resolved data further served as basis to set up and calibrate a comprehensive, mechanistic dynamic pathway model of the cell-intrinsic antiviral response system. This model accurately predicts the kinetics of signaling events downstream of RNA recognition by RIG-I, including the feedback and expansion of the response by secreted IFN and JAK/STAT signaling. Moreover, owing to its mechanistic structure, the model is capable to simulate viral immune antagonism and can thus be used to investigate the mechanisms of novel virus-encoded antagonists. Combining our model with models of virus infection and replication might provide further mechanistic understanding of these intricate virus-host interactions, which are decisive for, e.g., the development of diseases. Such models have for instance been described for the interplay between intracellular DENV replication and the

host innate immune signaling [483] and pathogen-host interactions have been modelled at various levels as well [348, 484–487].

Lastly, since previous work in the lab demonstrated an unexpectedly high overlap of ISG expression in A549 wt and IFN-blind cells, using transcriptomic profiling I began dissecting the differences between primary RLR-mediated and IFN-dependent antiviral responses. Further, I focused on the specific function of the transcription factors IRF3 and IRF1 in IFN-independent antiviral signaling. Whereas the IFN-blind cells already induced the expression of numerous genes upon dsRNA stimulation, they also induced the expression of IFN itself which was strictly IFN-independent and has not been highly appreciated previously. Although I only examined a limited set of time points (0 hours and 8 hours upon stimulation), the transcriptomic analysis gave further insights into possible regulatory functions of IRF1 and/or IRF3 on mRNA expression upon dsRNA stimulation. These findings provide a foundation for future research on deciphering the differences of RLR and IFN-mediated signaling and the underlying function of distinct transcription factors, in particular IRF1.

Bibliography

[1] Mackay, I. R., Rosen, F. S., Delves, P. J. & Roitt, I. M. The Immune System. *The New England Journal of Medicine* **343**, 108–117 (2000).

[2] Mackay, I. R., Rosen, F. S., Delves, P. J. & Roitt, I. M. The Immune System. *The New England Journal of Medicine* **343**, 37–49 (2000).

[3] Buchmann, K. Evolution of Innate Immunity: Clues from Invertebrates via Fish to Mammals. *Frontiers in Immunology* **5**, 459 (2014).

[4] Kimbrell, D. A. & Beutler, B. The evolution and genetics of innate immunity. *Nature Reviews Genetics* **2**, 256–267 (2001).

[5] Majzoub, K., Wrensch, F. & Baumert, T. F. The Innate Antiviral Response in Animals: An Evolutionary Perspective from Flagellates to Humans. *Viruses* **11**, 758 (2019).

[6] Kikkert, M. Innate Immune Evasion by Human Respiratory RNA Viruses. *Journal of Innate Immunity* **12**, 1–17 (2019).

[7] Badwey, J. A. *et al.* Comparative aspects of oxidative metabolism of neutrophils from human blood and guinea pig peritonea: Magnitude of the respiratory burst, dependence upon stimulating agents, and localization of the oxidases. *Journal of Cellular Physiology* **105**, 541–551 (1980).

[8] Bazzoni, F., Cassatella, M. A., Laudanna, C. & Rossi, F. Phagocytosis of Opsonized Yeast Induces Tumor Necrosis Factor-α mRNA Accumulation and Protein Release by Human Polymorphonuclear Leukocytes. *Journal of Leukocyte Biology* **50**, 223–228 (1991).

[9] Haziot, A., Tsuberi, B. Z. & Goyert, S. M. Neutrophil CD14: biochemical properties and role in the secretion of tumor necrosis factor-alpha in response to lipopolysaccharide. *Journal of Immunology* **150**, 5556 (1993).

[10] Cassatella, M. *et al.* IL-8 production by human polymorphonuclear leukocytes. The chemoattractant formyl-methionyl-leucyl-phenylalanine induces the gene expression and release of IL-8 through a pertussis toxin-sensitive pathway. *Journal of Immunology* **148**, 3216 (1992).

[11] Scapini, P. *et al.* The neutrophil as a cellular source of chemokines. *Immunological Reviews* **177**, 195–203 (2000).

[12] Moqbel, R., Levi-Schaffer, F. & Kay, A. Cytokine generation by eosinophils. *Journal of Allergy and Clinical Immunology* **94**, 1183–1188 (1994).

[13] Schwartz, C., Eberle, J. U. & Voehringer, D. Basophils in inflammation. *European Journal of Pharmacology* **778**, 90–95 (2016).

[14] Chaplin, D. D. Overview of the immune response. *Journal of Allergy and Clinical Immunology* **125**, S3–S23 (2010).

[15] Karsunky, H., Merad, M., Cozzio, A., Weissman, I. L. & Manz, M. G. Flt3 Ligand Regulates Dendritic Cell Development from Flt3+ Lymphoid and Myeloid-committed Progenitors to Flt3+ Dendritic Cells In Vivo. *The Journal of Experimental Medicine* **198**, 305–313 (2003).

[16] Manz, M. G., Traver, D., Miyamoto, T., Weissman, I. L. & Akashi, K. Dendritic cell potentials of early lymphoid and myeloid progenitors. *Blood* **97**, 3333–3341 (2001).

[17] Villadangos, J. A. & Young, L. Antigen-Presentation Properties of Plasmacytoid Dendritic Cells. *Immunity* **29**, 352–361 (2008).

[18] Feldman, M. & Fitzgerald-Bocasly, P. Sequential Enrichment and Immunocytochemical Visualization of Human Interferon-α-Producing Cells. *Journal of Interferon Research* **10**, 435–446 (1990).

[19] Fitzgerald-Bocarsly, P. Human natural interferon-α producing cells. *Pharmacology & Therapeutics* **60**, 39–62 (1993).

[20] Rönnblomo, L., Ramstedt, U. & Alm, G. V. Properties of human natural interferon-producing cells stimulated by tumor cell lines. *European Journal of Immunology* **13**, 471–476 (1983).

[21] Sandberg, K., Eloranta, M.-L., Johannisson, A. & Alm, G. V. Flow Cytometric Analysis of Natural Interferon-α Producing Cells. *Scandinavian Journal of Immunology* **34**, 565–576 (1991).

[22] Cella, M. *et al.* Plasmacytoid monocytes migrate to inflamed lymph nodes and produce large amounts of type I interferon. *Nature Medicine* **5**, 919–923 (1999).

[23] Jarrossay, D., Napolitani, G., Colonna, M., Sallusto, F. & Lanzavecchia, A. Specialization and complementarity in microbial molecule recognition by human myeloid and plasmacytoid dendritic cells. *European Journal of Immunology* **31**, 3388–3393 (2001).

[24] Lee, H. K., Lund, J. M., Ramanathan, B., Mizushima, N. & Iwasaki, A. Autophagy-Dependent Viral Recognition by Plasmacytoid Dendritic Cells. *Science* **315**, 1398–1401 (2007).

[25] Gilliet, M., Cao, W. & Liu, Y.-J. Plasmacytoid dendritic cells: sensing nucleic acids in viral infection and autoimmune diseases. *Nature Reviews Immunology* **8**, 594–606 (2008).

[26] Lee, S.-H., Miyagi, T. & Biron, C. A. Keeping NK cells in highly regulated antiviral warfare. *Trends in Immunology* **28**, 252–259 (2007).

[27] Prager, I. & Watzl, C. Mechanisms of natural killer cell-mediated cellular cytotoxicity. *Journal of Leukocyte Biology* **105**, 1319–1329 (2019).

[28] Watzl, C. Chapter Five How to Trigger a Killer Modulation of Natural Killer Cell Reactivity on Many Levels. *Advances in Immunology* **124**, 137–170 (2014).

[29] Watzl, C. & Urlaub, D. Molecular mechanisms of natural killer cell regulation. *Frontiers in Bioscience* **17**, 1418 (2012).

[30] Biron, C. A., Nguyen, K. B., Pien, G. C., Cousens, L. P. & Salazar-Mather, T. P. NATURAL KILLER CELLS IN ANTIVIRAL DEFENSE: Function and Regulation by Innate Cytokines. *Annual Review of Immunology* **17**, 189–220 (1999).

[31] Roh, J. S. & Sohn, D. H. Damage-Associated Molecular Patterns in Inflammatory Diseases. *Immune Network* **18**, e27 (2018).

[32] Tang, D., Kang, R., Coyne, C. B., Zeh, H. J. & Lotze, M. T. PAMPs and DAMPs: signal 0s that spur autophagy and immunity. *Immunological Reviews* **249**, 158–175 (2012).

[33] Zindel, J. & Kubes, P. DAMPs, PAMPs, and LAMPs in Immunity and Sterile Inflammation. *Annual Review of Pathology: Mechanisms of Disease* **15**, 1–26 (2019).

[34] Akira, S., Uematsu, S. & Takeuchi, O. Pathogen Recognition and Innate Immunity. *Cell* **124**, 783–801 (2006).

[35] Gasteiger, G. *et al.* Cellular Innate Immunity: An Old Game with New Players. *Journal of Innate Immunity* **9**, 111–125 (2017).

[36] Kumagai, Y., Takeuchi, O. & Akira, S. Pathogen recognition by innate receptors. *Journal of Infection and Chemotherapy* **14**, 86–92 (2008).

[37] Ting, J. P.-Y. *et al.* The NLR Gene Family: A Standard Nomenclature. *Immunity* **28**, 285–287 (2008).

[38] Philpott, D. J., Sorbara, M. T., Robertson, S. J., Croitoru, K. & Girardin, S. E. NOD proteins: regulators of inflammation in health and disease. *Nature Reviews Immunology* **14**, 9–23 (2014).

[39] Greaney, A. J., Leppla, S. H. & Moayeri, M. Bacterial Exotoxins and the Inflammasome. *Frontiers in Immunology* **6**, 570 (2015).

[40] Kasper, L. *et al.* The fungal peptide toxin Candidalysin activates the NLRP3 inflammasome and causes cytolysis in mononuclear phagocytes. *Nature Communications* **9**, 4260 (2018).

[41] Lee, M.-S. *et al.* Shiga Toxins Activate the NLRP3 Inflammasome Pathway To Promote Both Production of the Proinflammatory Cytokine Interleukin-1β and Apoptotic Cell Death. *Infection and Immunity* **84**, 172–186 (2016).

[42] Rogiers, O. *et al.* Candidalysin Crucially Contributes to Nlrp3 Inflammasome Activation by Candida albicans Hyphae. *mBio* **10**, e02221–18 (2019).

[43] Skeldon, A. & Saleh, M. The Inflammasomes: Molecular Effectors of Host Resistance Against Bacterial, Viral, Parasitic, and Fungal Infections. *Frontiers in Microbiology* **2**, 15 (2011).

[44] Eigenbrod, T. & Dalpke, A. H. Bacterial RNA: An Underestimated Stimulus for Innate Immune Responses. *The Journal of Immunology* **195**, 411–418 (2015).

[45] Kanneganti, T.-D. *et al.* Bacterial RNA and small antiviral compounds activate caspase-1 through cryopyrin/Nalp3. *Nature* **440**, 233–236 (2006).

[46] Sha, W. *et al.* Human NLRP3 inflammasome senses multiple types of bacterial RNAs. *Proceedings of the National Academy of Sciences* **111**, 16059–16064 (2014).

[47] Saxena, M. & Yeretssian, G. NOD-Like Receptors: Master Regulators of Inflammation and Cancer. *Frontiers in Immunology* **5**, 327 (2014).

[48] Zhong, Y., Kinio, A. & Saleh, M. Functions of NOD-Like Receptors in Human Diseases. *Frontiers in Immunology* **4**, 333 (2013).

[49] Geijtenbeek, T. B. H. & Gringhuis, S. I. Signalling through C-type lectin receptors: shaping immune responses. *Nature Reviews Immunology* **9**, 465–479 (2009).

[50] Li, T.-H., Liu, L., Hou, Y.-Y., Shen, S.-N. & Wang, T.-T. C-type lectin receptor-mediated immune recognition and response of the microbiota in the gut. *Gastroenterology Report* **7**, 312–321 (2019).

[51] Ishikawa, H., Ma, Z. & Barber, G. N. STING regulates intracellular DNA-mediated, type I interferon-dependent innate immunity. *Nature* **461**, 788–792 (2009).

[52] Ishikawa, H. & Barber, G. N. STING is an endoplasmic reticulum adaptor that facilitates innate immune signalling. *Nature* **455**, 674–678 (2008).

[53] Bürckstümmer, T. *et al.* An orthogonal proteomic-genomic screen identifies AIM2 as a cytoplasmic DNA sensor for the inflammasome. *Nature Immunology* **10**, 266–272 (2009).

[54] Fernandes-Alnemri, T., Yu, J.-W., Wu, J., Datta, P. & Alnemri, E. S. AIM2 activates the inflammasome and cell death in response to cytoplasmic DNA. *Nature* **458**, 509–513 (2009).

[55] Hornung, V. *et al.* AIM2 recognizes cytosolic dsDNA and forms a caspase-1 activating inflammasome with ASC. *Nature* **458**, 514–518 (2009).

[56] Ablasser, A. *et al.* cGAS produces a 2′-5′-linked cyclic dinucleotide second messenger that activates STING. *Nature* **498**, 380–384 (2013).

[57] Sun, L., Wu, J., Du, F., Chen, X. & Chen, Z. J. Cyclic GMP-AMP Synthase Is a Cytosolic DNA Sensor That Activates the Type I Interferon Pathway. *Science* **339**, 786–791 (2013).

[58] Fore, F., Indriputri, C., Mamutse, J. & Nugraha, J. TLR10 and Its Unique Anti-Inflammatory Properties and Potential Use as a Target in Therapeutics. *Immune Network* **20**, e21 (2020).

[59] Kawai, T. & Akira, S. TLR signaling. *Cell Death & Differentiation* **13**, 816–825 (2006).

[60] Kawasaki, T. & Kawai, T. Toll-Like Receptor Signaling Pathways. *Frontiers in Immunology* **5**, 461 (2014).

[61] Li, D. & Wu, M. Pattern recognition receptors in health and diseases. *Signal Transduction and Targeted Therapy* **6**, 291 (2021).

[62] Liu, G. & Gack, M. U. Distinct and Orchestrated Functions of RNA Sensors in Innate Immunity. *Immunity* **53**, 26–42 (2020).

[63] Loo, Y.-M. & Gale, M. Immune Signaling by RIG-I-like Receptors. *Immunity* **34**, 680–692 (2011).

[64] Rehwinkel, J. & Gack, M. U. RIG-I-like receptors: their regulation and roles in RNA sensing. *Nature reviews. Immunology* 1–15 (2020).

[65] Saito, T. *et al.* Regulation of innate antiviral defenses through a shared repressor domain in RIG-I and LGP2. *Proceedings of the National Academy of Sciences* **104**, 582–587 (2007).

[66] Pippig, D. A. *et al.* The regulatory domain of the RIG-I family ATPase LGP2 senses double-stranded RNA. *Nucleic Acids Research* **37**, 2014–2025 (2009).

[67] Rothenfusser, S. *et al.* The RNA Helicase Lgp2 Inhibits TLR-Independent Sensing of Viral Replication by Retinoic Acid-Inducible Gene-I. *The Journal of Immunology* **175**, 5260–5268 (2005).

[68] Bruns, A., Leser, G., Lamb, R. & Horvath, C. The Innate Immune Sensor LGP2 Activates Antiviral Signaling by Regulating MDA5-RNA Interaction and Filament Assembly. *Molecular Cell* **55**, 771–781 (2014).

[69] Childs, K. S., Randall, R. E. & Goodbourn, S. LGP2 Plays a Critical Role in Sensitizing mda-5 to Activation by Double-Stranded RNA. *PLoS ONE* **8**, e64202 (2013).

[70] Kato, H. *et al.* Differential roles of MDA5 and RIG-I helicases in the recognition of RNA viruses. *Nature* **441**, 101–105 (2006).

[71] Loo, Y.-M. *et al.* Distinct RIG-I and MDA5 Signaling by RNA Viruses in Innate Immunity. *Journal of Virology* **82**, 335–345 (2008).

[72] Hornung, V. *et al.* 5'-Triphosphate RNA Is the Ligand for RIG-I. *Science* **314**, 994–997 (2006).

[73] Pichlmair, A. *et al.* RIG-I-Mediated Antiviral Responses to Single-Stranded RNA Bearing 5'-Phosphates. *Science* **314**, 997–1001 (2006).

[74] Schlee, M. *et al.* Recognition of 5' Triphosphate by RIG-I Helicase Requires Short Blunt Double-Stranded RNA as Contained in Panhandle of Negative-Strand Virus. *Immunity* **31**, 25–34 (2009).

[75] Schmidt, A. *et al.* 5'-triphosphate RNA requires base-paired structures to activate antiviral signaling via RIG-I. *Proceedings of the National Academy of Sciences* **106**, 12067–12072 (2009).

[76] Schuberth-Wagner, C. *et al.* A Conserved Histidine in the RNA Sensor RIG-I Controls Immune Tolerance to N1-2'O-Methylated Self RNA. *Immunity* **43**, 41–51 (2015).

[77] Binder, M. *et al.* Molecular Mechanism of Signal Perception and Integration by the Innate Immune Sensor Retinoic Acid-inducible Gene-I (RIG-I). *Journal of Biological Chemistry* **286**, 27278–27287 (2011).

[78] Kato, H. *et al.* Length-dependent recognition of double-stranded ribonucleic acids by retinoic acid–inducible gene-I and melanoma differentiation–associated gene 5. *The Journal of Experimental Medicine* **205**, 1601–1610 (2008).

[79] Liu, G., Park, H.-S., Pyo, H.-M., Liu, Q. & Zhou, Y. Influenza A Virus Panhandle Structure Is Directly Involved in RIG-I Activation and Interferon Induction. *Journal of Virology* **89**, 6067–6079 (2015).

[80] Berke, I. C. & Modis, Y. MDA5 cooperatively forms dimers and ATP-sensitive filaments upon binding double-stranded RNA. *The EMBO Journal* **31**, 1714–1726 (2012).

[81] Peisley, A. *et al.* Cooperative assembly and dynamic disassembly of MDA5 filaments for viral dsRNA recognition. *Proceedings of the National Academy of Sciences* **108**, 21010–21015 (2011).

[82] Wu, B. *et al.* Structural Basis for dsRNA Recognition, Filament Formation, and Antiviral Signal Activation by MDA5. *Cell* **152**, 276–289 (2013).

[83] Yount, J. S., Gitlin, L., Moran, T. M. & López, C. B. MDA5 Participates in the Detection of Paramyxovirus Infection and Is Essential for the Early Activation of Dendritic Cells in Response to Sendai Virus Defective Interfering Particles. *The Journal of Immunology* **180**, 4910–4918 (2008).

[84] Huang, A. S. & Baltimore, D. Defective Viral Particles and Viral Disease Processes. *Nature* **226**, 325–327 (1970).

[85] Kowalinski, E. *et al.* Structural Basis for the Activation of Innate Immune Pattern-Recognition Receptor RIG-I by Viral RNA. *Cell* **147**, 423–435 (2011).

[86] Leung, D. W. & Amarasinghe, G. K. Structural insights into RNA recognition and activation of RIG-I-like receptors. *Current Opinion in Structural Biology* **22**, 297–303 (2012).

[87] Peisley, A., Wu, B., Xu, H., Chen, Z. J. & Hur, S. Structural basis for ubiquitin-mediated antiviral signal activation by RIG-I. *Nature* **509**, 110–114 (2014).

[88] Zeng, W. *et al.* Reconstitution of the RIG-I Pathway Reveals a Signaling Role of Unanchored Polyubiquitin Chains in Innate Immunity. *Cell* **141**, 315–330 (2010).

[89] Hayman, T. J. *et al.* RIPLET and not TRIM25 is required for endogenous RIG-I-dependent anti-viral responses. *Immunology and cell biology* **97**, 840–852 (2019).

[90] Oshiumi, H., Matsumoto, M., Hatakeyama, S. & Seya, T. Riplet/RNF135, a RING Finger Protein, Ubiquitinates RIG-I to Promote Interferon-β Induction during the Early Phase of Viral Infection. *Journal of Biological Chemistry* **284**, 807–817 (2009).

[91] Gack, M. U. *et al.* TRIM25 RING-finger E3 ubiquitin ligase is essential for RIG-I-mediated antiviral activity. *Nature* **446**, 916 (2007).

[92] Oshiumi, H. *et al.* The Ubiquitin Ligase Riplet Is Essential for RIG-I-Dependent Innate Immune Responses to RNA Virus Infection. *Cell Host & Microbe* **8**, 496–509 (2010).

[93] Li, X. *et al.* Structural basis of double-stranded RNA recognition by the RIG-I like receptor MDA5. *Archives of Biochemistry and Biophysics* **488**, 23–33 (2009).

[94] Lang, X. *et al.* TRIM65-catalized ubiquitination is essential for MDA5-mediated antiviral innate immunity. *The Journal of Experimental Medicine* **214**, 459–473 (2017).

[95] Bender, S. *et al.* Activation of Type I and III Interferon Response by Mitochondrial and Peroxisomal MAVS and Inhibition by Hepatitis C Virus. *PLOS Pathogens* **11**, e1005264 (2015).

[96] Chow, K. & Loo, Y.-M. RIG-I and Other RNA Sensors in Antiviral Immunity (2018).

[97] Dixit, E. *et al.* Peroxisomes Are Signaling Platforms for Antiviral Innate Immunity. *Cell* **141**, 668–681 (2010).

[98] Horner, S. M., Liu, H. M., Park, H. S., Briley, J. & Gale, M. Mitochondrial-associated endoplasmic reticulum membranes (MAM) form innate immune synapses and are targeted by hepatitis C virus. *Proceedings of the National Academy of Sciences* **108**, 14590–14595 (2011).

[99] Scott, I. & Youle, R. J. Mitochondrial fission and fusion. *Essays in Biochemistry* **47**, 85–98 (2010).

[100] Hiscott, J., Lacoste, J. & Lin, R. Recruitment of an interferon molecular signaling complex to the mitochondrial membrane: Disruption by hepatitis C virus NS3-4A protease. *Biochemical Pharmacology* **72**, 1477–1484 (2006).

[101] Hou, F. *et al.* MAVS Forms Functional Prion-like Aggregates to Activate and Propagate Antiviral Innate Immune Response. *Cell* **146**, 448–461 (2011).

[102] Lin, R. *et al.* Dissociation of a MAVS/IPS-1/VISA/Cardif-IKKε Molecular Complex from the Mitochondrial Outer Membrane by Hepatitis C Virus NS3-4A Proteolytic Cleavage. *Journal of Virology* **80**, 6072–6083 (2006).

[103] Öhman, T., Rintahaka, J., Kalkkinen, N., Matikainen, S. & Nyman, T. A. Actin and RIG-I/MAVS Signaling Components Translocate to Mitochondria upon Influenza A Virus Infection of Human Primary Macrophages. *The Journal of Immunology* **182**, 5682–5692 (2009).

[104] Liu, B. *et al.* The ubiquitin E3 ligase TRIM31 promotes aggregation and activation of the signaling adaptor MAVS through Lys63-linked polyubiquitination. *Nature Immunology* **18**, 214–224 (2017).

[105] Fitzgerald, K. A. *et al.* IKKε and TBK1 are essential components of the IRF3 signaling pathway. *Nature Immunology* **4**, ni921 (2003).

[106] Grandvaux, N. *et al.* Transcriptional Profiling of Interferon Regulatory Factor 3 Target Genes: Direct Involvement in the Regulation of Interferon-Stimulated Genes. *Journal of Virology* **76**, 5532–5539 (2002).

[107] Oganesyan, G. *et al.* Critical role of TRAF3 in the Toll-like receptor-dependent and -independent antiviral response. *Nature* **439**, 208–211 (2006).

[108] Saha, S. K. *et al.* Regulation of antiviral responses by a direct and specific interaction between TRAF3 and Cardif. *The EMBO Journal* **25**, 3257–3263 (2006).

[109] Yoneyama, M. *et al.* Direct triggering of the type I interferon system by virus infection: activation of a transcription factor complex containing IRF-3 and CBP/p300. *The EMBO Journal* **17**, 1087–1095 (1998).

[110] Izaguirre, A. *et al.* Comparative analysis of IRF and IFN-alpha expression in human plasmacytoid and monocyte-derived dendritic cells. *Journal of Leukocyte Biology* **74**, 1125–1138 (2003).

[111] Génin, P., Lin, R., Hiscott, J. & Civas, A. Differential Regulation of Human Interferon A Gene Expression by Interferon Regulatory Factors 3 and 7. *Molecular and Cellular Biology* **29**, 3435–3450 (2009).

[112] Liu, S. *et al.* MAVS recruits multiple ubiquitin E3 ligases to activate antiviral signaling cascades. *eLife* **2**, e00785 (2013).

[113] Michallet, M.-C. *et al.* TRADD Protein Is an Essential Component of the RIG-like Helicase Antiviral Pathway. *Immunity* **28**, 651–661 (2008).

[114] Sun, L., Deng, L., Ea, C.-K., Xia, Z.-P. & Chen, Z. J. The TRAF6 Ubiquitin Ligase and TAK1 Kinase Mediate IKK Activation by BCL10 and MALT1 in T Lymphocytes. *Molecular Cell* **14**, 289–301 (2004).

[115] Wang, C. *et al.* TAK1 is a ubiquitin-dependent kinase of MKK and IKK. *Nature* **412**, 346–351 (2001).

[116] Ninomiya-Tsuji, J. *et al.* The kinase TAK1 can activate the NIK-IκB as well as the MAP kinase cascade in the IL-1 signalling pathway. *Nature* **398**, 252–256 (1999).

[117] Yoshida, R. *et al.* TRAF6 and MEKK1 Play a Pivotal Role in the RIG-I-like Helicase Antiviral Pathway. *Journal of Biological Chemistry* **283**, 36211–36220 (2008).

[118] Refolo, G., Vescovo, T., Piacentini, M., Fimia, G. M. & Ciccosanti, F. Mitochondrial Interactome: A Focus on Antiviral Signaling Pathways. *Frontiers in Cell and Developmental Biology* **8**, 8 (2020).

[119] Krikos, A., Laherty, C. & Dixit, V. Transcriptional activation of the tumor necrosis factor alpha-inducible zinc finger protein, A20, is mediated by kappa B elements. *Journal of Biological Chemistry* **267**, 17971–17976 (1992).

[120] Ohmori, Y. & Hamilton, T. Cooperative interaction between interferon (IFN) stimulus response element and kappa B sequence motifs controls IFN gamma- and lipopolysaccharide-stimulated transcription from the murine IP-10 promoter. *Journal of Biological Chemistry* **268**, 6677–6688 (1993).

[121] Wickremasinghe, M. I., Thomas, L. H., O'Kane, C. M., Uddin, J. & Friedland, J. S. Transcriptional Mechanisms Regulating Alveolar Epithelial Cell-specific CCL5 Secretion in Pulmonary Tuberculosis. *Journal of Biological Chemistry* **279**, 27199–27210 (2004).

[122] Lu, C. & MacDougall, M. RIG-I-Like Receptor Signaling in Singleton-Merten Syndrome. *Frontiers in Genetics* **8**, 118 (2017).

[123] Oss-Ronen, L., Sarusi, T. & Cohen, I. Histone Mono-Ubiquitination in Transcriptional Regulation and Its Mark on Life: Emerging Roles in Tissue Development and Disease. *Cells* **11**, 2404 (2022).

[124] Kliza, K. & Husnjak, K. Resolving the Complexity of Ubiquitin Networks. *Frontiers in Molecular Biosciences* **7**, 21 (2020).

[125] Komander, D. & Rape, M. The Ubiquitin Code. *Annual Review of Biochemistry* **81**, 203–229 (2012).

[126] Tracz, M. & Bialek, W. Beyond K48 and K63: non-canonical protein ubiquitination. *Cellular & Molecular Biology Letters* **26**, 1 (2021).

[127] Pickart, C. M. Targeting of substrates to the 26S proteasome. *The FASEB Journal* **11**, 1055–1066 (1997).

[128] Thrower, J. S., Hoffman, L., Rechsteiner, M. & Pickart, C. M. Recognition of the polyubiquitin proteolytic signal. *The EMBO Journal* **19**, 94–102 (2000).

[129] Wang, Q. *et al.* The E3 Ubiquitin Ligase AMFR and INSIG1 Bridge the Activation of TBK1 Kinase by Modifying the Adaptor STING. *Immunity* **41**, 919–933 (2014).

[130] Wang, L. *et al.* USP4 Positively Regulates RIG-I-Mediated Antiviral Response through Deubiquitination and Stabilization of RIG-I. *Journal of Virology* **87**, 4507–4515 (2013).

[131] Arimoto, K.-i. *et al.* Negative regulation of the RIG-I signaling by the ubiquitin ligase RNF125. *Proceedings of the National Academy of Sciences* **104**, 7500–7505 (2007).

[132] Fan, Y. *et al.* USP21 negatively regulates antiviral response by acting as a RIG-I deubiquitinase. *Journal of Experimental Medicine* **211**, 313–328 (2014).

[133] Inn, K.-S. *et al.* Linear Ubiquitin Assembly Complex Negatively Regulates RIG-I- and TRIM25-Mediated Type I Interferon Induction. *Molecular Cell* **41**, 354–365 (2011).

[134] Cui, J. *et al.* USP3 inhibits type I interferon signaling by deubiquitinating RIG-I-like receptors. *Cell Research* **24**, 400–416 (2014).

[135] Castanier, C. *et al.* MAVS ubiquitination by the E3 ligase TRIM25 and degradation by the proteasome is involved in type I interferon production after activation of the antiviral RIG-I-like receptors. *BMC Biology* **10**, 44–44 (2012).

[136] Chen, H.-W. *et al.* Ring finger protein 166 potentiates RNA virus-induced interferon-β production via enhancing the ubiquitination of TRAF3 and TRAF6. *Scientific Reports* **5**, 14770 (2015).

[137] Li, S. *et al.* Regulation of Virus-triggered Signaling by OTUB1- and OTUB2-mediated Deubiquitination of TRAF3 and TRAF6. *Journal of Biological Chemistry* **285**, 4291–4297 (2010).

[138] Mao, A.-P. *et al.* Virus-triggered Ubiquitination of TRAF3/6 by cIAP1/2 Is Essential for Induction of Interferon-β (IFN-β) and Cellular Antiviral Response. *Journal of Biological Chemistry* **285**, 9470–9476 (2010).

[139] Tseng, P.-H. *et al.* Different modes of ubiquitination of the adaptor TRAF3 selectively activate the expression of type I interferons and proinflammatory cytokines. *Nature Immunology* **11**, 70–75 (2010).

[140] Wang, P., Zhao, W., Zhao, K., Zhang, L. & Gao, C. TRIM26 Negatively Regulates Interferon-β Production and Antiviral Response through Polyubiquitination and Degradation of Nuclear IRF3. *PLoS Pathogens* **11**, e1004726 (2015).

[141] Saitoh, T. *et al.* Negative regulation of interferon-regulatory factor 3–dependent innate antiviral response by the prolyl isomerase Pin1. *Nature Immunology* **7**, 598–605 (2006).

[142] Higgs, R. *et al.* The E3 Ubiquitin Ligase Ro52 Negatively Regulates IFN-β Production Post-Pathogen Recognition by Polyubiquitin-Mediated Degradation of IRF3. *The Journal of Immunology* **181**, 1780–1786 (2008).

[143] Yang, K. *et al.* TRIM21 Is Essential to Sustain IFN Regulatory Factor 3 Activation during Antiviral Response. *The Journal of Immunology* **182**, 3782–3792 (2009).

[144] Maharaj, N. P., Wies, E., Stoll, A. & Gack, M. U. Conventional Protein Kinase C-α (PKC-α) and PKC-β Negatively Regulate RIG-I Antiviral Signal Transduction. *Journal of Virology* **86**, 1358–1371 (2012).

[145] Wies, E. *et al.* Dephosphorylation of the RNA Sensors RIG-I and MDA5 by the Phosphatase PP1 Is Essential for Innate Immune Signaling. *Immunity* **38**, 437–449 (2013).

[146] Sun, Z., Ren, H., Liu, Y., Teeling, J. L. & Gu, J. Phosphorylation of RIG-I by Casein Kinase II Inhibits Its Antiviral Response. *Journal of Virology* **85**, 1036–1047 (2011).

[147] Takashima, K., Oshiumi, H., Takaki, H., Matsumoto, M. & Seya, T. RIOK3-Mediated Phosphorylation of MDA5 Interferes with Its Assembly and Attenuates the Innate Immune Response. *Cell Reports* **11**, 192–200 (2015).

[148] Willemsen, J. *et al.* Phosphorylation-Dependent Feedback Inhibition of RIG-I by DAPK1 Identified by Kinome-wide siRNA Screening. *Molecular Cell* **65**, 403–415.e8 (2017).

[149] Clark, K., Plater, L., Peggie, M. & Cohen, P. Use of the Pharmacological Inhibitor BX795 to Study the Regulation and Physiological Roles of TBK1 and IκB Kinase ε. *Journal of Biological Chemistry* **284**, 14136–14146 (2009).

[150] Ma, X. *et al.* Molecular basis of Tank-binding kinase 1 activation by transautophosphorylation. *Proceedings of the National Academy of Sciences* **109**, 9378–9383 (2012).

[151] Shu, C. *et al.* Structural Insights into the Functions of TBK1 in Innate Antimicrobial Immunity. *Structure* **21**, 1137–1148 (2013).

[152] Zhao, M., Zhang, J., Phatnani, H., Scheu, S. & Maniatis, T. Stochastic Expression of the Interferon-β Gene. *PLoS Biology* **10**, e1001249 (2012).

[153] Kumar, K. P., McBride, K. M., Weaver, B. K., Dingwall, C. & Reich, N. C. Regulated Nuclear-Cytoplasmic Localization of Interferon Regulatory Factor 3, a Subunit of Double-Stranded RNA-Activated Factor 1. *Molecular and Cellular Biology* **20**, 4159–4168 (2000).

[154] Lin, R., Heylbroeck, C., Pitha, P. M. & Hiscott, J. Virus-Dependent Phosphorylation of the IRF-3 Transcription Factor Regulates Nuclear Translocation, Transactivation Potential, and Proteasome-Mediated Degradation. *Molecular and Cellular Biology* **18**, 2986–2996 (1998).

[155] Weaver, B. K., Kumar, K. P. & Reich, N. C. Interferon Regulatory Factor 3 and CREB-Binding Protein/p300 Are Subunits of Double-Stranded RNA-Activated Transcription Factor DRAF1. *Molecular and Cellular Biology* **18**, 1359–1368 (1998).

[156] Long, L. *et al.* Recruitment of Phosphatase PP2A by RACK1 Adaptor Protein Deactivates Transcription Factor IRF3 and Limits Type I Interferon Signaling. *Immunity* **40**, 515–529 (2014).

[157] Hu, M.-M., Liao, C.-Y., Yang, Q., Xie, X.-Q. & Shu, H.-B. Innate immunity to RNA virus is regulated by temporal and reversible sumoylation of RIG-I and MDA5. *Journal of Experimental Medicine* **214**, 973–989 (2017).

[158] Choi, S. J. *et al.* HDAC6 regulates cellular viral RNA sensing by deacetylation of RIG-I. *The EMBO Journal* **35**, 429–442 (2016).

[159] Liu, H. M. *et al.* Regulation of Retinoic Acid Inducible Gene-I (RIG-I) Activation by the Histone Deacetylase 6. *EBioMedicine* **9**, 195–206 (2016).

[160] Yoneyama, M. *et al.* Shared and Unique Functions of the DExD/H-Box Helicases RIG-I, MDA5, and LGP2 in Antiviral Innate Immunity. *The Journal of Immunology* **175**, 2851–2858 (2005).

[161] Bruns, A. M. *et al.* ATP Hydrolysis Enhances RNA Recognition and Antiviral Signal Transduction by the Innate Immune Sensor, Laboratory of Genetics and Physiology 2 (LGP2). *Journal of Biological Chemistry* **288**, 938–946 (2013).

[162] Duic, I. *et al.* Viral RNA recognition by LGP2 and MDA5, and activation of signaling through step-by-step conformational changes. *Nucleic Acids Research* gkaa935– (2020).

[163] Liddicoat, B. J. *et al.* RNA editing by ADAR1 prevents MDA5 sensing of endogenous dsRNA as nonself. *Science* **349**, 1115–1120 (2015).

[164] Pujantell, M. *et al.* RNA editing by ADAR1 regulates innate and antiviral immune functions in primary macrophages. *Scientific Reports* **7**, 13339 (2017).

[165] Vitali, P. & Scadden, A. D. J. Double-stranded RNAs containing multiple IU pairs are sufficient to suppress interferon induction and apoptosis. *Nature Structural & Molecular Biology* **17**, 1043–1050 (2010).

[166] Yang, S. *et al.* Adenosine Deaminase Acting on RNA 1 Limits RIG-I RNA Detection and Suppresses IFN Production Responding to Viral and Endogenous RNAs. *The Journal of Immunology* **193**, 3436–3445 (2014).

[167] Kok, K.-H. *et al.* The Double-Stranded RNA-Binding Protein PACT Functions as a Cellular Activator of RIG-I to Facilitate Innate Antiviral Response. *Cell Host & Microbe* **9**, 299–309 (2011).

[168] Luthra, P. *et al.* Mutual Antagonism between the Ebola Virus VP35 Protein and the RIG-I Activator PACT Determines Infection Outcome. *Cell Host & Microbe* **14**, 74–84 (2013).

[169] Lui, P.-Y. *et al.* PACT Facilitates RNA-Induced Activation of MDA5 by Promoting MDA5 Oligomerization. *The Journal of Immunology* **199**, 1846–1855 (2017).

[170] Pattabhi, S., Knoll, M. L., Gale, M. & Loo, Y.-M. DHX15 Is a Coreceptor for RLR Signaling That Promotes Antiviral Defense Against RNA Virus Infection. *Journal of Interferon & Cytokine Research* (2019).

[171] Miyashita, M., Oshiumi, H., Matsumoto, M. & Seya, T. DDX60, a DEXD/H Box Helicase, Is a Novel Antiviral Factor Promoting RIG-I-Like Receptor-Mediated Signaling. *Molecular and Cellular Biology* **31**, 3802–3819 (2011).

[172] Oshiumi, H. *et al.* DDX60 Is Involved in RIG-I-Dependent and Independent Antiviral Responses, and Its Function Is Attenuated by Virus-Induced EGFR Activation. *Cell Reports* **11**, 1193–1207 (2015).

[173] Schoggins, J. W. *et al.* A diverse range of gene products are effectors of the type I interferon antiviral response. *Nature* **472**, 481 (2011).

[174] Lian, H. *et al.* The Zinc-Finger Protein ZCCHC3 Binds RNA and Facilitates Viral RNA Sensing and Activation of the RIG-I-like Receptors. *Immunity* **49**, 438–448.e5 (2018).

[175] Chen, S.-T. *et al.* NLRP12 Regulates Anti-viral RIG-I Activation via Interaction with TRIM25. *Cell Host & Microbe* (2019).

[176] Liu, H. *et al.* The Mitochondrial Targeting Chaperone 14-3-3ε Regulates a RIG-I Translocon that Mediates Membrane Association and Innate Antiviral Immunity. *Cell Host & Microbe* **11**, 528–537 (2012).

[177] Lin, J.-P., Fan, Y.-K. & Liu, H. M. The 14-3-3η chaperone protein promotes antiviral innate immunity via facilitating MDA5 oligomerization and intracellular redistribution. *PLoS Pathogens* **15**, e1007582 (2019).

[178] McNab, F., Mayer-Barber, K., Sher, A., Wack, A. & O'Garra, A. Type I interferons in infectious disease. *Nature Reviews Immunology* **15**, 87–103 (2015).

[179] Murira, A. & Lamarre, A. Type-I Interferon Responses: From Friend to Foe in the Battle against Chronic Viral Infection. *Frontiers in Immunology* **7**, 609 (2016).

[180] Pestka, S., Krause, C. D. & Walter, M. R. Interferons, interferon-like cytokines, and their receptors. *Immunological Reviews* **202**, 8–32 (2004).

[181] Kim, T. K. & Maniatis, T. The Mechanism of Transcriptional Synergy of an In Vitro Assembled Interferon-β Enhanceosome. *Molecular Cell* **1**, 119–129 (1997).

[182] Ryals, J., Dierks, P., Ragg, H. & Weissmann, C. A 46-nucleotide promoter segment from an IFN-α gene renders an unrelated promoter inducible by virus. *Cell* **41**, 497–507 (1985).

[183] Du, W. & Maniatis, T. An ATF/CREB binding site is required for virus induction of the human interferon beta gene [corrected]. *Proceedings of the National Academy of Sciences* **89**, 2150–2154 (1992).

[184] Du, W., Thanos, D. & Maniatis, T. Mechanisms of transcriptional synergism between distinct virus-inducible enhancer elements. *Cell* **74**, 887–898 (1993).

[185] Fujita, T., Miyamoto, M., Kimura, Y., Hammer, J. & Taniguchi, T. Involvement of a cis -element that binds an H2TF-I/NF x B like factor(s) in the virus-induced interferon-β gene expression. *Nucleic Acids Research* **17**, 3335–3346 (1989).

[186] Goodbourn, S. & Maniatis, T. Overlapping positive and negative regulatory domains of the human beta-interferon gene. *Proceedings of the National Academy of Sciences* **85**, 1447–1451 (1988).

[187] Leblanc, J. F., Cohen, L., Rodrigues, M. & Hiscott, J. Synergism between distinct enhanson domains in viral induction of the human beta interferon gene. *Molecular and Cellular Biology* **10**, 3987–3993 (1990).

[188] Panne, D., Maniatis, T. & Harrison, S. C. Crystal structure of ATF-2/c-Jun and IRF-3 bound to the interferon-β enhancer. *The EMBO Journal* **23**, 4384–4393 (2004).

[189] Visvanathan, K. V. & Goodbourn, S. Double-stranded RNA activates binding of NF-kappa B to an inducible element in the human beta-interferon promoter. *The EMBO Journal* **8**, 1129–1138 (1989).

[190] Piehler, J., Thomas, C., Garcia, K. & Schreiber, G. Structural and dynamic determinants of type I interferon receptor assembly and their functional interpretation. *Immunological Reviews* **250**, 317–334 (2012).

[191] Schreiber, G. The molecular basis for differential type I interferon signaling. *Journal of Biological Chemistry* **292**, 7285–7294 (2017).

[192] Lamken, P., Lata, S., Gavutis, M. & Piehler, J. Ligand-induced Assembling of the Type I Interferon Receptor on Supported Lipid Bilayers. *Journal of Molecular Biology* **341**, 303–318 (2004).

[193] Lavoie, T. B. *et al.* Binding and activity of all human alpha interferon subtypes. *Cytokine* **56**, 282–289 (2011).

[194] Piehler, J. & Schreiber, G. Fast Transient Cytokine–Receptor Interactions Monitored in Real Time by Reflectometric Interference Spectroscopy. *Analytical Biochemistry* **289**, 173–186 (2001).

[195] Göder, A. *et al.* STAT1 N-terminal domain discriminatively controls type I and type II IFN signaling. *Cytokine* **144**, 155552 (2021).

[196] Schindler, C., Fu, X. Y., Improta, T., Aebersold, R. & Darnell, J. E. Proteins of transcription factor ISGF-3: one gene encodes the 91-and 84-kDa ISGF-3 proteins that are activated by interferon alpha. *Proceedings of the National Academy of Sciences* **89**, 7836–7839 (1992).

[197] Levy, D. E., Kessler, D. S., Pine, R., Reich, N. & Darnell, J. E. Interferon-induced nuclear factors that bind a shared promoter element correlate with positive and negative transcriptional control. *Genes & Development* **2**, 383–393 (1988).

[198] González-Navajas, J. M., Lee, J., David, M. & Raz, E. Immunomodulatory functions of type I interferons. *Nature Reviews Immunology* **12**, 125–135 (2012).

[199] Ivashkiv, L. B. & Donlin, L. T. Regulation of type I interferon responses. *Nature Reviews Immunology* **14**, 36–49 (2014).

[200] Jr., J. E. D., Kerr, I. M. & Stark, G. R. Jak-STAT Pathways and Transcriptional Activation in Response to IFNs and Other Extracellular Signaling Proteins. *Science* **264**, 1415–1421 (1994).

[201] Mogensen, T. H. IRF and STAT Transcription Factors - From Basic Biology to Roles in Infection, Protective Immunity, and Primary Immunodeficiencies. *Frontiers in Immunology* **9**, 3047 (2019).

[202] Schoggins, J. W. Interferon-Stimulated Genes: What Do They All Do? *Annual Review of Virology* **6**, 1–18 (2019).

[203] Stanifer, M. L., Pervolaraki, K. & Boulant, S. Differential Regulation of Type I and Type III Interferon Signaling. *International Journal of Molecular Sciences* **20**, 1445 (2019).

[204] Schoenborn, J. R. & Wilson, C. B. Regulation of Interferon-γ During Innate and Adaptive Immune Responses. *Advances in Immunology* **96**, 41–101 (2007).

[205] Fountoulakis, M., Zulauf, M., LUSTIG, A. & GAROTTA, G. Stoichiometry of interaction between interferon γ and its receptor. *European Journal of Biochemistry* **208**, 781–787 (1992).

[206] Greenlund, A., Schreiber, R., Goeddel, D. & Pennica, D. Interferon-gamma induces receptor dimerization in solution and on cells. *Journal of Biological Chemistry* **268**, 18103–18110 (1993).

[207] Igarashi, K. *et al.* Interferon-gamma induces tyrosine phosphorylation of interferon-gamma receptor and regulated association of protein tyrosine kinases, Jak1 and Jak2, with its receptor. *Journal of Biological Chemistry* **269**, 14333–14336 (1994).

[208] Briscoe, J. *et al.* Kinase-negative mutants of JAK1 can sustain interferon-gamma-inducible gene expression but not an antiviral state. *The EMBO Journal* **15**, 799–809 (1996).

[209] Nguyen, H., Ramana, C. V., Bayes, J. & Stark, G. R. Roles of Phosphatidylinositol 3-Kinase in Interferon-γ-dependent Phosphorylation of STAT1 on Serine 727 and Activation of Gene Expression. *Journal of Biological Chemistry* **276**, 33361–33368 (2001).

[210] Krause, C. D. *et al.* Seeing the Light Preassembly and Ligand-Induced Changes of the Interferon γ Receptor Complex in Cells. *Molecular & Cellular Proteomics* **1**, 805–815 (2002).

[211] Shuai, K., Schindler, C., Prezioso, V. R. & Jr., J. E. D. Activation of Transcription by IFN-γ: Tyrosine Phosphorylation of a 91-kD DNA Binding Protein. *Science* **258**, 1808–1812 (1992).

[212] Greenlund, A., Farrar, M., Viviano, B. & Schreiber, R. Ligand-induced IFN gamma receptor tyrosine phosphorylation couples the receptor to its signal transduction system (p91). *The EMBO Journal* **13**, 1591–1600 (1994).

[213] Der, S. D., Zhou, A., Williams, B. R. & Silverman, R. H. Identification of genes differentially regulated by interferon α, β, or γ using oligonucleotide arrays. *Proceedings of the National Academy of Sciences* **95**, 15623–15628 (1998).

[214] Echebli, N. *et al.* Stage-specific IFN-induced and IFN gene expression reveal convergence of type I and type II IFN and highlight their role in both acute and chronic stage of pathogenic SIV infection. *PLoS ONE* **13**, e0190334 (2018).

[215] MacMicking, J., Xie, Q.-w. & Nathan, C. Nitric Oxide and Macrophage Function. *Annual Review of Immunology* **15**, 323–350 (1997).

[216] Spencer, N. G., Schilling, T., Miralles, F. & Eder, C. Mechanisms Underlying Interferon-γ-Induced Priming of Microglial Reactive Oxygen Species Production. *PLoS ONE* **11**, e0162497 (2016).

[217] Zhao, G. *et al.* Pivotal Role of Reactive Oxygen Species in Differential Regulation of Lipopolysaccharide-Induced Prostaglandins Production in Macrophages. *Molecular Pharmacology* **83**, 167–178 (2013).

[218] Kang, K. *et al.* Interferon-γ Represses M2 Gene Expression in Human Macrophages by Disassembling Enhancers Bound by the Transcription Factor MAF. *Immunity* **47**, 235–250.e4 (2017).

[219] Wang, F. *et al.* Interferon Gamma Induces Reversible Metabolic Reprogramming of M1 Macrophages to Sustain Cell Viability and Pro-Inflammatory Activity. *EBioMedicine* **30**, 303–316 (2018).

[220] Goldszmid, R. *et al.* NK Cell-Derived Interferon-γ Orchestrates Cellular Dynamics and the Differentiation of Monocytes into Dendritic Cells at the Site of Infection. *Immunity* **36**, 1047–1059 (2012).

[221] Martín-Fontecha, A. *et al.* Induced recruitment of NK cells to lymph nodes provides IFN-γ for TH1 priming. *Nature Immunology* **5**, 1260–1265 (2004).

[222] Lee, A. J. & Ashkar, A. A. The Dual Nature of Type I and Type II Interferons. *Frontiers in Immunology* **9**, 2061 (2018).

[223] Kotenko, S. V. *et al.* IFN-λs mediate antiviral protection through a distinct class II cytokine receptor complex. *Nature Immunology* **4**, 69–77 (2003).

[224] Prokunina-Olsson, L. *et al.* A variant upstream of IFNL3 (IL28B) creating a new interferon gene IFNL4 is associated with impaired clearance of hepatitis C virus. *Nature Genetics* **45**, 164–171 (2013).

[225] Sheppard, P. *et al.* IL-28, IL-29 and their class II cytokine receptor IL-28R. *Nature Immunology* **4**, 63–68 (2003).

[226] Syedbasha, M. *et al.* An ELISA Based Binding and Competition Method to Rapidly Determine Ligand-receptor Interactions. *Journal of Visualized Experiments* (2016).

[227] Hamming, O. J. *et al.* Interferon lambda 4 signals via the IFNλ receptor to regulate antiviral activity against HCV and coronaviruses. *The EMBO Journal* **32**, 3055–3065 (2013).

[228] Hong, M. *et al.* Interferon lambda 4 expression is suppressed by the host during viral infection. *Journal of Experimental Medicine* **213**, 2539–2552 (2016).

[229] Obajemu, A. A. *et al.* IFN-λ4 Attenuates Antiviral Responses by Enhancing Negative Regulation of IFN Signaling. *The Journal of Immunology* **199**, 3808–3820 (2017).

[230] Onabajo, O. O., Muchmore, B. & Prokunina-Olsson, L. The IFN-λ4 Conundrum: When a Good Interferon Goes Bad. *Journal of Interferon & Cytokine Research* **39**, 636–641 (2019).

[231] Mordstein, M. *et al.* Lambda Interferon Renders Epithelial Cells of the Respiratory and Gastrointestinal Tracts Resistant to Viral Infections. *Journal of Virology* **84**, 5670–5677 (2010).

[232] Pott, J. *et al.* IFN-λ determines the intestinal epithelial antiviral host defense. *Proceedings of the National Academy of Sciences* **108**, 7944–7949 (2011).

[233] Sommereyns, C., Paul, S., Staeheli, P. & Michiels, T. IFN-Lambda (IFN-λ) Is Expressed in a Tissue-Dependent Fashion and Primarily Acts on Epithelial Cells In Vivo. *PLoS Pathogens* **4**, e1000017 (2008).

[234] Blazek, K. *et al.* IFN-λ resolves inflammation via suppression of neutrophil infiltration and IL-1β production. *The Journal of Experimental Medicine* **212**, 845–853 (2015).

[235] Galani, I. E. *et al.* Interferon-λ Mediates Non-redundant Front-Line Antiviral Protection against Influenza Virus Infection without Compromising Host Fitness. *Immunity* **46**, 875–890.e6 (2017).

[236] Koltsida, O. *et al.* IL-28A (IFN-λ2) modulates lung DC function to promote Th1 immune skewing and suppress allergic airway disease. *EMBO Molecular Medicine* **3**, 348–361 (2011).

[237] Santer, D. M. *et al.* Differential expression of interferon-lambda receptor 1 splice variants determines the magnitude of the antiviral response induced by interferon-lambda 3 in human immune cells. *PLoS Pathogens* **16**, e1008515 (2020).

[238] Mendoza, J. L. *et al.* The IFN-λ-IFN-λR1-IL-10Rβ Complex Reveals Structural Features Underlying Type III IFN Functional Plasticity. *Immunity* **46**, 379–392 (2017).

[239] Zhou, Z. *et al.* Type III Interferon (IFN) Induces a Type I IFN-Like Response in a Restricted Subset of Cells through Signaling Pathways Involving both the Jak-STAT Pathway and the Mitogen-Activated Protein Kinases. *Journal of Virology* **81**, 7749–7758 (2007).

[240] Jilg, N. *et al.* Kinetic differences in the induction of interferon stimulated genes by interferon-α and interleukin 28B are altered by infection with hepatitis C virus. *Hepatology* **59**, 1250–1261 (2014).

[241] Pervolaraki, K. *et al.* Differential induction of interferon stimulated genes between type I and type III interferons is independent of interferon receptor abundance. *PLoS Pathogens* **14**, e1007420 (2018).

[242] Bolen, C. R., Ding, S., Robek, M. D. & Kleinstein, S. H. Dynamic expression profiling of type I and type III interferon-stimulated hepatocytes reveals a stable hierarchy of gene expression. *Hepatology* **59**, 1262–1272 (2014).

[243] François-Newton, V. *et al.* USP18-Based Negative Feedback Control Is Induced by Type I and Type III Interferons and Specifically Inactivates Interferon α Response. *PLoS ONE* **6**, e22200 (2011).

[244] Karaghiosoff, M. *et al.* Partial Impairment of Cytokine Responses in Tyk2-Deficient Mice. *Immunity* **13**, 549–560 (2000).

[245] Odendall, C. *et al.* Diverse intracellular pathogens activate type III interferon expression from peroxisomes. *Nature Immunology* **15**, 717–726 (2014).

[246] Fuchs, S. *et al.* Tyrosine kinase 2 is not limiting human antiviral type III interferon responses. *European Journal of Immunology* **46**, 2639–2649 (2016).

[247] Kreins, A. Y. *et al.* Human TYK2 deficiency: Mycobacterial and viral infections without hyper-IgE syndrome. *Journal of Experimental Medicine* **212**, 1641–1662 (2015).

[248] Crow, Y. J. Type I interferonopathies: a novel set of inborn errors of immunity. *Annals of the New York Academy of Sciences* **1238**, 91–98 (2011).

[249] Crow, Y. J. & Stetson, D. B. The type I interferonopathies: 10 years on. *Nature Reviews Immunology* 1–13 (2021).

[250] Aicardi, J. & Goutières, F. A Progressive familial encephalopathy in infancy with calcifications of the basal ganglia and chronic cerebrospinal fluid lymphocytosis. *Annals of Neurology* **15**, 49–54 (1984).

[251] Hooks, J. J. *et al.* Immune Interferon in the Circulation of Patients with Autoimmune Disease. *The New England Journal of Medicine* **301**, 5–8 (1979).

[252] Wen, Z., Zhong, Z. & Darnell, J. E. Maximal activation of transcription by statl and stat3 requires both tyrosine and serine phosphorylation. *Cell* **82**, 241–250 (1995).

[253] Fenner, J. E. *et al.* Suppressor of cytokine signaling 1 regulates the immune response to infection by a unique inhibition of type I interferon activity. *Nature Immunology* **7**, 33–39 (2006).

[254] David, M., Chen, H. E., Goelz, S., Larner, A. C. & Neel, B. G. Differential regulation of the alpha/beta interferon-stimulated Jak/Stat pathway by the SH2 domain-containing tyrosine phosphatase SHPTP1. *Molecular and Cellular Biology* **15**, 7050–7058 (1995).

[255] Wu, T. R. *et al.* SHP-2 Is a Dual-specificity Phosphatase Involved in Stat1 Dephosphorylation at Both Tyrosine and Serine Residues in Nuclei. *Journal of Biological Chemistry* **277**, 47572–47580 (2002).

[256] You, M., Yu, D.-H. & Feng, G.-S. Shp-2 Tyrosine Phosphatase Functions as a Negative Regulator of the Interferon-Stimulated Jak/STAT Pathway. *Molecular and Cellular Biology* **19**, 2416–2424 (1999).

[257] Kumar, K. *et al.* SCFHOS ubiquitin ligase mediates the ligand-induced down-regulation of the interferon-α receptor. *The EMBO Journal* **22**, 5480–5490 (2003).

[258] Tanaka, T., Soriano, M. A. & Grusby, M. J. SLIM Is a Nuclear Ubiquitin E3 Ligase that Negatively Regulates STAT Signaling. *Immunity* **22**, 729–736 (2005).

[259] Yuan, C., Qi, J., Zhao, X. & Gao, C. Smurf1 Protein Negatively Regulates Interferon-γ Signaling through Promoting STAT1 Protein Ubiquitination and Degradation. *Journal of Biological Chemistry* **287**, 17006–17015 (2012).

[260] Ren, Y. *et al.* Deubiquitinase USP2a Sustains Interferons Antiviral Activity by Restricting Ubiquitination of Activated STAT1 in the Nucleus. *PLoS Pathogens* **12**, e1005764 (2016).

[261] Lawrence, D. W. & Kornbluth, J. E3 ubiquitin ligase NKLAM ubiquitinates STAT1 and positively regulates STAT1-mediated transcriptional activity. *Cellular Signalling* **28**, 1833–1841 (2016).

[262] Ungureanu, D., Vanhatupa, S., Grönholm, J., Palvimo, J. J. & Silvennoinen, O. SUMO-1 conjugation selectively modulates STAT1-mediated gene responses. *Blood* **106**, 224–226 (2005).

[263] Tang, X. *et al.* Acetylation-Dependent Signal Transduction for Type I Interferon Receptor. *Cell* **131**, 93–105 (2007).

[264] Krämer, O. H. *et al.* A phosphorylation-acetylation switch regulates STAT1 signaling. *Genes & Development* **23**, 223–235 (2009).

[265] Haas, A. L., Ahrens, P., Bright, P. M. & Ankel, H. Interferon induces a 15-kilodalton protein exhibiting marked homology to ubiquitin. *Journal of Biological Chemistry* **262**, 11315–11323 (1987).

[266] Loeb, K. & Haas, A. The interferon-inducible 15-kDa ubiquitin homolog conjugates to intracellular proteins. *Journal of Biological Chemistry* **267**, 7806–7813 (1992).

[267] Basters, A. *et al.* Structural basis of the specificity of USP18 toward ISG15. *Nature Structural & Molecular Biology* **24**, 270–278 (2017).

[268] Kim, K. I., Giannakopoulos, N. V., Virgin, H. W. & Zhang, D.-E. Interferon-Inducible Ubiquitin E2, Ubc8, Is a Conjugating Enzyme for Protein ISGylation. *Molecular and Cellular Biology* **24**, 9592–9600 (2004).

[269] Malakhov, M. P., Malakhova, O. A., Kim, K. I., Ritchie, K. J. & Zhang, D.-E. UBP43 (USP18) Specifically Removes ISG15 from Conjugated Proteins. *Journal of Biological Chemistry* **277**, 9976–9981 (2002).

[270] Wong, J. J. Y., Pung, Y. F., Sze, N. S.-K. & Chin, K.-C. HERC5 is an IFN-induced HECT-type E3 protein ligase that mediates type I IFN-induced ISGylation of protein targets. *Proceedings of the National Academy of Sciences* **103**, 10735–10740 (2006).

[271] Yuan, W. & Krug, R. M. Influenza B virus NS1 protein inhibits conjugation of the interferon (IFN)-induced ubiquitin-like ISG15 protein. *The EMBO Journal* **20**, 362–371 (2001).

[272] Zhao, C. *et al.* The UbcH8 ubiquitin E2 enzyme is also the E2 enzyme for ISG15, an IFN-α/β-induced ubiquitin-like protein. *Proceedings of the National Academy of Sciences* **101**, 7578–7582 (2004).

[273] Malakhov, M. P. *et al.* High-throughput Immunoblotting: Ubiquitin-Like Protein ISG15 Modifies Key Regulators of Signal Transduction. *Journal of Biological Chemistry* **278**, 16608–16613 (2003).

[274] Malakhova, O. A. *et al.* Protein ISGylation modulates the JAK-STAT signaling pathway. *Genes & Development* **17**, 455–460 (2003).

[275] Ritchie, K. J. *et al.* Role of ISG15 protease UBP43 (USP18) in innate immunity to viral infection. *Nature Medicine* **10**, 1374–1378 (2004).

[276] Lai, C. *et al.* Mice Lacking the ISG15 E1 Enzyme UbE1L Demonstrate Increased Susceptibility to both Mouse-Adapted and Non-Mouse-Adapted Influenza B Virus Infection. *Journal of Virology* **83**, 1147–1151 (2009).

[277] Ashley, C. L., Abendroth, A., McSharry, B. P. & Slobedman, B. Interferon-Independent Upregulation of Interferon-Stimulated Genes during Human Cytomegalovirus Infection is Dependent on IRF3 Expression. *Viruses* **11**, 246 (2019).

[278] Ashley, C. L., Abendroth, A., McSharry, B. P. & Slobedman, B. Interferon-Independent Innate Responses to Cytomegalovirus. *Frontiers in Immunology* **10**, 2751 (2019).

[279] Green, R., Ireton, R. C. & Gale, M. Interferon-stimulated genes: new platforms and computational approaches. *Mammalian Genome* **29**, 593–602 (2018).

[280] Shimizu, K. & Kuroda, K. Expression of Host Genes in Influenza Virus Infected cells. *Uirusu* **54**, 189–196 (2004).

[281] Mostafavi, S. *et al.* Parsing the Interferon Transcriptional Network and Its Disease Associations. *Cell* **164**, 564–578 (2016).

[282] Kang, D.-c. *et al.* mda-5: An interferon-inducible putative RNA helicase with double-stranded RNA-dependent ATPase activity and melanoma growth-suppressive properties. *Proceedings of the National Academy of Sciences* **99**, 637–642 (2002).

[283] Xu, L. *et al.* RIG-I is a key antiviral interferon-stimulated gene against hepatitis E virus regardless of interferon production. *Hepatology* **65**, 1823–1839 (2017).

[284] Yoneyama, M. *et al.* The RNA helicase RIG-I has an essential function in double-stranded RNA-induced innate antiviral responses. *Nature Immunology* **5**, 730–737 (2004).

[285] Marié, I., Durbin, J. E. & Levy, D. E. Differential viral induction of distinct interferon-α genes by positive feedback through interferon regulatory factor-7. *The EMBO Journal* **17**, 6660–6669 (1998).

[286] Sato, M. *et al.* Positive feedback regulation of type I IFN genes by the IFN-inducible transcription factor IRF-7. *FEBS Letters* **441**, 106–110 (1998).

[287] Wüst, S., Schad, P., Burkart, S. & Binder, M. Comparative Analysis of Six IRF Family Members in Alveolar Epithelial Cell-Intrinsic Antiviral Responses. *Cells* **10**, 2600 (2021).

[288] Maiwald, T. *et al.* Combining theoretical analysis and experimental data generation reveals IRF9 as a crucial factor for accelerating interferon-α-induced early antiviral signalling. *FEBS Journal* **277**, 4741–4754 (2010).

[289] Chesarino, N. M. *et al.* IFITM3 requires an amphipathic helix for antiviral activity. *EMBO reports* **18**, 1740–1751 (2017).

[290] Desai, T. M. *et al.* IFITM3 Restricts Influenza A Virus Entry by Blocking the Formation of Fusion Pores following Virus-Endosome Hemifusion. *PLoS Pathogens* **10**, e1004048 (2014).

[291] Yount, J. S. *et al.* Palmitoylome profiling reveals S-palmitoylation–dependent antiviral activity of IFITM3. *Nature Chemical Biology* **6**, 610–614 (2010).

[292] Spence, J. S. *et al.* IFITM3 directly engages and shuttles incoming virus particles to lysosomes. *Nature Chemical Biology* **15**, 259–268 (2019).

[293] Dittmann, J. *et al.* Influenza A Virus Strains Differ in Sensitivity to the Antiviral Action of Mx-GTPase. *Journal of Virology* **82**, 3624–3631 (2008).

[294] Pavlovic, J., Haller, O. & Staeheli, P. Human and mouse Mx proteins inhibit different steps of the influenza virus multiplication cycle. *Journal of Virology* **66**, 2564–2569 (1992).

[295] Pavlovic, J. *et al.* Enhanced virus resistance of transgenic mice expressing the human MxA protein. *Journal of Virology* **69**, 4506–4510 (1995).

[296] Zimmermann, P., Mänz, B., Haller, O., Schwemmle, M. & Kochs, G. The Viral Nucleoprotein Determines Mx Sensitivity of Influenza A Viruses. *Journal of Virology* **85**, 8133–8140 (2011).

[297] Haller, O., Staeheli, P., Schwemmle, M. & Kochs, G. Mx GTPases: dynamin-like antiviral machines of innate immunity. *Trends in Microbiology* **23**, 154–163 (2015).

[298] Verhelst, J., Hulpiau, P. & Saelens, X. Mx Proteins: Antiviral Gatekeepers That Restrain the Uninvited. *Microbiology and Molecular Biology Reviews* **77**, 551–566 (2013).

[299] Dalet, A., Gatti, E. & Pierre, P. Integration of PKR-dependent translation inhibition with innate immunity is required for a coordinated anti-viral response. *FEBS Letters* **589**, 1539–1545 (2015).

[300] García, M. A. *et al.* Impact of Protein Kinase PKR in Cell Biology: from Antiviral to Antiproliferative Action. *Microbiology and Molecular Biology Reviews* **70**, 1032–1060 (2006).

[301] Pindel, A. & Sadler, A. The Role of Protein Kinase R in the Interferon Response. *Journal of Interferon & Cytokine Research* **31**, 59–70 (2011).

[302] Pichlmair, A. *et al.* IFIT1 is an antiviral protein that recognizes 5'-triphosphate RNA. *Nature Immunology* **12**, 624–630 (2011).

[303] Abbas, Y. M. *et al.* Structure of human IFIT1 with capped RNA reveals adaptable mRNA binding and mechanisms for sensing N1 and N2 ribose 2'-O methylations. *Proceedings of the National Academy of Sciences* **114**, E2106–E2115 (2017).

[304] Daffis, S. *et al.* 2'-O methylation of the viral mRNA cap evades host restriction by IFIT family members. *Nature* **468**, 452–456 (2010).

[305] Habjan, M. *et al.* Sequestration by IFIT1 Impairs Translation of 2'O-unmethylated Capped RNA. *PLoS Pathogens* **9**, e1003663 (2013).

[306] Kumar, P. *et al.* Inhibition of translation by IFIT family members is determined by their ability to interact selectively with the 5'-terminal regions of cap0-, cap1- and 5'ppp- mRNAs. *Nucleic Acids Research* **42**, 3228–3245 (2014).

[307] Szretter, K. J. *et al.* 2'-O Methylation of the Viral mRNA Cap by West Nile Virus Evades Ifit1-Dependent and -Independent Mechanisms of Host Restriction In Vivo. *PLoS Pathogens* **8**, e1002698 (2012).

[308] Cheriyath, V. *et al.* G1P3, an IFN-induced survival factor, antagonizes TRAIL-induced apoptosis in human myeloma cells. *Journal of Clinical Investigation* **117**, 3107–3117 (2007).

[309] Richardson, R. B. *et al.* A CRISPR screen identifies IFI6 as an ER-resident interferon effector that blocks flavivirus replication. *Nature Microbiology* **3**, 1214–1223 (2018).

[310] Sajid, M. *et al.* The Functional and Antiviral Activity of Interferon Alpha-Inducible IFI6 Against Hepatitis B Virus Replication and Gene Expression. *Frontiers in Immunology* **12**, 634937 (2021).

[311] Chakrabarti, A., Jha, B. K. & Silverman, R. H. New Insights into the Role of RNase L in Innate Immunity. *Journal of Interferon & Cytokine Research* **31**, 49–57 (2011).

[312] Kristiansen, H., Gad, H. H., Eskildsen-Larsen, S., Despres, P. & Hartmann, R. The Oligoadenylate Synthetase Family: An Ancient Protein Family with Multiple Antiviral Activities. *Journal of Interferon & Cytokine Research* **31**, 41–47 (2011).

[313] Guo, X., Ma, J., Sun, J. & Gao, G. The zinc-finger antiviral protein recruits the RNA processing exosome to degrade the target mRNA. *Proceedings of the National Academy of Sciences* **104**, 151–156 (2007).

[314] Espert, L. *et al.* ISG20, a New Interferon-induced RNase Specific for Single-stranded RNA, Defines an Alternative Antiviral Pathway against RNA Genomic Viruses. *Journal of Biological Chemistry* **278**, 16151–16158 (2003).

[315] Krapp, C. *et al.* Guanylate Binding Protein (GBP) 5 Is an Interferon-Inducible Inhibitor of HIV-1 Infectivity. *Cell Host & Microbe* **19**, 504–514 (2016).

[316] Neil, S. J. D., Zang, T. & Bieniasz, P. D. Tetherin inhibits retrovirus release and is antagonized by HIV-1 Vpu. *Nature* **451**, 425–430 (2008).

[317] García-Sastre, A. *et al.* Influenza A Virus Lacking the NS1 Gene Replicates in Interferon-Deficient Systems. *Virology* **252**, 324–330 (1998).

[318] Talon, J. *et al.* Activation of Interferon Regulatory Factor 3 Is Inhibited by the Influenza A Virus NS1 Protein. *Journal of Virology* **74**, 7989–7996 (2000).

[319] Wang, X. *et al.* Functional Replacement of the Carboxy-Terminal Two-Thirds of the Influenza A Virus NS1 Protein with Short Heterologous Dimerization Domains. *Journal of Virology* **76**, 12951–12962 (2002).

[320] Mibayashi, M. *et al.* Inhibition of Retinoic Acid-Inducible Gene I-Mediated Induction of Beta Interferon by the NS1 Protein of Influenza A Virus. *Journal of Virology* **81**, 514–524 (2007).

[321] Bauhofer, O. *et al.* Classical Swine Fever Virus N pro Interacts with Interferon Regulatory Factor 3 and Induces Its Proteasomal Degradation. *Journal of Virology* **81**, 3087–3096 (2007).

[322] Rocca, S. A. L. *et al.* Loss of Interferon Regulatory Factor 3 in Cells Infected with Classical Swine Fever Virus Involves the N-Terminal Protease, N pro. *Journal of Virology* **79**, 7239–7247 (2005).

[323] Ruggli, N. *et al.* Npro of classical swine fever virus is an antagonist of double-stranded RNA-mediated apoptosis and IFN-α/β induction. *Virology* **340**, 265–276 (2005).

[324] Sen, N. *et al.* Varicella-Zoster Virus Immediate-Early Protein 62 Blocks Interferon Regulatory Factor 3 (IRF3) Phosphorylation at Key Serine Residues: a Novel Mechanism of IRF3 Inhibition among Herpesviruses. *Journal of Virology* **84**, 9240–9253 (2010).

[325] Ferreira, A. R. *et al.* Hepatitis C virus NS3-4A inhibits the peroxisomal MAVS-dependent antiviral signalling response. *Journal of Cellular and Molecular Medicine* **20**, 750–757 (2016).

[326] Li, X.-D., Sun, L., Seth, R. B., Pineda, G. & Chen, Z. J. Hepatitis C virus protease NS3/4A cleaves mitochondrial antiviral signaling protein off the mitochondria to evade innate immunity. *Proceedings of the National Academy of Sciences of the United States of America* **102**, 17717–17722 (2005).

[327] Barathan, M. *et al.* Viral Persistence and Chronicity in Hepatitis C Virus Infection: Role of T-Cell Apoptosis, Senescence and Exhaustion. *Cells* **7**, 165 (2018).

[328] Chang, K. The mechanisms of chronicity in hepatitis C virus infection. *Gastroenterology* **115**, 1015–1018 (1998).

[329] Iannello, A. *et al.* Viral strategies for evading antiviral cellular immune responses of the host. *Journal of Leukocyte Biology* **79**, 16–35 (2006).

[330] Ke, H. & Yoo, D. The viral innate immune antagonism and an alternative vaccine design for PRRS virus. *Veterinary Microbiology* **209**, 75–89 (2017).

[331] Manns, M. P. *et al.* Peginterferon alfa-2b plus ribavirin compared with interferon alfa-2b plus ribavirin for initial treatment of chronic hepatitis C: a randomised trial. *The Lancet* **358**, 958–965 (2001).

[332] Ashour, J., Laurent-Rolle, M., Shi, P.-Y. & García-Sastre, A. NS5 of Dengue Virus Mediates STAT2 Binding and Degradation. *Journal of Virology* **83**, 5408–5418 (2009).

[333] Mazzon, M., Jones, M., Davidson, A., Chain, B. & Jacobs, M. Dengue Virus NS5 Inhibits Interferon-α Signaling by Blocking Signal Transducer and Activator of Transcription 2 Phosphorylation. *The Journal of Infectious Diseases* **200**, 1261–1270 (2009).

[334] Morrison, J. *et al.* Dengue Virus Co-opts UBR4 to Degrade STAT2 and Antagonize Type I Interferon Signaling. *PLoS Pathogens* **9**, e1003265 (2013).

[335] Muñoz-Jordán, J. L., Sánchez-Burgos, G. G., Laurent-Rolle, M. & García-Sastre, A. Inhibition of interferon signaling by dengue virus. *Proceedings of the National Academy of Sciences* **100**, 14333–14338 (2003).

[336] Muñoz-Jordán, J. L. *et al.* Inhibition of Alpha/Beta Interferon Signaling by the NS4B Protein of Flaviviruses. *Journal of Virology* **79**, 8004–8013 (2005).

[337] Rodriguez-Madoz, J. R. *et al.* Inhibition of the Type I Interferon Response in Human Dendritic Cells by Dengue Virus Infection Requires a Catalytically Active NS2B3 Complex. *Journal of Virology* **84**, 9760–9774 (2010).

[338] Laurent-Rolle, M. *et al.* The NS5 Protein of the Virulent West Nile Virus NY99 Strain Is a Potent Antagonist of Type I Interferon-Mediated JAK-STAT Signaling. *Journal of Virology* **84**, 3503–3515 (2010).

[339] Xu, D., Biswal, M., Neal, A. & Hai, R. Review Devil's tools: SARS-CoV-2 antagonists against innate immunity. *Current Research in Virological Science* **2**, 100013 (2021).

[340] Lei, X. *et al.* Activation and evasion of type I interferon responses by SARS-CoV-2. *Nature Communications* **11**, 3810 (2020).

[341] Xia, H. *et al.* Evasion of type-I interferon by SARS-CoV-2. *Cell Reports* **33**, 108234 (2020).

[342] Yuen, C.-K. *et al.* SARS-CoV-2 nsp13, nsp14, nsp15 and orf6 function as potent interferon antagonists. *Emerging Microbes & Infections* **9**, 1–29 (2020).

[343] Addetia, A. *et al.* SARS-CoV-2 ORF6 Disrupts Bidirectional Nucleocytoplasmic Transport through Interactions with Rae1 and Nup98. *mBio* **12**, e00065–21 (2021).

[344] Miorin, L. *et al.* SARS-CoV-2 Orf6 hijacks Nup98 to block STAT nuclear import and antagonize interferon signaling. *Proceedings of the National Academy of Sciences* **117**, 28344–28354 (2020).

[345] Motta, S. & Pappalardo, F. Mathematical modeling of biological systems. *Briefings in Bioinformatics* **14**, 411–422 (2013).

[346] Xavier, J. B. *et al.* Mathematical models to study the biology of pathogens and the infectious diseases they cause. *iScience* **25**, 104079 (2022).

[347] Tuszynski, J. A. *et al.* Mathematical and computational modeling in biology at multiple scales. *Theoretical Biology and Medical Modelling* **11**, 52 (2014).

[348] Qiao, L. *et al.* Immune Response Modeling of Interferon β-Pretreated Influenza Virus-Infected Human Dendritic Cells. *Biophysical Journal* **98**, 505–514 (2010).

[349] Kok, F. *et al.* Disentangling molecular mechanisms regulating sensitization of interferon alpha signal transduction. *Molecular Systems Biology* **16**, e8955 (2020).

[350] Park, A. & Iwasaki, A. Type I and Type III Interferons - Induction, Signaling, Evasion, and Application to Combat COVID-19. *Cell host & microbe* (2020).

[351] Voutouri, C. *et al.* In silico dynamics of COVID-19 phenotypes for optimizing clinical management. *Proceedings of the National Academy of Sciences of the United States of America* **118**, e2021642118 (2021).

[352] Wang, B., Mondal, J., Samui, P., Chatterjee, A. N. & Yusuf, A. Effect of an antiviral drug control and its variable order fractional network in host COVID-19 kinetics. *The European Physical Journal Special Topics* 1–15 (2022).

[353] Burkart, S. S. *et al.* High Resolution Kinetic Characterization and Dynamic Mathematical Modeling of the RIG-I Signaling Pathway and the Antiviral Responses. *bioRxiv* (2022).

[354] Urban, C. *et al.* Persistent Innate Immune Stimulation Results in IRF3-Mediated but Caspase-Independent Cytostasis. *Viruses* **12**, 635 (2020).

[355] Zander, D. Y., Burkart, S. S., Wüst, S., Magalhães, V. G. & Binder, M. Cooperative effects of RIG-I-like receptor signaling and IRF1 on DNA damage-induced cell death. *Cell Death & Disease* **13**, 364 (2022).

[356] Binder, M., Kochs, G., Bartenschlager, R. & Lohmann, V. Hepatitis C virus escape from the interferon regulatory factor 3 pathway by a passive and active evasion strategy. *Hepatology* **46**, 1365–1374 (2007).

[357] Heigwer, F., Kerr, G. & Boutros, M. E-CRISP: fast CRISPR target site identification. *Nature Methods* **11**, 122–123 (2014).

[358] Schmittgen, T. D. & Livak, K. J. Analyzing real-time PCR data by the comparative CT method. *Nature Protocols* **3**, 1101–1108 (2008).

[359] Berg, S. *et al.* ilastik: interactive machine learning for (bio)image analysis. *Nature Methods* **16**, 1226–1232 (2019).

[360] Thomas, P. D. *et al.* PANTHER: A Library of Protein Families and Subfamilies Indexed by Function. *Genome Research* **13**, 2129–2141 (2003).

[361] Mi, H., Muruganujan, A. & Thomas, P. D. PANTHER in 2013: modeling the evolution of gene function, and other gene attributes, in the context of phylogenetic trees. *Nucleic Acids Research* **41**, D377–D386 (2013).

[362] Beachboard, D. C. & Horner, S. M. Innate immune evasion strategies of DNA and RNA viruses. *Current Opinion in Microbiology* **32**, 113–119 (2016).

[363] Haller, O., Kochs, G. & Weber, F. The interferon response circuit: Induction and suppression by pathogenic viruses. *Virology* **344**, 119–130 (2006).

[364] Esser-Nobis, K., Hatfield, L. D. & Gale, M. Spatiotemporal dynamics of innate immune signaling via RIG-I–like receptors. *Proceedings of the National Academy of Sciences* (2020).

[365] Rand, U. *et al.* Multi-layered stochasticity and paracrine signal propagation shape the type-I interferon response. *Molecular Systems Biology* **8**, 584 (2012).

[366] Seago, J. *et al.* The Npro product of classical swine fever virus and bovine viral diarrhea virus uses a conserved mechanism to target interferon regulatory factor-3. *Journal of General Virology* **88**, 3002–3006 (2007).

[367] Hatada, E., Saito, S., Okishio, N. & Fukuda, R. Binding of the influenza virus NS1 protein to model genome RNAs. *Journal of General Virology* **78**, 1059–1063 (1997).

[368] Hatada, E. & Fukuda, R. Binding of influenza A virus NS1 protein to dsRNA in vitro. *Journal of General Virology* **73**, 3325–3329 (1992).

[369] Hayn, M. *et al.* Imperfect innate immune antagonism renders SARS-CoV-2 vulnerable towards IFN-γ and -λ. *bioRxiv* 2020.10.15.340612 (2020).

[370] Meewan, I. *et al.* Discovery of New Inhibitors of Hepatitis C Virus NS3/4A Protease and Its D168A Mutant. *ACS Omega* **4**, 16999–17008 (2019).

[371] Rosenquist, A. *et al.* Discovery and Development of Simeprevir (TMC435), a HCV NS3/4A Protease Inhibitor. *Journal of Medicinal Chemistry* **57**, 1673–1693 (2014).

[372] Pessoa, L. S. *et al.* Development of a rapid phenotypic test for HCV protease inhibitors with potential use in clinical decisions. *Genetics and Molecular Biology* **39**, 358–364 (2016).

[373] Sharma, M., Sharma, S., Roy, S., Varma, S. & Bose, M. Pulmonary epithelial cells are a source of interferon-γ in response to Mycobacterium tuberculosis infection. *Immunology and Cell Biology* **85**, 229–237 (2007).

[374] Onoguchi, K., Yoneyama, M. & Fujita, T. Retinoic Acid-Inducible Gene-I-Like Receptors. *Journal of Interferon & Cytokine Research* **31**, 27–31 (2011).

[375] Dumoutier, L., Leemans, C., Lejeune, D., Kotenko, S. V. & Renauld, J.-C. Cutting Edge: STAT Activation By IL-19, IL-20 and mda-7 Through IL-20 Receptor Complexes of Two Types. *The Journal of Immunology* **167**, 3545–3549 (2001).

[376] Poindexter, N. J., Walch, E. T., Chada, S. & Grimm, E. A. Cytokine induction of interleukin-24 in human peripheral blood mononuclear cells. *Journal of Leukocyte Biology* **78**, 745–752 (2005).

[377] Wang, M., Tan, Z., Zhang, R., Kotenko, S. V. & Liang, P. Interleukin 24 (MDA-7/MOB-5) Signals through Two Heterodimeric Receptors, IL-22R1/IL-20R2 and IL-20R1/IL-20R2. *Journal of Biological Chemistry* **277**, 7341–7347 (2002).

[378] Wang, X., Tu, F., Zhu, Y. & Gao, G. Zinc-Finger Antiviral Protein Inhibits XMRV Infection. *PLoS ONE* **7**, e39159 (2012).

[379] Zhu, Y. *et al.* Zinc-finger antiviral protein inhibits HIV-1 infection by selectively targeting multiply spliced viral mRNAs for degradation. *Proceedings of the National Academy of Sciences* **108**, 15834–15839 (2011).

[380] Iwata, H. *et al.* PARP9 and PARP14 cross-regulate macrophage activation via STAT1 ADP-ribosylation. *Nature Communications* **7**, 12849 (2016).

[381] Amarante-Mendes, G. P. *et al.* Pattern Recognition Receptors and the Host Cell Death Molecular Machinery. *Frontiers in Immunology* **9**, 2379 (2018).

[382] Dinarello, C. A. Overview of the IL-1 family in innate inflammation and acquired immunity. *Immunological Reviews* **281**, 8–27 (2017).

[383] El-Zayat, S. R., Sibaii, H. & Mannaa, F. A. Toll-like receptors activation, signaling, and targeting: an overview. *Bulletin of the National Research Centre* **43**, 187 (2019).

[384] Eyndhoven, L. C. V., Singh, A. & Tel, J. Decoding the dynamics of multilayered stochastic antiviral IFN-I responses. *Trends in Immunology* **42**, 824–839 (2021).

[385] Drayman, N., Patel, P., Vistain, L. & Tay, S. HSV-1 single-cell analysis reveals the activation of anti-viral and developmental programs in distinct sub-populations. *eLife* **8**, e46339 (2019).

[386] Oyler-Yaniv, A. *et al.* A Tunable Diffusion-Consumption Mechanism of Cytokine Propagation Enables Plasticity in Cell-to-Cell Communication in the Immune System. *Immunity* **46**, 609–620 (2017).

[387] Bates, G. W. Chapter 26 Electroporation of Plant Protoplasts and Tissues. *Methods in Cell Biology* **50**, 363–373 (1995).

[388] Chassy, B. M., Mercenier, A. & Flickinger, J. Transformation of bacteria by electroporation. *Trends in Biotechnology* **6**, 303–309 (1988).

[389] Chicaybam, L. *et al.* An Efficient Electroporation Protocol for the Genetic Modification of Mammalian Cells. *Frontiers in Bioengineering and Biotechnology* **4**, 99 (2017).

[390] Neumann, E., Schaefer-Ridder, M., Wang, Y. & Hofschneider, P. Gene transfer into mouse lyoma cells by electroporation in high electric fields. *The EMBO Journal* **1**, 841–845 (1982).

[391] Neumann, E. & Rosenheck, K. Permeability changes induced by electric impulses in vesicular membranes. *The Journal of Membrane Biology* **10**, 279–290 (1972).

[392] Castanier, C., Garcin, D., Vazquez, A. & Arnoult, D. Mitochondrial dynamics regulate the RIG-I-like receptor antiviral pathway. *EMBO reports* **11**, 133–138 (2010).

[393] Mäkelä, S. M. *et al.* RIG-I Signaling Is Essential for Influenza B Virus-Induced Rapid Interferon Gene Expression. *Journal of Virology* **89**, 12014–12025 (2015).

[394] Ding, G. J. *et al.* Characterization and Quantitation of NF-κB Nuclear Translocation Induced by Interleukin-1 and Tumor Necrosis Factor-α. Development and Use of a High Capacity Fluorescence Cytometric System. *Journal of Biological Chemistry* **273**, 28897–28905 (1998).

[395] Nelson, G. *et al.* Multi-parameter analysis of the kinetics of NF-κB signalling and transcription in single living cells. *Journal of Cell Science* **115**, 1137–1148 (2002).

[396] Wang, J. *et al.* NF-κB RelA Subunit Is Crucial for Early IFN-β Expression and Resistance to RNA Virus Replication. *The Journal of Immunology* **185**, 1720–1729 (2010).

[397] Wang, X. *et al.* Lack of Essential Role of NF-κB p50, RelA, and cRel Subunits in Virus-Induced Type 1 IFN Expression. *The Journal of Immunology* **178**, 6770–6776 (2007).

[398] Weber, M. & Weber, F. Monitoring Activation of the Antiviral Pattern Recognition Receptors RIG-I And PKR By Limited Protease Digestion and Native PAGE. *Journal of Visualized Experiments* e51415 (2014).

[399] Lee, D., Ding, Y., Jayaraman, A. & Kwon, J. S. Mathematical Modeling and Parameter Estimation of Intracellular Signaling Pathway: Application to LPS-induced NFκB Activation and TNFα Production in Macrophages. *Processes* **6**, 21 (2018).

[400] Klipp, E. & Liebermeister, W. Mathematical modeling of intracellular signaling pathways. *BMC Neuroscience* **7**, S10 (2006).

[401] Cheong, R., Hoffmann, A. & Levchenko, A. Understanding NF-κB signaling via mathematical modeling. *Molecular Systems Biology* **4**, 192–192 (2008).

[402] Bachmann, J. *et al.* Predictive mathematical models of cancer signalling pathways. *Journal of Internal Medicine* **271**, 155–165 (2012).

[403] Bertolusso, R. *et al.* Dynamic Cross Talk Model of the Epithelial Innate Immune Response to Double-Stranded RNA Stimulation: Coordinated Dynamics Emerging from Cell-Level Noise. *PLoS ONE* **9**, e93396 (2014).

[404] Schweinoch, D., Bachmann, P., Clausznitzer, D., Binder, M. & Kaderali, L. Mechanistic modeling explains the dsRNA length-dependent activation of the RIG-I mediated immune response. *Journal of Theoretical Biology* 110336 (2020).

[405] Baker, R. E., Peña, J.-M., Jayamohan, J. & Jérusalem, A. Mechanistic models versus machine learning, a fight worth fighting for the biological community? *Biology Letters* **14**, 20170660 (2018).

[406] Collins, S. E., Noyce, R. S. & Mossman, K. L. Innate Cellular Response to Virus Particle Entry Requires IRF3 but Not Virus Replication. *Journal of Virology* **78**, 1706–1717 (2004).

[407] Doğanay, S. *et al.* Single-cell analysis of early antiviral gene expression reveals a determinant of stochastic IFNB1 expression. *Integrative Biology* **9**, 857–867 (2017).

[408] Kell, A. M., Hemann, E. A., Turnbull, J. B. & Gale, M. RIG-I-like receptor activation drives type I IFN and antiviral signaling to limit Hantaan orthohantavirus replication. *PLoS Pathogens* **16**, e1008483 (2020).

[409] Haller, O. & Kochs, G. Interferon-Induced Mx Proteins: Dynamin-Like GTPases with Antiviral Activity. *Traffic* **3**, 710–717 (2002).

[410] Ronni, T. *et al.* The Proximal Interferon-Stimulated Response Elements Are Essential for Interferon Responsiveness: A Promoter Analysis of the Antiviral MxA Gene. *Journal of Interferon & Cytokine Research* **18**, 773–781 (1998).

[411] Yan, R., Qureshi, S., Zhong, Z., Wen, Z. & Darnell, J. E. The genomic structure of the STAT genes: multiple exons in coincident sites in Stat1 and Stat2. *Nucleic Acids Research* **23**, 459–463 (1995).

[412] Cheon, H. & Stark, G. R. Unphosphorylated STAT1 prolongs the expression of interferon-induced immune regulatory genes. *Proceedings of the National Academy of Sciences* **106**, 9373–9378 (2009).

[413] Reich, N. C. & Liu, L. Tracking STAT nuclear traffic. *Nature Reviews Immunology* **6**, 602–612 (2006).

[414] Marg, A. *et al.* Nucleocytoplasmic shuttling by nucleoporins Nup153 and Nup214 and CRM1-dependent nuclear export control the subcellular distribution of latent Stat1. *The Journal of Cell Biology* **165**, 823–833 (2004).

[415] Meyer, T., Gavenis, K. & Vinkemeier, U. Cell Type-Specific and Tyrosine Phosphorylation-Independent Nuclear Presence of STAT1 and STAT3. *Experimental Cell Research* **272**, 45–55 (2002).

[416] Chatterjee-Kishore, M. & Stark, G. How Stat1 mediates constitutive gene expression: a complex of unphosphorylated Stat1 and IRF1 supports transcription of the LMP2 gene (2000).

[417] Cheon, H. *et al.* IFNβ-dependent increases in STAT1, STAT2, and IRF9 mediate resistance to viruses and DNA damage. *The EMBO Journal* **32**, 2751–2763 (2013).

[418] Sumpter, R. *et al.* Regulating Intracellular Antiviral Defense and Permissiveness to Hepatitis C Virus RNA Replication through a Cellular RNA Helicase, RIG-I. *Journal of Virology* **79**, 2689–2699 (2005).

[419] Sato, M. *et al.* Distinct and Essential Roles of Transcription Factors IRF-3 and IRF-7 in Response to Viruses for IFN-α/β Gene Induction. *Immunity* **13**, 539–548 (2000).

[420] Mutz, P. *et al.* HBV Bypasses the Innate Immune Response and Does Not Protect HCV From Antiviral Activity of Interferon. *Gastroenterology* **154**, 1791–1804.e22 (2018).

[421] Wieland, S. F. & Chisari, F. V. Stealth and Cunning: Hepatitis B and Hepatitis C Viruses. *Journal of Virology* **79**, 9369–9380 (2005).

[422] García-Sastre, A. Identification and Characterization of Viral Antagonists of Type I Interferon in Negative-Strand RNA Viruses. *Kawaoka Y. (eds) Biology of Negative Strand RNA Viruses: The Power of Reverse Genetics. Current Topics in Microbiology and Immunology, vol 283. Springer, Berlin, Heidelberg* **283** (2004).

[423] Pichlmair, A. *et al.* Viral immune modulators perturb the human molecular network by common and unique strategies. *Nature* **487**, 486 (2012).

[424] Neufeldt, C. J. *et al.* The Hepatitis C Virus-Induced Membranous Web and Associated Nuclear Transport Machinery Limit Access of Pattern Recognition Receptors to Viral Replication Sites. *PLoS Pathogens* **12**, e1005428 (2016).

[425] Foy, E. *et al.* Regulation of Interferon Regulatory Factor-3 by the Hepatitis C Virus Serine Protease. *Science* **300**, 1145–1148 (2003).

[426] Li, K. *et al.* Immune evasion by hepatitis C virus NS3/4A protease-mediated cleavage of the Toll-like receptor 3 adaptor protein TRIF. *Proceedings of the National Academy of Sciences* **102**, 2992–2997 (2005).

[427] Loo, Y.-M. *et al.* Viral and therapeutic control of IFN-β promoter stimulator 1 during hepatitis C virus infection. *Proceedings of the National Academy of Sciences* **103**, 6001–6006 (2006).

[428] Meylan, E. *et al.* Cardif is an adaptor protein in the RIG-I antiviral pathway and is targeted by hepatitis C virus. *Nature* **437**, 1167–1172 (2005).

[429] Oshiumi, H., Miyashita, M., Matsumoto, M. & Seya, T. A Distinct Role of Riplet-Mediated K63-Linked Polyubiquitination of the RIG-I Repressor Domain in Human Antiviral Innate Immune Responses. *PLoS Pathogens* **9**, e1003533 (2013).

[430] Kim, S.-J. *et al.* Hepatitis C virus triggers mitochondrial fission and attenuates apoptosis to promote viral persistence. *Proceedings of the National Academy of Sciences* **111**, 6413–6418 (2014).

[431] Stone, A. E. L. *et al.* Hepatitis C Virus Core Protein Inhibits Interferon Production by a Human Plasmacytoid Dendritic Cell Line and Dysregulates Interferon Regulatory Factor-7 and Signal Transducer and Activator of Transcription (STAT) 1 Protein Expression. *PLoS ONE* **9**, e95627 (2014).

[432] Bartenschlager, R., Ahlborn-Laake, L., Mous, J. & Jacobsen, H. Kinetic and structural analyses of hepatitis C virus polyprotein processing. *Journal of Virology* **68**, 5045–5055 (1994).

[433] Falade-Nwulia, O. *et al.* Oral Direct-Acting Agent Therapy for Hepatitis C Virus Infection: A Systematic Review. *Annals of Internal Medicine* **166**, 637 (2017).

[434] González-Grande, R., Jiménez-Pérez, M., Arjona, C. G. & Torres, J. M. New approaches in the treatment of hepatitis C. *World Journal of Gastroenterology* **22**, 1421–1432 (2016).

[435] Fiebach, A. R., Guzylack-Piriou, L., Python, S., Summerfield, A. & Ruggli, N. Classical Swine Fever Virus N pro Limits Type I Interferon Induction in Plasmacytoid Dendritic Cells by Interacting with Interferon Regulatory Factor 7. *Journal of Virology* **85**, 8002–8011 (2011).

[436] Honda, K. *et al.* IRF-7 is the master regulator of type-I interferon-dependent immune responses. *Nature* **434**, 772–777 (2005).

[437] Doceul, V. *et al.* The Npro product of classical swine fever virus interacts with IκBα, the NF-κB inhibitor. *Journal of General Virology* **89**, 1881–1889 (2008).

[438] Fan, S. *et al.* Activation of Interleukin-1β Release by the Classical Swine Fever Virus Is Dependent on the NLRP3 Inflammasome, Which Affects Virus Growth in Monocytes. *Frontiers in Cellular and Infection Microbiology* **8**, 225 (2018).

[439] Khatoon, E. *et al.* Cytokine responses in pigs after natural infection with classical swine fever virus. *Acta virologica* **63**, 60–69 (2019).

[440] Summerfield, A. & Ruggli, N. Immune Responses Against Classical Swine Fever Virus: Between Ignorance and Lunacy. *Frontiers in Veterinary Science* **2**, 10 (2015).

[441] Klema, V. J. *et al.* Dengue Virus Nonstructural Protein 5 (NS5) Assembles into a Dimer with a Unique Methyltransferase and Polymerase Interface. *PLoS Pathogens* **12**, e1005451 (2016).

[442] Iglesias, N. G., Filomatori, C. V. & Gamarnik, A. V. The F1 Motif of Dengue Virus Polymerase NS5 Is Involved in Promoter-Dependent RNA Synthesis. *Journal of Virology* **85**, 5745–5756 (2011).

[443] Khunchai, S. *et al.* Interaction of dengue virus nonstructural protein 5 with Daxx modulates RANTES production. *Biochemical and Biophysical Research Communications* **423**, 398–403 (2012).

[444] Sahili, A. E. & Lescar, J. Dengue Virus Non-Structural Protein 5. *Viruses* **9**, 91 (2017).

[445] Bhatnagar, P., Sreekanth, G. P., Murali-Krishna, K., Chandele, A. & Sitaraman, R. Dengue Virus Non-Structural Protein 5 as a Versatile, Multi-Functional Effector in Host–Pathogen Interactions. *Frontiers in Cellular and Infection Microbiology* **11**, 574067 (2021).

[446] Maio, F. A. D. *et al.* The Dengue Virus NS5 Protein Intrudes in the Cellular Spliceosome and Modulates Splicing. *PLoS Pathogens* **12**, e1005841 (2016).

[447] Green, J. A., Cooperband, S. R. & Kibrick, S. Immune Specific Induction of Interferon Production in Cultures of Human Blood Lymphocytes. *Science* **164**, 1415–1417 (1969).

[448] Wheelock, E. F. Interferon-Like Virus-Inhibitor Induced in Human Leukocytes by Phytohemagglutinin. *Science* **149**, 310–311 (1965).

[449] Melchjorsen, J., Sørensen, L. N. & Paludan, S. R. Expression and function of chemokines during viral infections: from molecular mechanisms to in vivo function. *Journal of Leukocyte Biology* **74**, 331–343 (2003).

[450] Ramshaw, I. A. *et al.* Cytokines and immunity to viral infections. *Immunological Reviews* **159**, 119–135 (1997).

[451] Salazar-Mather, T. P. & Hokeness, K. L. Chemokines and Viral Infection. *Current Topics in Microbiology and Immunology* **303**, 29–46 (2006).

[452] Poeck, H. *et al.* Recognition of RNA virus by RIG-I results in activation of CARD9 and inflammasome signaling for interleukin 1β production. *Nature Immunology* **11**, 63–69 (2010).

[453] Rauch, I., Müller, M. & Decker, T. The regulation of inflammation by interferons and their STATs. *JAK-STAT* **2**, e23820 (2014).

[454] Lin, A. A., Tripathi, P. K., Sholl, A., Jordan, M. B. & Hildeman, D. A. Gamma Interferon Signaling in Macrophage Lineage Cells Regulates Central Nervous System Inflammation and Chemokine Production. *Journal of Virology* **83**, 8604–8615 (2009).

[455] Salazar-Mather, T. P., Lewis, C. A. & Biron, C. A. Type I interferons regulate inflammatory cell trafficking and macrophage inflammatory protein 1α delivery to the liver. *Journal of Clinical Investigation* **110**, 321–330 (2002).

[456] Aung, L. L., Fitzgerald-Bocarsly, P., Dhib-Jalbut, S. & Balashov, K. Plasmacytoid dendritic cells in multiple sclerosis: Chemokine and chemokine receptor modulation by interferon-beta. *Journal of Neuroimmunology* **226**, 158–164 (2010).

[457] Zang, Y. C. *et al.* Regulation of chemokine receptor CCR5 and production of RANTES and MIP-1α by interferon-β. *Journal of Neuroimmunology* **112**, 174–180 (2001).

[458] Szabo, A. *et al.* TLR ligands upregulate RIG-I expression in human plasmacytoid dendritic cells in a type I IFN-independent manner. *Immunology and Cell Biology* **92**, 671–678 (2014).

[459] Su, Z., Sarkar, D., Emdad, L., Barral, P. M. & Fisher, P. B. Central role of interferon regulatory factor-1 (IRF-1) in controlling retinoic acid inducible gene-I (RIG-I) expression. *Journal of Cellular Physiology* **213**, 502–510 (2007).

[460] Masumi, A. *et al.* Enhanced RIG-I expression is mediated by interferon regulatory factor-2 in peripheral blood B cells from hepatitis C virus-infected patients. *Biochemical and Biophysical Research Communications* **391**, 1623–1628 (2010).

[461] Ku, H.-C. & Cheng, C.-F. Master Regulator Activating Transcription Factor 3 (ATF3) in Metabolic Homeostasis and Cancer. *Frontiers in Endocrinology* **11**, 556 (2020).

[462] Chen, B. P., Wolfgang, C. D. & Hai, T. Analysis of ATF3, a transcription factor induced by physiological stresses and modulated by gadd153/Chop10. *Molecular and Cellular Biology* **16**, 1157–1168 (1996).

[463] Liu, J. *et al.* Role of ATF3 in synergistic cancer cell killing by a combination of HDAC inhibitors and agonistic anti-DR5 antibody through ER stress in human colon cancer cells. *Biochemical and Biophysical Research Communications* **445**, 320–326 (2014).

[464] Tian, X. *et al.* Modulation of CCAAT/Enhancer Binding Protein Homologous Protein (CHOP)-dependent DR5 Expression by Nelfinavir Sensitizes Glioblastoma Multiforme Cells to Tumor Necrosis Factor-related Apoptosis-inducing Ligand (TRAIL). *Journal of Biological Chemistry* **286**, 29408–29416 (2011).

[465] Xu, L., Su, L. & Liu, X. PKCδ Regulates Death Receptor 5 Expression Induced by PS-341 through ATF4–ATF3/CHOP Axis in Human Lung Cancer Cells. *Molecular Cancer Therapeutics* **11**, 2174–2182 (2012).

[466] Sood, V. *et al.* ATF3 negatively regulates cellular antiviral signaling and autophagy in the absence of type I interferons. *Scientific Reports* **7**, 8789 (2017).

[467] Xiang, Y. *et al.* Identification of Cholesterol 25-Hydroxylase as a Novel Host Restriction Factor and a Part of the Primary Innate Immune Responses against Hepatitis C Virus Infection. *Journal of Virology* **89**, 6805–6816 (2015).

[468] Zang, R. *et al.* Cholesterol 25-hydroxylase suppresses SARS-CoV-2 replication by blocking membrane fusion. *Proceedings of the National Academy of Sciences of the United States of America* **117**, 32105–32113 (2020).

[469] Anggakusuma *et al.* Interferon-inducible cholesterol-25-hydroxylase restricts hepatitis C virus replication through blockage of membranous web formation. *Hepatology* **62**, 702–714 (2015).

[470] Mboko, W. P. *et al.* Interferon Regulatory Factor 1 Restricts Gammaherpesvirus Replication in Primary Immune Cells. *Journal of Virology* **88**, 6993–7004 (2014).

[471] Panda, D. *et al.* IRF1 Maintains Optimal Constitutive Expression of Antiviral Genes and Regulates the Early Antiviral Response. *Frontiers in Immunology* **10**, 1019 (2019).

[472] Wang, Y. *et al.* Mitochondria-localised ZNFX1 functions as a dsRNA sensor to initiate antiviral responses through MAVS. *Nature Cell Biology* **21**, 1346–1356 (2019).

[473] Vavassori, S. *et al.* Multisystem inflammation and susceptibility to viral infections in human ZNFX1 deficiency. *Journal of Allergy and Clinical Immunology* **148**, 381–393 (2021).

[474] Zattoni, M. *et al.* Serpin Signatures in Prion and Alzheimer's Diseases. *Molecular Neurobiology* **59**, 3778–3799 (2022).

[475] Azouz, N. P. *et al.* Alpha 1 Antitrypsin is an Inhibitor of the SARS-CoV-2–Priming Protease TMPRSS2. *Pathogens and Immunity* **6**, 55–74 (2021).

[476] SHAPIRO, L., POTT, G. B. & RALSTON, A. H. Alpha-1-antitrypsin inhibits human immunodeficiency virus type 1. *The FASEB Journal* **15**, 115–122 (2001).

[477] Wettstein, L. *et al.* Alpha-1 antitrypsin inhibits TMPRSS2 protease activity and SARS-CoV-2 infection. *Nature Communications* **12**, 1726 (2021).

[478] Gopalan, S. M., Wilczynska, K. M., Konik, B. S., Bryan, L. & Kordula, T. Astrocyte-specific Expression of the α1-Antichymotrypsin and Glial Fibrillary Acidic Protein Genes Requires Activator Protein-1. *Journal of Biological Chemistry* **281**, 1956–1963 (2006).

[479] Kiss, D. L. *et al.* Duration of α1-antichymotrypsin gene activation by interleukin-1 is determined by efficiency of inhibitor of nuclear factor κBα resynthesis in primary human astrocytes. *Journal of Neurochemistry* **92**, 730–738 (2005).

[480] Kordula, T. *et al.* Oncostatin M and the Interleukin-6 and Soluble Interleukin-6 Receptor Complex Regulate α1-Antichymotrypsin Expression in Human Cortical Astrocytes. *Journal of Biological Chemistry* **273**, 4112–4118 (1998).

[481] Kordula, T., Bugno, M., Rydel, R. E. & Travis, J. Mechanism of Interleukin-1- and Tumor Necrosis Factor α-Dependent Regulation of the α1-Antichymotrypsin Gene in Human Astrocytes. *The Journal of Neuroscience* **20**, 7510–7516 (2000).

[482] Naidoo, N., Cooperman, B. S., Wang, Z.-m., Liu, X.-z. & Rubin, H. Identification of Lysines within α1-Antichymotrypsin Important for DNA Binding. An Unusual Combination of DNA-Binding Elements. *Journal of Biological Chemistry* **270**, 14548–14555 (1995).

[483] Zitzmann, C. *et al.* A Coupled Mathematical Model of the Intracellular Replication of Dengue Virus and the Host Cell Immune Response to Infection. *Frontiers in Microbiology* **11**, 725 (2020).

[484] Bocharov, G. *et al.* A Systems Immunology Approach to Plasmacytoid Dendritic Cell Function in Cytopathic Virus Infections. *PLoS Pathogens* **6**, e1001017 (2010).

[485] Cai, C. & Yu, X. A mathematic model to reveal delicate cross-regulation between MAVS/STING, inflammasome and MyD88-dependent type I interferon signalling. *Journal of Cellular and Molecular Medicine* **24**, 11535–11545 (2020).

[486] Talemi, S. R. *et al.* Dengue virus is sensitive to inhibition prior to productive replication. *Cell Reports* **37**, 109801 (2021).

[487] Wang, S., Hao, M., Pan, Z., Lei, J. & Zou, X. Data-driven multi-scale mathematical modeling of SARS-CoV-2 infection reveals heterogeneity among COVID-19 patients. *PLoS Computational Biology* **17**, e1009587 (2021).

Supplement

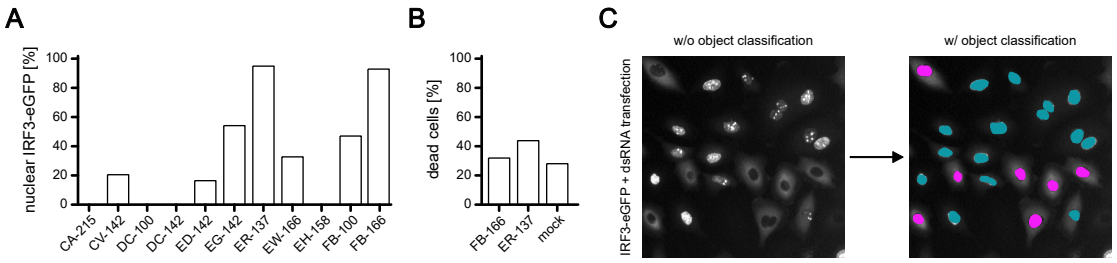

Figure S1: Experimental optimization for in-well electroporation with the Lonza Nucleofector system.

For synchronous dsRNA stimulation, A549 IRF3-eGFP H2B-mCherry cells were in-well electroporated with 1 µg 5'ppp-dsRNA using the Lonza Nucleofector system. **(A)** IRF3-eGFP translocation efficiency upon in-well electroporation of 5'ppp-dsRNA using various predefined nucleofection programs on the Nucleofector system. IRF3-eGFP subcellular localization was examined by fluorescence microscopy. **(B)** Programs yielding the highest translocation efficiency were tested for cytotoxicity upon in-well electroporation of 1 µg 5'ppp-dsRNA and compared to mock stimulation. **(C)** Exemplary image excerpt of ilastik quantification depicting object classification for IRF3-eGFP. Nuclear IRF3-eGFP is marked in blue, cytoplasmic IRF3-eGFP and thereby empty nuclei are marked in magenta, and colocalization with nuclear H2B-mCherry is quantified for each cell.

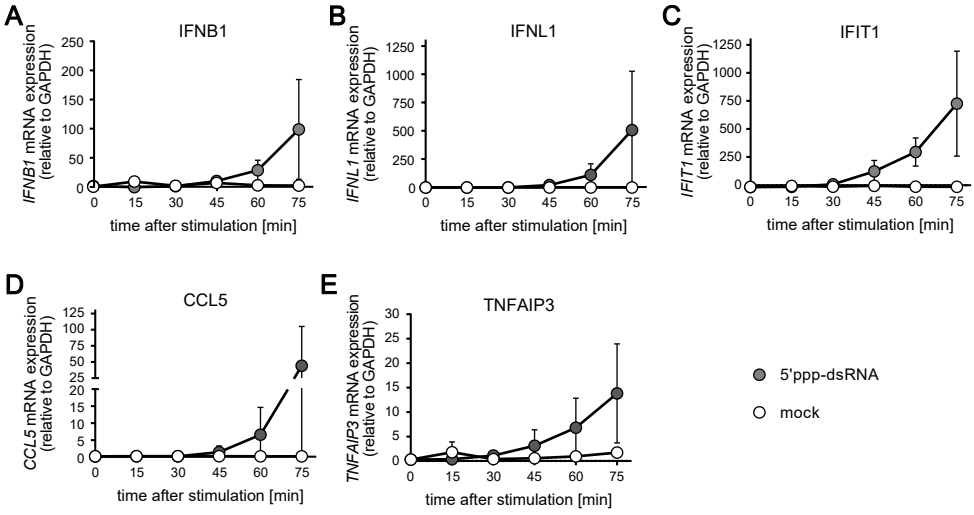

Figure S2: Early RIG-I signaling kinetics upon mock electroporation in A549 wt cells.

A549 wt cells were either mock-treated or synchronously stimulated with 220 ng 5'ppp-dsRNA by electroporation. **(A)** IFNB1, **(B)** IFNL1, **(C)** IFIT1, **(D)** CCL5, and **(E)** TNFAIP3 mRNA expression was measured using qRT-PCR. Values were normalized to the housekeeping gene GAPDH using the $2^{-\Delta Ct}$ method [358]. Graphs depict mean and individual, biological replicate values of 3 biologically independent experiments.

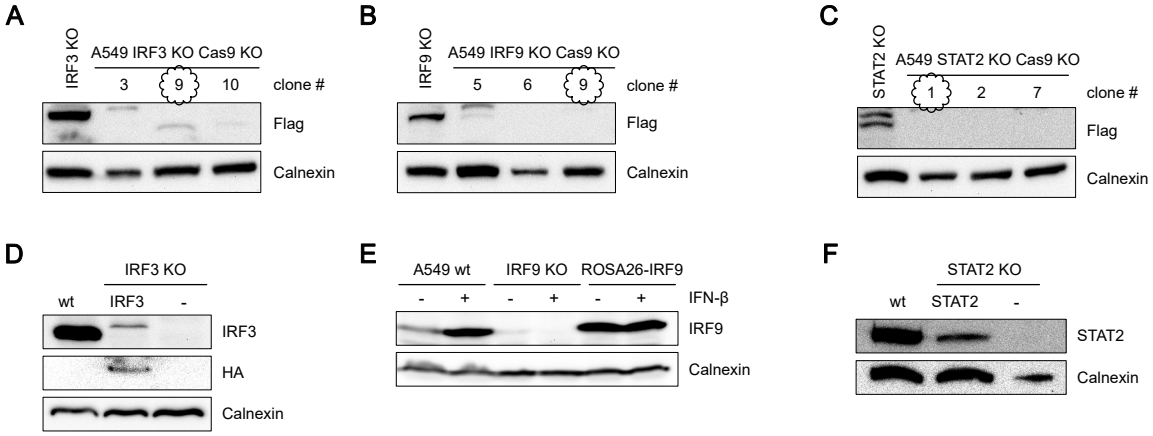

Figure S3: Validation of newly generated A549 KO and overexpression cell lines.

Validation of A549 CRISPR/Cas9 KO single cell clones. KO of the Flag-tagged Cas9 in **(A)** A549 IRF3 KO, **(B)** A549 IRF9 KO, and **(C)** A549 STAT2 KO cells was examined by western blot analysis. Overexpression of **(D)** ROSA26-IRF3-HA in A549 IRF3 KO Cas9 KO cells, **(E)** ROSA26-IRF9 in A549 IRF9 KO Cas9 KO cells, and **(F)** ROSA26-STAT2 in A549 STAT2 KO Cas9 KO cells was analyzed using western blot analysis.

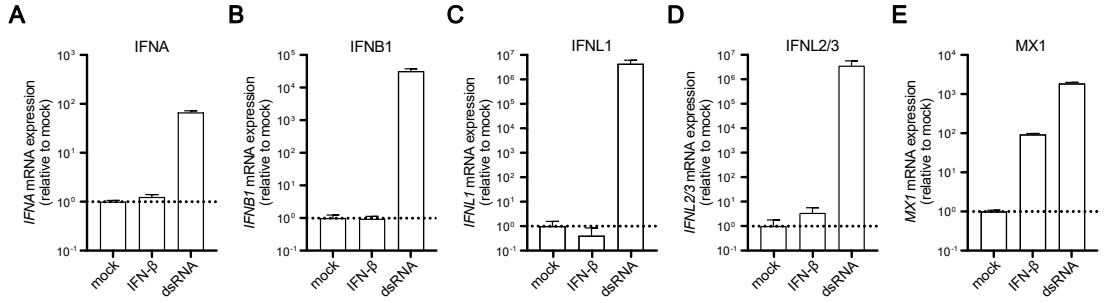

Figure S4: IFN expression upon IFN and 5'ppp-dsRNA stimulation in A549 cells.

A549 wt cells were either mock-treated, stimulated with 200 IU IFN-β, or transfected with 100 ng 5'ppp-dsRNA for 16 hours and **(A)** IFNA1, **(B)** IFNB1, **(C)** IFNL1, **(D)** IFNL2/3, and **(E)** MX1 mRNA expression was analyzed using qRT-PCR. Values were normalized to the housekeeping gene GAPDH and the mock control subsequently using $2^{-\Delta\Delta Ct}$ [358]. Graph depicts mean ± SD of 3 technical replicates. Figure was originally published in Burkart *et al.* [353].

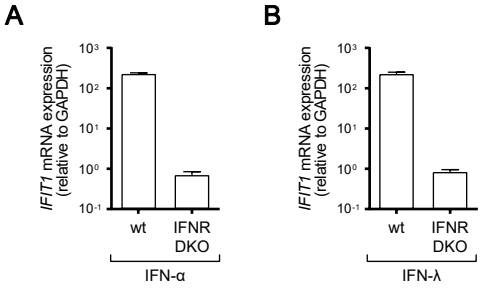

Figure S5: Functional validation of A549 IFNR DKO cells.

Validation of A549 CRISPR/Cas9 knockout single cell clones. A549 wt and IFNR DKO cells were **(A)** stimulated with 1 ng/µl IFN-α, or **(B)** 2 ng/µl IU IFN-λ for 16 hours and IFIT1 mRNA expression was examined using qRT-PCR. Values were normalized to GAPDH using the using $2^{-\Delta Ct}$ method [358]. Graph depicts mean ± SD of 3 technical replicates. KO generation and functional validation were conducted by Sandra Wüst.

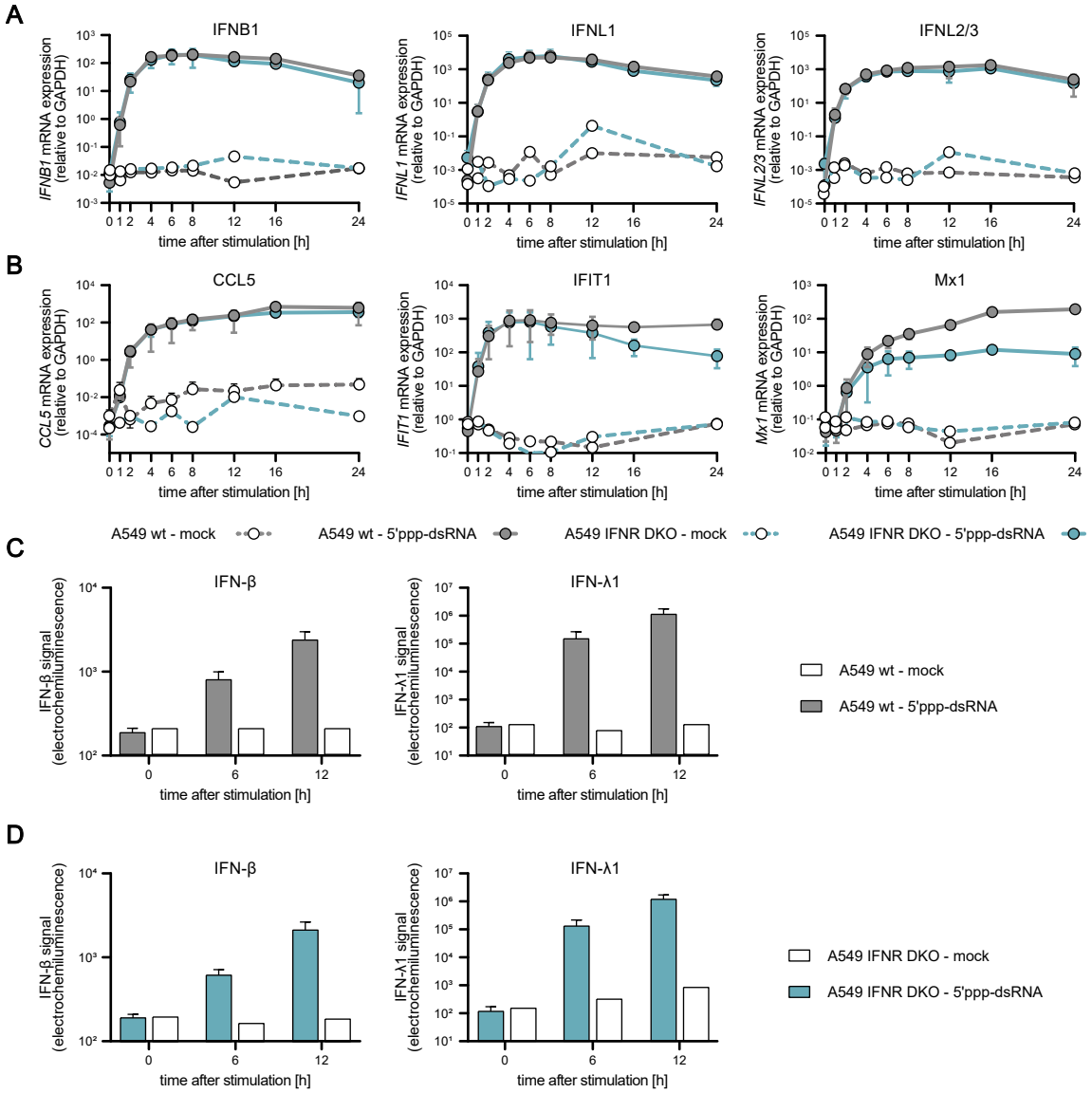

Figure S6: RIG-I signaling kinetics upon mock electroporation in A549 wt and IFNR DKO cells.

A549 wt and A549 IFNR DKO cells were either mock-treated or synchronously stimulated with 220 ng 5'ppp-dsRNA. **(A)** IFNB1, IFNL1, and IFNL2/3, or **(B)** CCL5, IFIT1, and MX1 mRNA expression kinetics was analyzed using quantitative RT-PCR in mock and 5'ppp-dsRNA conditions. Values were normalized to the housekeeping gene GAPDH. Secreted IFN-β and IFN-λ1 protein concentrations in pg/ml were determined using a multiplex immunoassay (U-PLEX IFN Combo, Meso Scale Diagnostics) in **(C)** A549 wt and **(D)** A549 IFNR DKO cells upon mock and 5'ppp-dsRNA stimulation after 0, 6, and 12 hours. Graphs depict (A-B) mean ± SD of 3 independent experiments. 5'ppp-dsRNA stimulated parts of subfigures (A-D) were previously published in Burkart *et al.* [353].

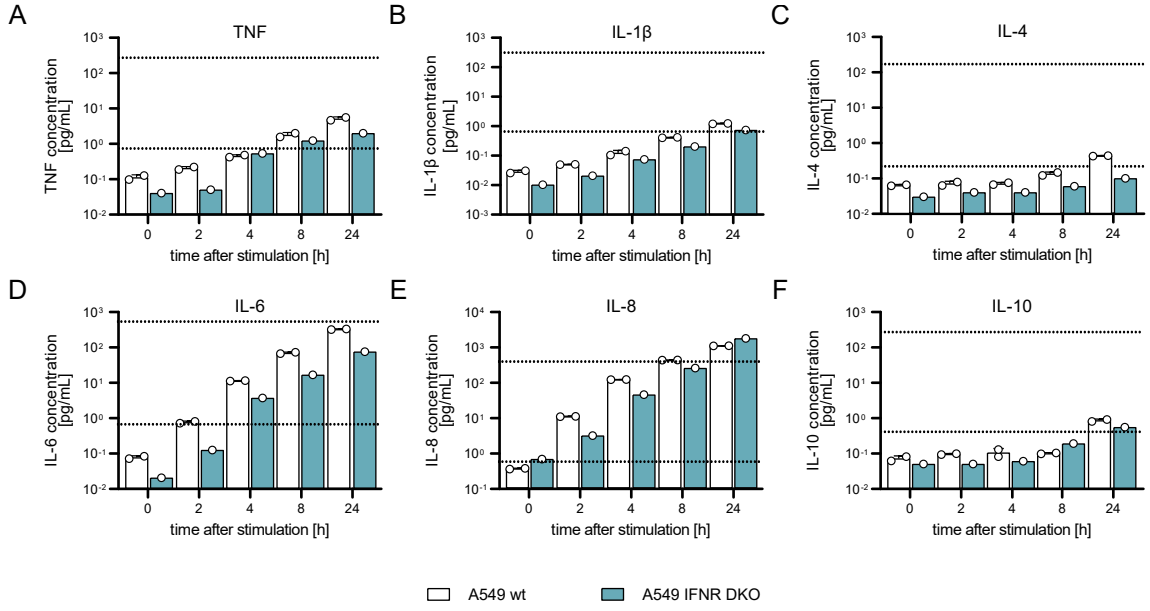

Figure S7: Cytokine production in A549 wt and IFNR DKO cells upon synchronous 5'ppp-dsRNA stimulation.

A549 wt and IFNR DKO cells were synchronously stimulated with 220 ng 5'ppp-dsRNA and supernatants were harvested at different time points. Cytokine production for **(A)** TNF, **(B)** IL-β, **(C)** IL-4, **(D)** IL-6, **(E)** IL-8, and **(F)** IL-10 was determined using a multiplex immunoassay (V-PLEX Viral Panel, Meso Scale Diagnostics). Dashed lines indicate upper and lower limit of quantification, respectively.

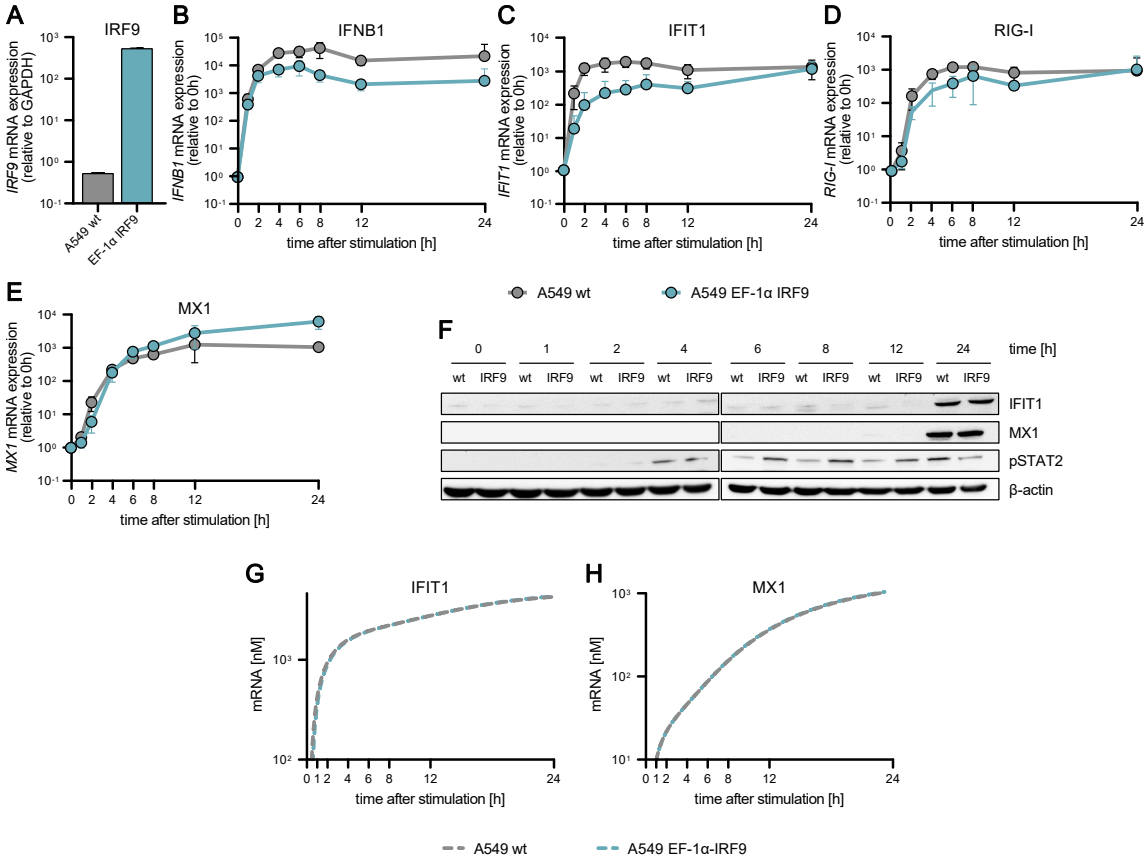

Figure S8: RIG-I signaling kinetics in A549 wt and IRF9 overexpressing cells.

(A) IRF9 mRNA expression in A549 wt and A549 cells stably expressing EF-1α-IRF9 was measured using qRT-PCR. Values were normalized to the housekeeping gene GAPDH. (B-E) A549 wt and EF-1α-IRF9 expressing cells were synchronously stimulated with 220 ng 5'ppp-dsRNA and **(B)** IFNB1, **(C)** IFIT1, **(D)** RIG-I, as well as **(E)** MX1 mRNA expression kinetics was analyzed using qRT-PCR. Values were normalized to the housekeeping gene GAPDH and the 0 hour time point subsequently. **(F)** Protein abundance and phosphorylation status of RIG-I and IFN signaling components was analyzed upon 5'ppp-dsRNA stimulation of A549 wt and A549 EF-1α-IRF9 cells using western blot analysis. (G-H) Model simulation of **(G)** IFIT1 and **(H)** MX1 mRNA expression upon regular (wt) and increased IRF9 (EF-1α-IRF9) protein levels. Graphs depict (B-E) mean ± SD or (F) representative blot of 3 biologically independent experiments. Subfigures (G-H) were originally published in Burkart *et al.* [353].

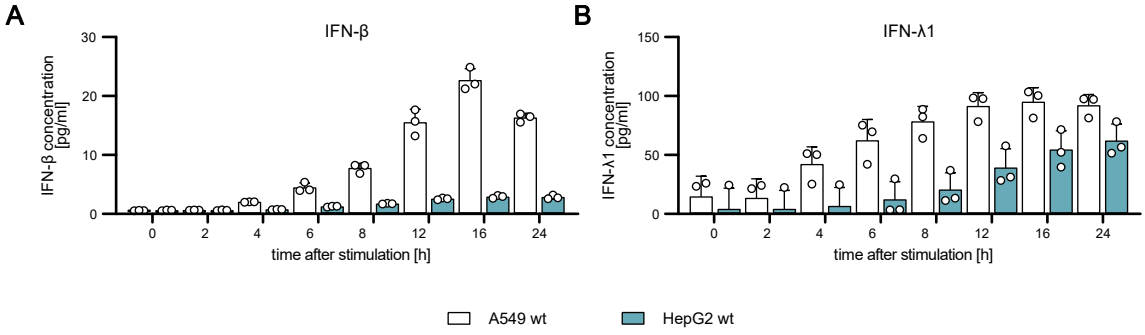

Figure S9: IFN production in A549 and HepG2 cells upon synchronous 5'ppp-dsRNA stimulation using standard ELISA kits.

A549 wt and HepG2 wt cells were synchronously stimulated with 220 ng 5'ppp-dsRNA and supernatants were harvested at different time points. **(A)** IFN-β and **(B)** IFN-λ1 protein concentrations were determined using distinct ELISA kits. Graphs depict individual values ± SD of 3 biologically independent experiments.

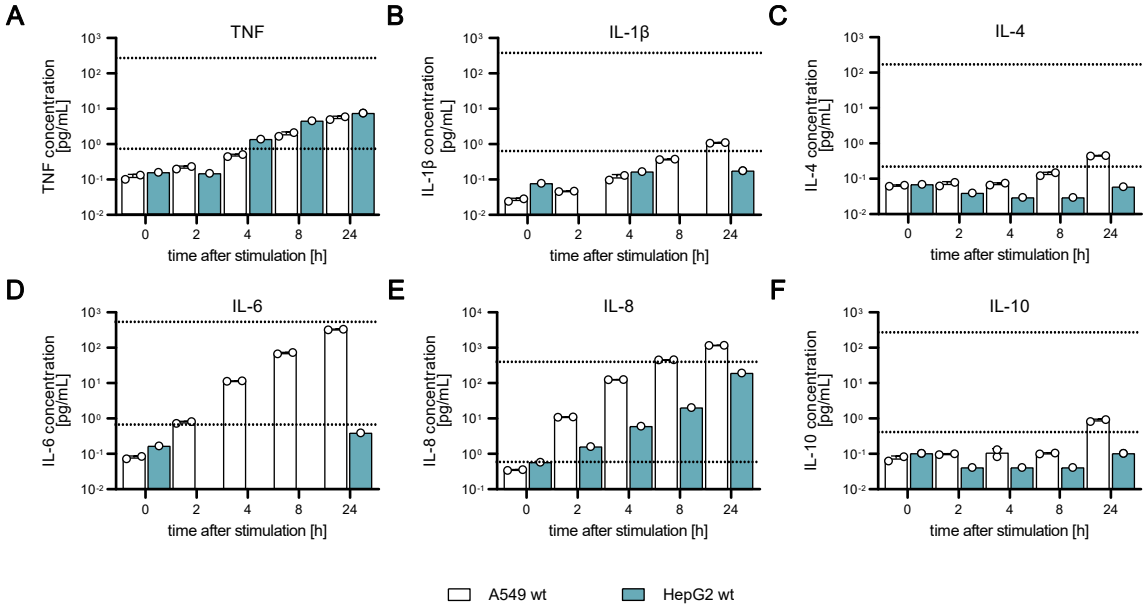

Figure S10: Cytokine secretion upon synchronous 5'ppp-dsRNA stimulation in A549 and HepG2 cells.

A549 wt and HepG2 wt cells were synchronously stimulated with 220 ng 5'ppp-dsRNA and supernatants were harvested at different time points. Cytokine production for **(A)** TNF, **(B)** IL-1β, **(C)** IL-4, **(D)** IL-6, **(E)** IL-8, and **(F)** IL-10 was determined using a multiplex immunoassay (V-PLEX Viral Panel, Meso Scale Diagnostics) in supernatants of A549 wt and HepG2 wt cells. Dashed lines indicate upper and lower limit of quantification, respectively. Graphs depict individual values ± SD of 2 biologically independent experiments.

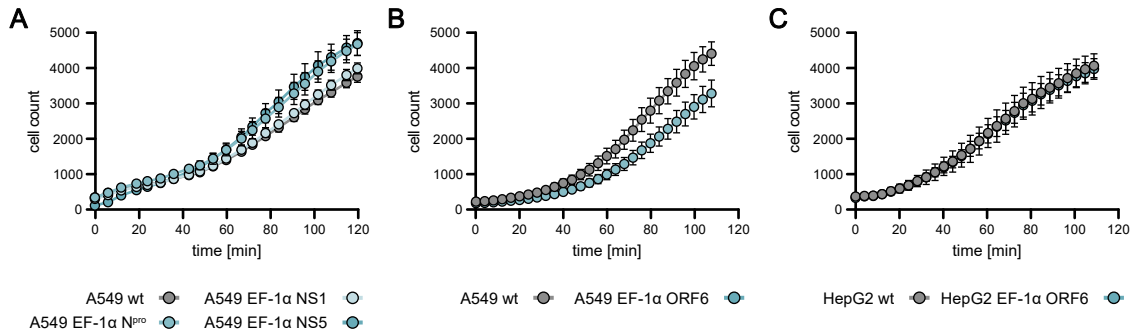

Figure S11: Effect of viral protein expression on cell proliferation in A549 and HepG2 cells.

A549 and HepG2 cells stably expressing viral proteins under the control of the EF-1α promoter were seeded on 96 well plates, treated with the Incucyte NucLight Rapid Red Reagent, and cell proliferation was monitored over time using the live-cell imaging system Incucyte. **(A)** Cell count of A549 wt cells compared to A549 cells stably expressing CSFV N^{pro}, IAV NS1, or DENV NS5. **(B)** Cell count of A549 wt cells compared to A549 cells stably expressing SARS-CoV-2 ORF6. **(C)** Cell count of HepG2 wt cells or cells stably expressing SARS-CoV-2 ORF6. Graphs depict mean ± SD of 3 technical replicates.

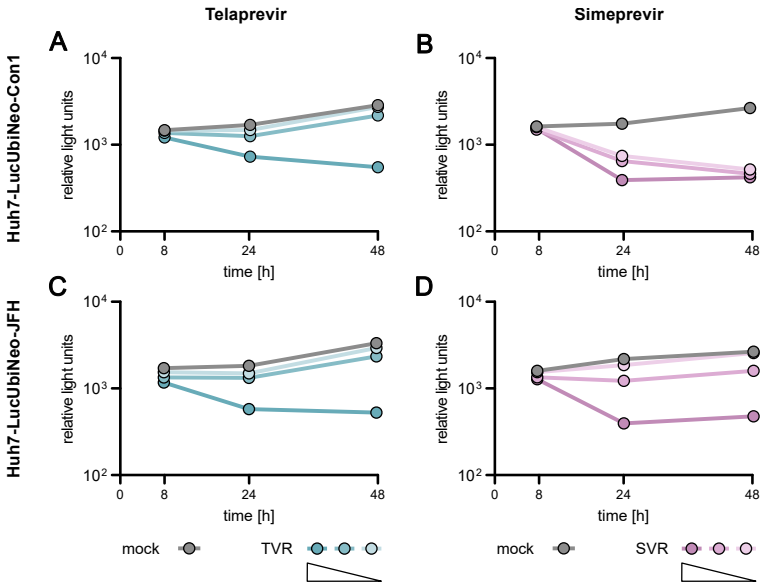

Figure S12: Comparison of inhibitory efficiency of different NS3/4A protease inhibitors in Huh7-LucUbiNeo cells.

The NS3/4A protease inhibitors Telaprevir (TVR) and Simeprevir (SVR) were titrated (1 µM, 100 nM, 10 nM) on Huh7-LucUbiNeo cells of different genotypes and Firefly luciferase was measured at different time points. **(A)** Telaprevir and **(B)** Simeprevir titration on Huh7-LucUbiNeo (Con1) cells, **(C)** Telaprevir and **(D)** Simeprevir titration on Huh7-LucUbiNeo (JFH) cells.

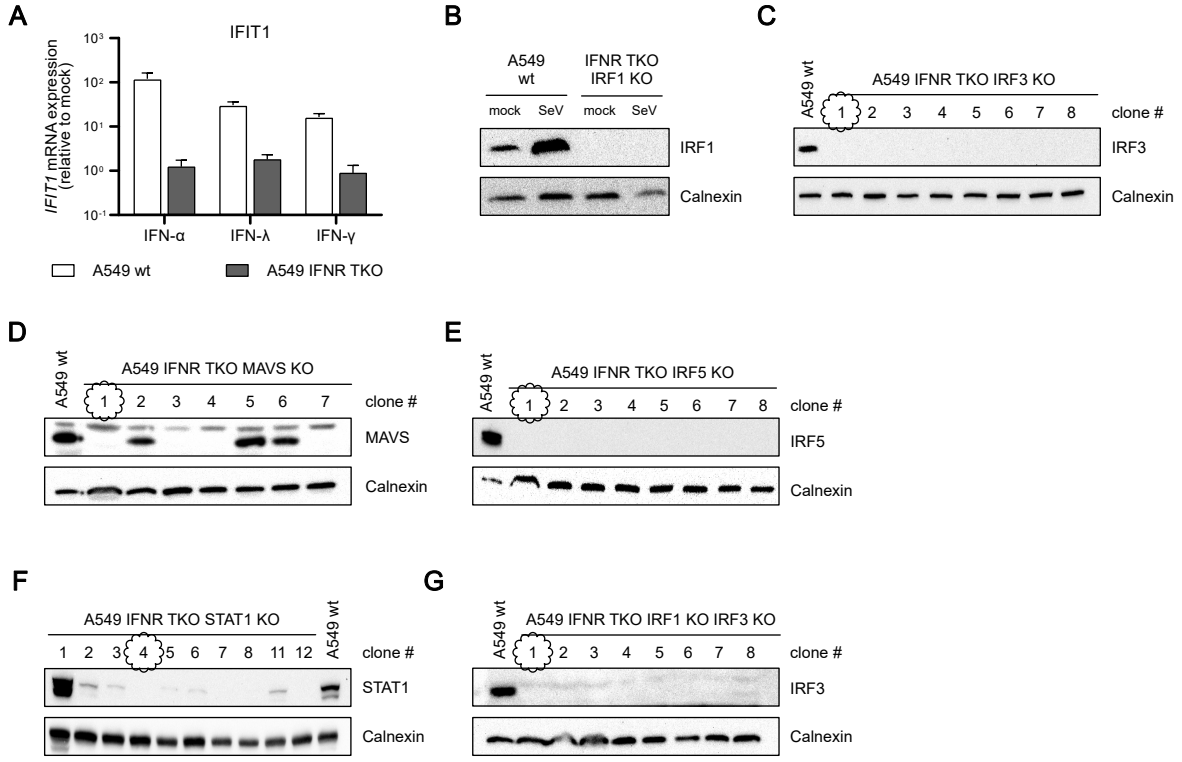

Figure S13: Validation of additional KOs in A549 IFNR TKO cells.

Validation of A549 CRISPR/Cas9 KO single cell clones. **(A)** Additional KO of IFN-gamma receptor was introduced in previously established IFNR DKO cell line, generating an A549 IFNR triple KO cell line (INFR TKO, IFNAR1 IFNLR IFNGR1 KO). A549 wt and IFNR TKO single cell clones were stimulated with 200 IU IFN-α, IFN-β, or IFN-γ and IFIT1 mRNA expression was measured using qRT-PCR. Additional KOs of **(B)** IRF1, **(C)** IRF3, **(D)** MAVS, **(E)** IRF5, **(F)** STAT1, and **(G)** a double IRF3 IRF1 KO were introduced in the A549 IFNR TKO cell line. Successful KO in single cell clones was examined using western blot analysis. Subfigure (A) was previously published [287].

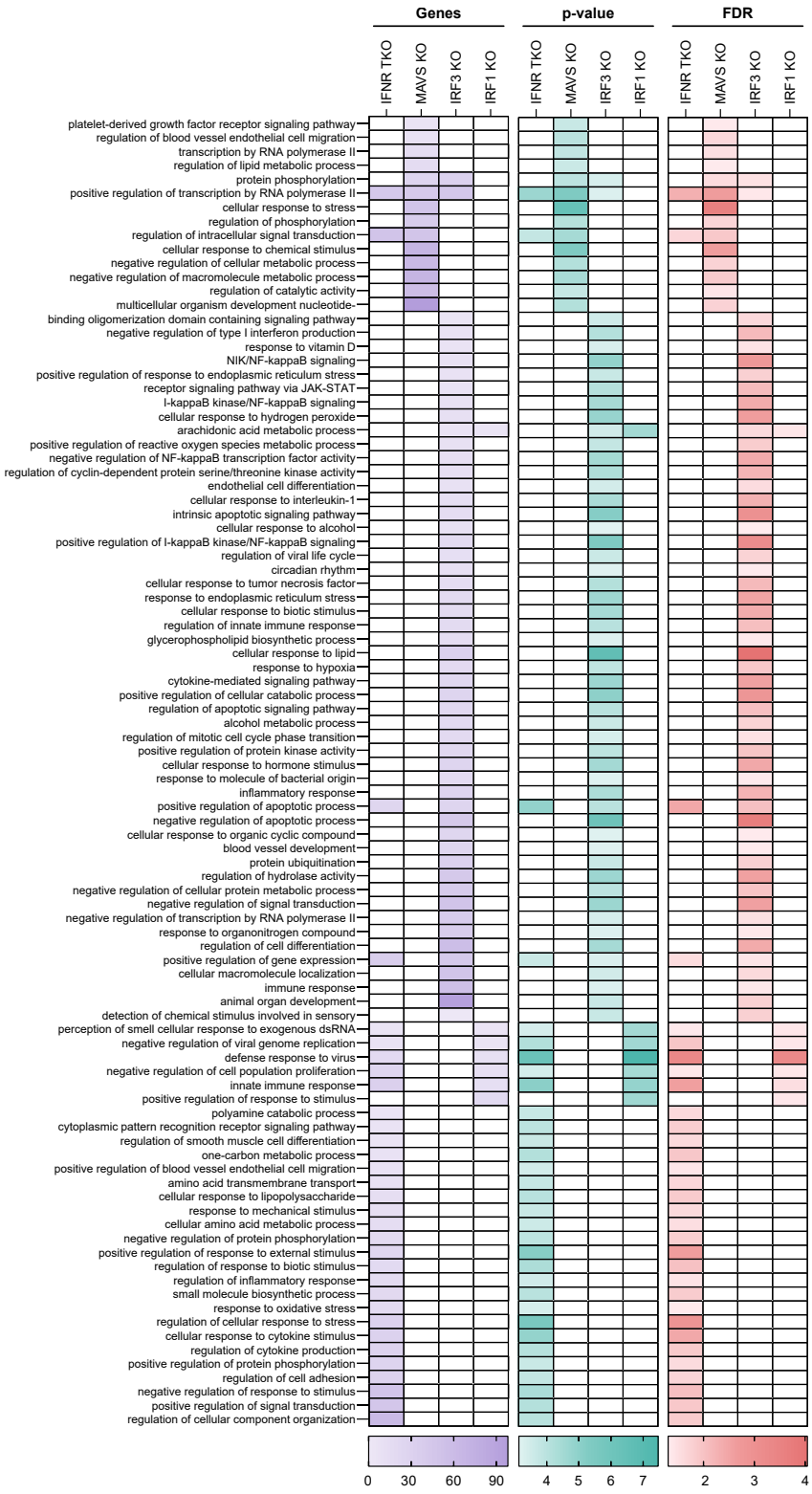

Figure S14: GOBP enrichment analysis of significantly regulated genes in A549 cells synchronously stimulated with 5'ppp-dsRNA.

Heat maps displaying number of genes, the p-value ($-\log_{10}$), as well as the false discovery rate (FDR, $-\log_{10}$) of Gene Ontology terms for biological processes (GOBP) enriched in A549 IFNR TKO, IFNR TKO MAVS KO, IFNR TKO IRF3 KO, and IFNR TKO IRF1 KO cells upon synchronous stimulation with 220 ng 5'ppp-dsRNA and whole-transcriptome expression profiling. Genes were classified as significantly regulated if they were at least 2-fold up or downregulated and p-value after correction for multiple testing was below 0.05. Values were normalized to the 0 hour time point of the corresponding cell line and the FDR was set to be below 0.05.

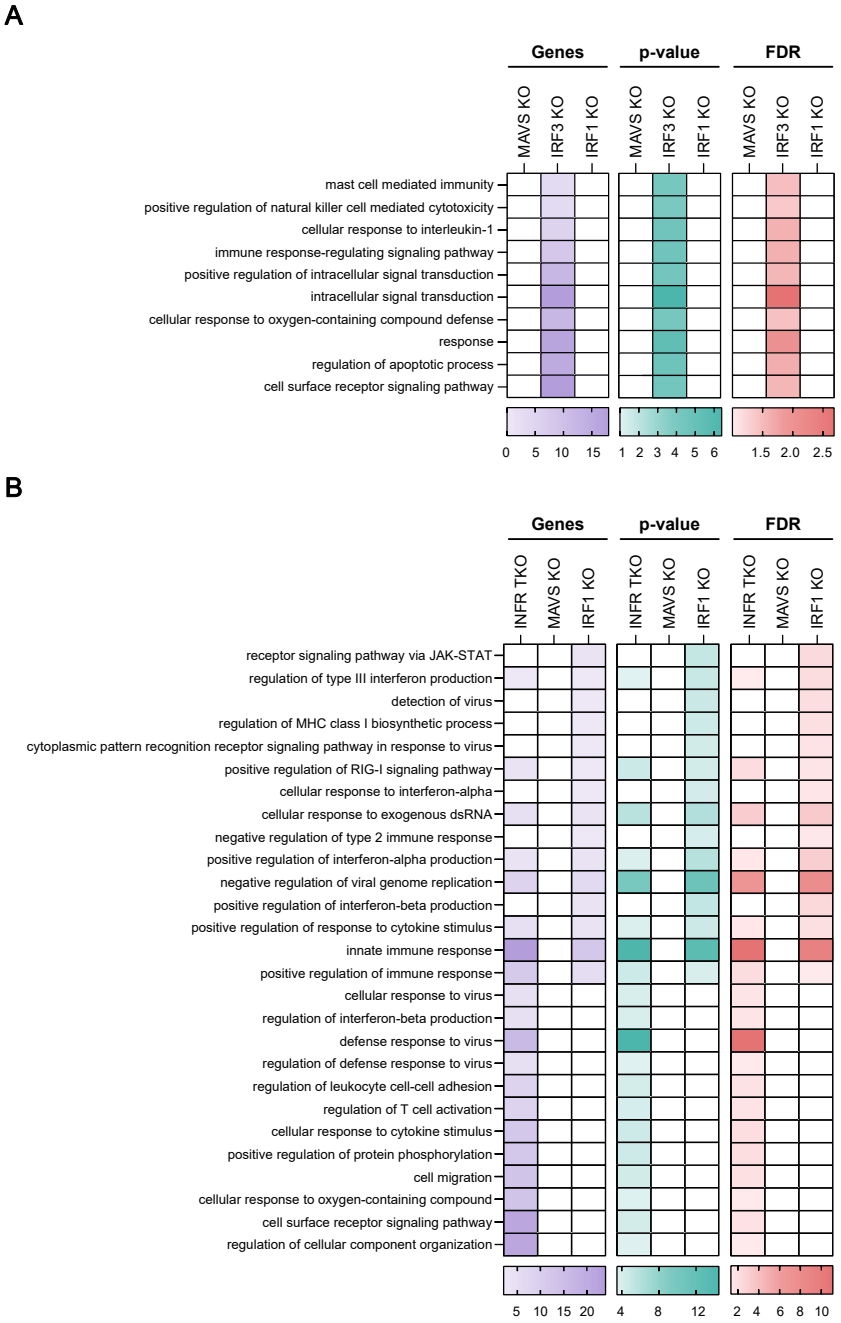

Figure S15: GOBP enrichment analysis of significantly regulated genes in A549 cells synchronously stimulated with 5'ppp-dsRNA.

Heat maps displaying number of genes, the p-value ($-\log_{10}$), as well as the false discovery rate (FDR, $-\log_{10}$) of Gene Ontology terms for biological processes (GOBP) enriched in **(A)** the corresponding KO cell lines normalized to the IFNR TKO cell line, **(B)** the corresponding KO cell line normalized to the IFNR TKO IRF3 KO cell line upon synchronous stimulation with 220 ng 5'ppp-dsRNA and whole-transcriptome expression profiling. Genes were classified as significantly regulated if they were at least 2-fold up or downregulated and p-value after correction for multiple testing was below 0.05. Values were normalized to the 0 hour time point of the corresponding cell line and the FDR was set to be below 0.05.

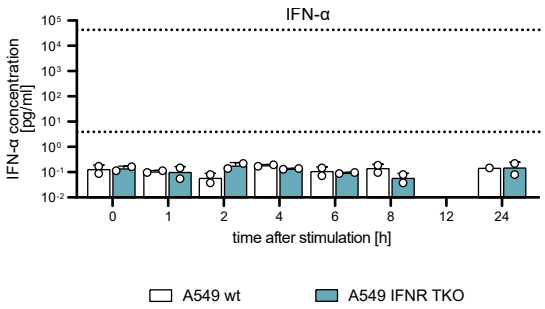

Figure S16: IFN-α production in A549 wt and IFNR TKO cells upon synchronous 5'ppp-dsRNA stimulation.

Secreted IFN-α protein concentrations in pg/ml were determined using a multiplex immunoassay (U-PLEX IFN Combo, Meso Scale Diagnostics) in the supernatants of 5'ppp-dsRNA-stimulated A549 wt and A549 IFNR TKO cells. Dashed lines indicate upper and lower limit of quantification, respectively. Graph depicts individual values ± SD of 2 biologically independent experiments.

Table S1: DEGs in A549 IFNR TKO cells upon 5'ppp-dsRNA stimulation.

DEGs in A549 IFNR TKO cells synchronously stimulated with 5'ppp-dsRNA (fold change 8 hour over 0 hour time point). Genes were classified as significantly regulated if they were at least 2-fold up or downregulated and the p-value was below 0.05 after Benjamini-Hochberg correction for multiple testing

Gene	Fold change	p-value
IFNL1	110.29065	0.04563
IFIT2	92.14517	0.00486
IFNL2	82.96687	0.01041
IFIT1	81.46322	0.01041
IFNB1	75.16873	0.01834
OASL	66.67435	0.01041
IFNL3	61.07929	0.01834
IFIH1	60.41277	0.01775
IFIT3	48.01600	0.01368
HERC5	47.92687	0.01664
CH25H	42.68318	0.01834
TNFAIP3	39.71163	0.01354
CYP1A1	35.50265	0.04223
CXCL11	32.54807	0.03192
GBP4	32.18492	0.04908
CFB	31.45838	0.01041
OTUD1	27.81824	0.03841
EGR2	27.45449	0.01738
ATF3	26.85169	0.01775
RIG-I	25.96941	0.00486
RND1	24.64381	0.01738
NR4A3	22.63122	0.04058
DDX60	20.13950	0.02480
SLC1A3	19.74182	0.02894
IFI44	19.13632	0.02573
CXCL8	18.43852	0.02773
PMAIP1	17.95325	0.01368
GBP5	17.86076	0.02409
FAM129A	17.62617	0.04299
RANBP3L	16.76676	0.01834
NOCT	15.98729	0.03997
CD274	12.48254	0.01834
ISG20	11.61158	0.01836
CSRNP1	11.51564	0.02773
PLAUR	11.09292	0.03016
MAP3K14	10.95105	0.01368
CHEK2	10.52995	0.02409
RHCG	10.45571	0.02293
SLC8A2	10.42806	0.01836
GLCCI1	10.25528	0.01368
PARP14	10.23451	0.01368
TSPYL2	10.09316	0.02539
ULBP2	9.94989	0.01664
FYN	9.83602	0.04812
STC2	9.51429	0.01116
BIRC3	9.46289	0.01738
IRAK2	9.41787	0.03841
ZC3HAV1	9.37224	0.01834
ALOXE3	9.15493	0.03746
IGF2	8.92307	0.04209
NFKB2	8.89669	0.01873
NFIL3	8.77674	0.04915
CYLD	8.61607	0.01116
NFKB1	8.50695	0.01775
ETS1	8.43068	0.04573
SLCO5A1	8.39412	0.01836
CXCR4	8.38365	0.03841
GADD45A	8.28750	0.02539
SPRY2	8.22179	0.02555
ABL2	8.15467	0.03700
GRB10	8.05651	0.03809
FOSL1	7.87124	0.03167
CMPK2	7.70489	0.01738

Gene	Fold change	p-value
CA8	7.56670	0.04889
RAPH1	7.42073	0.03746
PPM1K	7.21120	0.02094
CREBRF	7.12564	0.04908
RCAN1	7.10984	0.03254
SPRED2	6.90788	0.01368
EGR3	6.87258	0.01630
FAM46A	6.86552	0.02421
ETV3	6.71208	0.04209
PTGER4	6.68024	0.02409
PIK3R3	6.62596	0.01628
SOD2	6.57069	0.03841
JUN	6.49535	0.04111
CHD2	6.44840	0.04048
PTGS2	6.31942	0.02729
WHAMM	6.20920	0.01368
GCA	5.92502	0.02773
ARHGEF28	5.86810	0.01850
NFE2L3	5.80168	0.04974
FNDC3A	5.75257	0.02935
HDAC5	5.71688	0.04546
FZD4	5.62488	0.04552
ARL5B	5.29452	0.01775
SPAG9	5.22194	0.01664
CSF1	5.21095	0.01850
SCN3A	5.13129	0.03252
LSMEM1	5.05717	0.03718
GOT1	4.95692	0.02522
SAT1	4.89212	0.03841
NFKBIA	4.88527	0.01368
H1F0	4.87273	0.04563
ARG2	4.84592	0.02409
BCO1	4.80547	0.04180
CRLF2	4.69600	0.04908
KMT2C	4.68750	0.04914
GORAB	4.66738	0.04036
PLCG2	4.65703	0.04885
MAP2K3	4.65239	0.04885
CCNL1	4.58459	0.04908
TSC22D3	4.53904	0.04546
FAP	4.49952	0.04885
GABARAPL1	4.45836	0.04149
PPP1R15B	4.39832	0.03746
FAM83G	4.33958	0.02935
LATS2	4.30756	0.01834
NHSL1	4.27000	0.01836
RYBP	4.24824	0.04223
GEM	4.22816	0.01873
DNMBP	4.18427	0.02522
NFATC2	4.17338	0.04292
SEMA3A	4.15958	0.02006
HIPK3	4.02407	0.01041
ZC3H12C	4.01015	0.01931
DCHS1	3.99363	0.01368
PRDM6	3.97308	0.02161
TESK2	3.93535	0.04767
KCNN1	3.85530	0.04036
FAM193A	3.84968	0.04744
RAB9A	3.79811	0.04058
DNAJB4	3.79252	0.04945
MSANTD3	3.79061	0.04563
MAP4K4	3.76167	0.04058
KLF6	3.70552	0.03452
HEY2	3.66706	0.03746
WARS	3.65631	0.04180
RP11-875O11.1	3.63154	0.02522
ELL2	3.62080	0.03746
HMGCS1	3.59672	0.04058

Gene	Fold change	p-value
NCOA7	3.56540	0.04995
TRIM38	3.55672	0.02006
MB21D2	3.53716	0.02409
C3	3.52897	0.01116
FAM210A	3.52580	0.01041
PIK3AP1	3.48858	0.02161
MREG	3.46970	0.03841
BRD2	3.28307	0.01775
B2M	3.25102	0.02006
STK10	3.24812	0.03736
ANKS1A	3.22525	0.04563
RFX3	3.17389	0.04036
AARS	3.17095	0.04132
TAF4B	3.14104	0.04563
LIF	3.07277	0.01605
TP53BP2	3.03895	0.03727
ETV5	3.01964	0.04058
HOXD11	3.01593	0.04986
ING1	3.01197	0.02509
MYCBP2	2.96307	0.04563
ZNF317	2.92399	0.02773
ATF4	2.90130	0.03746
KLHL15	2.89254	0.04433
RBM24	2.86758	0.01738
LY6K	2.85522	0.03252
MKX	2.85372	0.03543
HOXD10	2.84990	0.01449
CCNB1IP1	2.80345	0.03781
AGO2	2.79246	0.02409
CBS	2.79053	0.04843
TAAR3	2.77410	0.04231
DENND5A	2.74988	0.03841
MTMR3	2.72514	0.04885
HPS5	2.72293	0.04132
FMR1	2.71383	0.04974
SMAP2	2.67680	0.01850
CA13	2.65816	0.04974
SLC7A1	2.65174	0.02539
ADAMTS16	2.65002	0.02421
SAR1A	2.64862	0.04914
PELI2	2.64388	0.04132
RIC8B	2.63816	0.04209
TBC1D3B	2.63576	0.04889
TIMM23B	2.61287	0.01834
SAP30BP	2.57264	0.03841
ZNF597	2.53478	0.04132
GARS	2.51496	0.03841
GON4L	2.50723	0.04655
RSRC2	2.50257	0.04058
GPATCH2L	2.49875	0.02293
STK24	2.49610	0.04132
RAB5A	2.49603	0.04915
ANKRD28	2.48081	0.05000
NBPF10	2.43685	0.01850
TRMT10B	2.42295	0.03997
HRASLS2	2.37634	0.04180
SLC2A13	2.37314	0.01977
ZFY	2.33985	0.03791
LRCH1	2.33844	0.04292
DUSP6	2.33765	0.03167
ZNF394	2.32909	0.04292
IARS	2.30759	0.02001
NPIPB15	2.29732	0.04223
HIST2H3D	2.28420	0.04383
TRIO	2.25628	0.04853
ZNF217	2.25604	0.04563
SERF1B	2.24372	0.02909
SERF1A	2.24372	0.02909

Gene	Fold change	p-value
FILIP1L	2.23598	0.04180
BTN2A3P	2.23294	0.04983
CRTC2	2.23228	0.04983
SUPT6H	2.23053	0.02313
RAB11FIP1	2.21989	0.04986
MAK	2.21159	0.04563
STX1A	2.20580	0.04908
FGGY	2.20530	0.01628
PLEKHM1	2.19407	0.04766
NPIPB9	2.17946	0.01956
INPP1	2.15957	0.04861
MTHFD2	2.15684	0.04812
SMOX	2.14789	0.03601
SUPT5H	2.14533	0.01368
DCUN1D3	2.12686	0.04766
CD2AP	2.10999	0.02006
OSBP	2.10583	0.04111
CNOT2	2.10079	0.04766
PISD	2.08288	0.04058
NPIPB6	2.07873	0.04563
TRMT44	2.06250	0.04563
MDGA1	2.06048	0.05000
PDLIM2	2.05399	0.04909
MYOM2	2.02746	0.01473
CRIM1	2.00907	0.02409
PLK2	2.00197	0.01041

Table S2: DEGs in A549 IFNR TKO MAVS KO cells upon 5'ppp-dsRNA stimulation.

DEGs in A549 IFNR TKO MAVS KO cells synchronously stimulated with 5'ppp-dsRNA (fold change 8 hour over 0 hour time point). Genes were classified as significantly regulated if they were at least 2-fold up or downregulated and the p-value was below 0.05 after Benjamini-Hochberg correction for multiple testing

Gene	Fold change	p-value
CYP1A1	87.70310	0.01200
NR4A3	39.08745	0.03883
ARID5B	23.06461	0.01756
EGR2	21.28687	0.03301
ALOXE3	20.17470	0.03591
CSRNP1	19.64691	0.03123
ZNF331	18.62518	0.03222
CREB5	17.70421	0.03222
KDM6B	16.55898	0.04120
TMEM156	16.46771	0.04671
NR1D1	15.34145	0.03584
TSPYL2	14.82667	0.02813
ETS1	13.89422	0.03317
IL24	13.50632	0.02657
MUC13	12.43204	0.03883
CHAC1	12.29669	0.04090
MAP3K14	11.52525	0.02021
VDR	11.51266	0.01632
NOCT	11.44633	0.03879
RHCG	11.07872	0.03222
PRDM1	11.07736	0.02170
SESN2	9.81447	0.01200
FOSL1	9.43763	0.03584
NFIL3	9.14512	0.03317
C17orf53	9.12762	0.03222
HDAC5	9.02425	0.02657
ABL2	9.00537	0.03222
TUFT1	8.73546	0.03715
GADD45A	8.17273	0.04885
NFKB2	7.99848	0.03426
MAP2K3	7.56187	0.03247
MAMLD1	7.54513	0.03842
DUSP14	7.50020	0.03247
CHD2	7.36303	0.04889
TIPARP	7.19846	0.04325
LY6K	7.15142	0.01756
TRIB3	7.09434	0.04261
LIMA1	6.98436	0.02687
STARD13	6.87950	0.03842
FA2H	6.86200	0.03322
TANC2	6.64671	0.00291
SERTAD1	6.62485	0.03913
TSC22D3	6.48397	0.04580
YTHDC1	6.34304	0.03883
CCNL1	6.33563	0.03222
BHLHE41	6.33412	0.02677
TCP11L2	6.19522	0.04671
ATXN7	6.04514	0.03842
ELL2	6.01209	0.03594
JMJD1C	5.94977	0.02779
PCID2	5.74447	0.03883
ARL5B	5.52167	0.03013
NEK1	5.49772	0.04289
LIF	5.46591	0.04889
UGCG	5.46485	0.04337
RIOK3	5.46277	0.03913
EREG	5.44164	0.03913
MEF2D	5.40565	0.03591
TRAF4	5.40561	0.03780
KIAA1217	5.37455	0.02677
KLF10	5.36332	0.03013
RUSC2	5.35486	0.02657
SIPA1L2	5.30165	0.04370

Gene	Fold change	p-value
SIM2	5.28403	0.02657
FAM83G	5.27796	0.04792
CYLD	5.27157	0.03301
CLCN4	5.20131	0.01756
H1F0	5.19579	0.03584
FAM129A	5.11670	0.04219
PPP1R15B	5.08135	0.03883
ELMSAN1	5.03410	0.03301
NFKB1	4.93617	0.02784
NUAK2	4.90987	0.03222
SBNO2	4.89520	0.04807
LINC00473	4.87791	0.04797
DDIT4	4.83787	0.04671
SMAP2	4.50766	0.03883
MCCC1	4.42800	0.03566
DUSP8	4.39494	0.03883
AKAP17A	4.39198	0.03883
AGO2	4.30549	0.03222
EPHA2	4.29116	0.03301
TMEM236	4.28302	0.04062
INHBA	4.25801	0.04204
ZBTB21	4.22126	0.03013
FOSL2	4.21971	0.04370
BRAF	4.13148	0.03301
PTHLH	4.11376	0.03753
LHX4-AS1	4.10803	0.04090
PPP1R3C	4.09346	0.03301
OSER1	4.07082	0.03012
RYBP	4.06552	0.03301
TRIM39	4.02143	0.03780
IFRD1	4.01608	0.03627
SNX9	4.01037	0.03301
MAPK8IP3	3.98786	0.04289
WHAMM	3.97903	0.03584
RND1	3.89412	0.01200
REL	3.87022	0.03301
SYCP2L	3.87011	0.04671
SPIRE1	3.86292	0.03222
SPAG9	3.85896	0.03301
HIVEP2	3.85620	0.04131
GPRC5C	3.80662	0.03913
EPC1	3.75893	0.03222
CPEB4	3.72845	0.02178
TSC22D2	3.68332	0.03222
ODC1	3.62783	0.03416
XPO6	3.60475	0.03222
RUBCN	3.60336	0.03594
BRD2	3.57458	0.04807
VPS37B	3.57156	0.03735
VASN	3.56974	0.04921
YY1AP1	3.53579	0.03322
TBC1D3B	3.53551	0.03687
ARHGAP26	3.51764	0.03013
ADAMTS16	3.48032	0.03879
LMCD1	3.47897	0.04131
TRIO	3.44692	0.03222
RIMKLB	3.44620	0.04306
ATP6V0A1	3.44355	0.04580
LSMEM1	3.42791	0.03883
AGAP4	3.40264	0.01756
UIMC1	3.39245	0.03951
ZBTB43	3.38253	0.03584
MTMR3	3.33185	0.03828
DENND3	3.32972	0.02657
SIK3	3.23113	0.03584
PMAIP1	3.22960	0.04797
TIMM23B	3.22701	0.02657
GPATCH2L	3.21694	0.04246

Gene	Fold change	p-value
KHNYN	3.19450	0.04803
STX1A	3.19065	0.04671
CEBPG	3.14849	0.03584
AGAP6	3.11266	0.03322
FAM193A	3.07032	0.02784
CYTH3	3.06383	0.04897
ZSWIM4	3.00661	0.03883
CWC25	3.00534	0.03222
ARNTL	2.99514	0.03222
GTF2IRD1	2.98315	0.03317
SMURF1	2.97753	0.03301
INPP1	2.95929	0.03883
ANKRD28	2.95041	0.04131
AADAC	2.94470	0.01200
KPNA7	2.93677	0.04807
MCL1	2.89611	0.03222
SMG9	2.89247	0.03222
AGAP9	2.87299	0.03584
NFKBIA	2.82811	0.04671
SOCS2	2.82412	0.04146
KIAA0513	2.82352	0.04446
ZNF317	2.80897	0.04682
VEGFA	2.80735	0.03913
FAM231D	2.79534	0.03715
CCL2	2.78572	0.04090
IRX5	2.78314	0.04797
ZNF212	2.77897	0.03339
GON4L	2.76791	0.03317
RNF19B	2.76607	0.03222
CSNK1D	2.75924	0.04337
WDR26	2.75794	0.04131
BRD9	2.75580	0.03715
PHACTR4	2.75158	0.02872
PRICKLE2	2.70546	0.04370
SLC7A1	2.70416	0.03842
ZNF419	2.69968	0.04090
ZNF394	2.69908	0.04337
SNAI2	2.69378	0.03316
EAF1	2.66611	0.03222
RELA	2.66500	0.02657
SPRED1	2.66052	0.04671
LHX4	2.64792	0.02784
MED15	2.63735	0.03883
SRGAP1	2.62149	0.03591
NPIPB3	2.61171	0.01200
AGAP5	2.56664	0.04337
KRTAP5-AS1	2.55201	0.01756
OTUD7B	2.54884	0.03497
PARP6	2.53258	0.03913
SYT5	2.52557	0.04545
WDR45B	2.52133	0.03423
CRIM1	2.52128	0.03883
NPIPB15	2.51967	0.03222
JMJD6	2.50621	0.04468
NPIPB6	2.49209	0.02237
NPIPB9	2.47590	0.03883
USP43	2.44955	0.03378
SMCR8	2.44054	0.02657
TRMO	2.43563	0.02021
IARS	2.42216	0.02657
TRIM38	2.42010	0.03913
ARHGEF28	2.41682	0.04580
C16orf46	2.40442	0.03322
ZFAND3	2.39378	0.04563
TBC1D3	2.38555	0.03942
ACOT9	2.37817	0.04803
PLEKHM1	2.37616	0.02657
ZNF687	2.34801	0.04090

Gene	Fold change	p-value
SUPT5H	2.32444	0.03842
SUPT6H	2.31992	0.03423
NPIPB8	2.30855	0.03883
TNKS	2.30852	0.01200
MAPK1IP1L	2.29530	0.03301
ZC3H7A	2.28225	0.03222
ABTB2	2.27262	0.04204
THAP9	2.25369	0.03301
SYNGAP1	2.25049	0.04671
PANK2	2.22654	0.04370
PTPN14	2.20711	0.03301
TRMT10B	2.19896	0.03222
GLIS3	2.18148	0.02657
TP53BP2	2.16690	0.04370
OSBP	2.16594	0.03222
SDE2	2.16542	0.02657
STX5	2.16085	0.03883
GAD1	2.14339	0.04246
AASS	2.13326	0.03584
MPP5	2.11757	0.03591
CDK7	2.11552	0.04131
ATP8B3	2.09543	0.02784
RBM22	2.09098	0.02021
ARID3B	2.07195	0.04416
NBPF14	2.06224	0.04090
ZNF543	2.04018	0.03591
GOLGA6L9	2.01464	0.04041
ZBTB49	2.01102	0.02170

Table S3: DEGs in A549 IFNR TKO IRF3 KO cells upon 5'ppp-dsRNA stimulation.

DEGs in A549 IFNR TKO IRF3 KO cells synchronously stimulated with 5'ppp-dsRNA (fold change 8 hour over 0 hour time point). Genes were classified as significantly regulated if they were at least 2-fold up or downregulated and the p-value was below 0.05 after Benjamini-Hochberg correction for multiple testing

Gene	Fold change	p-value
CYP1A1	65.91872	0.02916
TNFAIP3	43.21929	0.04706
ATF3	38.03149	0.03212
INHBA	36.58878	0.03458
ICAM1	34.71787	0.03240
TRAF1	27.25679	0.02085
FAM129A	26.98226	0.04051
NR4A3	26.26633	0.02085
EGR2	25.23600	0.02085
CXCL8	24.96245	0.02136
RHCG	24.30209	0.02085
IRAK2	21.71472	0.01838
VDR	21.06598	0.03458
EFNA1	20.12515	0.04051
DDIT3	18.64283	0.02136
STC2	18.03540	0.04040
IL32	17.49661	0.04222
SLCO5A1	17.04055	0.01838
KDM6B	16.96300	0.02136
ALOXE3	15.12598	0.01838
TRIML2	14.58565	0.04798
KLRC2	14.52415	0.04128
SERPINA3	14.50075	0.03638
ZNF331	14.25823	0.02175
RND1	13.19042	0.04865
SLC7A2	13.04393	0.02660
RELB	12.82070	0.03412
NOCT	12.76407	0.02175
BIRC3	12.50462	0.02091
CYLD	12.23685	0.04172
GADD45A	12.17528	0.01838
MUC13	11.84378	0.04254
NFKB1	11.82630	0.01017
BCL2A1	11.74554	0.01838
NFKB2	11.45599	0.03494
CREB5	11.35848	0.04028
USP43	11.07603	0.04254
SOD2	10.85733	0.01017
BHLHE41	10.33591	0.02672
KLRC3	10.31610	0.04040
NFATC2	10.22545	0.03804
FOSL1	10.21005	0.03184
ABTB2	9.98419	0.04256
ERN1	9.83026	0.02085
GBP2	9.81465	0.03011
IFNL2	9.31139	0.01838
CLIP2	8.56765	0.02570
DENND4A	8.51337	0.04330
KDM7A	8.50091	0.02136
GATA6	8.45510	0.03010
ABL2	8.16360	0.02085
IFNL3	8.07884	0.04065
NR4A2	7.91789	0.03725
CCL2	7.86459	0.03788
PLA2G4C	7.77203	0.03494
CYP1B1	7.72684	0.01017
GEM	7.55240	0.04421
PLAU	7.47124	0.02902
RAPH1	7.43754	0.03803
PINLYP	7.29552	0.03011
RAB30	7.23090	0.02175
C1QTNF1	7.15907	0.04706
IKBKE	7.07166	0.03458

Gene	Fold change	p-value
SERPINB9	6.98763	0.02631
AGO2	6.92984	0.02672
ANKLE2	6.86868	0.02085
CD83	6.81698	0.04065
ARL5B	6.73795	0.02323
SERPINB8	6.60320	0.03992
REL	6.59833	0.03899
PPP1R15B	6.50554	0.02175
NCR3LG1	6.44071	0.04021
CLEC4E	6.40760	0.02555
RASSF5	6.38005	0.02969
ELL2	6.29584	0.03184
EREG	6.28627	0.03501
GORAB	5.98176	0.03834
TUFT1	5.92368	0.03843
STC1	5.89128	0.04710
KLF10	5.82148	0.02136
AJUBA	5.80765	0.02631
TNIP2	5.71601	0.03270
NFKBIA	5.70137	0.01838
KLF6	5.60644	0.02175
PCID2	5.56740	0.02631
DUSP14	5.54455	0.03816
MSANTD3	5.52354	0.03273
SPRY2	5.52212	0.04065
STK40	5.47605	0.04040
SPECC1L-ADORA2A	5.46768	0.03184
CACTIN	5.43613	0.04254
STAT5A	5.21968	0.02085
RASGRP1	5.18081	0.04254
SLC37A1	5.17575	0.04222
PHKG2	5.10785	0.02730
ING1	4.89445	0.04111
LATS2	4.76484	0.03184
BIRC2	4.60758	0.04471
PROX1	4.60622	0.03637
DENND3	4.60247	0.03784
CEP95	4.56454	0.03791
CA13	4.56289	0.02323
SIM2	4.54343	0.04225
SYCP2L	4.52047	0.04706
SIPA1L2	4.51081	0.03011
ELMSAN1	4.50204	0.04706
SLC25A25	4.49014	0.03501
NFATC1	4.48920	0.02333
LPXN	4.47909	0.04955
GOT1	4.46774	0.02175
SEC24A	4.43839	0.02323
SPRED2	4.43284	0.02175
USP36	4.42757	0.01838
IGF2BP2	4.41743	0.02323
MTMR4	4.40382	0.03768
SNX9	4.35938	0.02813
TNFRSF10B	4.29197	0.03184
PDLIM2	4.18174	0.03494
ITPKC	4.16918	0.03059
BHLHE40	4.13820	0.03059
CRY1	4.12610	0.01017
DNAH17	4.09533	0.04878
DAGLB	4.08626	0.04040
UVRAG	4.08348	0.03184
HMGCS1	4.07876	0.03011
RYBP	4.07354	0.03835
NFE2L2	4.05482	0.03494
GPATCH2L	4.05101	0.03788
FAM222A	3.97847	0.03260
DNMBP	3.97075	0.03834
TAF4B	3.96721	0.03739

Gene	Fold change	p-value
GPR3	3.96616	0.04171
PIK3CD	3.94780	0.04111
STX3	3.84173	0.01838
RNF24	3.82234	0.04286
VEGFC	3.80389	0.03011
PHLDA1	3.79449	0.04710
UGCG	3.78807	0.04111
TRIO	3.77701	0.03669
NEURL3	3.75968	0.04706
DOT1L	3.70155	0.04577
OPTN	3.67831	0.04537
DLX2	3.65685	0.04111
TJAP1	3.63248	0.03719
NBR1	3.62830	0.04046
IPPK	3.60477	0.03494
TUBE1	3.58094	0.03992
SOCS2	3.56285	0.03458
TRIM25	3.55088	0.02902
ISL2	3.53500	0.04482
MAP3K8	3.53200	0.04111
ODC1	3.51467	0.02175
CXCL3	3.49943	0.02085
INO80	3.46955	0.03638
RBM24	3.46847	0.01838
SSBP2	3.46799	0.03270
GFRA2	3.46115	0.04111
TBC1D22B	3.41911	0.02085
YY1AP1	3.41612	0.03843
FAM167A	3.41229	0.04706
NKX3-1	3.40879	0.01838
LDLR	3.39915	0.04145
IFNL1	3.38221	0.03458
SSH1	3.38088	0.02085
MAPK8IP3	3.37551	0.04402
GPR75	3.35654	0.04636
CXCR4	3.32927	0.03494
NBPF14	3.32586	0.04704
TMEM63B	3.32468	0.04711
PRKCD	3.30586	0.03458
NFX1	3.28924	0.03719
ARG2	3.24035	0.03458
TMEM236	3.23440	0.02546
ABR	3.20762	0.02085
CXCL2	3.16913	0.02175
CLIC4	3.08408	0.03494
AEN	3.07931	0.01838
ZNF436	3.07797	0.04051
ITGAM	3.07648	0.03184
OSER1	3.05766	0.02552
B3GNT5	3.05034	0.04838
ZBTB1	3.03287	0.03010
AARS	3.02862	0.03842
TP53BP2	3.01996	0.02891
SIN3A	3.01699	0.03458
ALKBH1	2.99913	0.04044
FRMD6	2.99431	0.04393
NOTCH2	2.94652	0.01838
HIST2H2AC	2.93924	0.03458
ATP6V0A1	2.93756	0.03788
AHRR	2.91671	0.04172
DCAF8	2.91494	0.02085
ADAMTS16	2.89780	0.04921
LGALSL	2.88056	0.03458
RFFL	2.87052	0.04552
WTAP	2.86923	0.03827
ATP13A3	2.83498	0.04254
KRTAP5-AS1	2.83333	0.04423
BBC3	2.82732	0.03270

Gene	Fold change	p-value
CD163L1	2.82337	0.04044
ARHGAP24	2.82126	0.04706
TRIP10	2.81649	0.04111
ETS2	2.81153	0.03346
UNC13A	2.79396	0.04360
PRR7	2.78215	0.04878
IER3	2.78141	0.04634
MAK	2.77334	0.04253
PDE9A	2.77320	0.04708
IRX5	2.75102	0.02902
WDR45B	2.73375	0.02634
HERPUD1	2.73145	0.04602
MOB3C	2.71297	0.03475
LONRF1	2.70899	0.04065
SAMD4A	2.70264	0.04145
CWC25	2.69297	0.04473
GPR176	2.68757	0.03725
ZFAND3	2.68401	0.03928
TFE3	2.66056	0.04537
NR0B1	2.64002	0.04700
TBC1D3E	2.62472	0.03527
ARL14EP	2.58788	0.04838
UIMC1	2.58706	0.03254
CLK1	2.57720	0.03899
NKD2	2.57331	0.02136
RGL2	2.57089	0.02546
GFPT2	2.56688	0.04710
RNF169	2.56506	0.04065
ADPRM	2.53250	0.01838
CRIM1	2.53217	0.01838
ITCH	2.51036	0.03638
CYTH1	2.50796	0.04878
RNF19B	2.49856	0.04848
DNAJC25	2.49670	0.04021
TYK2	2.48826	0.04734
ROR1	2.47814	0.04526
BRAP	2.47465	0.02891
TRIM39-RPP21	2.46631	0.03736
LRCH3	2.46608	0.02891
ZNF655	2.46075	0.02175
SDR16C5	2.43357	0.03458
ACOT9	2.41585	0.02085
TRMO	2.41533	0.04903
JAK1	2.41305	0.04046
NSUN4	2.41016	0.01017
INTS3	2.40497	0.04473
CDK7	2.39016	0.04065
GARS	2.38650	0.04537
ANKRD28	2.37569	0.04254
NR3C1	2.36565	0.02175
ATXN2	2.34881	0.04040
ZNF394	2.33133	0.04706
SVIL	2.32697	0.03736
GMEB1	2.30805	0.04708
PTPRK	2.28621	0.02085
NEK6	2.28110	0.04040
MPP5	2.24842	0.04140
KLF9	2.23051	0.04706
ZNFX1	2.22689	0.03579
SUPT6H	2.22303	0.02136
INPP1	2.22107	0.04798
CTNNAL1	2.20197	0.03059
EGFR	2.19862	0.04432
VEZT	2.19698	0.03638
CRTC2	2.18615	0.02546
MTHFD2	2.17385	0.03519
ZSCAN9	2.13603	0.02085
NFKBIZ	2.10951	0.01838

Gene	Fold change	p-value
RASAL2	2.09943	0.03868
KCTD9	2.09687	0.04954
NUFIP1	2.08000	0.04833
TBC1D3K	2.07440	0.02313
ZNF79	2.06240	0.02924
LAMP3	2.04105	0.03011
TRMT10B	2.03902	0.04878
NPHS1	2.02446	0.04706
KCTD5	2.02020	0.04133

Table S4: DEGs in A549 IFNR TKO IRF1 KO cells upon 5'ppp-dsRNA stimulation.

DEGs in A549 IFNR TKO IRF1 KO cells synchronously stimulated with 5'ppp-dsRNA (fold change 8 hour over 0 hour time point). Genes were classified as significantly regulated if they were at least 2-fold up or downregulated and the p-value was below 0.05 after Benjamini-Hochberg correction for multiple testing

Gene	Fold change	p-value
IFIH1	97.42409	0.01460
IFIT2	85.23108	0.01670
IFNL1	78.11992	0.01670
IFIT3	65.23643	0.01323
IFNB1	55.10669	0.01323
IFNL2	48.80415	0.02563
OASL	47.90786	0.03340
TNFAIP3	32.90324	0.03205
RIG-I	31.05069	0.02977
CH25H	20.14521	0.04002
EGR2	19.09207	0.03319
ALOXE3	14.35334	0.04076
CITED2	13.69775	0.01323
ETS1	12.96201	0.02393
MUC13	10.80807	0.03066
USP41	10.37754	0.02287
PARP14	9.81651	0.03205
RAET1L	9.27928	0.04228
PLA2G4C	8.68772	0.02659
ABL2	7.59181	0.04076
SPRY2	6.82572	0.01670
ZC3HAV1	6.49210	0.01548
CYP1B1	6.21301	0.02977
ARL5B	6.10111	0.04718
USP36	4.86570	0.02504
VPS37B	4.83842	0.04342
SLC8A2	4.44542	0.01460
ELL2	4.37529	0.04136
MSANTD3	3.77930	0.01548
GRB10	3.70116	0.04076
HSD17B7	3.60444	0.01323
TES	3.56723	0.03415
TRIM39-RPP21	3.10681	0.03205
ATP6V0A1	3.06755	0.02504
VASN	2.96565	0.02504
TBC1D22B	2.94037	0.02479
GPATCH2L	2.89228	0.02977
HBEGF	2.78405	0.02039
NR3C1	2.34696	0.02584
RIC1	2.10630	0.02393
VANGL2	2.02440	0.01323

Table S5: GOBP terms enriched in A549 IFNR TKO cells upon 5'ppp-dsRNA stimulation.

Gene ontology (GO) terms for biological processes enriched in A549 IFNR TKO cells synchronously stimulated with 5'ppp-dsRNA (8 hour over 0 hour time point). False discovery rate (FDR) < 0.05. GOBP term enrichment analysis was performed with PANTHER.

Term	GO ID	FDR	Genes
polyamine catabolic process	GO:0006598	2.54E-02	SMOX, SAT1
cellular response to exogenous dsRNA	GO:0071360	4.62E-02	IFIH1, IFNB1, RIG-I, IFIT1
cytoplasmic pattern recognition receptor signaling pathway	GO:0002753	1.68E-02	NFKBIA, IFIH1, CYLD, RIG-I, TNFAIP3
regulation of smooth muscle cell differentiation	GO:0051150	2.60E-02	BMP4, PRDM6, HEY2, NFATC2, SOD2
one-carbon metabolic process	GO:0006730	1.25E-02	DHFRL1, MAT2A, MTHFD2, SFXN1, CA8, CA13
negative regulation of viral genome replication	GO:0045071	1.19E-02	ISG20, IFIH1, IFNB1, ZC3HAV1, IFIT1, IFNL3, OASL
positive regulation of blood vessel endothelial cell migration	GO:0043536	4.07E-02	MAP2K3, TMSB4X, PLK2, HMGB1, PTGS2, ETS1
amino acid transmembrane transport	GO:0003333	2.29E-02	SLC25A15, ARL6IP5, LRRC8D, SLC1A3, SFXN1, SLC16A2, SAT1, SLC7A1
defense response to virus	GO:0051607	5.19E-04	IFNB1, RIG-I, ZC3HAV1, IFIT1, DDX60, IFIT3, IFIT2, OASL, HERC5, ISG20, IFIH1, IFNL2, IFNL1, IFNE, PMAIP1, MAP3K14, IFNL3
cellular response to lipopolysaccharide	GO:0071222	1.48E-02	MAP2K3, NFKBIA, CD274, CXCL11, CXCL8, IRAK2, PLCG2, TNFAIP3, CMPK2, HMGB1, B2M, NFKB1
response to mechanical stimulus	GO:0009612	2.63E-02	PTGER4, NFKBIA, FOSL1, JUN, GADD45A, CXCR4, SLC1A3, FYN, PTGS2, MAP3K14, NFKB1, TNFRSF1A
cellular amino acid metabolic process	GO:0006520	3.07E-02	ARG2, WARS, CARNMT1, GOT1, SLC1A3, SRR, DHFRL1, CBS, GARS, IARS, ALDH18A1, SLC16A2, ATF4
negative regulation of protein phosphorylation	GO:0001933	1.72E-02	SPAG9, PPP1R15B, JUN, WARS, GADD45A, CTDSPL, FAM129A, TNFAIP3, PARP14, DUSP6, HIPK3, BMP4, SPRED2, LATS2, CAMK2N1, SPRY2
positive regulation of response to external stimulus	GO:0032103	2.46E-03	PTGER4, GBP5, CXCL8, CSF1, IFNB1, CXCR4, HMGB1, ZC3HAV1, DDX60, CHD2, PTGS2, ETS1, TNFRSF1A, OASL, C3, NFKBIA, STK24, CAMK2N1, APOH, TMSB4X, PLCG2, FYN
regulation of response to biotic stimulus	GO:0002831	1.00E-02	GBP5, CD274, ARG2, IFNB1, RIG-I, TNFAIP3, HMGB1, ZC3HAV1, IFIT1, DDX60, PARP14, OASL, C3, HERC5, PLCG2, FYN, TRIM38, BIRC3
positive regulation of apoptotic process	GO:0043065	3.67E-03	CD274, JUN, IFNB1, GADD45A, DCUN1D3, HMGB1, PTGS2, SOD2, DUSP6, IFIT2, TNFRSF1A, BMP4, FOSL1, CYLD, RYBP, LATS2, FAP, CHEK2, TP53BP2, ARL6IP5, PMAIP1, ATF3, ATF4
regulation of inflammatory response	GO:0050727	3.67E-02	PTGER4, PLK2, TNFAIP3, PTGS2, ETS1, NFKB1, TNFRSF1A, C3, NFKBIA, CYLD, CAMK2N1, TMSB4X, PLCG2, FYN, PIK3AP1, BIRC3
small molecule biosynthetic process	GO:0044283	1.51E-02	CRTC2, ASAH1, HMGCS1, GOT1, SLC1A3, MSMO1, PTGS2, SRR, AMACR, DHFRL1, CBS, OSBP, CYP1A1, PLCG2, ALDH18A1, BCO1, ALOXE3, ATF3, ATF4

Term	GO ID	FDR	Genes
response to oxidative stress	GO:0006979	4.78E-02	PPP1R15B, JUN, TOR1A, GPX8, TNFAIP3, PTGS2, SOD2, ETV5, FOSL1, RCAN1, STK24, STC2, ARL6IP5, NCOA7, FYN, ATF4
regulation of cellular response to stress	GO:0080135	1.36E-03	PSMD10, PPP1R15B, KLHL15, FMR1, SEMA3A, HMGB1, PTGS2, SPRED2, CHEK2, SPP1, ARL6IP5, PMAIP1, FYN, B2M, MAP4K4, RMI2, ARG2, GADD45A, PLK2, SOD2, HIPK3, BMP4, CYLD, NR4A3, STK24, CREBRF, NCOA7, SMAP2, ATF4
cellular response to cytokine stimulus	GO:0071345	3.80E-03	NRP2, ASAH1, CXCL8, CSF1, CXCR4, IFIT1, IFIT3, IFIT2, OASL, NFIL3, MAT2A, IRAK2, TMSB4X, CCNL1, GBP4, GBP5, IFNB1, FZD4, ETV3, NFKB1, TNFRSF1A, NFKBIA, CXCL11, LRCH1, IFNE, SPRY2, CRLF2, VAMP3, BIRC3
innate immune response	GO:0045087	2.68E-03	CSF1, HMGB3, HMGB1, ZC3HAV1, IFIT1, DDX60, IFIT3, IFIT2, OASL, C3, HERC5, IFIH1, IFNL2, IFNL1, PLCG2, FYN, B2M, IFNL3, GBP4, GBP5, ARG2, IFNB1, RIG-I, PARP14, ISG20, CYLD, CH25H, TRIM38, ULBP2, CFB, VAMP3
regulation of cytokine production	GO:0001817	1.39E-02	PTGER4, CD274, TNFAIP3, HMGB1, ZC3HAV1, PTGS2, C3, IFIH1, IFNL1, TMSB4X, PLCG2, BTN2A3P, B2M, MAP2K3, GBP5, ARG2, IFNB1, RIG-I, NFKB1, CD2AP, CYLD, FERMT1, NR4A3, FAP, TRIM38, ATF4, CRLF2
positive regulation of protein phosphorylation	GO:0001934	2.75E-02	PSMD10, CSF1, FMR1, PELI2, FAM129A, PIK3R3, PTGS2, SLC8A2, C3, IFNL1, CHEK2, OSBP, PLCG2, FYN, MAP2K3, IFNB1, FZD4, AKTIP, PLAUR, IGF2, LIF, PARP14, TNFRSF1A, BMP4, IFNE, SPRY2
regulation of cell adhesion	GO:0030155	2.17E-02	CD274, CXCL8, CSF1, CXCR4, HMGB1, CHD2, ETS1, SLC7A1, RND1, IFNL1, ABL2, FYN, HOXA7, B2M, MAP4K4, ARG2, EGR3, IFNB1, FZD4, PLAUR, IGF2, LIF, BMP4, FERMT1, NR4A3, FAP, MDGA1
negative regulation of cell population proliferation	GO:0008285	4.28E-02	CD274, JUN, ARG2, CXCL8, WARS, LIF, TNFAIP3, ETV3, PTGS2, SOD2, ETS1, ING1, IFIT3, BMP4, TGFBR3, FOSL1, FERMT1, IFNL1, FAP, APOH, MED31, SPRY2, SLC16A2, B2M
positive regulation of transcription by RNA polymerase II	GO:0045944	5.23E-03	HDAC5, CSRNP1, CRTC2, EHF, KMT2C, HMGB1, ETS1, HOXD10, SUPT6H, ZNF208, HEY2, HOXA7, EGR2, JUN, EGR3, IFNB1, RIG-I, IGF2, LIF, NFATC2, RFX3, ZFY, SUPT5H, ELL2, ETV5, NFKB1, TNFRSF1A, NFKB2, BMP4, NFKBIA, FOSL1, KLF6, NR4A3, AGO2, CREBRF, TAF4B, NCOA7, SMAP2, ATF3, ZNF597, ATF4
positive regulation of gene expression	GO:0010628	2.85E-02	PTGER4, CD274, CDC123, CXCL8, CSF1, FMR1, FAM129A, PIK3R3, HMGB1, ZC3HAV1, PTGS2, ETS1, C3, IFIH1, IFNL1, NFIL3, NOCT, HEY2, PLCG2, B2M, GBP5, WARS, RIG-I, LIF, NFATC2, BMP4, FERMT1, NR4A3, FAP, AGO2, SPRY2, RBM24, ATF3, ATF4, CRLF2

Term	GO ID	FDR	Genes
negative regulation of response to stimulus	GO:0048585	9.35E-03	PTGER4, PSMD10, PPP1R15B, CXCL8, KLHL15, SEMA3A, TNFAIP3, PTGS2, SPRED2, IFNL1, APOH, CHEK2, TMSB4X, HEY2, GRB10, SPP1, ABL2, FYN, MAP2K3, RMI2, ARG2, IFNB1, FZD4, PLK2, PLAUR, CRIM1, LIF, SOD2, PARP14, DUSP6, HIPK3, NFKB1, CD2AP, TNFRSF1A, BMP4, TGFBR3, NFKBIA, RCAN1, CYLD, FERMT1, LATS2, NR4A3, CNOT2, CREBRF, SPRY2, NCOA7, TRIM38, ATF3
positive regulation of signal transduction	GO:0009967	1.30E-02	CSF1, SEMA3A, GORAB, PELI2, TNFAIP3, CXCR4, HMGB1, ZC3HAV1, DDX60, OASL, C3, SPRED2, IFNL1, GRB10, ARL6IP5, PLCG2, PMAIP1, FYN, MAP4K4, MAP2K3, SPAG9, JUN, IFNB1, FZD4, GADD45A, PLK2, PLAUR, IGF2, LIF, AKR1C2, PARP14, NFKB1, TNFRSF1A, BMP4, TGFBR3, CYLD, FERMT1, SPRY2, TRIM38, PIK3AP1, MAP3K14, ATF3, STX1A, CRLF2, BIRC3
regulation of intracellular signal transduction	GO:1902531	2.27E-02	PSMD10, TRIO, CSF1, SEMA3A, ARHGEF28, PELI2, TNFAIP3, HMGB1, ZC3HAV1, DDX60, PTGS2, SLC8A2, OASL, SPRED2, CHEK2, TMSB4X, ARL6IP5, PLCG2, ABL2, PMAIP1, FYN, MAP4K4, MAP2K3, SPAG9, JUN, FZD4, GADD45A, PLK2, PLAUR, IGF2, LIF, AKR1C2, SOD2, DUSP6, HIPK3, CD2AP, TNFRSF1A, BMP4, NFKBIA, RCAN1, CYLD, DNMBP, SPRY2, TRIM38, PIK3AP1, MAP3K14, ATF3, BIRC3
regulation of cellular component organization	GO:0051128	1.50E-02	NRP2, FMR1, TMEM97, HMGB1, CHD2, ING1, RND1, TMSB4X, OSBP, DENND5A, CCNL1, B2M, TSPYL2, GBP5, RMI2, WARS, PLAUR, CD2AP, TNFRSF1A, PISD, CH25H, MAK, STX1A, PTGER4, PSMD10, MTMR3, SAR1A, SEMA3A, DCUN1D3, MYCBP2, CXCR4, C3, ADAMTS16, SPP1, PLCG2, ABL2, TBC1D14, PMAIP1, FYN, WHAMM, SNX7, MAP4K4, SPAG9, TOR1A, LRRN2, FZD4, PLK2, CRIM1, IGF2, LIF, NFATC2, BMP4, CYLD, FERMT1, STK24, FAP, CNOT2, PLEKHM1, SPRY2, RAB5A, MDGA1

Table S6: GOBP terms enriched in A549 IFNR TKO MAVS KO cells upon 5'ppp-dsRNA stimulation.

Gene ontology (GO) terms for biological processes enriched in A549 IFNR TKO MAVS KO cells synchronously stimulated with 5'ppp-dsRNA (8 hour over 0 hour time point). False discovery rate (FDR) < 0.05. GOBP term enrichment analysis was performed with PANTHER.

Term	GO ID	FDR	Genes
platelet-derived growth factor receptor signaling pathway	GO:0048008	4.66E-02	CSRNP1, NR4A3, TIPARP, ARID5B, VEGFA
regulation of blood vessel endothelial cell migration	GO:0043535	2.47E-02	MAP2K3, HDAC5, STARD13, SPRED1, GADD45A, ETS1, EPHA2, VEGFA
transcription by RNA polymerase II	GO:0006366	3.30E-02	PCID2, VDR, GLIS3, SUPT5H, ETS1, ELL2, SUPT6H, GTF2H5, NFKB1, CDK7, NFIL3, NOCT, GTF2IRD1
regulation of lipid metabolic process	GO:0019216	4.94E-02	RUBCN, PANK2, MTMR3, IDH1, AKR1C3, NR1D1, NFKB1, SOD1, RNF213, NR4A3, AADAC, SNAI2, PIP4K2B, TRIB3, PDK2
protein phosphorylation	GO:0006468	2.79E-02	TRIO, TNKS, IL24, NUAK2, EEF2K, RSRC1, ABL2, CCL2, NEK1, PDK2, MAP2K3, BRD2, RIOK3, MMD, STRADB, LIF, CSNK1D, BRAF, GTF2H5, CDK7, NR4A3, SIK3, TRIB3, MAP3K14, EPHA2
positive regulation of transcription by RNA polymerase II	GO:0045944	2.35E-03	HDAC5, CSRNP1, TNKS, ZBTB49, CEBPG, GLIS3, SIX1, ETS1, SUPT6H, RELA, ARNTL, SBNO2, SERTAD1, SESN2, EPC1, MEF2D, SOX4, KLF10, KDM6B, EGR2, VDR, LIF, INHBA, ARID3B, NR1D1, SUPT5H, ELL2, NFKB1, JMJD6, FOSL2, VEGFA, NFKB2, NFKBIA, FOSL1, CDK7, NR4A3, AGO2, REL, LHX4, SMAP2
cellular response to stress	GO:0033554	2.93E-04	HILPDA, EEF2K, C17orf53, FAM162A, SESN2, UIMC1, CHAC1, CCNL1, PDK2, MAP2K3, KLF10, KDM6B, RMI2, USP43, HSBP1, STRADB, MAPK8IP3, DDIT4, MCM3, SDE2, TRIB3, SLC29A1, EPHA2, OSER1, PPP1R15B, MTMR3, WDR45B, FAM129A, SAMHD1, RELA, ARNTL, NUAK2, PRDX1, PMAIP1, MCL1, TOR1A, GADD45A, AKR1C3, BRAF, GTF2H5, NFKB1, VASN, VEGFA, SOD1, NFKBIA, CDK7, TRIM39, REL, CPEB4
regulation of phosphorylation	GO:0042325	2.11E-02	PPP1R15B, IL24, FAM129A, CHD2, EFNA5, SOCS2, SPRED1, PRRC1, EEF2K, SERTAD1, OSBP, SESN2, SNX9, PIP4K2B, CCNL1, MAP2K3, TSPYL2, SPAG9, RUBCN, MMD, GADD45A, STRADB, LIF, CSNK1D, BRAF, INHBA, VEGFA, SOD1, EREG, CDK7, TRAF4, IFNE, DDIT4, SMCR8, TRIB3, GPRC5C, EPHA2
regulation of intracellular signal transduction	GO:1902531	1.33E-02	TRIO, ARHGEF28, LPAR1, OTUD7B, DENND3, SIPA1L2, RELA, ARNTL, CYTH3, SPRED1, SYNGAP1, PRDX1, SESN2, ABL2, CCL2, PMAIP1, LMCD1, SOX4, PDK2, MCL1, MAP2K3, SPAG9, PCID2, STARD13, RIOK3, GADD45A, LIF, AKR1C3, BRAF, NR1D1, ARHGAP26, DUSP8, MAPK8IP3, VEGFA, SOD1, NFKBIA, CYLD, TRIM39, TRAF4, DDIT4, SIK3, REL, SNAI2, SMCR8, TRIM38, MAP3K14, EPHA2

Term	GO ID	FDR	Genes
cellular response to chemical stimulus	GO:0070887	2.47E-03	NRP2, IFITM2, IL24, HILPDA, SIX1, EEF2K, FAM162A, SESN2, CCNL1, SOX4, PDK2, MAP2K3, KDM6B, CBR1, GSTO1, STX8, ARID5B, CSNK1D, EREG, OAS1, IFNE, DDIT4, TRIB3, SLC29A1, EPHA2, RBM22, OSER1, HDAC5, LPAR1, EFNA5, RELA, ARNTL, SOCS2, UGCG, FAM83G, SBNO2, LARP1, NFIL3, PRDX1, ABL2, CCL2, PMAIP1, SYT5, EGR2, TOR1A, TIPARP, RIOK3, VDR, SMURF1, AKR1C3, BRAF, INHBA, NR1D1, FAM213A, NFKB1, VASN, VEGFA, SOD1, ABTB2, NFKBIA, NR4A3, AADAC, ID1, CYP1A1, SNAI2, SMAP2, CPEB4
negative regulation of cellular metabolic process	GO:0031324	1.99E-02	BHLHE41, ZBTB21, OTUD7B, SIX1, PRDM1, LAPTM4B, SPRED1, SESN2, UIMC1, EPC1, PIP4K2B, CHAC1, LMCD1, SOX4, AASS, KLF10, TSPYL2, RUBCN, RMI2, PCID2, HSBP1, ARID5B, EREG, DDIT4, SMCR8, TRIB3, PPP1R15B, HDAC5, TNKS, ZBTB49, GLIS3, FAM129A, SUPT6H, RELA, ARNTL, SBNO2, LARP1, NFIL3, NOCT, MCL1, SPAG9, LRRN2, VDR, GADD45A, CRIM1, AKR1C3, INHBA, NR1D1, SUPT5H, YY1AP1, NFKB1, VEGFA, GON4L, RYBP, NR4A3, TRIM39, AGO2, ID1, SNAI2, GTF2IRD1, SIM2, CPEB4
negative regulation of macromolecule metabolic process	GO:0010605	1.46E-02	BHLHE41, ZBTB21, OTUD7B, SIX1, SMG9, PRDM1, LAPTM4B, SPRED1, ZC3H7A, SESN2, UIMC1, KPNA7, EPC1, CHAC1, LMCD1, SOX4, AASS, KLF10, TSPYL2, RMI2, PCID2, HSBP1, ARID5B, EREG, OAS1, DDIT4, SMCR8, TRIB3, PFDN6, EPHA2, PPP1R15B, HDAC5, TNKS, ZBTB49, GLIS3, FAM129A, SUPT6H, RELA, ARNTL, SBNO2, LARP1, NFIL3, NOCT, SPAG9, TIPARP, LRRN2, VDR, GADD45A, CRIM1, INHBA, NR1D1, SUPT5H, YY1AP1, NFKB1, VEGFA, CYLD, GON4L, RYBP, NR4A3, TRIM39, AGO2, ID1, REL, SNAI2, GTF2IRD1, SIM2, CPEB4
regulation of catalytic activity	GO:0050790	4.17E-02	TRIO, TBC1D3B, SIPA1L2, SPRED1, SYNGAP1, FAM162A, SESN2, PIP4K2B, CCNL1, PHACTR4, MAP2K3, TSPYL2, RUBCN, PCID2, MMD, STRADB, EREG, AGAP9, TBC1D3, OAS1, AGAP6, TRAF4, AGAP5, SMCR8, TRIB3, GPRC5C, EPHA2, PPP1R15B, TNKS, ARHGEF28, LPAR1, DENND3, AGAP4, EFNA5, SOCS2, CYTH3, PRRC1, SERTAD1, APOH, ABL2, CCL2, PMAIP1, SNX9, RSU1, SRGAP1, STARD13, VDR, GADD45A, CRIM1, ARHGAP26, NFKB1, VEGFA, SOD1, CDK7, SMAP2

Term	GO ID	FDR	Genes
multicellular organism development	GO:0007275	1.96E-02	PANK2, TRIO, PRDM1, LIPA, SYNGAP1, KPNA7, CHAC1, CCNL1, SOX4, MAP2K3, PCID2, ARID5B, MAPK8IP3, JMJD6, EREG, KIAA1217, ALDH3A2, DDIT4, EPHA2, YTHDC1, LPAR1, EFNA5, SUPT6H, SOCS2, ADAMTS16, UGCG, SBNO2, RNF213, PRDX1, EGR2, STARD13, TOR1A, TIPARP, VDR, IDH1, CRIM1, LIF, BRAF, INHBA, NR1D1, ARHGAP26, FOSL2, NFKB2, FOSL1, FA2H, GON4L, NR4A3, AGO2, ID1, CYP1A1, SNAI2, LHX4, SIM2, CSRNP1, NRP2, BHLHE41, OTUD7B, SIX1, SMG9, CHD2, RND1, SPRED1, EEF2K, PHACTR4, KLF10, KDM6B, BRD2, PARP6, HSBP1, POMGNT2, TRAF4, IFNE, SLC29A1, HDAC5, TUFT1, CEBPG, ODC1, SAMHD1, FSTL1, PTHLH, RELA, ARNTL, SRR, NFIL3, CCL2, ALOXE3, MEF2D, CMTM7, IRX5, AKR1C3, MPP5, PTPN14, YY1AP1, VEGFA, SOD1, RYBP, MAMLD1

Table S7: GOBP terms enriched in A549 IFNR TKO IRF3 KO cells upon 5'ppp-dsRNA stimulation.

Gene ontology (GO) terms for biological processes enriched in A549 IFNR TKO IRF3 KO cells synchronously stimulated with 5'ppp-dsRNA (8 hour over 0 hour time point). False discovery rate (FDR) < 0.05. GOBP term enrichment analysis was performed with PANTHER.

Term	GO ID	FDR	Genes
nucleotide-binding oligomerization domain containing signaling pathway	GO:0070423	2.48E-02	NFKBIA, CYLD, ITCH, TNFAIP3
negative regulation of type I interferon production	GO:0032480	7.72E-03	CYLD, ITCH, CAD, REL, CACTIN, RELB
response to vitamin D	GO:0033280	3.60E-02	VDR, STC2, SPP1, TRIM25, STC1
NIK/NF-kappaB signaling	GO:0038061	1.95E-03	PSMA6, REL, TNFRSF10B, IKBKE, BIRC2, NFKB2, BIRC3, RELB
positive regulation of response to endoplasmic reticulum stress	GO:1905898	1.79E-02	ERN1, RNFT2, DDIT3, HERPUD1, NFE2L2, BBC3
receptor signaling pathway via JAK-STAT	GO:0007259	7.92E-03	SOCS2, STAT5A, IFNL2, IFNL1, CCL2, IFNL3, JAK1
I-kappaB kinase/NF-kappaB signaling	GO:0007249	4.36E-03	NFKBIA, PRDX4, IRAK2, REL, IKBKE, BIRC2, BIRC3, RELB
cellular response to hydrogen peroxide	GO:0070301	2.43E-03	ERN1, OSER1, KDM6B, PCNA, SIGMAR1, PRKCD, TNFAIP3, CYP1B1, NFE2L2
arachidonic acid metabolic process	GO:0019369	2.58E-02	PLA2G4C, CYP1A1, AKR1C3, CYP1B1, ABHD6, DAGLB, ALOXE3
positive regulation of reactive oxygen species metabolic process	GO:2000379	1.56E-02	ITGAM, GADD45A, PRKCD, CAD, AKR1C3, CYP1B1, SOD2, NFE2L2
negative regulation of NF-kappaB transcription factor activity	GO:0032088	4.07E-03	NFKBIA, PSMD10, CYLD, ITCH, IRAK2, DDIT3, CAD, TNFAIP3, CYP1B1, CACTIN
regulation of cyclin-dependent protein serine/threonine kinase activity	GO:0000079	6.07E-03	PSMD10, CDK7, LATS2, CCNE1, GADD45A, TNFAIP3, PROX1, NR2F2, CDC25A, EGFR
endothelial cell differentiation	GO:0045446	2.87E-02	KDM6B, CLIC4, CXCR4, STC1, PROX1, NR2F2, MYD88, ICAM1
cellular response to interleukin-1	GO:0071347	5.26E-03	PSMA6, CXCL8, IRAK2, TNIP2, CAD, CCL2, CACTIN, GBP2, MYD88, NFKB1, NKX3-1
intrinsic apoptotic signaling pathway	GO:0097193	1.09E-03	BCL2A1, PRKCD, TNFRSF10B, AEN, SOD2, BBC3, ERN1, DDIT3, CASP4, TP53BP2, SPP1, CYP1B1, CD24, IKBKE
cellular response to alcohol	GO:0097306	5.00E-02	KLF9, DAG1, AKR1C3, CYP1B1, AKR1C2, INHBA, EFNA5, SOD2
positive regulation of I-kappaB kinase/NF-kappaB signaling	GO:0043123	8.07E-04	NEK6, LPAR1, TNFRSF10B, ZC3HAV1, FKBP1A, TRIML2, TNIP2, REL, TRIM25, TRIM14, ROR1, AJUBA, IKBKE, MYD88, BIRC2, BIRC3
regulation of viral life cycle	GO:1903900	1.97E-02	IL32, CXCL8, ZNFX1, TRIML2, LAMP3, MPI, TRIM25, TRIM14, PROX1, ZC3HAV1, IFNL3
circadian rhythm	GO:0007623	4.93E-02	KLF10, GPR176, NOCT, BHLHE40, KLF9, ID1, CRY1, BHLHE41, PROX1, RELB
cellular response to tumor necrosis factor	GO:0071356	7.61E-03	CXCL8, CAD, TRAF1, NFKB1, NFKBIA, PSMA6, CCL2, CYP1B1, CACTIN, GBP2, BIRC2, NFE2L2, BIRC3, NKX3-1
response to endoplasmic reticulum stress	GO:0034976	3.09E-03	PPP1R15B, TOR1A, CXCL8, SYVN1, ATG10, FAM129A, TNFRSF10B, HERPUD1, BBC3, ERN1, STC2, DDIT3, CASP4, TRIM25, ATF3, NFE2L2

Term	GO ID	FDR	Genes
cellular response to biotic stimulus	GO:0071216	4.38E-03	NOTCH2, PPP1R15B, CXCL8, CAD, ATG10, TNFAIP3, CXCL3, CXCL2, NFKB1, NFKBIA, IRAK2, TNIP2, DDIT3, CCL2, CACTIN, MYD88
regulation of innate immune response	GO:0045088	9.03E-03	KLRC2, KLRC3, CAD, TNFAIP3, SERPINB9, RASGRP1, EREG, PSMA6, ZNFX1, SIN3A, CACTIN, IKBKE, BIRC2, APPL1, NFE2L2, BIRC3
glycerophospholipid biosynthetic process	GO:0046474	4.41E-02	UVRAG, PIGU, INPP1, PLA2G4C, PIK3CD, MTMR4, SOCS2, ITPKC, LPCAT4, LPCAT3, PIP4K2A, CHPT1, AJUBA
cellular response to lipid	GO:0071396	9.16E-05	CXCL8, TNFAIP3, STC1, CXCL3, EFNA5, NR3C1, CXCL2, EGFR, PGRMC2, IRAK2, DAG1, SPP1, ABL2, CCL2, CYP1B1, LDLR, NKX3-1, VDR, CAD, AKR1C3, AKR1C2, INHBA, NFKB1, NFKBIA, NR4A3, TNIP2, KLF9, PADI2, CACTIN, MYD88
response to hypoxia	GO:0001666	1.26E-02	GATA6, CXCR4, STC1, VEGFC, SOD2, BBC3, NR4A2, PSMA6, PLAU, STC2, CYP1A1, PGK1, CD24, AJUBA, BIRC2, NFE2L2, NKX3-1
cytokine-mediated signaling pathway	GO:0019221	2.85E-03	STAT5A, CXCL8, CXCR4, GPR75, TRAF1, TYK2, CXCL3, CXCL2, EREG, NFKBIA, UGCG, PSMA6, IRAK2, TNIP2, IFNE, CCL2, IKBKE, MYD88, BIRC2, APPL1, JAK1, BIRC3
positive regulation of cellular catabolic process	GO:0031331	1.56E-03	RNFT2, PSMD10, TNFAIP3, RNF19B, ZC3HAV1, HERPUD1, NKD2, NOCT, PHKG2, PIP4K2A, SNX9, LDLR, EXOSC2, CTSC, UVRAG, PRKCD, SAMD4A, ITCH, TRIML2, AGO2, TRIM14, DAGLB, RBM24, OPTN, NFE2L2
regulation of apoptotic signaling pathway	GO:2001233	9.25E-03	PSMD10, STRADB, PRKCD, SYVN1, TNFAIP3, TXNDC12, TRAF1, INHBA, SOD2, HERPUD1, ICAM1, BBC3, NR4A2, CYLD, DDIT3, RFFL, CTSC, ATF3, NFE2L2, NKX3-1
alcohol metabolic process	GO:0006066	1.97E-02	IPPK, HMGCS1, GOT1, INPP1, IDH1, AKR1C3, AKR1C2, ALDH3A2, SDR16C5, ACLY, ITPKC, ALDH1B1, CYP1A1, SPP1, SC5D, CYP1B1, PCBD1, LDLR
regulation of mitotic cell cycle phase transition	GO:1901990	3.46E-02	PCID2, NEK6, INTS3, INHBA, INO80, CDC25A, EGFR, PSMA6, CDK7, TFDP1, SIN3A, UIMC1, CYP1A1, NABP2, CCL2, ZNF655, APPL1
positive regulation of protein kinase activity	GO:0045860	1.16E-02	PSMD10, STRADB, PRKCD, TNFRSF10B, VEGFC, PROX1, EFNA5, RASGRP1, EGFR, EREG, EFNA1, ERN1, MOB3C, PRRC1, DAG1, SPRY2, SNX9, ITGB1BP1, CD24, AJUBA, BMPR1A
cellular response to hormone stimulus	GO:0032870	3.79E-03	GATA6, STC1, EFNA5, NR3C1, SOCS2, UGCG, PGRMC2, CYP1B1, APPL1, NKX3-1, STAT5A, GOT1, PRKCD, CAD, AKR1C3, AKR1C2, SERPINB9, INHBA, NFKB1, NR4A2, LATS2, NR4A3, KLF9, PADI2, NFE2L2
response to molecule of bacterial origin	GO:0002237	4.70E-02	CXCL8, MPI, CAD, TNFAIP3, CXCL3, SOD2, CXCL2, NFKB1, NFKBIA, IRAK2, TNIP2, NOCT, CYP1A1, CCL2, CACTIN, CD24, MYD88

Term	GO ID	FDR	Genes
inflammatory response	GO:0006954	5.78E-03	NOTCH2, SERPINA3, CXCL8, TNFAIP3, CXCR4, PIK3CD, CXCL3, RASGRP1, CXCL2, LIPA, RELB, IRAK2, CASP4, NFKBIZ, SPP1, CCL2, KDM6B, PLA2G4C, CAD, NFKB1, ITCH, NFX1, TNIP2, REL, MYD88, NFE2L2
positive regulation of apoptotic process	GO:0043065	9.66E-03	NOTCH2, PRR7, ITGAM, GATA6, PIK3CD, BBC3, TP53BP2, CCL2, CYP1B1, PHLDA1, CTSC, NKX3-1, VDR, GADD45A, PRKCD, AKR1C3, TNFRSF10B, INHBA, SOD2, FOSL1, CYLD, RYBP, LATS2, DDIT3, ATF3
negative regulation of apoptotic process	GO:0043066	2.24E-04	NOTCH2, PSMD10, ANKLE2, BCL2A1, GLO1, GATA6, TNFAIP3, TXNDC12, EGFR, HERPUD1, ICAM1, UNG, SOCS2, SIN3A, ALKBH1, LAMP3, CCL2, RFFL, TXNDC5, IER3, PCID2, ARG2, GABRA5, STRADB, PRKCD, SYVN1, SERPINB9, SOD2, MAPK8IP3, NFKB1, EFNA1, NR4A2, ITCH, TNIP2, ID1, PPT1, SPRY2, RGL2, STK40, BIRC2, NFE2L2, BIRC3
cellular response to organic cyclic compound	GO:0071407	4.95E-02	GNAZ, VDR, CAD, AKR1C3, STC1, INHBA, EFNA5, NR3C1, EGFR, NFKB1, SSH1, PGRMC2, NR4A3, SIN3A, KLF9, ID1, CYP1A1, DAG1, SPP1, PADI2, CCL2, CYP1B1, NKX3-1
blood vessel development	GO:0001568	4.99E-02	NOTCH2, EGR2, CLIC4, CXCL8, CAD, GATA6, VEGFC, PROX1, NR2F2, ARHGAP24, EREG, EFNA1, FOSL1, DDIT3, ID1, DAG1, CCL2, CYP1B1, ITGB1BP1, CKLF, LDLR, BMPR1A, NKX3-1
protein ubiquitination	GO:0016567	1.83E-02	RNFT2, TNFAIP3, DCAF8, RNF19B, UBE2L6, HERPUD1, SOCS2, MED31, TRIM25, RFFL, SKP1, BRAP, RNF24, SYVN1, TRAF1, FANCF, KCTD9, PSMA6, ITCH, RYBP, RNF169, TRIML2, NEURL3, NFX1, ASB9, TRIM14, BIRC2, NFE2L2, BIRC3
regulation of hydrolase activity	GO:0051336	2.85E-03	PPP1R15B, SERPINA3, PRR7, TMED10, PCNA, MPI, LPAR1, TBC1D3E, RASAL2, EFNA5, SIPA1L2, RASGRP1, EGFR, BBC3, ABR, LAMP3, ABL2, CCL2, TBC1D14, SNX9, RFFL, TBC1D22B, NKX3-1, BRAP, PCID2, PRKCD, CRIM1, SERPINB9, HSPE1, SERPINB8, ARHGAP24, EFNA1, FKBP1A, TBC1D3K, PPT1, SPRY2, ITGB1BP1, AJUBA, RGL2, BIRC2, BIRC3
protein phosphorylation	GO:0006468	3.39E-02	TRIO, PIK3CD, EGFR, ABR, PRDX4, IRAK2, PHKG2, ABL2, CCL2, MAP3K8, IKBKE, JAK1, UVRAG, NEK6, STRADB, CAD, PRKCD, TYK2, ERN1, CLK1, CDK7, LATS2, NR4A3, CCNE1, MAK, CRY1, TAF4B, ROR1, STK40, BMPR1A
negative regulation of cellular protein metabolic process	GO:0032269	1.09E-02	PPP1R15B, SERPINA3, PRR7, TMED10, MPI, FAM129A, TNFAIP3, SUPT6H, GLG1, SDR16C5, SPRED2, LAPTM4B, SIN3A, NOCT, LAMP3, IGF2BP2, RFFL, EXOSC2, PCID2, GADD45A, PRKCD, CRIM1, SAMD4A, SERPINB9, NR2F2, SERPINB8, NFKB1, EFNA1, FKBP1A, RYBP, LATS2, AGO2, CRY1, SPRY2, ITGB1BP1, CACTIN, RBM24, BIRC2, BIRC3

Term	GO ID	FDR	Genes
negative regulation of signal transduction	GO:0009968	2.79E-03	CXCL8, TNFAIP3, TXNDC12, HERPUD1, ICAM1, SPRED2, DAG1, PIP4K2A, APPL1, NKX3-1, STRADB, PRKCD, CAD, PSMA6, LATS2, DDIT3, CRY1, PADI2, ITGB1BP1, CACTIN, AJUBA, OPTN, ATF3, PSMD10, PPP1R15B, DLX2, MTMR4, EGFR, GLG1, NKD2, SOCS2, LPXN, ABL2, RFFL, BRAP, SYVN1, CRIM1, NR0B1, NFATC1, SOD2, ARHGAP24, EFNA1, FKBP1A, NFKBIA, NR4A2, CYLD, ITCH, SPRY2, NFE2L2
negative regulation of transcription by RNA polymerase II	GO:0000122	3.29E-02	NOTCH2, PSMD10, DLX2, PCNA, BHLHE41, GATA6, ZBTB1, NR3C1, ETS2, SDR16C5, SIN3A, KLF10, HSBP1, VDR, GADD45A, NFATC2, NR0B1, PROX1, NR2F2, ZNF79, NFKB1, EFNA1, NR4A2, EID1, RYBP, NR4A3, NFX1, CCNE1, DDIT3, BHLHE40, ID1, CRY1, ZNF436, CKLF, AJUBA, SIM2, ATF3
response to organonitrogen compound	GO:0010243	4.45E-02	GNAZ, PCNA, GATA6, TNFAIP3, CXCR4, STC1, EGFR, HERPUD1, ICAM1, SOCS2, SIN3A, STC2, CASP4, DAG1, TRIM25, CYP1B1, LDLR, APPL1, STAT5A, EGR2, TOR1A, GOT1, PRKCD, SYVN1, NFKB1, SSH1, EREG, NFKBIA, FOSL1, NR4A2, NR4A3, ID1, CRY1, MYD88, BIRC2, NFE2L2
regulation of cell differentiation	GO:0045595	4.16E-03	TRIO, CD83, BHLHE41, SPRED2, SIN3A, NFKBIZ, DAG1, KLF10, PCID2, TFE3, PROX1, EREG, EID1, PSMA6, ISL2, DDIT3, ITGB1BP1, RBM24, BIRC2, NOTCH2, DLX2, GATA6, ZBTB1, CXCR4, EFNA5, RASGRP1, SUPT6H, EGFR, GLG1, SOCS2, IFNL1, NOCT, SPP1, LDLR, EGR2, VDR, CRIM1, NFATC2, VEGFC, NFATC1, INHBA, FAM213A, SOD2, NFKB1, EFNA1, NFKBIA, ITCH, BHLHE40, NBR1, ID1, SPRY2, CD24, CKLF, BMPR1A, NFE2L2
positive regulation of gene expression	GO:0010628	3.92E-02	TMED10, CXCL8, CD83, GATA6, FAM129A, PIK3CD, ZC3HAV1, RASGRP1, EGFR, NKD2, RELB, IFNL1, C1QTNF1, NOCT, LAMP3, CYP1B1, LDLR, IKBKE, APPL1, NKX3-1, IL32, VDR, SAMD4A, NFATC2, INHBA, TYK2, EREG, ERN1, NR4A3, LPCAT3, DDIT3, AGO2, ID1, PADI2, SPRY2, CLEC4E, RBM24, MYD88, ATF3, BMPR1A, NFE2L2
positive regulation of transcription by RNA polymerase II	GO:0045944	4.43E-02	CRTC2, GMEB1, DLX2, NUFIP1, DOT1L, GATA6, NR3C1, SUPT6H, EGFR, ETS2, SIN3A, NKX3-1, KLF10, KDM6B, EGR2, VDR, TFE3, NFATC2, NFATC1, PROX1, INHBA, NR2F2, INO80, ELL2, NFKB1, NFKB2, NFKBIA, FOSL1, NR4A2, CDK7, KLF6, TFDP1, NR4A3, TNIP2, DDIT3, AGO2, REL, TAF4B, ITGB1BP1, SSBP2, CKLF, ATF3, BMPR1A, NFE2L2

Term	GO ID	FDR	Genes
cellular macromolecule localization	GO:0070727	2.64E-02	PIGU, TMED10, WDR45B, TNFAIP3, PTPRK, ING1, EGFR, HERPUD1, NKD2, ARL5B, SAMM50, SIN3A, PDZD11, LAMP3, TMEM107, TMSB4Y, TIMM17A, SNX9, STX3, GBP2, EXOSC2, APPL1, SKP1, TIMM8A, TRMT10B, EGR2, PCID2, TOR1A, SEC24A, STRADB, SYVN1, TIMM21, MPP5, MAPK8IP3, COPZ1, NFKBIA, SPCS3, FRMD6, NEURL3, DDIT3, ID1, NABP2, ITGB1BP1, KDELR3, CD24, CKLF, AJUBA, OPTN
immune response	GO:0006955	4.38E-02	PRR7, CXCL8, CD83, ITGAM, MPI, PIK3CD, RNF19B, CXCL3, CXCL2, ICAM1, LAMP3, CASP4, TRIM25, IKBKE, CTSC, JAK1, ARG2, TFE3, PRKCD, CAD, SERPINB9, TYK2, GEM, IFNE, TRIM14, CACTIN, CLEC4E, OPTN, NOTCH2, ZBTB1, CXCR4, ZC3HAV1, RASGRP1, UNG, RELB, IFNL2, IFNL1, HLA-DMB, CCL2, FLNB, GBP2, IFNL3, IL32, KLRC2, NFKB2, CYLD, ITCH, NR4A3, TRIML2, REL, POLR3H, MYD88, BMPR1A
animal organ development	GO:0048513	1.87E-02	CLIC4, PRR7, CXCL8, ITGAM, GORAB, PIK3CD, LIPA, SIN3A, ALKBH1, TMEM107, DAG1, CYP1B1, PIP4K2A, NKX3-1, KLF10, KDM6B, PCID2, ARG2, PROX1, EREG, ISL2, IFNE, B3GNT5, PADI2, ROR1, GARS, ITGB1BP1, CLEC4E, RBM24, STK40, ATF3, KDM7A, BIRC2, NOTCH2, DLX2, PCNA, TUFT1, GLO1, ODC1, GATA6, ZBTB1, CXCR4, STC1, EGFR, GLG1, RELB, SOCS2, ADAMTS16, UGCG, PRDX4, PGRMC2, PDLIM2, STC2, SPP1, CCL2, FLNB, ALOXE3, SLC25A25, CMTM7, STAT5A, SVIL, EGR2, IRX5, VDR, GABRA5, IDH1, SYVN1, AKR1C3, VEGFC, NR0B1, NFATC1, ARPC5, INHBA, NR2F2, SOD2, MPP5, YY1AP1, NFKB2, EFNA1, FKBP1A, FOSL1, NR4A2, KLF6, NR4A3, NPHS1, ID1, CYP1A1, PPT1, SPRY2, CD24, CKLF, SIM2, BMPR1A, MEGF9

Table S8: GOBP terms enriched in A549 IFNR TKO IRF1 KO cells upon 5'ppp-dsRNA stimulation.

Gene ontology (GO) terms for biological processes enriched in A549 IFNR TKO IRF1 KO cells synchronously stimulated with 5'ppp-dsRNA (8 hour over 0 hour time point). False discovery rate (FDR) < 0.05. GOBP term enrichment analysis was performed with PANTHER.

Term	GO ID	FDR	Genes
cellular response to exogenous dsRNA	GO:0071360	4.16E-02	IFIH1, IFNB1, RIG-I
negative regulation of viral genome replication	GO:0045071	4.23E-02	IFIH1, IFNB1, ZC3HAV1, OASL
arachidonic acid metabolic process	GO:0019369	4.13E-02	PLA2G4C, AKR1C3, CYP1B1, ALOXE3
defense response to virus	GO:0051607	5.49E-04	IFIH1, IFNL2, IFNL1, IFNB1, RIG-I, ZC3HAV1, IFIT3, IFIT2, OASL
negative regulation of cell population proliferation	GO:0008285	4.29E-02	TGFBR3, IFNL1, TES, CITED2, TNFAIP3, SPRY2, CYP1B1, SLC16A2, ETS1, IFIT3
innate immune response	GO:0045087	3.10E-02	IFIH1, CH25H, IFNL2, IFNL1, IFNB1, RIG-I, ZC3HAV1, PARP14, IFIT3, IFIT2, OASL
positive regulation of response to stimulus	GO:0048584	4.34E-02	IFNB1, RIG-I, CITED2, AKR1C3, TNFAIP3, INHBB, ZC3HAV1, PARP14, ETS1, OASL, TGFBR3, IFIH1, IFNL2, IFNL1, GRB10, SPRY2, CYP1B1, HBEGF

Table S9: GOBP terms enriched in A549 IFNR TKO cells normalized to IFNR TKO MAVS KO upon 5'ppp-dsRNA stimulation.

Gene ontology (GO) terms for biological processes enriched in A549 IFNR TKO cells normalized to IFNR TKO MAVS KO cells synchronously stimulated with 5'ppp-dsRNA (8 hour over 0 hour time point). False discovery rate (FDR) < 0.05. GOBP term enrichment analysis was performed with PANTHER.

Term	GO ID	FDR	Genes
regulation of type III interferon production	GO:0034344	3.93E-02	IFIH1, RIG-I
branchiomotor neuron axon guidance	GO:0021785	4.98E-02	SEMA3A, MYCBP2
detection of virus	GO:0009597	4.95E-02	IFIH1, RIG-I
positive regulation of RIG-I signaling pathway	GO:1900246	4.41E-03	ZC3HAV1, DDX60, OASL
cellular response to interferon-alpha	GO:0035457	5.22E-03	OAS1, IFIT3, IFIT2
neuron remodeling	GO:0016322	6.28E-03	C3, ANKS1A, RND1
antiviral innate immune response	GO:0140374	1.18E-02	OAS1, RIG-I, IFIT1
positive regulation of interferon-alpha production	GO:0032727	2.09E-02	IFIH1, RIG-I, ZC3HAV1
cellular response to type I interferon	GO:0071357	3.62E-02	OAS1, IFNB1, IFIT1
cellular response to exogenous dsRNA	GO:0071360	6.88E-04	IFIH1, IFNB1, RIG-I, IFIT1
positive regulation of interferon-beta production	GO:0032728	6.32E-03	IFIH1, OAS1, RIG-I, ZC3HAV1
positive regulation of receptor-mediated endocytosis	GO:0048260	1.61E-02	C3, FMR1, PLCG2, B2M
toll-like receptor signaling pathway	GO:0002224	1.73E-02	OAS1, IRAK2, PLCG2, PIK3AP1
cellular response to virus	GO:0098586	1.39E-03	IFIH1, OAS1, IFNB1, RIG-I, FMR1
positive regulation of response to cytokine stimulus	GO:0060760	2.01E-03	IFIH1, CSF1, RIG-I, CXCR4, PARP14
cellular response to lipopolysaccharide	GO:0071222	3.56E-03	CD274, CXCL11, CXCL8, IRAK2, PLCG2, CMPK2, B2M
regulation of innate immune response	GO:0045088	1.42E-02	C3, GBP5, OAS1, IFNB1, PLCG2, FYN, PARP14
negative regulation of cell adhesion	GO:0007162	2.88E-02	CD274, IFNL1, FAP, IFNB1, FZD4, MAP4K4, RND1
negative regulation of viral genome replication	GO:0045071	2.52E-07	ISG20, IFIH1, OAS1, IFNB1, ZC3HAV1, IFIT1, IFNL3, OASL
regulation of leukocyte cell-cell adhesion	GO:1903037	1.48E-02	CD274, IFNL1, EGR3, FAP, IFNB1, IGF2, FYN, B2M
regulation of T cell activation	GO:0050863	1.64E-02	CD274, IFNL1, EGR3, FAP, IFNB1, IGF2, FYN, B2M
negative regulation of immune system process	GO:0002683	4.48E-02	PTGER4, CD274, IFNL1, OAS1, FAP, IFNB1, FYN, PARP14
cytokine-mediated signaling pathway	GO:0019221	1.23E-03	CXCL11, CXCL8, OAS1, CSF1, IFNB1, IRAK2, FZD4, CXCR4, CRLF2, OASL
positive regulation of cell migration	GO:0030335	1.30E-02	CD274, CXCL8, CSF1, FZD4, SEMA3A, PLCG2, CXCR4, PIK3R3, SOD2, MAP4K4
positive regulation of immune response	GO:0050778	7.23E-03	C3, GBP5, CD274, IFNL2, IFNL1, IFNB1, PLCG2, FYN, B2M, IFNL3, CFB
tube morphogenesis	GO:0035239	1.69E-02	CXCL8, EGR3, WARS, CSF1, FAP, FZD4, CXCR4, PIK3R3, DCHS1, HOXD11
positive regulation of protein phosphorylation	GO:0001934	1.53E-04	CSF1, IFNB1, FZD4, FMR1, PLAUR, IGF2, FAM129A, PIK3R3, PARP14, SLC8A2, C3, IFNL1, CHEK2, PLCG2, FYN
cell migration	GO:0016477	1.02E-03	CXCL8, EGR3, SEMA3A, CXCR4, PIK3R3, CD2AP, RND1, CH25H, CXCL11, FAP, GRB10, DCHS1, FYN, ANKS1A, MDGA1

Term	GO ID	FDR	Genes
intracellular signal transduction	GO:0035556	1.97E-02	PTGER4, CXCL8, RIG-I, ARHGEF28, CXCR4, PIK3R3, SOD2, RND1, IFIH1, IRAK2, CHEK2, GRB10, PLCG2, PMAIP1, DCHS1, FYN, MAP4K4
regulation of molecular function	GO:0065009	4.26E-02	CSF1, FMR1, ARHGEF28, MYCBP2, PIK3R3, IFIT1, IFIT2, SLC8A2, OASL, C3, HERC5, RANBP3L, IRAK2, PLCG2, PMAIP1, FYN, B2M, MAP4K4, WARS, RIG-I, FZD4, PLAUR, IGF2, SOD2, HIPK3, OAS1

Table S10: GOBP terms enriched in A549 IFNR TKO cells normalized to IFNR TKO IRF3 KO upon 5'ppp-dsRNA stimulation.

Gene ontology (GO) terms for biological processes enriched in A549 IFNR TKO cells normalized to IFNR TKO IRF3 KO cells synchronously stimulated with 5'ppp-dsRNA (8 hour over 0 hour time point). False discovery rate (FDR) < 0.05. GOBP term enrichment analysis was performed with PANTHER.

Term	GO ID	FDR	Genes
regulation of type III interferon production	GO:0034344	4.83E-02	IFIH1, RIG-I
positive regulation of RIG-I signaling pathway	GO:1900246	6.05E-03	ZC3HAV1, DDX60, OASL
cellular response to exogenous dsRNA	GO:0071360	8.54E-04	IFIH1, IFNB1, RIG-I, IFIT1
negative regulation of viral genome replication	GO:0045071	1.84E-07	ISG20, IFIH1, ZNFX1, IFNB1, ZC3HAV1, IFIT1, IFNL3, OASL
positive regulation of interferon-alpha production	GO:0032727	2.58E-02	IFIH1, RIG-I, ZC3HAV1
cellular response to virus	GO:0098586	2.05E-02	IFIH1, IFNB1, RIG-I, FMR1
regulation of interferon-beta production	GO:0032648	2.13E-02	IFIH1, RIG-I, TRIM38, ZC3HAV1
defense response to virus	GO:0051607	8.22E-12	IFNB1, RIG-I, ZC3HAV1, IFIT1, DDX60, IFIT3, IFIT2, OASL, HERC5, ISG20, IFIH1, IFNL2, IFNL1, ZNFX1, PMAIP1, IFNL3
positive regulation of response to cytokine stimulus	GO:0060760	2.57E-02	IFIH1, RIG-I, CXCR4, PARP14
regulation of defense response to virus	GO:0050688	4.48E-02	HERC5, RIG-I, TRIM38, IFIT1
innate immune response	GO:0045087	1.06E-11	GBP5, IFNB1, RIG-I, ZC3HAV1, IFIT1, DDX60, PARP14, IFIT3, IFIT2, OASL, HERC5, ISG20, IFIH1, CH25H, IFNL2, IFNL1, PLCG2, FYN, TRIM38, ULBP2, B2M, IFNL3, CFB, GBP4
regulation of leukocyte cell-cell adhesion	GO:1903037	1.47E-02	CD274, IFNL1, EGR3, FAP, IFNB1, IGF2, FYN, B2M
regulation of T cell activation	GO:0050863	1.68E-02	CD274, IFNL1, EGR3, FAP, IFNB1, IGF2, FYN, B2M
positive regulation of immune response	GO:0050778	7.01E-03	GBP5, CD274, IFNL2, IFNL1, ZNFX1, IFNB1, PLCG2, FYN, B2M, IFNL3, CFB
cellular response to cytokine stimulus	GO:0071345	8.18E-03	GBP5, CXCL11, IFNB1, FZD4, CXCR4, IFIT1, ETV3, GBP4, IFIT3, IFIT2, CRLF2, OASL
positive regulation of protein phosphorylation	GO:0001934	8.26E-03	IFNL1, IFNB1, FZD4, FMR1, CHEK2, PLAUR, IGF2, PLCG2, PIK3R3, FYN, PARP14, SLC8A2
cell migration	GO:0016477	1.09E-02	EGR3, SEMA3A, CXCR4, PIK3R3, CD2AP, CH25H, CXCL11, FAP, GRB10, DCHS1, FYN, ANKS1A, MDGA1
cellular response to oxygen-containing compound	GO:1901701	3.94E-02	PTGER4, CD274, FZD4, IGF2, PIK3R3, SLC1A3, CXCL11, CHEK2, GRB10, PLCG2, CMPK2, FYN, B2M
cell surface receptor signaling pathway	GO:0007166	1.33E-02	CD274, IFNB1, FZD4, FMR1, SEMA3A, ARHGEF28, PLAUR, IGF2, CXCR4, PIK3R3, OASL, CXCL11, IFNL2, IFNL1, FAP, GRB10, PLCG2, FYN, ANKS1A, IFNL3, CRLF2
regulation of cellular component organization	GO:0051128	4.19E-02	PTGER4, GBP5, WARS, SAR1A, FZD4, FMR1, SEMA3A, MYCBP2, PLAUR, IGF2, CXCR4, CD2AP, CH25H, STK24, FAP, PLCG2, PMAIP1, FYN, MDGA1, B2M, MAP4K4

Table S11: GOBP terms enriched in A549 IFNR TKO cells normalized to IFNR TKO IRF1 KO upon 5'ppp-dsRNA stimulation.

Gene ontology (GO) terms for biological processes enriched in A549 IFNR TKO cells normalized to IFNR TKO IRF1 KO cells synchronously stimulated with 5'ppp-dsRNA (8 hour over 0 hour time point). False discovery rate (FDR) < 0.05. GOBP term enrichment analysis was performed with PANTHER.

Term	GO ID	FDR	Genes
positive regulation of phosphorylation	GO:0042327	3.02E-02	C3, FAP, IGF2, GRB10, PLCG2, FYN, SLC8A2
response to biotic stimulus	GO:0009607	3.15E-02	C3, CD274, CH25H, FAP, PLCG2, FYN, CFB, GBP4
regulation of immune system process	GO:0002682	2.63E-02	C3, CD274, FAP, IGF2, PLCG2, FYN, PIK3AP1, CFB

Table S12: GOBP terms enriched in A549 IFNR TKO IRF3 KO cells normalized to IFNR TKO MAVS KO upon 5'ppp-dsRNA stimulation.

Gene ontology (GO) terms for biological processes enriched in A549 IFNR TKO IRF3 KO cells normalized to IFNR TKO MAVS KO cells synchronously stimulated with 5'ppp-dsRNA (8 hour over 0 hour time point). False discovery rate (FDR) < 0.05. GOBP term enrichment analysis was performed with PANTHER.

Term	GO ID	FDR	Genes
receptor signaling pathway via JAK-STAT	GO:0007259	2.91E-04	STAT5A, IFNL2, IFNL1, CCL2, IFNL3
regulation of endocrine process	GO:0044060	4.51E-02	C1QTNF1, INHBA, NKX3-1
lipopolysaccharide-mediated signaling pathway	GO:0031663	4.76E-02	NFKBIA, IRAK2, CCL2
cellular response to interleukin-1	GO:0071347	9.08E-05	CXCL8, IRAK2, TNIP2, CCL2, GBP2, NFKB1, NKX3-1
intrinsic apoptotic signaling pathway in response to DNA damage	GO:0008630	1.85E-02	BCL2A1, SOD2, IKBKE, BBC3
pattern recognition receptor signaling pathway	GO:0002221	3.50E-03	NFKBIA, CYLD, IRAK2, TNIP2, CLEC4E
positive regulation of lipid transport	GO:0032370	3.97E-02	NFKBIA, C1QTNF1, PRKCD, NKX3-1
positive regulation of apoptotic signaling pathway	GO:2001235	1.48E-02	CYLD, PRKCD, INHBA, NKX3-1, BBC3
cellular response to tumor necrosis factor	GO:0071356	1.16E-03	NFKBIA, CXCL8, CCL2, TRAF1, GBP2, NFKB1, NKX3-1
cytokine-mediated signaling pathway	GO:0019221	2.36E-04	STAT5A, NFKBIA, CXCL8, IRAK2, TNIP2, CCL2, TRAF1, TYK2, CXCL3, IKBKE
inflammatory response	GO:0006954	8.49E-03	NOTCH2, SERPINA3, CXCL8, IRAK2, TNIP2, CCL2, CXCL3, RASGRP1, NFKB1
positive regulation of immune system process	GO:0002684	5.59E-04	NOTCH2, CXCL8, CD83, KLRC3, PRKCD, TYK2, RASGRP1, ICAM1, IFNL2, IFNL1, TNIP2, CCL2, IKBKE, IFNL3
regulation of cell adhesion	GO:0030155	6.27E-03	EFNA1, IFNL1, C1QTNF1, CXCL8, CD83, PLAU, PRKCD, CCL2, TYK2, RASGRP1, RND1
regulation of MAPK cascade	GO:0043408	4.56E-02	NOTCH2, EFNA1, CYLD, C1QTNF1, PRKCD, CCL2, TRAF1, RASGRP1, ICAM1
regulation of response to external stimulus	GO:0032101	3.84E-02	NFKBIA, CYLD, C1QTNF1, CXCL8, PLAU, KLRC3, PRKCD, CCL2, RASGRP1, IKBKE, NFKB1
immune response	GO:0006955	5.69E-04	NOTCH2, IL32, CXCL8, CD83, GCH1, PRKCD, TYK2, CXCL3, RASGRP1, ICAM1, CYLD, IFNL2, IFNL1, CCL2, CLEC4E, GBP2, IKBKE, IFNL3
positive regulation of intracellular signal transduction	GO:1902533	4.42E-02	NOTCH2, EFNA1, C1QTNF1, TNIP2, CCL2, TRAF1, RASGRP1, IKBKE, ICAM1, NKX3-1, BBC3
negative regulation of multicellular organismal process	GO:0051241	4.85E-02	EFNA1, CYLD, DLX2, IFNL1, C1QTNF1, CD83, PLAU, PRKCD, INHBA, NFKB1, NKX3-1
positive regulation of gene expression	GO:0010628	3.88E-02	IL32, IFNL1, C1QTNF1, CXCL8, CD83, FAM129A, INHBA, TYK2, CLEC4E, RASGRP1, IKBKE, NKX3-1
regulation of response to stress	GO:0080134	1.31E-02	GCH1, KLRC3, PRKCD, TRAF1, SOD2, RASGRP1, NFKB1, BBC3, NFKBIA, CYLD, C1QTNF1, PLAU, IKBKE, NKX3-1
negative regulation of response to stimulus	GO:0048585	7.91E-03	DLX2, CXCL8, PRKCD, NFATC1, MTMR4, SOD2, NFKB1, ICAM1, EFNA1, NFKBIA, CYLD, IFNL1, C1QTNF1, PLAU, CCL2, NKX3-1

Table S13: GOBP terms enriched in A549 IFNR TKO IRF3 KO cells normalized to IFNR TKO IRF1 KO upon 5'ppp-dsRNA stimulation.

Gene ontology (GO) terms for biological processes enriched in A549 IFNR TKO IRF3 KO cells normalized to IFNR TKO MAVS KO cells synchronously stimulated with 5'ppp-dsRNA (8 hour over 0 hour time point). False discovery rate (FDR) < 0.05. GOBP term enrichment analysis was performed with PANTHER.

Term	GO ID	FDR	Genes
positive regulation of natural killer cell mediated cytotoxicity	GO:0045954	4.76E-02	KLRC2, KLRC3, RASGRP1
cellular response to interleukin-1	GO:0071347	1.64E-02	IRAK2, TNIP2, CCL2, GBP2, NKX3-1
cytokine-mediated signaling pathway	GO:0019221	1.11E-02	STAT5A, IRAK2, TNIP2, CCL2, TRAF1, TYK2, CXCL3, IKBKE
defense response	GO:0006952	1.10E-03	STAT5A, IL32, SERPINA3, CD83, KLRC2, KLRC3, PRKCD, INHBA, TYK2, CXCL3, RASGRP1, TRIML2, IRAK2, TNIP2, CCL2, CLEC4E, GBP2
positive regulation of intracellular signal transduction	GO:1902533	4.76E-02	EFNA1, C1QTNF1, TRIML2, TNIP2, CCL2, TRAF1, RASGRP1, RGL2, IKBKE, ICAM1, NKX3-1
intracellular signal transduction	GO:0035556	1.17E-02	UNC13A, BCL2A1, PRKCD, NFATC1, TYK2, SOD2, RASGRP1, ABR, IRAK2, RASSF5, CCL2, RGL2, IKBKE, PDE9A, NKX3-1